RATIONAL DESIGN AND ENGINEERING OF QUINONE REDOX MEDIATORS FOR ENZYMATIC BIOELECTROCATALYSIS

By

Lincoln Mtemeri

A DISSERTATION

Submitted to
Michigan State University
in partial fulfillment of the requirements
for the degree of

Chemical Engineering – Doctor of Philosophy

2024

ABSTRACT

Cell-free bioelectrocatalysis has drawn significant research attention as the world transitions towards sustainable bioenergy sources. This technology utilizes electrodes to drive challenging enzymatic redox reactions, such as CO_2 reduction and selective oxidation of lignin biomass. At these bioelectrochemical interfaces, enzymes are rarely capable of direct exchange of electrons with the electrode surface because many redox enzymes harbor cofactors that are buried within protein matrices that act as an electrical insulator. In such cases, electrochemically active small molecules, called redox mediators, have been proven effective in enabling efficient electron transfer by acting as electron shuttles between the electrode and enzyme cofactor. However, the task of selecting suitable redox mediators remains challenging due to lack of comprehensive design criteria. Presently, their design relies on a trial-and-error approach that emphasizes redox potential as the only parameter while overlooking the significance of other structural features. It is crucial to acknowledge that while the redox potential of the mediator serves as a thermodynamic descriptor, it falls short in fully describing the kinetic behavior of redox mediators. This thesis describes efforts in developing strategies for designing and understanding the behavior of redox species using quinone-mediated glucose oxidation by glucose oxidase as a model system.

The work begins by showcasing the application of parameterized modeling – specifically, supervised machine learning – to identify which structural components of quinone redox mediators correlate to enhanced reactivity with a model enzyme, glucose oxidase (GOx). Through this analysis, redox potential and mediator area (or molecular size) were identified as crucial chemical parameters to optimize when designing mediators. The role of other steric parameters (i.e. redox mediator projected area) when accessing GOx via its active site tunnel was investigated further. Using two complementary computational techniques, steered molecular dynamics and umbrella sampling, a rate-limiting step was identified from a series of elementary

steps. Specifically, it was determined that the transport of redox species in the protein tunnel constitutes the rate-limiting step in the overall process.

Utilizing molecular docking and molecular dynamics simulations, a specific quinone-functionalized polymer was examined with the goal of determining why it exhibits activity with glucose dehydrogenase (FAD-GDH) but not with GOx, despite both structurally similar enzymes exhibiting activity to the corresponding freely diffusing mediator. Docking simulations coupled with MD refinement reveal that the active site of GOx is inaccessible to the polymer-bound redox mediator due to the added steric bulk; this contrasts with FAD-GDH which has a wider molecular tunnel to its active site.

This work serves as an exemplary demonstration of employing parameterized modeling in the design and engineering of redox mediators. Although these strategies were developed using GOx as a model system, a similar approach holds promise for designing bioelectrocatalytic platforms involving redox mediators. Additionally, these computational simulations can effectively address fundamental questions where experimental continuum models are inadequate. This integrated effort brings us closer to design of next-generation effective bioelectrodes for mediated bioelectrocatalysis.

This thesis is dedicated to my grandmother, Marceyline Mutemeri aka Mbuya VaLee.
I deeply appreciate your commitment to fostering the value of education from the very beginning.

ACKNOWLEDGEMENTS

I would like to express my heartfelt gratitude to my advisor, Dr. David Hickey for his unwavering guidance and support throughout my PhD journey. His mentorship has been instrumental in shaping me into the scientist and engineer I am today. Working with him has been an honor and I am grateful for the invaluable lessons in conducting good science.

I extend my sincere appreciation to my PhD committee, particularly Dr. Scott C. Barton for his guidance and resources. I also want to thank Dr. S. Patrick Walton, Dr. Daniel Woldring, and Dr. Michaela TerAvest for their support and constructive feedback.

I am thankful for the opportunities provided by the Department of Chemical Engineering, the college, and the university, which have made this journey possible. Special thanks go to my colleagues in the Hickey Lab and other research groups; your support and camaraderie have been invaluable. You are all true superstars.

To my friends and communities who have stood by me during this challenging journey, I am immensely grateful. Your friendship has been a source of comfort during difficult times, reminding me that perseverance and resilience are key – Together, we represent a generation that continuously strives for improvement and progress.

Finally, I wish to dedicate this achievement to my family, with a special mention to my son, Kendric. Your presence has been a constant source of motivation, driving me to strive harder every day. I aspire to set a positive example for you to follow, and I am grateful for your support.

To my grandfather, grandmother who always emphasized the idea of education from my young age “kudya ma Bs”, my aunt, parents, and all relatives who have supported me during times of need, I am profoundly grateful. Your unwavering encouragement and assistance have been invaluable to me, and I deeply appreciate all the efforts you have made to support my journey.

I acknowledge that not everyone may fully grasp the significance of their support, especially as a first-generation college graduate, but I am thankful for the unique challenges and experiences that have shaped my journey.

TABLE OF CONTENTS

Chapter 1: Introduction.

1.1 Introduction to Bioelectrocatalysis

The growing demand for sustainable and environmentally friendly energy technologies continues to drive research and innovation in renewable electrochemical systems, particularly those that facilitate chemical transformations through biological processes, such as bioelectrocatalysis.[1] Bioelectrocatalysis harnesses the merits of electricity and biocatalysts to accelerate valuable chemical transformations in biofuel cells,[2–11] biosensors[11–15] and electrosynthesis.[16–18] Biocatalysts, including enzymes and microbes, excel at driving the oxidation or reduction of chemical bonds in substrates under favorable conditions (mild operating temperatures and pressures), unlike the requirements of their inorganic catalyst counterparts.[8] These oxidoreductase enzymes operate at the electrode interface of the electrochemical system either immobilized or freely diffusing in bulk electrolytes.[19–21] The success of bioelectrocatalysis relies on rapid electron transfer between two key surfaces: the enzyme active site and the inert electrode. As we address the major challenges in enzymatic electrochemical systems development, a fundamental question consistently emerges: How can we design an efficient enzyme-electrode interface capable of enabling high electron transfer rates in both immobilized and freely diffusing systems?

Early research in this field demonstrated that the interface between the enzyme and electrode can be achieved by directly integrating the enzyme onto the electrode interface, enabling direct electron transfer.[20–24] Alternatively, a redox active species can be introduced to facilitate mediated electron transfer. In the case of direct enzyme-electrode interfacing,[22,23,25] heterogeneous electron transfer involves the direct movement of electrons between the enzyme cofactor and the electrode. While direct electron transfer has proven effective in many bioelectrocatalytic systems, challenges arise in enzymes like glucose oxidase (GOx), often referred to as the “Enzyme Ferrari”,[26] where the active site is located deep within a protein shell,

further away from the electrode surface. In such cases, the use of an exogenous molecule, known as a redox mediator, becomes the only means to enable transfer of electrons from the enzyme cofactor to the electrode as depicted in Scheme 1.1.[27]

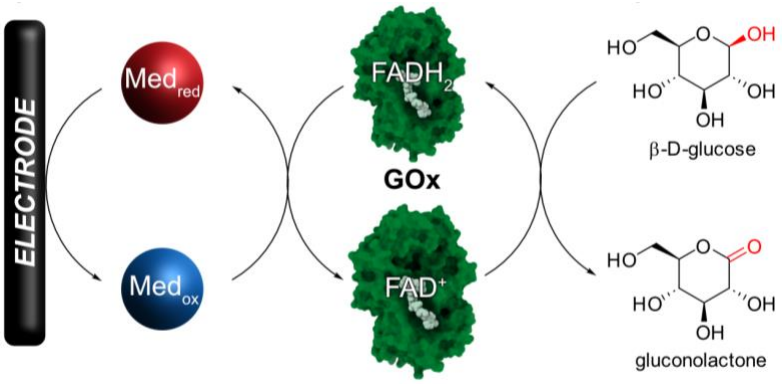

Scheme 1.1 Simplified schematic showing mediated electron transfer between electrode surface via mediator (Med_{red} and Med_{ox}), glucose oxidase (GOx) and substrate glucose. [28]

One central research theme explored to date is the effective design of redox mediators to enhance electron transfer rates at electrode interfaces when using workhorse enzymes like GOx. To design redox mediators for these enzyme interfaces, several criteria must be met. Redox mediators are required to be small enough to fit into the active site of the enzyme, possess an appropriate redox potential (i.e., driving force of the reaction), and maintain electrochemical stability.[16,29] This criterion has been used to select various redox mediators, both organic and inspired by biological electron chains, such as photosynthesis and respiration. These biologically inspired cofactors include redox mediators like flavins, and quinones.[30–32] Another group of redox mediators consist of synthesized artificial small molecules, such as organometallic compounds like ferrocenes[33] and osmium complexes.[15,34,35] These redox mediators have demonstrated success with a wide range of oxidoreductases, spanning nitrogenases,[36–38] hydrogenases,[39–41] and cytochromes P450.[32,42]

Nonetheless, despite the considerable progress in field, there is still a knowledge gap in engineering these redox mediators for efficient electron transfer at the enzyme-electrodes surface. A perspective shared by some scholars suggests that apart from understanding the

significance of redox potential, everything else remains in the realm of "black arts," implying a lack of comprehensive knowledge in this domain.[43] Crucially, employing a structure-function-based understanding to select mediators could offer a promising solution. Thus, this robust approach in selecting mediators could potentially advance next-generation mediated bioelectrocatalysis.

1.2 Bioelectrocatalysis in Application

Electrochemical systems utilizing redox mediators have been constructed for various applications including biosensors, biofuel cells and bioelectrochemical synthesis. The general approach in selecting a redox mediator for these systems is to tailor the mediator's properties to suit the specific application. In the context of enzymatic biofuel cells, where electrodes are responsible for the oxidation or reduction of a substrate, the redox potential of the redox mediator should not be too close to the thermodynamic potential of the enzyme.[2] For reductive reactions, it should be lower, while for oxidative reactions, it should be higher, facilitating a thermodynamically favorable electron transfer between the enzyme cofactor and redox mediator. However, redox potential of the redox mediator should not be too high because that can decrease the overall cell voltage.[2] The cell voltage is significantly influenced by the difference in redox potential between the anodic and cathodic mediators. Therefore, an optimal catalytic rate and cell voltage must be carefully chosen to maximize power output.[5,8]

Following these requirements, enzymatic fuel cells[4] have been designed. As notable examples, Heller and coworkers reduced water at a current density of 5 mA/cm^2 at 0.1 V (NHE) using polymer linked osmium based redox mediators.[44] This study showcased the capability of biofuel cells as high-power output devices. Palmore and Kim designed an enzymatic biofuel cell using 2,2'-azinobis (3-ethylbenzothiazoline-6-sulfonate) ($ABTS^{2-}$) as a mediator and reduced oxygen via a laccase enzyme at 0.5 V versus a saturated calomel electrode (SCE) at the current density of 50 μAcm^{-2}.[5,11,44] This demonstration is particularly novel because the redox potential of O_2/H_2O is 0.75 V vs. SCE, and this system is 0.25 V more negative than the onset reduction of

oxygen. This represents a significantly smaller overpotential compared to what has been reported in other systems. [11]

Apart from large scale applications, these biofuel cells have been studied as implantable power devices.[5] These advancements have found applications in powering temperature sensor systems, various medical devices, including implantable artificial organs, achieving power densities of up to 38 nW/cm².[3] The success of these biofuel cells can largely be attributed to the strategic use of redox mediators. [45]

Building on the same principle, biosensors have been created to leverage the advantages of mediated biocatalytic reactions. The evolution of glucose biosensors for accurate diabetes mellitus detection is rooted in the core concept of bioelectrocatalysis. The earlier model of the biosensors operated by measuring glucose concentration in the blood through the enzymatic action of GOx, which converts glucose, producing hydrogen peroxide as a co-product.[12,46] However, the electrochemical detection of hydrogen peroxide requires high redox potential causing interference from the reaction of electro-active species in the blood.[8] To eliminate this challenge, redox mediators were employed to replace the native mediator oxygen.[47] The oxidation of these redox mediators at the electrode surface provides a signal which is proportional to the concentration of glucose in the blood. The use of exogenous redox mediators enabled the success of glucose oxidase biosensors to precisely detect glucose in the blood at lower overpotentials.

1.3 Background

The biointerface between enzymes and electrodes in electrochemical systems is established through the immobilization of enzymes via crosslinking of polymer chains functionalized with redox mediators.[48–52] This interface facilitates the movement of substrates, ions, and electrons into the matrix for enzymatic reactions. In mechanistic studies where rapid electron transfer characterizes the mediator-electrode interaction, the rate-limiting step is typically determined by the interaction between the redox mediator and the enzyme.[53–57] In that case, the

non-immobilized system is frequently employed for its ease of setup, particularly when conducting fundamental studies of the system. This interaction is analyzed with the enzyme, redox mediator, and substrate all dissolved in an electrolyte solution.

The performance of the interface is evaluated by a combination of factors, including the rate of heterogeneous electron transfer at the electrode-mediator interface, homogeneous electron transfer at the enzyme-mediator-electrode surface, and the rate of enzyme turnover. It is crucial to assess the thermodynamics and kinetics of bioelectrocatalytic systems in this arrangement due to the movement of species resulting from diffusion, concentration gradients, convection (when stirring is introduced), and migration influenced by charge gradients.

1.3.1 Kinetics of Species – Substrate, Enzyme and Redox Mediator

When investigating electrochemical reactions, it is imperative to measure key parameters such as the redox potential (E^0) of redox species (mediators), and current densities. These measurements are commonly performed using various voltammetry techniques, including cyclic voltammetry,[58,59] square wave voltammetry,[60–64] chronoamperometry, and chronopotentiometry. These techniques involve sweeping the potential while observing current response or maintaining a constant potential (or current) while monitoring current (or potential response). Typically, data from these measurements are collected using a three-electrode setup consisting of a working electrode, a reference electrode, and a counter electrode connected to a potentiostat, which perform all the operations. These experiments together with fundamental electron transfer principles are integrated in studying the kinetic and thermodynamic parameters governing the electrochemical reactions.

The kinetics of electron transfer can be explored using fundamental principles such as Michaelis-Menten,[65,66] Fick's Law of diffusion, Faraday's Law,[67] Marcus Theory[68–70] and Butler-Volmer equations.[67,71] To illustrate, consider a reaction involving GOx, central to the work in this thesis, and a redox mediator that reacts with GOx at the interface. This reaction can be mathematically analyzed using these established principles.[72]

The mediated reaction of GOx encompasses the oxidation of glucose to gluconolactone, described by equations 1.1-1.3.[53,57,65] This mediated GOx reaction with glucose follows a ping-pong bi-bi mechanism. In the initial reductive half-reaction, both proton and hydride transfers occur stepwise, leading to the transformation of substrate glucose into the reduced GOx and gluconolactone as shown in reaction 1.1.[73]

The subsequent step involves the reduction of the redox mediator, a process that proceeds stepwise, depending on whether the mediator transfers two or a single electron, as depicted in reaction 1.2. Finally, the reduced redox mediator participates in heterogeneous electron transfer at the electrode, as exemplified in reaction 1.3.

(1.1) GOx-FAD + glucose (S) → GOx-$FADH_2$ + gluconolactone

(1.2) GOx-$FADH_2$ + $Mediator_{ox}$ (M_{ox}) → GOx-FAD + $Mediator_{red}$ (M_{red})

(1.3) $M_{red} \overset{k_1, k_{-1}}{\longleftrightarrow} ne^- + M_{ox}$

where k_1 and k_{-1} are the rate constants of the forward and backward heterogenous electron transfer processes.

At the electrode surface, the heterogeneous electron transfer process allows electrons to flow through the electrode when the oxidation potential of the redox mediator is set. When measured using a potentiostat, this results in a cyclic voltammetry waveform depicting a catalytic current density, denoted as j_c controlled by the independent applied redox potential. The current density, j_c, can be described through the Faradaic relationship, which relates the reaction rate to the current produced and Fick's law of diffusion as expressed in equations 1.4 and 1.5.

(1.4) $$\frac{j_c}{nF} = -D_M \left(\frac{d[M_{ox}(x)]}{dx}\right)_{x=0}$$

(1.5) $$\frac{\partial[M_{ox}(x,t)]}{\partial t} = D_M \frac{(\partial^2[M_{ox}(x,t)])}{\partial x^2} - v_M(x,t)$$

where F, n, D_M, v_M, x, and t are the Faraday constant, the number of electrons transferred, diffusion coefficient of M_{ox}, the enzymatic reaction rate of M_{ox} reduction, distance from the electrode surface

and time, respectively. Assuming the electrode reaction of the mediator couple follows Nernstian behavior, the following boundary conditions can be adopted.

(1.6) $M_{ox}(x=0) = \frac{\eta[M]^*}{(1+\eta_M)}$

where

(1.7) $\eta_M = \left(\frac{([M_{ox}(x)])}{[M_{red}(x)]}\right)_{x=0} = exp\left[\frac{nF}{RT\left(E-E_M^{0'}\right)}\right]$

and

(1.8) $[M_{ox}(x=0)] + [M_{red}(x=0)] = [M]^*$

where $E^{o'}_M$ is the formal potential of the M_{red}/M_{ox} couple and *E* is the applied electrode potential. When the mediator is fully reduced, no enzyme reaction occurs in the bulk phase and the boundary conditions can be summarized as

(1.9) $[M_{ox}(\infty, t)] = 0$

(1.10) $\left(\frac{\partial[M_{ox}(x,t)]}{\partial x}\right)_{x=\infty} = 0$

when the concentration of the substrate is in excess, i.e., $\frac{[S]^*}{K_S} \gg 1$, the reduction rate of M_{ox} is given by

(1.11) $v_M = \frac{\left({}^{n_S}/_{n_M}\right)k_{cat}c}{1+{}^{K_M}/_{[M_{ox}]}}$

where k_{cat}, K_M, K_S and [*E*] are the catalytic constant, Michaelis constants of the mediator and substrates and the bulk concentration of the enzyme, respectively. Under these conditions, the limiting steady state value of the catalytic current density, j_{max}, is given by:

(1.12) $j_{max} = n_M F c_M^* \sqrt{2\left(\frac{n_s}{n_M}\right) D_M c_E^* k_{ET}}$

This equation provides a solution that establishes a correlation between the measured current density, and the homogeneous transfer rate constant between the enzyme cofactor and the redox mediator, k_{ET}. This rate constant serves as a performance metric, indicating the

efficiency of a redox mediator. It offers a means to distinguish between redox mediators with varying levels of activity in this work.

1.3.2 Butler-Volmer and Marcus Theory

After determining all these parameters as demonstrated in previous sections, the theoretical frameworks come into play to elucidate the physical implications of the data. The Butler-Volmer and Marcus approximations are among the prominent theories utilized for this purpose. These theories, Butler-Volmer[67,71] and Marcus-Hush,[68–70,74–77] provide fundamental relationships crucial for understanding electron transfer kinetics especially in the context of donor-acceptor interactions central to this thesis.

1.3.3 Butler-Volmer

According to Butler-Volmer kinetics, the electron transfer rate is exponentially dependent on the applied overpotential, the standard rate constant, k_0, and the transfer coefficient, α.[70,74,78] The overpotential represents the difference between the applied and the formal potential of the redox species, while k_0 signifies the self-exchange electron transfer rate. The transfer coefficient α is a parameter with values ranging from 0 to 1.[70] A value of 0 corresponds to a reactant-like transition state, whereas a value of 1 indicates a product-like transition state as shown in Figure 1.1, considering an electron transfer reaction shown below.[71]

$O + e^- \leftrightarrow R.$

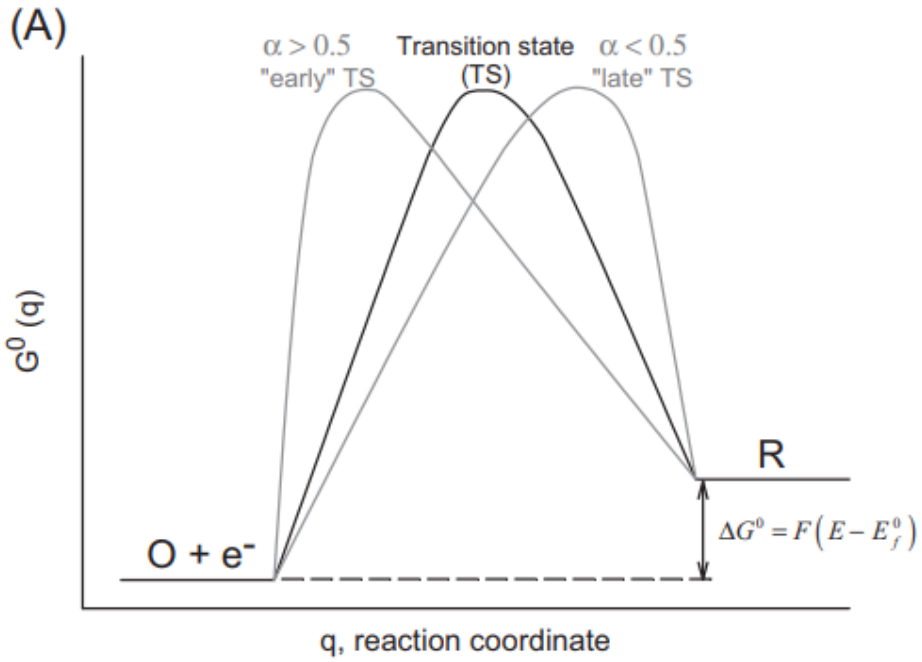

Figure 1.1 The relationship between Gibbs energy and the reaction coordinate for electron transfer reaction as described by Butler-Volmer.[70]

From this model, the rate constant for the reductive and oxidative reaction are described by equation 1.13 and 1.14 respectively.

(1.13) $k_{red}^{BV} = k_0 e^{-\alpha\theta}$

(1.14) $k_{ox}^{BV} = k_0 e^{(1-\alpha)\theta}$

where $\theta = F/RT(E - E^{0\prime})$ and *F, R, T, E* and $E^{0\prime}$ are the Faraday's constant, gas constant, absolute temperature, applied potential and formal potential, respectively.

These mathematical functions are often applied when exploring the relationship between the heterogenous rate constant of electron transfer (related to current density) and variations in overpotential, namely polarization at the electrode. [79,80] However, the utilization of this framework is somewhat limited due to the primary focus of the thesis which is investigating electron transfer between mediators and enzymes.

1.3.4 Marcus-Hush-Chidsey

Similar to the Butler-Volmer (BV) model, the Marcus-Hush-Chidsey (MHC) theory is employed to describe electron transfer between donor and acceptor. This work describes it in the context of homogeneous transfer rates in biological systems.

The Marcus classical theory treats Gibbs free energy surfaces as parabolas, where the transition state corresponds to the interaction of these parabolas as shown in Figure 1.2.

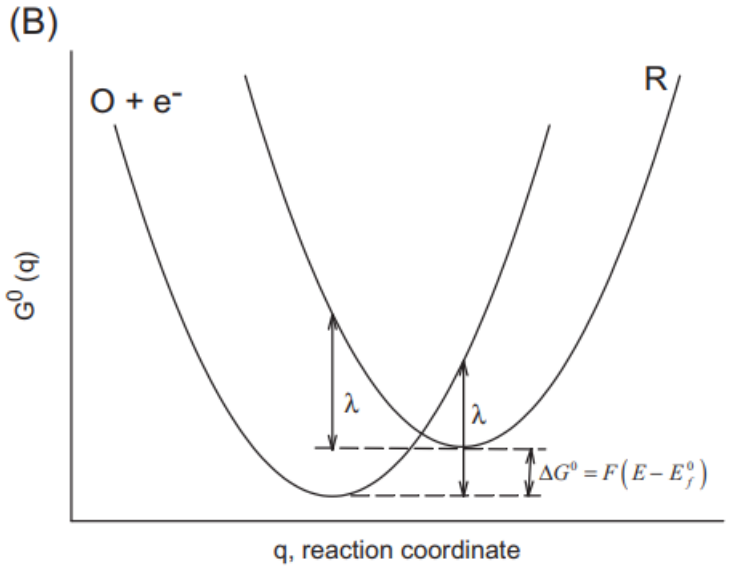

Figure 1.2 The relationship between Gibbs energy and the reaction coordinate for electron transfer reaction as described by Marcus-Hush Theory. [70]

The relatable parameters include the rate constant, k_{ET}, the transmission coefficient, $\kappa(r)$, and the free energy of activation, ΔG^*. The simplified representation is shown in equation 1.15.

(1.15) $$k_{ET} = \kappa(r) \nu e^{-\frac{\Delta G^*}{RT}}$$

The transmission coefficient is associated with the electron coupling matrix which is related to the distance between the orbitals of the reacting redox species, providing a description of the degree of orbital coupling.[68] The term $\kappa(r)$ varies exponentially with distance, r. The collision frequency, ν, depends on the distance between reacting species in the transition state.[81] The free energy of activation which is a function of the free energy of reaction, ΔG^0 and the reorganization

energy, λ, is represented by equation 1.16. This energy comprises contributions from changes in intramolecular vibrations (inner sphere reorganization energy), and changes in solvent orientation coordinates (outer sphere reorganization energy).

(1.16) $\Delta G^* = \frac{\lambda}{4}\left(\frac{1+\Delta G^0}{\lambda}\right)^2$

The free energy of reaction is calculated by the difference in redox potential between the donor and acceptor. It can be calculated by using equation 1.17.

(1.17) $\Delta G^0 = -nF\Delta E^0$

1.3.5 Marcus Theory and Butler-Volmer Comparison

These models have been instrumental in investigating interactions involving electrochemical mediators and in designing mediators with enhanced electron transfer rates. However, they each demonstrate strengths and weaknesses in their practical application.

In the BV model, it is assumed that the reduction rate constant exponentially increases with overpotential, while the Marcus-Hush-Chidsey (MHC) model predicts that the rate constant reaches a limiting value.[67,71] Notably, the MHC model provides a more comprehensive connection between kinetic parameters and the physicochemical characteristics of systems. Both BV and MHC will be used in explaining electron transfer behavior between the enzyme and redox mediator.

1.4 Methods in Mediator Design

1.4.1 Review of Mediator Design

Redox mediators have been developed by various research groups through a range of methods such as empirical iteration. This method is typically considered a traditional trial-and-error approach. It begins with the selection of a core redox molecule, and then chemical properties, such as functional groups, are systematically modified guided by chemical intuition.[82–85] The resulting molecule is synthesized and tested for enhanced bioelectrocatalytic activity. If improvements are not achieved, further fine-tuning of functional groups is performed followed by

additional testing. This iterative process has yielded successful outcomes in numerous studies, leading to the development of organic, inorganic coordination complexes, or organometallic compounds with redox-active ligands.

Early research findings revealed that traditional mediators, including phenazine methosulfate, 2,6-dichloroindophenol, and quinones,[72,86] were among the first diffusible mediators identified to enhance the performance of glucose oxidase (GOx), alongside the native oxygen-based mediator. In a study conducted by Cenas and Kulys, a correlation was established between the rate of electron transfer and the reduction potential of 14 quinone-based redox mediators.[86] The alignment of redox potential with the oxidation rate constant corresponds with Marcus' theory of electron transfer. However, it fails to offer a comprehensive explanation as to why 1,2-naphthoquinone-6-sulfonate, despite having the highest redox potential, doesn't demonstrate a proportionately higher electron transfer rate compared to mediators with lower redox potentials. Such uncertainties hinder the dependable selection of mediators for all intended purposes, as relying solely on one criterion—such as potential in this instance.

A more structured approach called Quantitative Structure-Activity Relationship (QSAR)[87,88] modeling has been employed by other groups to design mediators. Minteer's group designed phenazine mediators for extracellular electron transfer in *E. coli* and concluded that redox potential of these species correlates to the measured output – current density. [89]

The research studies have underscored the pivotal role of redox potential as a crucial parameter in mediator design, while investigations from other groups have highlighted the significance of size in minimizing steric hindrance within the active site of glucose.[43,90,91] Nonetheless, these studies have inherent limitations as they have drawn conclusions from a relatively small subset of mediators, constraining the range of correlations available for determining bimolecular rate constants.

The selected design parameters, whether redox potential or steric hindrance, may not be universally applied. While individual studies have examined the potential influence of redox

potential, coulombic interactions, and steric hindrance as parameters controlling electron transfer rates, they are interrelated and not individually sufficient as standalone design criteria.

1.4.2 Computational Methods

1.4.2.1 Historic Applications

Experimental analysis coupled with electrochemical models described earlier, has proven instrumental in understanding the behavior of electrochemical systems. However, recent advancements have introduced computational methods including first-principles simulations to complement these methods. Computational tools play a crucial role in describing the behavior of electrochemical species, especially when experimental methods are impractical or unfeasible.[92–94]

These computational methods have found wide applications in various domains, including drug design especially in the context of high-throughput screening of potential drug candidates.[95–100] Beyond pharmaceuticals, computational techniques have also been embraced in the design of electrocatalysts, redox mediators and exploring their non-covalent interactions with enzymes.[92,101] This understanding is fundamental for the development of efficient redox mediators for next-generation mediated bioelectrocatalytic systems.

In the domain of molecular design, conventional computational modeling approaches often rely on parameterized modeling techniques. These methods employ fundamental levels of supervised machine learning algorithms, such as linear regression modeling to establish structure-function relationships. These relationships are derived from electronic or structural descriptors obtained from optimized molecular structures using first-principles calculations, such as Density Functional Theory (DFT).

To comprehend the interaction between small molecules and their biocatalysts during chemical reactions (i.e specific binding and unbinding events), computational methods such as docking simulations are normally applied. Molecular docking simulations offer valuable insights into the orientation of redox molecules and their binding within the active sites of enzymes.[102–105]

Additionally, classical molecular dynamics simulations can be employed to investigate the movement and egress of redox mediators within the active site channels. This multifaceted computational approach empowers researchers to gain a deeper understanding of the intricate interplay between enzymes and redox mediators, ultimately facilitating the design of more efficient redox mediators for advanced bioelectrocatalytic systems.

1.4.2.2 Parameterized Modeling

This approach focuses on identifying structural features that govern activity, traditionally referred to as quantitative-structure activity (QSAR) modeling. The method follows a systematic workflow, which typically comprises the following steps:[88,106,107]

(1) Building a diverse library of molecules incorporating diversity in structural and electronic features.

(2) Correlating the electronic and structural descriptors of a molecule under study with a measured property, such as its activity (in this study) using only a define set called training set. Some molecules are reserved for a validation set.

(3) Data preparation (i.e. normalization) and performing a multivariate linear regression model on the training data set to identify parameters that exhibit strong correlations with the measured experimental values. The goodness of fit is assessed through statistical metrics like R^2 or leave-one-out analysis.

(4) Validating the model using the reserved validation set, ensuring that the established linear trends hold.

1.4.2.3 Molecular Docking

Docking simulations are employed in exploring conformational spaces and predicting the binding orientation of small molecules – ligands (or mediators in this work). The conformation and orientation of ligands within the binding site (active site) are assessed using a scoring function, which evaluates the fitness of various ligand poses. This function considers favorable interactions such as hydrogen bonding, electrostatic interactions, and desolvation energies.[102,103,108] Various

search algorithms are utilized to efficiently explore the potential of ligand binding orientations within the active site of the receptor. Gaining insights into how redox mediators bind within the enzyme active site is crucial. Molecular docking techniques can offer precise information regarding the orientation of redox mediators and elucidate their associated contacts.[109]

1.4.2.4 Molecular Dynamics

While molecular docking is valuable for predicting binding positions, conformations, and binding affinities, molecular dynamics goes further by evaluating the dynamic nature of the systems as they evolve towards equilibrium. Molecular dynamics (MD) is a time-dependent simulation of atoms following Newtonian mechanisms. This technique relies on forcefields which is a mathematical model or set of equations used to describe the interactions between atoms and molecules in a system. It defines the potential energy of the system as a function of the positions of all the particles (atoms or molecules) of bonded interactions and non-bonded interactions.[105,110,111]

MD simulations then integrate Newton's laws of motion to determine the configurations of an evolving system with trajectories, positions, and velocities of particles over time. From MD trajectories, properties such as free energy, kinetic behavior and other macroscopic quantities can be obtained.[96]

The key idea of Molecular Dynamics is to study the time-dependent behavior of particles using Newton's second law of motion. From the second-order differential equation, represented in equation 1.18, the force of the particles can be determined.

(1.18) $$f_i(t) = m_i a_i(t) = -\frac{\partial(x(t))}{\partial x_i(t)}$$

where $f_i(t)$, m and t, are the net forces acting on the i^{th} atom with mass m and an acceleration of $a_i(t)$ time, t respectively. In a 3D cartesian space, all vectors for the system with N interacting atoms have the x, y and z component for every atom. This approximation considers massive nuclei, but electrons are averaged.

A potential energy function V(x) arising from the force field (FF) is represented by Equation 1.19[110,112]

(1.19) $V = \sum_i^{bonds} \frac{k_{l,i}}{2}\left(l_i - l_{0,i}\right)^2 + \sum_i^{angles} \frac{k_{\alpha,i}}{2}\left(\alpha_i - \alpha_{0,i}\right)^2 + \sum_i^{torsions} \left\{\sum_k^M \frac{V_{ik}}{2}\left[1 + cos\ (n_{ik}\theta_{ik} - \theta_{0,ik})\right]\right\} + \sum_{i,j}^{pairs} \varepsilon_{ij}\left[\left(\frac{r_{0,ij}}{r_{ij}}\right)^{12} - 2\left(\frac{r_{0,ij}}{r_{ij}}\right)^{6}\right] + \sum_{i,j}^{pairs} \frac{q_i q_j}{4\pi\varepsilon_0\varepsilon_r r_{ij}}$

The first three terms represent intramolecular interactions of atoms which are described by changes in potential energy as a function of bond stretching, bending, and torsions between bonded atoms. These are represented by the summation of bond length (l), angles (α), and dihedral angles (θ) with their reference values (l_0) and (α_0) and force constants k_1 and k_α , respectively. The last two terms of the potential equation represent non-bonded van der Waals and electrostatic forces between atoms, respectively. The van der Waals forces are represented by the Lennard-Jones potential where ε_{ij} defines the energy well depth, and $r_{0,ij}$ is the minimum energy distance summing the van der Waals radii of interacting particles. The electrostatic interaction energy is donated by coulombic potential of atoms with charges q_i and q_j and ε_0 is the permittivity of free space, ε_r is the relative permittivity. [112]

A special type of MD is steered molecular dynamics which works by applying a time-dependent external potential to induce the movement of a molecule along a reaction trajectory.[111–114] This class of MD is useful when modeling the movement of small molecules in confined spaces. The response of the system to the external force is recorded. The interaction of an enzyme active site tunnel with the redox mediator produces information about structure-function relationships involved in the transport of mediator from the bulk solution to the cofactor of the enzyme.

In SMD, the enzyme/redox mediator complex is restrained to a point is space by a potential. The redox mediator restraining force is lifted and a pulling force is applied to the redox mediator to induce the movement following a direction vector. The redox mediator is allowed to explore new contacts along the active site tunnel until it reaches the bulk solution. Microscopic

detail of the interaction of the mediator along the channel can be understood. Assuming a linear reaction coordinate x, the external potential is given by

(1.20) $U = \frac{1}{2}k(x - x_0)^2$

where *k, x_0*, and *x* are spring constant, initial and time-dependent position, respectively. If the redox mediator is pulled by a constant velocity, v, the external force exerted on the system is given by:

(1.21) $F = k(x_0 + vt - x)$

The redox mediator is pulled by the force in (2) which is a harmonic spring with a constant *k* and moving at a velocity.

Through the application of SMD, various system parameters can be explored, encompassing the positions of molecules, their motion behaviors, as well as the forces and potential energies involved. These techniques offer integration opportunities for studying crucial molecular interactions, thereby facilitating the design of efficient mediator bioelectrocatalysis processes.

1.5 Overview of Thesis

This thesis explores the design of redox mediators by investigating structure-function relationships using a comprehensive methodology that combines experimental and computational techniques. This first chapter has introduced some background theories, methods and established concepts that will be employed in subsequent chapters.

In the second chapter, a structured investigation is conducted on a library of quinone-based redox mediators to identify the critical parameters governing electron transfer rates at the electrode interface, particularly with glucose oxidase. Docking simulations and spectrophotometry is employed to understand the nature of electron transfer within GOx.

The third chapter presents an examination of redox mediator transport within the active site tunnel with specific analysis of interactions within the active site of the enzyme (GOx) using

classical MD. This chapter demonstrates efforts in identifying the limiting step in the electron exchange between the model systems—quinone-mediated bioelectrocatalysis with GOx.

In the fourth chapter, the computational methods employed in Chapter 3 are applied in investigating the different electrochemical behavior between quinone-based mediators in glucose dehydrogenase (FAD-GDH) as compared to GOx, despite their similar phyisoelectrochemical properties. These lessons from this comparative analysis are used to guide the design of a more effective quinone modified polymer with GOx.

The fifth chapter offers key lessons and conclusions, summarizing the findings of the thesis and offering insights into potential directions for future research and development in this field. Lastly, an appendix containing raw data, derivations, supplemental work, and optimized coordinates of the molecular species investigated are provided at the end of the thesis.

Chapter 2: Rational Design of Quinone Redox Mediators for Bioelectrocatalysis with Glucose Oxidase.[1]

2.1 Abstract

Successful application of emerging bioelectrocatalysis technologies depends upon an efficient electrochemical interaction between redox enzymes as biocatalysts and conductive electrode surfaces. One approach to establishing such enzyme-electrode interfaces utilizes small redox-active molecules to act as electron mediators between an enzyme active site and electrode surface. While redox mediators have been successfully used in bioelectrocatalysis applications ranging from enzymatic electrosynthesis to enzymatic biofuel cells, they are often selected using a guess-and-check approach. Herein, structure-function relationships in redox mediators that describe the bimolecular rate constant for its reaction with a model enzyme, glucose oxidase (GOx) are identified. Based on a library of quinone-based redox mediators, a quantitative structure-activity relationship (QSAR) model is developed to describe the importance of mediator redox potential and projected molecular area as two key parameters for predicting the activity of quinone/GOx-based electroenzymatic systems. Additionally, rapid scan stopped-flow spectrophotometry was used to provide fundamental insights into the kinetics and the stoichiometry of reactions between different quinones and the flavin adenine dinucleotide ($FAD^+/FADH_2$) cofactor of GOx. This work provides a critical foundation for both designing new enzyme-electrode interfaces and understanding the role that quinone structure plays in altering electron flux in electroenzymatic reactions.

2.2 Introduction

Recent advances in bioelectrocatalysis have drawn considerable interest as an environmentally friendly means of facilitating enzyme catalysed oxidation and reduction reactions

[1] This work was published in collaboration with my PhD Advisor, Dr. David P. Hickey as: “Mtemeri, L.; Hickey, D. P. Model-Driven Design of Redox Mediators: Quantifying the Impact of Quinone Structure on Bioelectrocatalytic Activity with Glucose Oxidase. J Phys Chem B 2023. https://doi.org/10.1021/acs.jpcb.3c03740.”

that will be critical as the world transitions towards a green economy.[1] Enzymatic bioelectrocatalysis employs an electrochemical interface to regenerate enzymatic redox cofactors. While there are some notable examples of direct electrochemical cofactor regeneration, electron transfer between electrode surfaces and many redox enzymes is not possible because their cofactor is buried within an insulating protein matrix.[12,115–117] For such oxidoreductases, an efficient electrode-enzyme interface can be accomplished with the use of small redox-active molecules, known as mediators, to act as electron shuttles as shown in Scheme 2.1.[5,9,81,118] In mediated enzymatic electrocatalysis, electrochemical regeneration of the biological cofactor depends on the use of a compatible redox mediator which exhibits high homogenous electron transfer rates. Currently, the design of mediators is a challenging process that is largely accomplished by using a guess-and-check approach. This method considers only the redox potential of the mediator as a selection criterion, while ignoring the role that its structural features may have in altering enzyme-mediator kinetics.[118] Consequently, there is a need to develop a comprehensive understanding of the relationship between mediator structure and homogeneous electron transfer rates in order to effectively design compatible redox species.

Previous investigations into mediated bioelectrocatalysis have demonstrated practical methods for fabricating efficient mediated enzyme systems, including the use of iterative rational design.[119] However, existing attempts to elucidate relationships between mediator structure and bioelectrocatalytic activity have relied on a small number of redox mediators to extrapolate structure-activity trends. While many prior works have demonstrated the use of a variety of redox active molecules (e.g., osmium complexes, quinones, methyl viologen, cobaltocene and ferrocene derivatives) as enzymatic mediators, these studies often relied on only three to five mediators to evaluate parameters that control electron transfer rates.[14,120,121] As a result, such studies may be less reliable for identifying the design principles necessary to expedite preparation of novel enzymatic redox mediators.

Parameterized modelling of quantitative structure-activity relationships (QSARs) has been employed as a powerful tool for accelerating molecular design in a variety of applications. This approach uses multivariate linear regression analysis to simultaneously examine several structural characteristics of a class of molecules (molecular descriptors) to differentiate ones that correlate to a desired output.[87] The output of parameterized modelling is commonly either catalyst activity or selectivity, while the inputs (molecular descriptors) are comprised of both experimentally measured and computationally determined properties. All inputs and outputs are normalized and then analyzed by multivariate linear regression, which filters out extraneous descriptors while resulting in linear combinations of descriptors that correlate to a desired output. This method has been extensively used in drug design and modelling structure-activity relationships of homogeneous catalysts; however, comparatively little work has been done using parameterized modelling to design redox mediators.[88,89,122–124]

In this chapter, parameterized modelling is utilized to elucidate structure-activity relationships of a class of redox mediators for enzymatic bioelectrocatalysis. Glucose oxidase (GOx) in combination with a variety of quinone redox mediators as a model bioelectrocatalytic system is employed to probe enzyme-mediator QSARs. The enzyme, GOx, contains a non-dissociable flavin adenine dinucleotide ($FAD^+/FADH_2$) cofactor and catalyzes the oxidation of glucose. As a model enzyme, GOx is ideal because its native electron acceptor (molecular oxygen) can be readily supplanted by exogenous redox mediators such as quinones, and its protein structure, mechanism, kinetics, and electrochemical performance are well-established in the literature.[121,125–127]

Similarly, quinones are ubiquitous as both physiological and electrochemical redox mediators, and their role in biological electron transport chains and fundamental electrochemistry has been extensively studied.[128–131] Furthermore, quinones have been reported to undergo electron transfer with several flavoenzymes, including GOx, via an outer-sphere electron transfer mechanism, thus making them ideal model mediators for studying effects of structural features

on apparent electron transfer rates.[119,132–134] In this chapter, the use of parameterized modelling to identify QSARs of a library of 25 structurally diverse quinone-based redox mediators with GOx is demonstrated. The activity of each mediator with GOx was measured using cyclic voltammetry (CV), and structural descriptors were extracted from density functional theory (DFT) computations. Furthermore, a combination of molecular docking simulations and stopped-flow spectrophotometry were used to investigate the role of mediator structure in dictating the mechanism of electron transfer with the $FAD^+/FADH_2$ cofactor in GOx.

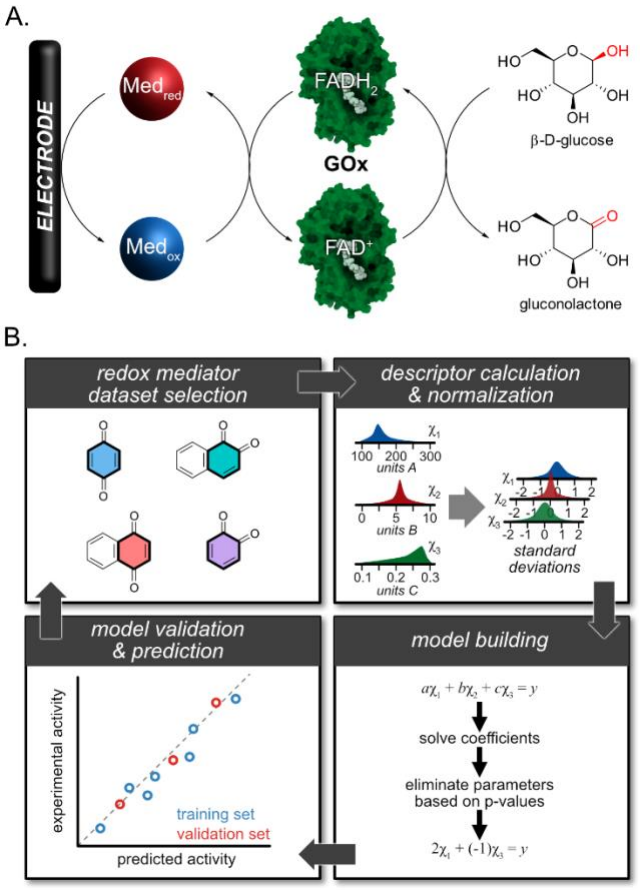

Scheme 2.1 (A) Depiction of mediated bioelectrocatalytic oxidation of glucose by glucose oxidase (GOx). (B) Workflow for the development of quantitative structure-activity relationships (QSARs) of electrochemical redox mediators using parameterized modelling.

2.3 Experimental

2.3.1 Materials

All mediators were obtained from Sigma-Aldrich, TCI Chemicals, and Alfa Aesar and were used as received. Glucose oxidase from Aspergillus niger (E.C. 1.1.3.4, 147,000 U / g solid), D-glucose, and phosphate buffer was purchased from Sigma Aldrich and used as received. In order to ensure consistent enzyme activity, all experiments were performed with glucose oxidase from the same commercial batch. Stock solutions of glucose were prepared 24 hours prior to use and allowed to mutarotate at 4 °C.

2.3.2 Electrochemical characterization

Electrochemical experiments were performed on a Biologic VSP multichannel potentiostat using a standard three-electrode cell with a 3 mm glassy carbon working electrode, a platinum wire counter electrode and a saturated calomel reference electrode (SCE). All experiments were performed with solutions containing 0.5 mM quinone with 0.5% dimethyl sulfoxide (DMSO) to improve the solubility of quinones and 100 mM phosphate buffer at pH 7 and 25 °C. The activity of GOx is not significantly altered in the presence of 0.5% DMSO (as determined by spectroscopic activity assays). Electrochemical characterization of quinone mediators was accomplished using square wave voltammetry (SWV) and cyclic voltammetry (CV). SWV experiments were performed using pulse heights of 10 and 20 mV, pulse width of either 1, 5, 10 or 20 ms and step height of 5 mV. Mediator diffusivities were determined by cyclic voltammetry using 0.5 mM quinone in 100 mM phosphate buffer at 50, 100, 150, 200, 250, and 300 mV s^{-1}. Bioelectrocatalytic current of quinones with GOx was measured by performing cyclic voltammetry (CV) on solutions of 0.5 mM quinone alone, with 10 mM glucose oxidase, and 100 mM glucose at 5 mV s^{-1}. All stock solutions were purged with N_2 for 30 mins prior to use. Additionally, solutions of mediators and GOx/glucose were degassed for further 10 mins prior CV experiments.

2.3.3 Chemical Kinetics and Mediator-Enzyme Stoichiometry Measurements

Homogeneous reaction kinetics between the redox mediator and glucose oxidase, and mediator stoichiometries were measured spectrophotometrically using an Olis Stopped Flow Spectrophotometer. Stopped-flow experiments were performed by rapidly injecting two solutions, one containing dissolved mediator and one containing a mixture of glucose and GOx at a 500:1 molar ratio. The ratio of glucose-GOx was kept constant throughout all stopped-flow experiments. Changes in absorbance were monitored between 320 nm and 420 nm upon rapid mixing of 150 mL glucose/GOx solution (1 mM with respect to glucose) and 150 mL of 1,2-naphthoquinone (0.0, 0.5, 1.0, 1.5, 2.0, 2.5 or 5.0 mM) in the fully oxidized state. The same experiment was repeated using a constant concentration of 1,2-naphthoquinone (1 mM) with varying concentrations of the glucose/GOx solution (0.0, 0.5, 1.0, 1.5, 2.0, 2.5 and 5.0 mM with respect to glucose). For mediator-enzyme stoichiometry, 150 mL of 1 mM oxidized mediator (either 1,2-naphthoquinone or 2,6-dimethoxy-1,4-benzoquinone) was rapidly mixed with variable concentrations of the glucose/GOx solution (0.10, 0.25, 0.30, 0.35, 0.40, 0.50, 0.60, 0.75 ,0.80, 0.90, 1.00, 1.50 and 2.0 mM with respect to glucose for 1,2-naphthoquinone, and 0, 0.25, 0.50, 0.75, 0.85, 1.00, 1.50, 2.00, 2.50, and 3.50 mM with respect to glucose for 2,6-dimethoxy-1,4-benzoquinone). Absorbance spectra were taken every 0.1 s. Solutions were purged with N_2 gas for 10 mins before mixing in the Stopped Flow chamber. All reactants were dissolved in 100 mM phosphate buffer at pH 7 and 25 °C. Quinone solutions were prepared immediately prior to use and shielded from light to minimize photodegradation.

2.3.4 Computational Calculations and Descriptors

All geometry optimization and DFT free energy calculations were performed in Gaussian 09 using the B3LYP level of theory, 6-31+G (d,p) basis set and CPCM (water) solvation model.[135] The free energy of all the charged states required in the calculation of the $2e^-/2H^+$ reduction potential was obtained, and the corresponding redox potentials were calculated as described previously.[136] Descriptors for the multi-variate regression analysis were obtained from geometry-

optimized structures for each mediator in the fully oxidized state from the graphical molecular viewer software, UCSF ChimeraX and Chemcraft. Molecular docking experiments were performed with AutoDock Vina using geometry-optimized mediator structures from DFT computations and GOx (PDB 1CF3). Docking simulations were performed with energy range cutoff, exhaustiveness, and number of modes of 5, 160 and 40, respectively.

2.4 Results and Discussion

2.4.1 Bioelectrocatalysis Characterization

To initiate the investigation, the catalytic current density of 1,2-naphthoquinone (***1***) (Scheme 2.2) as a representative redox mediator for the oxidation of glucose by GOx was measured using cyclic voltammetry. Representative voltammograms of ***1*** in the absence or presence of GOx and glucose are shown in Figure 2.1A. The relative concentrations of **1**:GOx:glucose were selected to ensure the quinone mediator was the limiting reactant for oxidation of glucose by GOx in all cases. The concentration of the mediator was carefully controlled to ensure it was the limiting factor using stoichiometric analysis detailed later in the chapter. In the absence of GOx or glucose, the CV of **1** resulted in two overlapping reversible proton-coupled redox waves (Figure 2.1A). The CV of **1** is unaltered upon addition of GOx, indicating that neither its fully oxidized nor reduced forms react with solvent-accessible residues of GOx. However, upon the addition of glucose, the CV of **1**/GOx results in a sigmoidal shape that plateaus at a steady state current density of approximately 200 $\mu A\,cm^{-2}$. This voltametric response is evidence of a homogeneous electrocatalytic (EC') mechanism and is consistent with previous report of quinones behaving as redox mediators for the bioelectrocatalytic oxidation of glucose by GOx.[137,138]

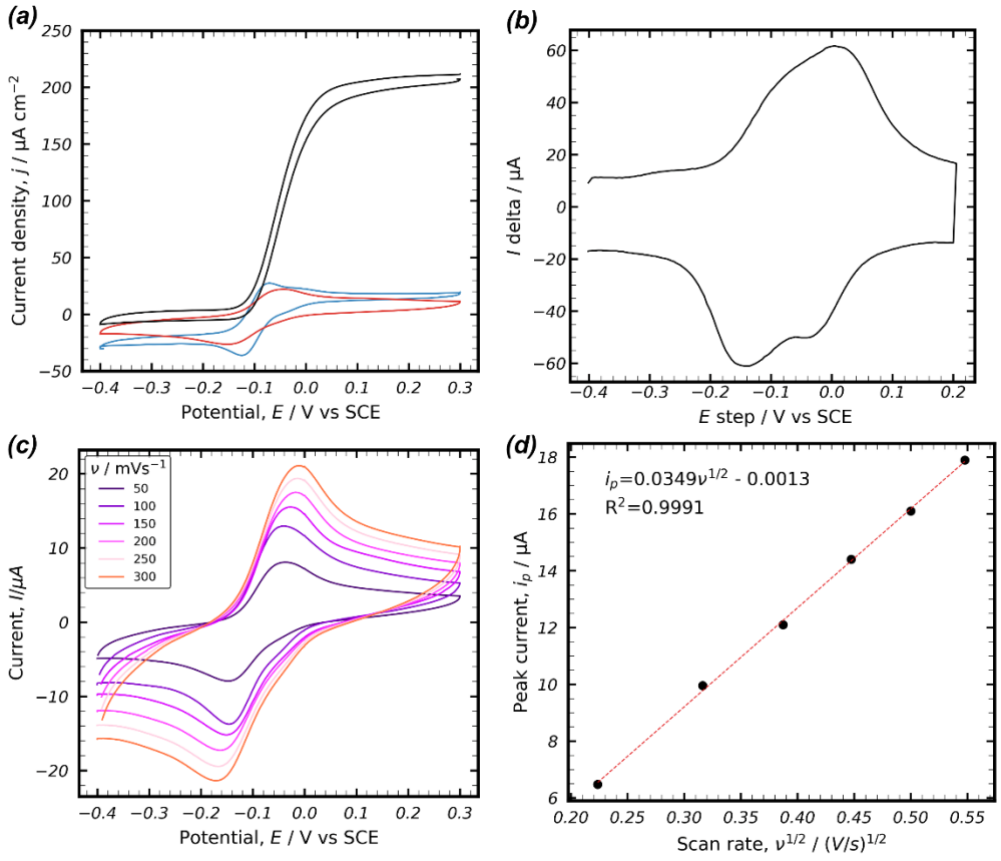

Figure 2.1 CVs showing the catalytic current density of the glucose oxidase-**1** mediated system. The CV in (blue) is 0.5 mM **1**, (red) with 10 μM glucose oxidase and (black) with 100 mM glucose in 100mM phosphate buffer at pH 7 and 5mV/s scan rate. (b) shows the SWV of 0.5 mM **1** showing peak reduction (E_1) and oxidation potential (E_2). The pulse height, width, and step height of 10 mV, 1 ms and -5 mV, respectively. (c) describes the scan rate dependence study and (d) shows the correlation between the square root of scan rate and the respective peak potentials.

The catalytic current density (j_{max}) of **1**/GOx/glucose is an important metric in the context of glucose biosensors and biofuel cells, but it can also be used to determine the rate constant for the reaction between **1** and GOx. This second-order bimolecular rate constant (k) is related to the overall energy barrier for a mediator to regenerate the FAD^+ cofactor of GOx, and it allows for direct comparison between the relative activity of different mediators towards GOx. The bimolecular rate constant of **1** with GOx was calculated using the steady-state analytical solution derived in chapter **1** where j_{max} is given by equation 1.12.

(1.12) $$j_{max} = n_M F c_M^* \sqrt{2\left(\frac{n_s}{n_M}\right) D_M c_E^* k}$$

where k the bimolecular rate constant between the enzyme and **1**, *F* is the Faraday constant, D_M is the mediator diffusivity (assuming that diffusivity of the oxidized and reduced mediator are approximately equivalent), c_E* and c_M* are the bulk concentrations of GOx and mediator, respectively, n_s and n_M represent the number of electrons from the substrate and mediator, respectively (both n_s and n_M were assumed to be 2).[139] The diffusivity of **1** was calculated from variable scan rate CV analysis of data in Figure 2.1C and D. Randles-Sevcik equation was applied and the slope of the line in Figure 2.1D is proportional to the diffusivity. D_M was found to be 5.7×10^{-6} cm^2 s^{-1} from equation 2.1.

(2.1) $i_p = 0.4463n^{3/2}F^{3/2}A\frac{D_M^{1/2}c^*v^{1/2}}{(RT)^{1/2}}$

Where *n, A,* D_M*, R, T,* and *c** are number of electrons transferred, electrode area (cm^2), diffusivity (cm^2 s^{-1}), gas constant (8.3144 J mol^{-1} K^{-1}), temperature (K) and bulk concentration of the mediator (mol cm^{-3}), respectively. Using equation 1.12, the bimolecular rate constant for **1** with GOx was calculated to be $k = 8\times10^4$ M^{-1} s^{-1}.

2.4.2 Structurally Diverse Quinone Mediator Library

Upon establishing a procedure for experimentally determining the bimolecular rate constant for a representative quinone, the same method was applied to a library of 24 additional quinone-based mediators (Scheme 2.2). This library of quinones was selected to include a structurally and electronically diverse set of redox mediators, including substituted naphthoquinones (**1**-**9**), benzoquinones (**10**-**17**), and catechols (**18**-**25**). The calculated bimolecular rate constants for all 25 quinone-based mediators varied significantly from $k = (2.5 \pm 0.8)\times10^1$ M^{-1} s^{-1} for 2-methoxy-1,4-naphthoquinone (***6***) to $k = (2.29 \pm 0.04)\times10^6$ M^{-1} s^{-1} for 4-ethylcatechol (***20***) with naphthoquinones generally exhibiting lower rate constants than benzoquinones, which in turn exhibited lower rate constants than catechols ($k_{NQ} < k_{BQ} < k_{catechols}$).

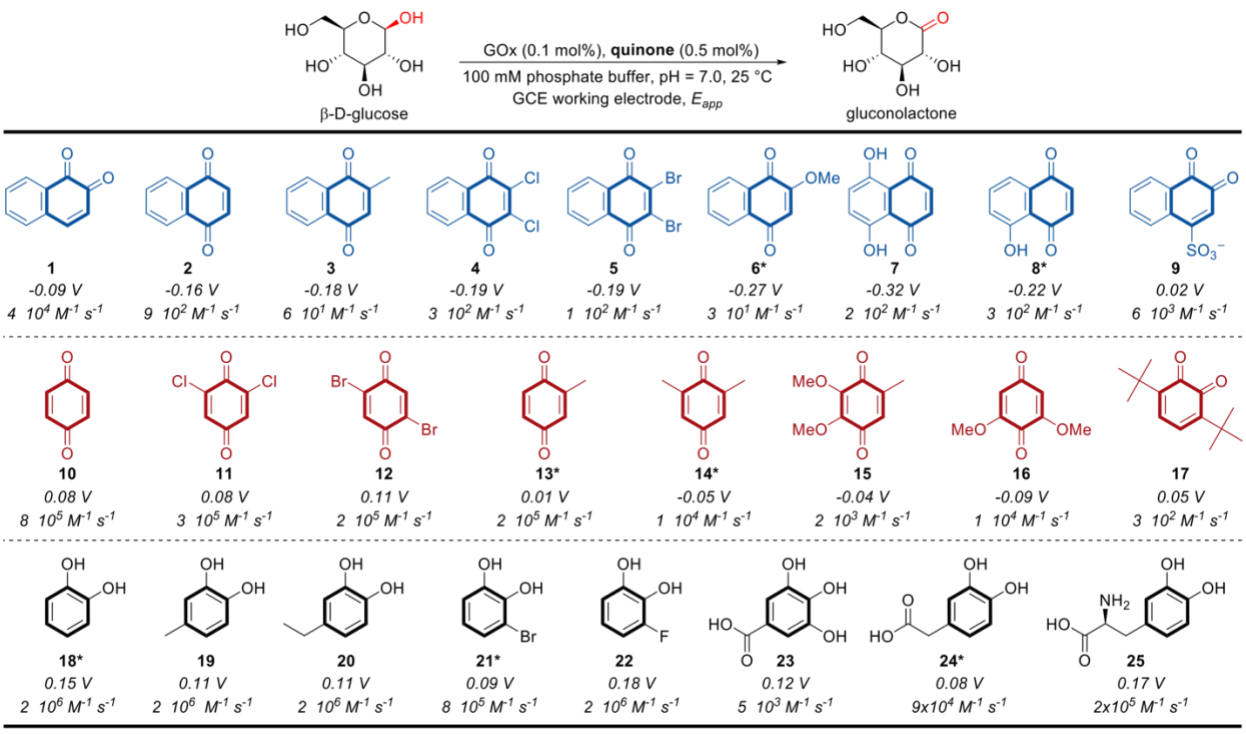

Scheme 2.2 Chemical structures of quinone redox mediators investigated, comprised of naphthoquinones (blue), benzoquinones (red) and catechols (black), with midpoint potentials ($E°_{Q/QH2}$) vs SCE and bimolecular rate constants with GOx (k) reported beneath each structure. Error associated with each rate constant is reported in the supporting information but does not exceed 20% for any reported value with n =*3*.

Previous studies have suggested that unfavorable electrostatic repulsion between the entrance of the GOx active site and negatively charged redox mediators leads to sluggish homogeneous electron transfer kinetics.[134] This can be seen in the direct comparison of **1** (k = (4.0 ± 0.5)×10^4 M^{-1} s^{-1}) and 1,2-napthoquinone-4-sulfonate (***9***, k = (6 ± 1)×10^3 M^{-1} s^{-1}) or the comparison of **20** (k = (2.29 ± 0.04)×10^6 M^{-1} s^{-1}) with 1,2-catechol-4-acetic acid (24, k = (9 ± 1)×10^4 M^{-1} s^{-1}); however, this does not appear to be an absolute trend as the rate constant of 24 is greater than that of **1** despite being anionic at pH 7. Furthermore, it should be noted that the amino acid derivative (**25**) exhibits an exceptionally large rate constant (k = (2.3 ± 0.3) ×10^5 M^{-1} s^{-1}) despite containing a zwitterion at pH 7. These results suggest that repulsive coulombic interactions between the protein surface of GOx near its active site and redox mediators may be partially mitigated with complementary intramolecular ion pairs. Even with these qualitative correlations

among small subsets of mediators, no obvious generalizable trends were found between steric features of quinone mediators and bimolecular rate constants with GOx.

In addition to measuring bimolecular rate constants, the redox potentials were measured for all 25 quinone mediators using square wave voltammetry as shown in Figure 2.1B. (full SWV data included in the Appendix). All quinones studied here exhibited two reversible (or quasireversible) proton-coupled redox events consistent with a square scheme shown in Figure 2.1A, in which the first reduction potential ($E°_{Q/QH•-}$) was always equal to or less than the second reduction potential ($E°_{QH•-/QH2}$). The midpoint potential ($E°_{Q/QH2}$) for each quinone is shown under each corresponding structure in Scheme 2.2. The thermodynamic driving force for mediated bioelectrocatalysis comes from the difference in redox potential between the redox mediator and the flavin cofactor of GOx. For electron transfer to be energetically favorable, the formal reduction potential of the mediator must be greater than that of the $FAD^+/FADH_2$ cofactor. Furthermore, both Butler-Volmer (BV) and Marcus-Hush (MH) kinetic models predict a direct relationship (either linear or approximately linear for BV and MH, respectively) between the log of the bimolecular rate constant, log(k), and the difference in reduction potential of the mediator and $FAD^+/FADH_2$ cofactor (assuming that the reaction is not diffusion controlled).[74,140–144] To test the adherence of a broad set of quinones to these kinetic models, we plotted log(k) and E_m for all quinones (shown in Figure 2.2B). Although some linear trends may be found from isolated quinone derivatives, this plot does not result in the expected correlation. The absence of a strong linear trend between log(k) and $E°_{Q/QH2}$, combined with the lack of an obvious qualitative relationship between mediator sterics and k, compelled us to investigate combinations of molecular descriptors that may be influencing electron transfer rates in the quinone/GOx bioelectrocatalytic system.

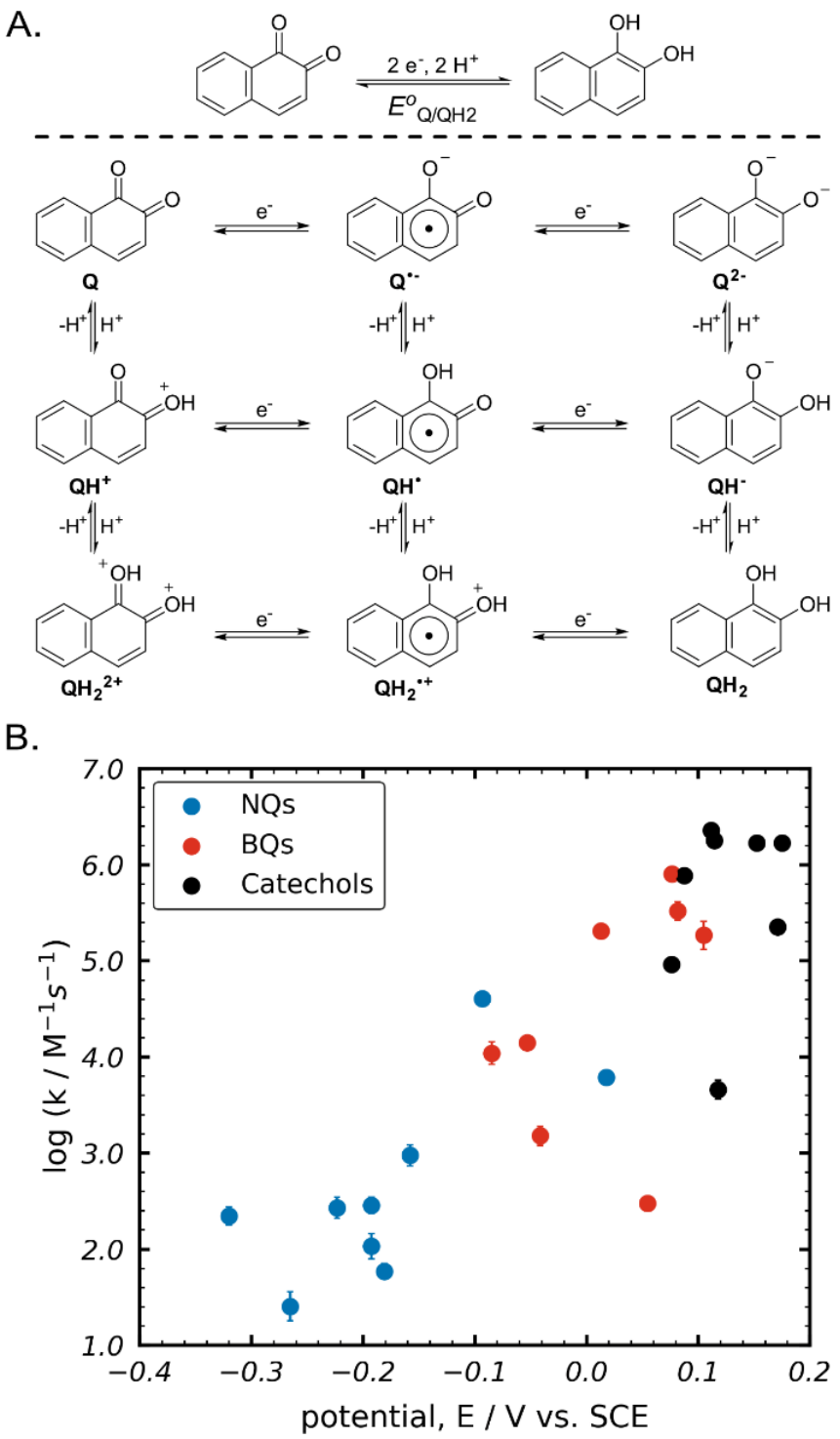

Figure 2.2 (A) Reaction scheme of the overall 2 e^-/2 H^+ electrochemical reduction of a representative quinone to the corresponding hydroquinone. (B) A plot of experimental quinone midpoint potential ($E°_{Q/QH2}$) vs SCE and the corresponding log of bimolecular rate constants broken up into naphthoquinones (●), benzoquinones (●) and catechols (●).

2.4.3 Multivariate Linear Regression Model

In order to identify combinations of quantitative electronic and steric features correlating to the bimolecular rate constant, *k,* a parameterized modelling that uses computationally derived molecular descriptors (inputs) to predict an experimentally observable property (output) was employed. The log of the bimolecular rate constants (i.e., log(*k*)) were used as the experimentally measured property, and descriptors were extracted from geometry-optimized structures of quinones computed using density functional theory (DFT). Computed quinone structures were used to calculate the corresponding $2e^-/2H^+$ reduction potentials using the following equations,[136]

(2.2) $$E^o_{Q/Q^{2-}} = \frac{1}{2}\left[E^\circ{}_{Q/Q^{\cdot-}} + E^\circ{}_{Q^{\cdot-}/Q^{2-}}\right]$$

(2.3) $$E^o_{Q/QH_2} = E^o_{Q/Q^{2-}} + \frac{RT}{2F}\left[pKa_{QH_2} + pKa_{QH^-}\right]$$

The accuracy of computed quinone structures was confirmed by comparing the experimental and computed midpoint potentials for all quinone mediators, as shown in Figure 2.3A (full computational analysis and calculation of redox potentials provided in the Appendix). It should be noted that a constant correction factor was required for halogenated quinones to shift their potential to match the scale of non-halogenated quinones. Similar benchmark adjustments were described previously for computation of structurally diverse quinone derivatives.[136] The resulting plot of experimental and computation potential provides a good linear correlation with an $R^2 = 0.85$, suggesting that the computed quinone structures accurately reflect those measured under experimental conditions.

For parameterized modelling efforts, a subset of 19 quinones we pre-selected as a representative training set for model development, and two mediators were selected from each quinone subclass (i.e., naphthoquinones, benzoquinones, and catechols) for a total of six quinones (**6, 8, 13, 14, 21, 24**) to validate potential models. Several commonly used electronic and steric descriptors were investigated as possible input parameters, including the calculated reduction potential, NBO charges, polarizability, molecular surface area and various Sterimol

parameters (which quantify steric demands and dimensions along different principal axes).[124,145] While several models were found to weakly predict log(*k*) (unused models included in the Appendix), the most compelling and descriptive relationship, based on linearity of fit (R^2) and statistical significance (p-values), was comprised of reduction potential ($E°_{Q/QH2}$) and the projected molecular area of the quinones (*A*). The resulting model is summarized in equation 2.4 and plotted in Figure 2.3C,

(2.4) $$log\ k = 0.38E^{o}_{Q/QH_2} - 0.67A$$

The projected molecular area is defined as the maximum two-dimensional area of the three-dimensional geometry-optimized quinone structure in the oxidized state (depicted in Figure 2.3B). This model easily explains the exceptionally high rate constants exhibited by halogenated benzoquinones and catechols, which have the combination of high redox potential and small size compared to naphthoquinones. These effects are exemplified in compounds with small electron withdrawing substituents (i.e., partially halogenated quinones), such as 3-fluoro-1,2-catechol (**22**), 3-bromo-1,2-catechol (**21**), 2,6-dichloro-1,4-benzoquinone (**11**) and 2,5-dibromo-1,2-benzoquinone (**12**) that all have among the fastest rate constants of the mediators studied. The coefficients associated with each term correspond to their relative weight in the model. Accordingly, the reduction potential coefficient magnitude (*0.38*) is small compared to that of molecular size (*0.67*). This suggests that redox potential is less influential than area when predicting biocatalytic activity; however, high redox potential is still significant as it provides the driving force of the bioelectrocatalytic reaction. Furthermore, the A coefficient is negative while the $E°_{Q/QH2}$ coefficient is positive, indicating that small molecular footprint and high redox potential of the mediator correlates to faster reaction rates with GOx.

To more easily interpret the physical significance of this model, the predicted and experimental values of log(k) were plotted in two regions divided by the statistical

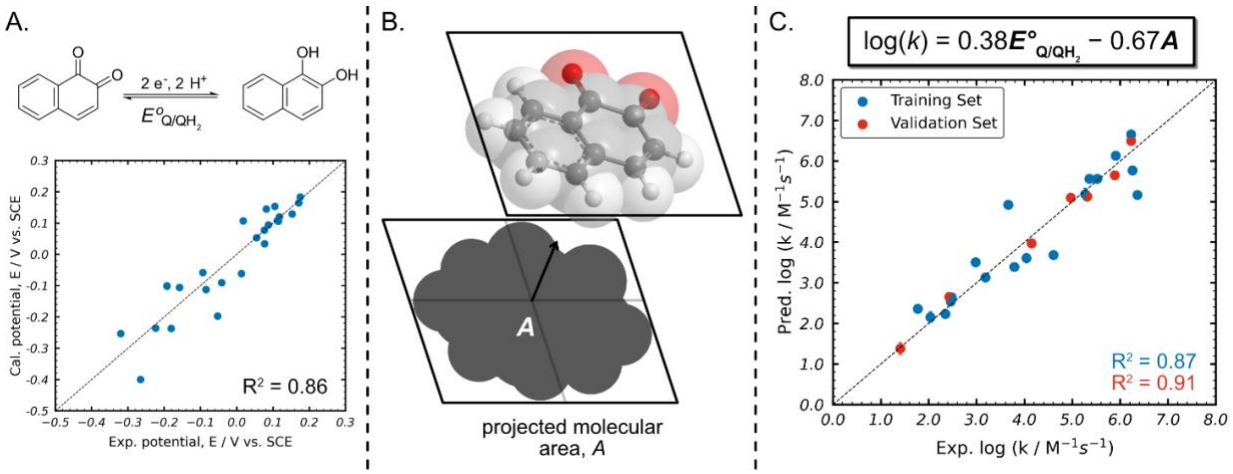

Figure 2.3 (A) A plot comparing experimentally measured quinone reduction potentials ($E°_{Q/QH2}$) and those computed by DFT. (B) Visualization of the projected molecular area of **1**. (C) A plot of experimental and predicted log of the bimolecular rate constants for the training (●) and validation (●) set of quinone mediators based on the newly described QSAR model. Error bars represent one standard deviation from the mean with n = 3.

average of experimental bioelectrocatalytic activity (shown in Figure 2.4 where pink and blue regions denote high and low activity, respectively). The size and color of each point represents the magnitude of either $E°_{Q/QH2}$ or *A* relative to the entire data set. From this visualization, it is easy to identify mediators that deviate from their expected rate constant based on either $E°_{Q/QH2}$ or *A* alone. Furthermore, several mediators whose reaction rates with GOx fall outside of the expected trend according to $E°_{Q/QH2}$. Specifically, 1,4-benzoquinone (***10***), 2-methyl-1,4-benzoquinone (***13***), and 2,6-dimethyl-1,4-benzoquinone (***14***) react slightly more quickly with GOx than expected based on their mild redox potential, whereas **9** and 3,6-di-tert-butyl-1,2-benzoquinone (***17***) react significantly slower than expected despite having a relatively high redox potential. Using a similar data visualization for the projected molecular area, it is apparent that the mild redox potentials of **10**, **13**, and **14** are compensated by their small molecular footprint, while the large projected area of **9** and **17** hinders their ability to access the $FAD^+/FADH_2$ active site of GOx. It should be noted that 3,4,5-trihydroxybenzoic acid (***23***) exhibits a lower rate constant than expected based on both its redox potential and molecular size. Voltametric analysis (provided in the supporting information) suggests that it undergoes a deleterious chemical

reaction upon electrochemical oxidation in the absence of GOx and/or glucose. If the rate of the undesired reaction is greater than that with GOx, this may account for the lower observed bimolecular rate constant than expected based on the QSAR model.

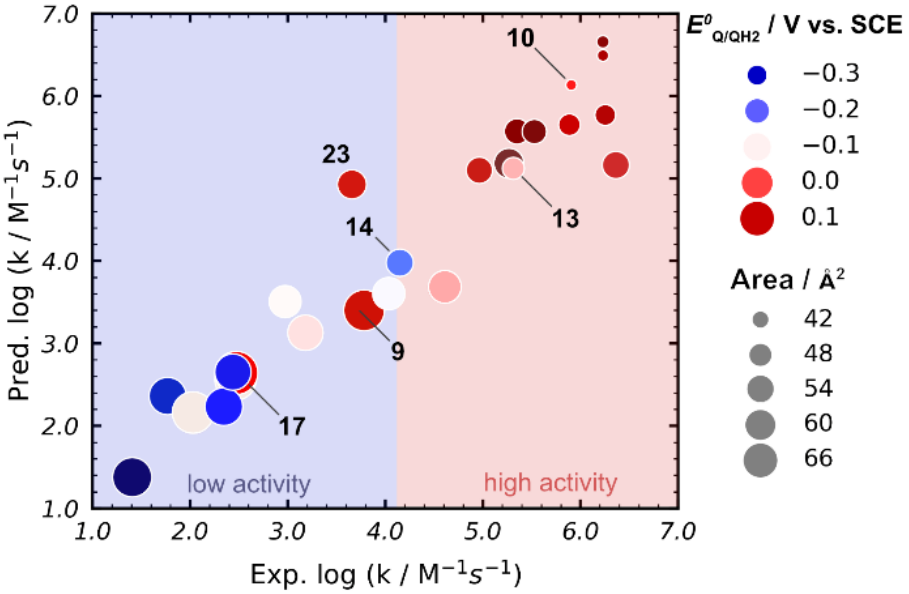

Figure 2.4 Plots of experimental and predicted log of the bimolecular rate constants for all quinone mediators studied, where the colour and size for each point describes the mediator redox potential, $E°_{Q/QH2}$, and the projected area of each corresponding mediator, A, respectively. Plots are divided into high activity (red background) and low activity (blue background) relative to the mean value of experimentally determined log(k) based on the newly described QSAR model.

Comparing the deviations from expected behaviour based on both $E°_{Q/QH2}$ and A, the model demonstrates that the size of a redox mediator plays an important role in describing the ability of a mediator to access the $FADH_2$ cofactor in GOx, which is buried inside the protein shell. This suggests that the overall mediator size may provide sufficient steric hinderance to slow down apparent reaction rates with the GOx active site.[146,147] To further investigate the role that sterics of a mediator play in binding to the active site of GOx, we employed molecular docking simulations.

2.4.4 Understanding Mediator Interactions in GOx Active Site

Both 1,2- and 1,4-quinones occur naturally and are used as exogenous mediators. Given the strong influence of quinone size on the bimolecular rate constant, we considered the

possibility that molecular sterics may influence each of these quinone types differently in the active site of GOx. Molecular docking experiments were performed using Autodock Vina with two representative quinones, 1,2-napthoquinone (***1***) and 2,6-dimethoxy-1,4-benzoquinone (***16***) and GOx with the reduced $FADH_2$ cofactor. Of the 400 docking simulations performed for **1** and **16**, each mediator was found to consistently favor one binding mode with at least one dione oxygen atom in close proximity to the 5-nitrogen atom of $FADH_2$ (depicted in Figure 2.5). Previous molecular docking experiments indicate that the reaction between 1,2-naphthoquinone-4-sulfonate (***9***) and $FADH_2$ in GOx may occur through two oxidative half-reactions that requires a large orientation of the mediator within the GOx active site to allow for subsequent proton transfer.[130,148] Our docking simulation results suggest that, despite its large molecular footprint, **1** is capable of reorientation due to the proximity of both oxygen atoms to the $FADH_2$ center. In contrast, the distal position of dione oxygen atoms on **16** prevent the large reorientation required for protonation following the first redox half reaction. If this were the case, it is expected that **16** should only be capable of one single electron transfer prior to dissociating from the GOx active site in the semi-quinone state. Given the similar bimolecular rate constants between **1** and **16**, it's

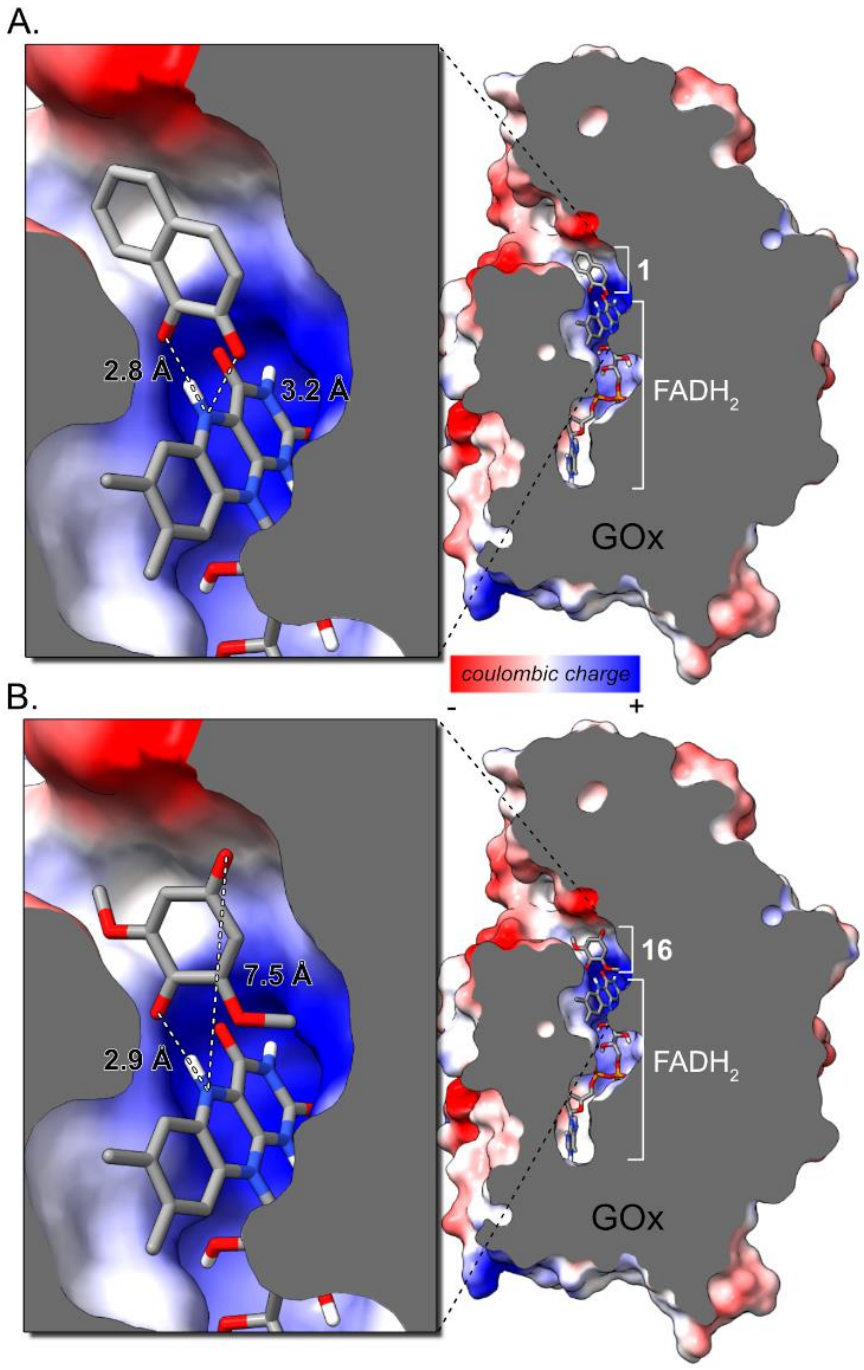

Figure 2.5 Representative results of molecular docking simulations of either (A) **1** or (B) **16** in the oxidized state with GOx. Images depict the most stable binding configuration of 400 simulations each. A crystal structure of GOx (PDB 1CF3) was used in which the $FAD^{+}/FADH_2$ cofactor is in the reduced state. The surface of GOx is colored by electrostatic charge of solvent-accessible is unlikely that the semi-quinone residues, and the enzyme volume has been clipped to show the entire binding pocket of the cofactor as well as the negatively charged entrance to the active site.

form of **16** undergoes reorientation outside of the GOx active site followed by subsequent re-binding, but rather behaves as a one-electron mediator (i.e., would exhibit 2:1 16-$FADH_2$ stoichiometry).

To probe this hypothesis, stopped-flow spectrophotometry was used to measure the kinetics and stoichiometry of reactions between either **1** or **16** and GOx for the oxidation of glucose at pH = 7 and 25 °C. The reaction progress was monitored from the change in absorbance of mediator as a function of time as shown in Figure 2.6. In all cases, the reaction was allowed to go to completion where all glucose was consumed, and reactions were studied with varying concentrations of either mediator or glucose.

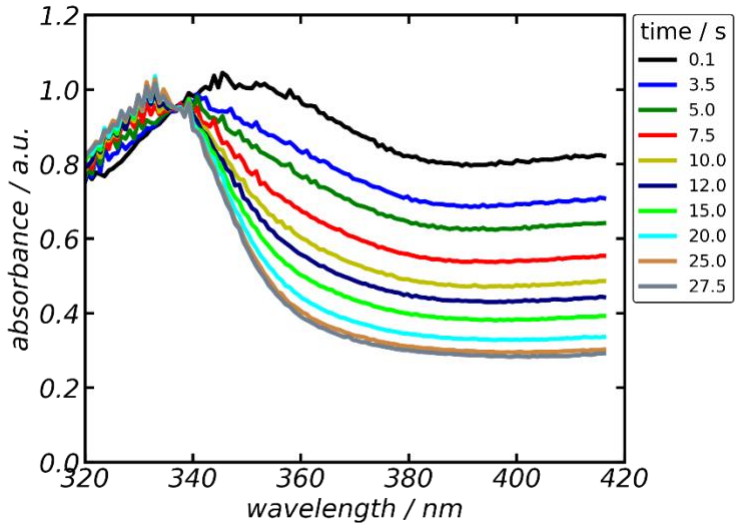

Figure 2.6 Representative spectra of 1 mM **1** with 1 mM reduced GOx dissolved in 100 mM phosphate buffer at pH 7 and room temperature showing normalized absorbance values as a function of wavelength and time.

The spectra for different concentrations were analyzed at 370 nm wavelengths to obtain absorbance and time values for each concentration of enzyme and quinone used respectively as shown in Figure 2.7.

To ensure that glucose was not limiting, a constant ratio of 500:1 glucose-GOx was maintained for all experiments. Initial rate kinetics were studied to confirm the reaction order with respect to both quinone mediator and GOx. These spectrophotometry experiments confirmed that

the reaction is first order with respect to both mediator (**1** and **16**) and GOx, which suggests that only one mediator is involved in the rate limiting step regardless of the quinone used (See Appendix).

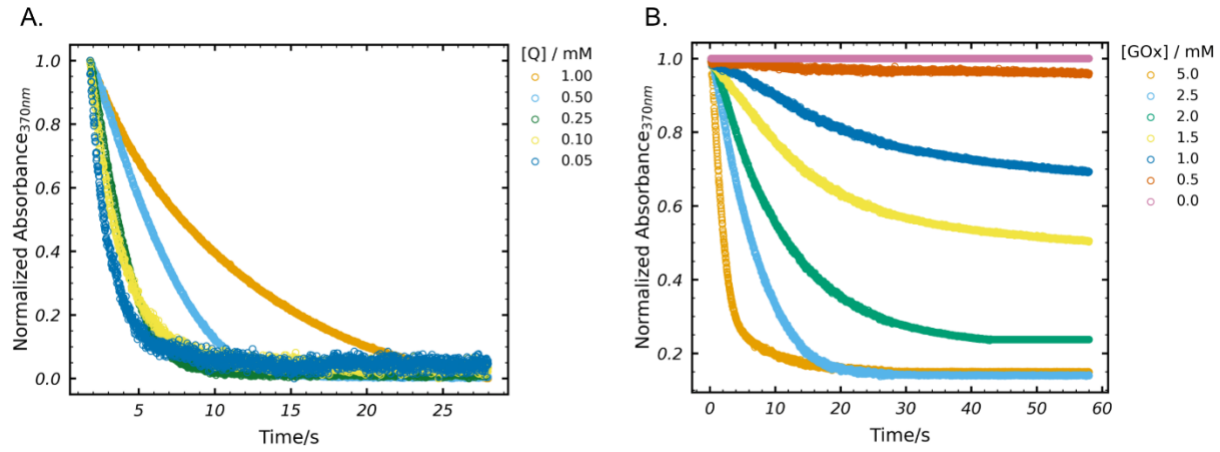

Figure 2.7 Plots of the normalized absorbance at 370 nm as a function of time (A) 100:1 glucose/GOx (1 mM with respect to glucose) with increasing concentration of **1**, and (B) 1 mM of **1** reacted with different concentrations of glucose/GOx (concentrations are of glucose in a 100:1 glucose/GOx mixture).

The stoichiometric quantities of **1** and **16** required to oxidize glucose via GOx were determined by stopped-flow spectrophotometry. A solution containing a fixed concentration of either **1** or **16** was rapidly mixed with solutions containing variable concentrations of a 500:1 glucose/GOx mixture and the absorbance was monitored to the reaction completion (45 s or 500 s for **1** and **16**, respectively). To identify saturated and non-saturated conditions with respect to each quinone, the relative equivalents of each quinone for various glucose/GOx concentrations were plotted against the final remaining oxidized quinone concentration (shown in Figure 2.8). From this plot, the intersection point between saturated and non-saturated

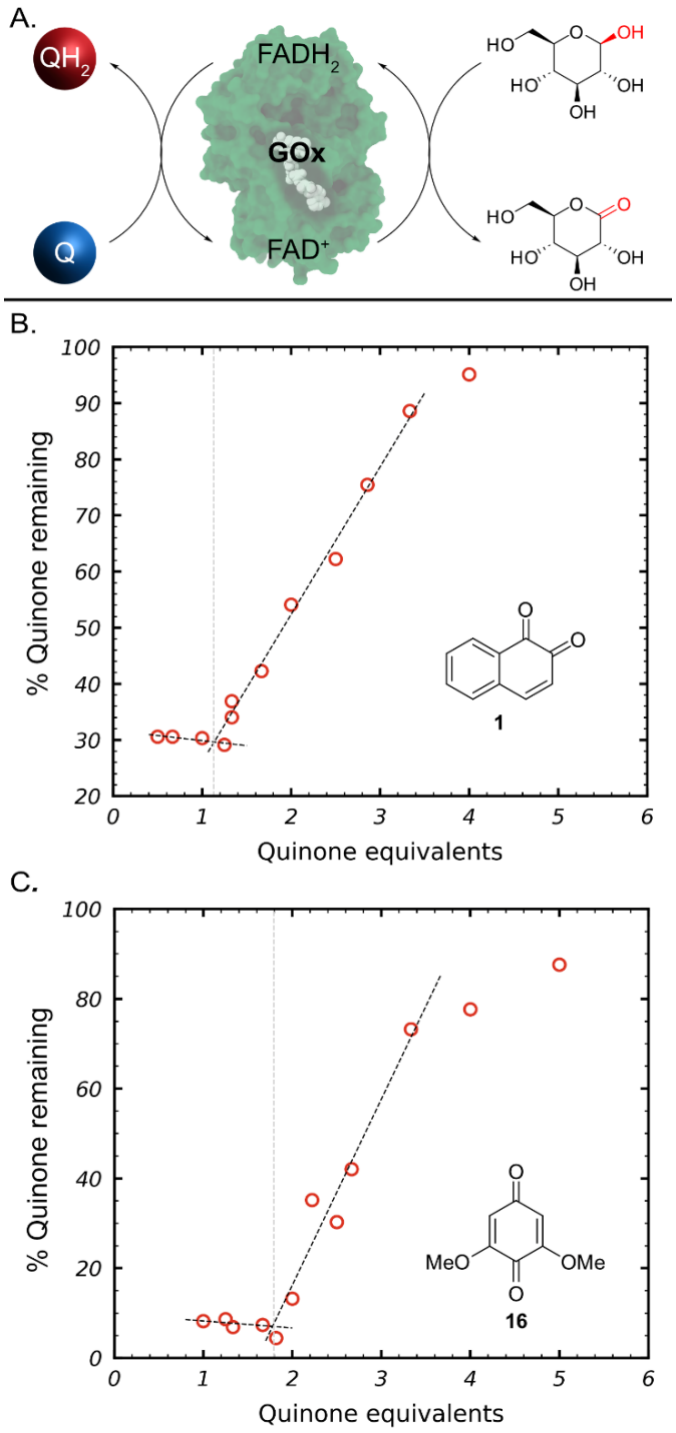

Figure 2.8 (A) Schematic of the reaction used in kinetic and stoichiometry studies. Plots of the percent of oxidized quinone remaining once the reaction had gone to completion as a function of the equivalents of quinone used with respect to glucose when using (B) **1** or (C) **16** as the oxidant. Reactions were performed using 100 mM phosphate buffer at pH 7 and 25 °C.

regions indicate the stoichiometric equivalents of quinone required to fully oxidize $FADH_2$ in GOx. This data indicates that one equivalent of **1**, or two equivalents of **16** are required, respectively, for a complete two-electron oxidation of $FADH_2$ to FAD^+. Furthermore, **1** and **16** both exhibit a midpoint potential of -0.09 V vs SCE; which suggests that the mediator structure alone can significantly influence the stoichiometry of reactions between quinone mediators and GOx. The observed 2:1 stoichiometry required for reaction of **16** with glucose/GOx would result in formation of the high-energy semiquinone intermediate form of the mediator (QH* in Figure 2.2A). These energetic species are known to play an important role in biological electron transport pathways,[141,149] and this result illustrates that quinone structure can promote the formation of QH* intermediates by limiting the kinetics of a second electron transfer in the GOx active site.

The observed difference in stoichiometry for representative 1,2- and 1,4-quinones suggests that these exogenous redox species may behave as either one- or two-electron mediators. It should be noted that, as two-electron mediators with GOx, 1,2-quinones may react either via two single electron transfer (SET) steps with intervening protonation, or via a single hydride transfer/protonation.[130] The data presented here does not provide evidence that **1** operates via the SET pathway; however, it is clear that 16 does proceed through SET and both **1** and **16** exhibit similar first and second redox potentials. Finally, it should be emphasized that, despite the different stoichiometries for **1** and **16**, they are both accurately described by the model presented above. This suggests that electron transfer between quinone mediators and $FADH_2$ is not rate-limiting to the overall reaction but instead indicates that transport of the mediator from the bulk solution to the active site of GOx may provide a kinetic bottleneck to mediated bioelectrocatalysis.

2.5 Conclusion

This fundamental study explored the role that the structure of a quinone redox mediator plays in regulating electron transfer to glucose oxidase during the bioelectrocatalytic oxidation of glucose. Parameterized modelling was used with a library of 25 structurally diverse quinone-

based mediators to construct a QSAR model that implicates redox potential and the projected molecular area of a mediator as two critical parameters in describing homogeneous bimolecular rate constants for the reaction between a quinone mediator and the $FADH_2$ cofactor of GOx. Specifically, it was found that neither redox potential nor mediator size independently provides a strong correlation with the bimolecular rate constant, but a combination of the two parameters accurately predicts *k*. Furthermore, the QSAR model indicates that a quinone mediator with a combination of high redox potential and small projected molecular area will result in the fastest reaction rate with GOx. Finally, a combination of molecular docking simulations and stopped-flow spectrophotometry experiments reveal 1 reacts as a 2 e^- mediator, while **16** reacts as a **1** e^- mediator for GOx during the oxidation of glucose. These results demonstrate that the structure of a quinone mediator (even independent of the corresponding redox potential) can dictate the overall reaction stoichiometry, and, by extension, the types of reaction intermediates formed during mediated bioelectrocatalysis.

Chapter 3: Role of Redox Mediator Size in Controlling Electron Transfer Rates.

3.1 Abstract

Electrochemical redox mediators have enabled the successful application of oxidoreductase enzymes like glucose oxidase (GOx) in catalyzing bioelectrochemical reactions in biofuel cells and biosensors. Previous research has primarily focused on elucidating the structural features redox mediators must possess to effectively interact with GOx in the electron transfer processes. In the previous chapter, parameters such as redox potential and redox mediator size were identified as crucial factors controlling electron transfer in quinone-GOx systems. While the role of redox potential in driving electron transfer has been extensively studied, the influence of mediator size remains less understood or is often generalized as steric hindrance effects. However, it is unclear whether these effects impact mediator transport or binding to enzyme cofactors. To address this gap, computational simulations were conducted to elucidate the specific role of size in mediator transport and binding kinetics. First, the molecular tunnel of GOx was characterized in MoleOnline to gain detailed insights into its structure-function features. Subsequently, a combination of molecular docking simulations was performed to determine the most stable positions of redox mediators within the GOx active site tunnel. This was followed by employing Steered Molecular Dynamics (SMD) and Umbrella Sampling (US) techniques to simulate mediator transport through the tunnel and calculate the Potential of Mean Force (PMF) profiles describing their binding free energies. The results show that the surface area of redox mediators influences molecular transport rates within the active site tunnel. Smaller mediators exhibit higher diffusivities inside the tunnel compared to larger ones suggesting that transport into the active site constitutes the rate-determining step in the overall electron transfer. This insight offers crucial guidance for designing more efficient redox mediator systems for mediated enzymatic catalysis. Understanding the interplay between redox mediator size, transport kinetics, and binding affinity is imperative for optimizing electron transfer rates and enhancing the efficiency of enzymatic catalytic reactions. This study not only addresses longstanding questions in the field

but also provides an example where computational tools are employed to answer fundamental questions that are challenging to address through experimental means.

3.2 Introduction

Electrochemical redox mediators play a pivotal role as diffusible small molecules that facilitate transfer of redox equivalents between cofactors and electrode surfaces in enzymatic electrocatalysis. Enzymes like glucose oxidase (GOx) which harbor a cofactor inside protein shells, depend on these redox species to minimize the distance which electrons must travel during catalysis.[56,65,73,86,104,150–152] However, effective electron exchange requires redox mediators to overcome kinetic and thermodynamic barriers along the ingress path from bulk solution to the GOx cofactor. These barriers include migrating to the GOx active site surface, diffusing within the active site tunnel, and binding by assuming specific interactions with catalytic residues near the cofactor. The interplay between the structure and function of both GOx active site tunnel and redox mediators leads to recognition which allows transport and formation of enzyme-mediator complexes at binding sites.[67,92,153–156] Nonetheless, a significant challenge remains in understanding how these structure-function relationships affect transport and binding processes which ultimately determine electron transfer kinetics in mediated electron transfer. Insights into the rate-determining aspects of these processes can inform the design of next-generation mediators for enzymatic electrocatalysis.

Over the years, extensive research has aimed to precisely identify essential parameters redox mediators must exhibit to interact effectively with GOx in a redox process.[8,31,41,43,50,82,86,155] While previous studies have emphasized the significance of redox potential in controlling mediator activity, recent investigations have shed light on the complementary role of surface area or size.[28] Our Quantitative Structure-Activity Relationship (QSAR) model revealed a correlation between surface area and electron transfer rates, surpassing the influence of redox potential alone.[28] In the model $\log k_{ET} = 0.38E_{1/2} - 0.67A$, where k_{ET}, $E_{1/2}$, and A represents the bimolecular rate constant between redox mediators and the GOx cofactor, the formal potential of mediator and

surface area of the redox mediator, respectively, the coefficient of surface area (*0.67*) was found to have a greater influence than the redox potential. This underscored the predominant role of mediator size in predicting electron transfer rates, yet its significance was not fully explored.

Although the role of redox potential is associated with the driving force of electron transfer between donor and acceptor in terms of Marcus theory[68,140], a crucial question remains unanswered: Does surface area or size control mediator transport to the cofactor via the active site channel, or does it predominantly impact binding to the cofactor site during enzyme-mediator complex formation? Size of ligands has been linked to affecting one or the other depending on the enzyme – ligand interaction.[157,158] Addressing this question is imperative in the mediator design space. Probing this issue can potentially settle a longstanding inquiry in designing mediators for GOx: whether the bimolecular rate constant is primarily controlled by molecular transport, favorable binding, or electron transfer kinetics.

To investigate this question, we hypothesized that the surface area of quinone redox mediators plays a greater role in facilitating their transport in GOx tunnel than binding. Contrary to previous arguments by several scholars in this field, it has been rationalized that transport of redox mediator in fact predicts proximity of binding to the enzyme cofactor.[153] In exploring this question, a comprehensive examination of the active site tunnel of our model enzyme, GOx, was explored which mediators must transverse through. Molecular transport and binding kinetics parameters were acquired and compared to determine the rate-limiting step. Subsequently, this rate-limiting step was correlated with structural features of both redox mediators and GOx.

Specifically, computational simulations were performed to calculate the thermodynamics and kinetic parameters of redox mediators during their ingress through the protein channel to the cofactor. Molecular dynamics simulations were employed to mimic the motion of mediators. Initially, Steered Molecular Dynamics (SMD) was utilized to define the ingress path through applying an external pulling force to the atoms the redox mediator through its center of mass (COM).[105,111–114,159,160] Subsequently, Umbrella Sampling (US) technique was employed in each

independent sampling window created by dividing the ingress path.[161]These sampling windows connect to form a continuous path between the final and initial states. The results of the sampling were analyzed using Weighted Histogram Analysis (WHAM) providing a comprehensive thermodynamic evaluation along the reaction coordinate represented by a Potential of Mean Force (PMF).[160,162–164] The PMF profile describes the chemical potential of redox mediators along the diffusion pathway and captures the non-covalent association and dissociation of redox mediators with catalytic residues surrounding the FAD cofactor.[164,165]

3.3 Computational Methods

3.3.1 Molecular Docking

Autodock Vina[108] was employed for docking simulations with an energy range, exhaustiveness, and number of modes set to 5, 160, and 60, respectively. The search box dimensions were set at 126 Å, 122 Å, and 126 Å for GOx. The center coordinates for GOx were 50.323 Å, 40.369 Å, and 47.802 Å. A total of 300 simulations were performed for each enzyme-mediator system. After simulation, the configuration with the lowest binding affinity was selected for further analysis.

3.3.2 Steered Molecular Dynamics (SMD)

Molecular dynamics simulations were conducted using the Gromacs Package, following the instructions provided in previous research.[166] The initial protein structure files of Glucose Oxidase (GOx) were obtained from the Protein Data Bank (PDB code: 1CF3), while the structure of the redox mediator was optimized using Density Functional Theory (DFT) calculations from chapter 1. To prepare the system for simulation, crystallographic agents were removed from the GOx structure. The redox mediator was positioned at the entrance of the enzyme tunnel by adjusting its coordinates relative to those of GOx. The resulting complex was then placed in a simulation box 10 nm by 10 by 10 nm in dimension and solvated with water of SPC type molecules. The simulations were conducted under both NPT (constant number of particles, pressure, and temperature) and NVT (constant number of particles, volume, and temperature)

ensembles to maintain the desired conditions. The force constant used for the simulations was optimized to be 3300 kJ/mol/nm, ensuring adequate pulling force during the simulations. Additionally, the simulation speed was adjusted to be approximately 0.0024 nm per picosecond to achieve an appropriate timescale for the simulations. SMD simulations were performed to exert a force on the center of mass (COM) of the redox mediator, pulling it towards the N5 atom of the FAD cofactor within GOx. This pulling process was carried out for a duration of 1000 ps. to allow the mediator to ingress into the active site and interact with the enzyme.

3.3.3 Umbrella Sampling (US)

Sampling windows were obtained by dividing the path defined by SMD into 25 windows, each spaced by increments of 0.1 nm to connect the final predicted distance from the initial position. Umbrella samplings were conducted in each window for 1 ns until equilibrium was attained.

3.3.4 Diffusivity Calculation and Diffusion Rate Constant

The diffusion constant was calculated by least squares fitting a straight line (D*t + c) through fitting MSD(t) from initial and end point. This diffusion is calculated based on equation 3.1

(3.1) $D = 16t\langle\left(r(t) - r(0)\right)^2\rangle$

were *r (0)* is the distance at time zero and *r(t)* is distance at time *t*. This diffusivity analysis is built into a Gromacs module.

3.3.5 Binding Free Energy Calculation

The binding process of redox mediators can be considered to be a two-state transition involving the unbound state (state A) and the bound state (state B). The transition state equation (equation 3.2) can be expressed as:

(3.2) $k_{ON} = \frac{k_B}{h} exp\left(-\frac{\Delta G}{RT}\right)$

where k_{ON}, k_B, h, ΔG, T and R are rate constant associated with binding of redox mediators at their respective distance, Boltzmann constant, Planck's constant, free energy of activation, temperature and gas constant, respectively.

3.4 Results and Discussion

3.4.1 Characterization of GOx Active Site Tunnel

To initiate the investigation, it was noteworthy to present a comprehensive picture of the GOx tunnel which mediators must travel through to reach the FAD cofactor. While previous research in this field merely described it as an active site without going much into details of its architecture, newer scholars in this area may not know whether it resembles just a depression on the protein surface or indeed a hollow tunnel. Therefore, a detailed characterization of the GOx active site tunnel using MoleOnline was performed. First, a 2 ns molecular dynamics simulation on the structure of GOx, was conducted to ensure that the protein structure was thoroughly solvated with water and had reached equilibrium in a solution-like environment. MoleOnline was used to search for channels, tunnels, or cavities within the protein structure. From all possible tunnels identified in Figure 3.1A, the one extending from the FAD cofactor (Figure 3.1B) was selected as the most prevalent used by mediators during catalysis. As far as my knowledge extends, this represents the first attempt to report the architecture of GOx active site tunnel.

The GOx tunnel showcases intricate structure-function relationships which are primarily influenced by the presence of charged amino acid residues such as Arg, Gln, His and Tyr. These residues provide various roles ranging from defining the chemical environment within the tunnel to acting as catalytic residues.[155] Specifically, these residues contribute to the creation of hydrophobic and polar regions within the tunnel which positively or negatively affect mediator transport and binding as depicted in Figure 1C to F.

In terms of geometry, it was observed that the tunnel is 2.27 nm long, more specific than reports from crystallography data on GOx from decades ago.[167] There is presence of bottleneck region approximately 1.5 nm from the entrance and towards the FAD cofactor. In comparison of

this bottleneck diameter of the tunnel (~0.24 nm) to the most favorable dimension of approach of most quinone mediators (0.40 - 0.56 nm), these mediators are initially unable to fit within these bottleneck regions. However, molecular motion of residues allows mediators to pass through. Consequently, their transport distance is primarily governed by micro changes in tunnel diameter.

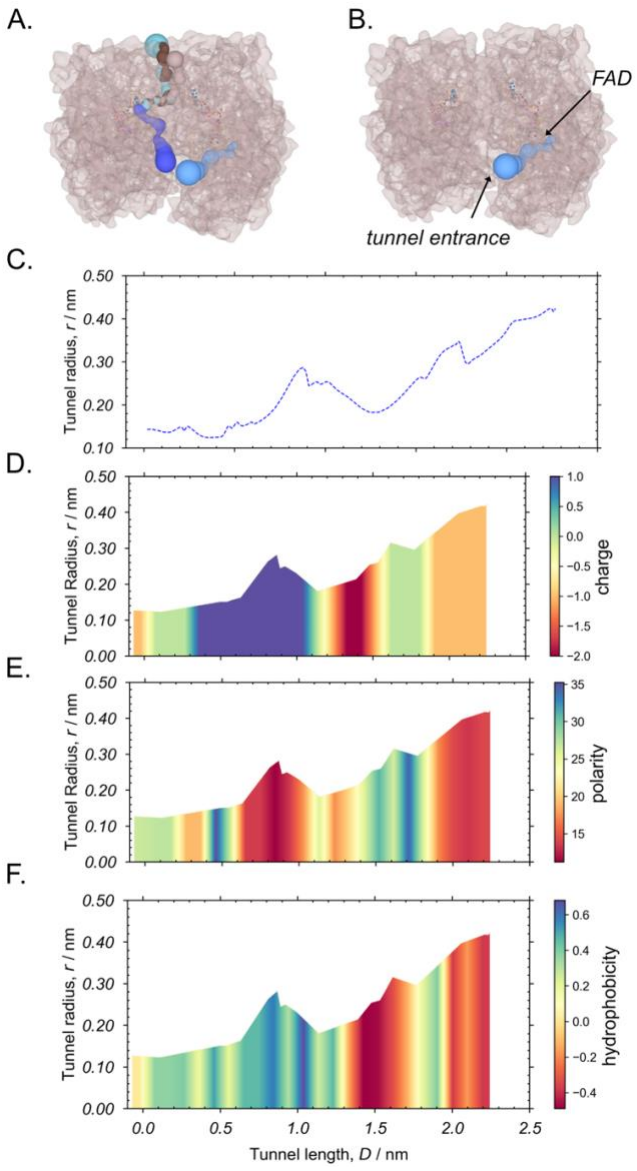

Figure 3.1 (A) illustrates the most prevalent tunnels and cavities identified within the dimeric structure of GOx following 2 ns of molecular dynamics simulation. (B) highlights the selected tunnel depicting the architectural features of the active site, extending from the entrance to the N5 atom of FAD. The distances and radii of the GOx tunnel for both dimeric units are shown in (C), with the origin set at the N5 of the cofactor FAD (0 nm) and the tunnel exit at 2.5 nm. (D) to (F) showcase examples of chemical features (charge state, polarity, and hydrophobicity) created by amino acid residues lining the GOx tunnel.

3.4.2 Redox Mediator Selection

A small library of quinone redox mediators was selected for computational simulations as depicted in Figure 3.2. Experimental data of these redox mediators was acquired in Chapter 2. The selection of these candidates was guided by their variations in surface area while still falling within a similar redox potential range (formal potential standard deviation is 0.11V). Moreover, we aimed to minimize the effects of potential difference in the overall electron exchange within the library. As shown in Figure 3.2 there is a trend between mediator surface area and corresponding bimolecular rate constants. Generally, an increase in area correlates to a decrease in bimolecular rate constant.

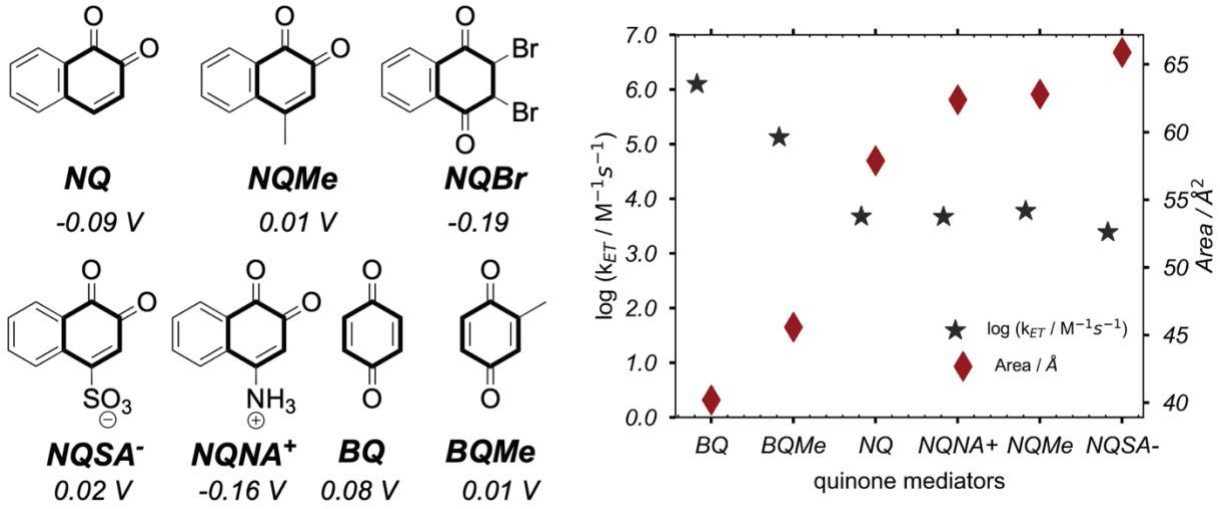

Figure 3.2 A representation of quinone redox mediators selected in exploring the impact of surface area in controlling electron transfer rates. The abbreviated names are 1,2-naphthoquinone (**NQ**), 4-methyl-1,2-naphthoquinone (**NQMe**), 2-bromo-1,4-naphthoquinone (**NQBr**), 1,2-naphthoquinone-6-sulfonate (**NQSA**$^-$), 4-ammonio-1,2-naphthoquinone (**NQNA**$^+$), 1,4-benzoquinone (**BQ**) and 2-methyl-1,4-benzoquinone (**BQMe**). These redox mediators represent a range of surface area relative to their rate constants.

3.4.3 Molecular Docking Simulations, Steered Molecular Dynamics, and Umbrella Sampling (SMD-US) for Potential of Mean Force (PMF)

3.4.3.1 Docking Simulations.

Docking simulations were conducted for all the mediators to determine their most stable positions within the active site of GOx tunnel. These positions were considered the destinations

which the mediators must diffuse through the active site tunnel to reach as demonstrated in Scheme 3.1. The distances of all mediators are summarized in Table. 3. These distances obtained were subsequently used in SMD simulations.

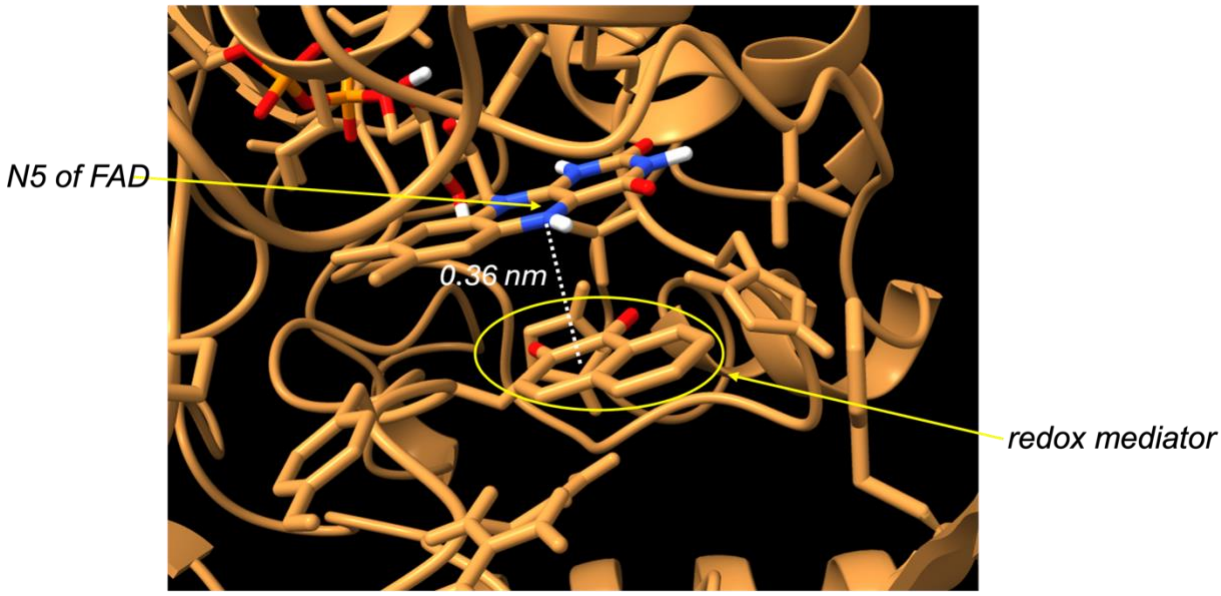

Scheme 3.1 illustrates a representative distance predicted by molecular docking showing the placement of NQ within the active site tunnel of GOx. This distance is measured from the center of mass (COM) of the active benzene ring (the one attached to oxygen) to N5 of FAD.

Table 3.1 A summary of distances predicted by molecular docking of all redox mediators used.

Mediator	Distance /nm
BQ	0.384
BQMe	0.415
NQ	0.362
$NQNA^+$	0.620
NQMe	0.634
$NQSA^-$	0.878
NQBr	0.761

Benzoquinones diffuse closer to the binding position compared to naphthoquinones. The negatively charged quinone (**$NQSA^-$**) appears to have the longest distance from the cofactor, followed by **NQBr**. Relative to their sizes, as illustrated in Figure 3.3, this trend is anticipated. This observation suggests that the negatively charged quinone may experience strong interactions with positively charged arginine residues early in the transport process, hindering its progression

towards the cofactor due to both electrostatic forces and steric hindrance from the bulky -SO_3 group.[86,155] Similarly, **NQBr** face similar challenges, particularly due to the presence of two bulky bromine groups. Conversely, there appears to be no significant effect observed on positively charged quinones and neutrally charged ones, as their interactions and steric hindrance may facilitate their diffusion closer to the cofactor.

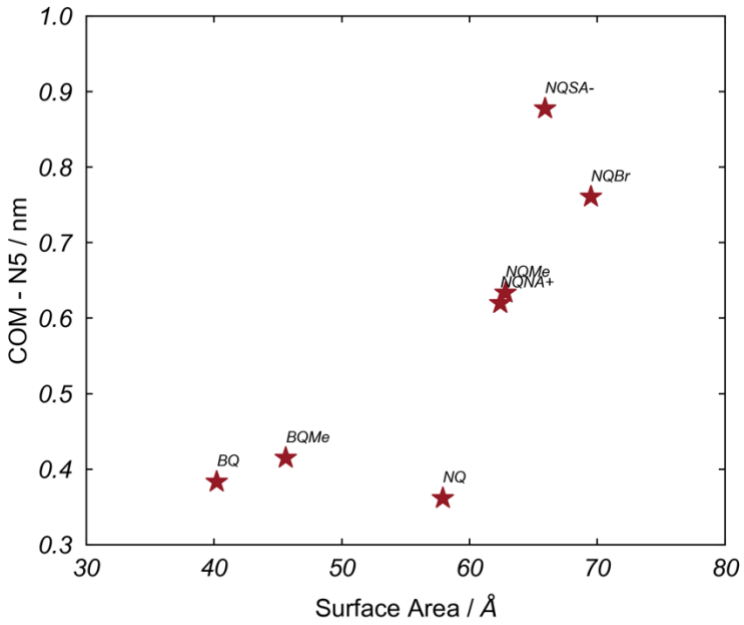

Figure 3.3 A representation of surface area and the final distances predicted by molecular docking from COM of quinones to N5 of GOx.

3.4.3.2 Steered Molecular Dynamics (SMD) and Umbrella Sampling (US) for PMF profile

SMD simulations were performed using the final distances obtained from molecular docking as the endpoint for the redox mediator path from the bulk solution. In these simulations, a force was applied to COM of each redox mediator using a carefully calibrated force constant, as illustrated in Figure 3.4A. Additionally, the travel speed was optimized to make sure the mediator can reach all possible positions along the path. A representative distance-time profile for NQ mediator is depicted in Figure 3.4B. These profiles exhibit similarities due to controlled movement at a constant speed. The total distance was divided into 24 to 30 sampling windows for each mediator. Within each window, three independent 3 ns long equilibrium simulations were

conducted. These simulations were followed by a thermodynamic analysis in each window using the Weighted Histogram Analysis Method (WHAM) to capture the probability distribution of free energies and histograms covering the sampling distance. A successful umbrella sampling is indicated by histograms that overlap as shown in Figure 3.4C.

A resulting PMF profile describing the binding and unbinding dynamics of the redox mediators as they traverse the active site channel is depicted in Figure 3.4D. The PMF profiles exhibit a flat region between 1.0 and 2.5 nm which is the bulk of the transport channel followed by a sharp increase in free energy towards the respective binding positions. This profile can be conceptualized in two distinct steps - the transport phase spanning 1.0 to 2.5 nm and the

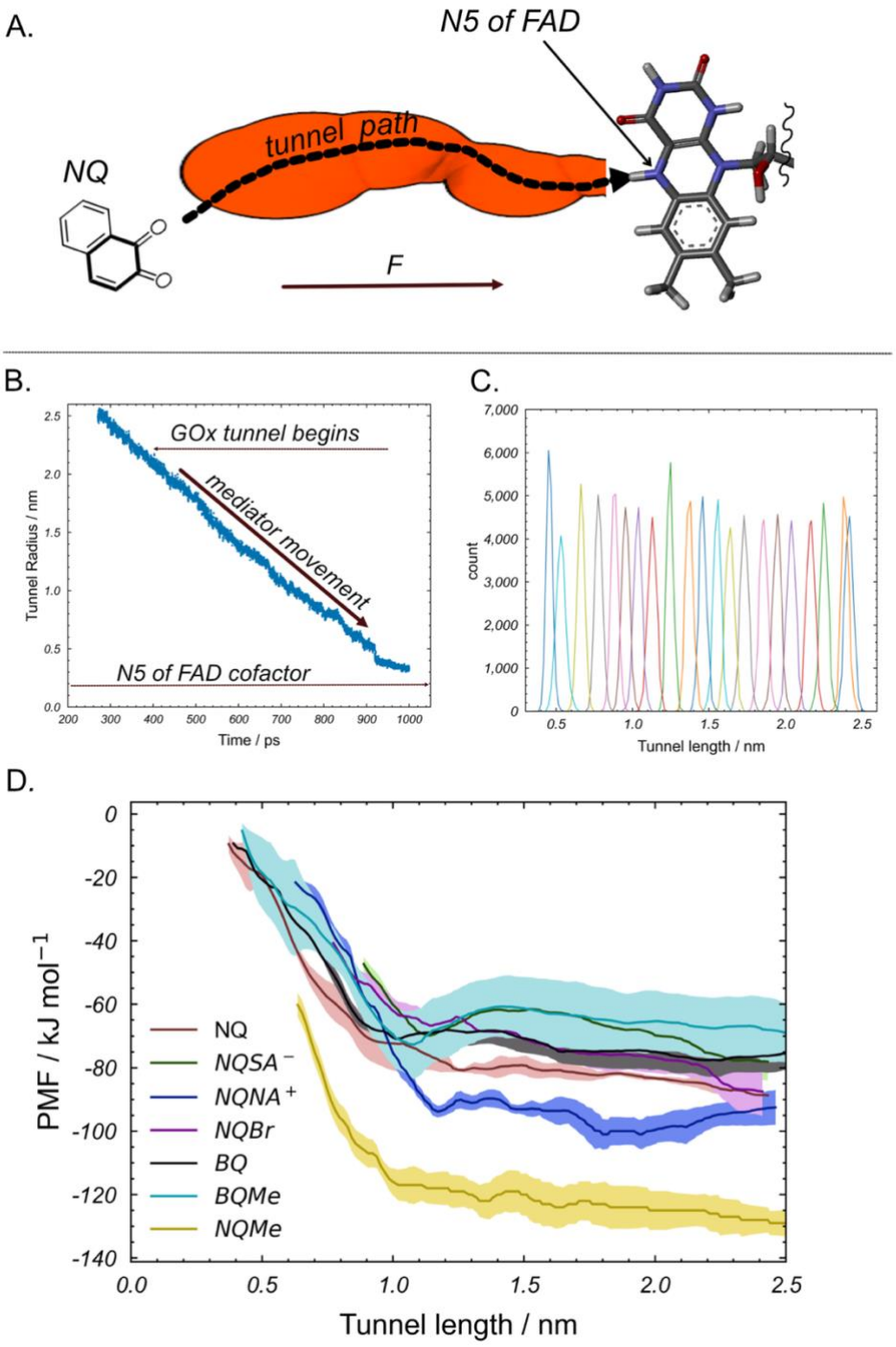

Figure 3.4 A representation of steered molecular dynamics set up where a mediator is pulled from the bulky solution into GOx active site tunnel and dragged along until they reach their predicted distances as shown in (A). (B) shows the distance-time profile of mediators translocating from the bulk solution to their predicted distances. The velocity varied between 0.0023 to 0.0024 ps/nm depending on the distance that had to be traveled. The force constant was set to 3300 kcal/nm/mol for all simulations. In (C), the PMF profiles show the free energies for all 7 redox mediators with their respective error bars.

transition to binding between x_M and 0.1 nm where x_M denotes the predicted binding position of the mediator.

To assess transport rates inside the tunnel, the diffusion coefficients in this transport phase were estimated using the Gromacs module (msd) and equation 3.1. The coefficient was computed at various positions, averaged, and then compared to experimental diffusivities as illustrated in Figure 3.6A. The coefficients generally fall within the same range, however, there are differences. There is a significant decrease in the estimated diffusivities of naphthoquinones compared to experimental values, suggesting a reduction in molecular speed within constricted tunnels. Conversely, the diffusion coefficients for benzoquinones are lower than the experimental values. These diffusion coefficients were then converted into diffusion rate constants by dividing by the transport distance ($2.5 - x_M$) as shown in Table 3.2.

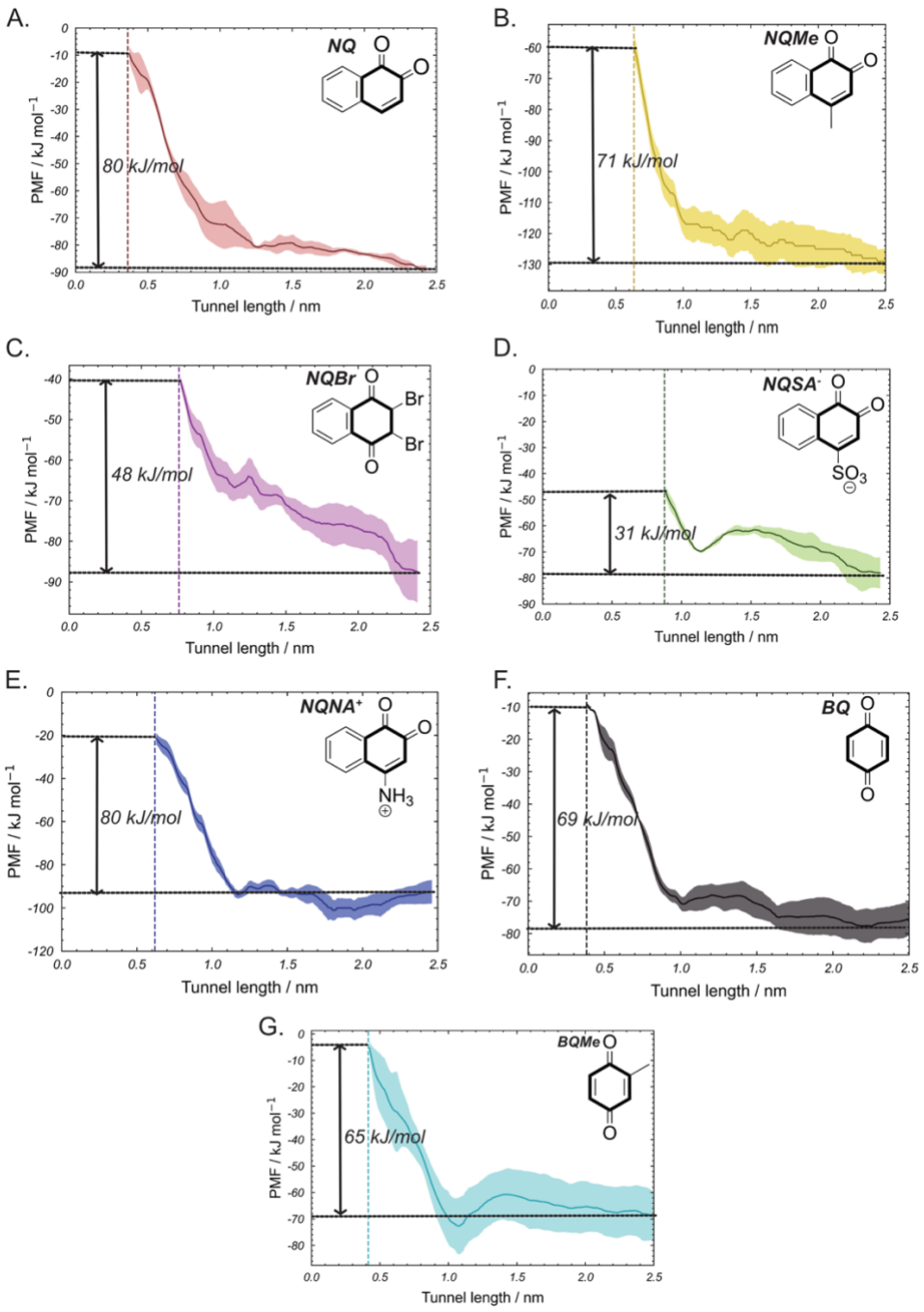

Figure 3.5 Potential of Mean Force (PMF) profiles of all redox mediators showing tunnel length as a function of free energy. The difference between the unbound and bound state energies were used as free energies in the calculation of the binding rate constant.

The free energies at the binding positions were estimated by the difference between the energy of initial unbound state and the peak bound state. This free energy was used to calculate the rate constant of binding. The transition state approximation (equation 3.2) was applied on the

free binding energies as shown in Figure 3.5 to obtain the binding constants illustrated in Table 3.2.

Table 3.2 Diffusion rate constant of redox mediators and respective binding constants at x_M.

Mediator	Diffusion Rate Constant k_{diff} (cms^{-1})	Binding Rate Constant k_{ON} (s^{-1})
BQ	3.6×10^{-2}	3.2×10^{1}
BQMe	1.2×10^{-2}	1.6×10^{2}
NQ	1.1×10^{-2}	5.5×10^{-1}
$NQNA^{+}$	4.4×10^{-3}	6.3×10^{0}
NQMe	1.2×10^{-2}	2.1×10^{1}
$NQSA^{-}$	6.9×10^{-3}	1.4×10^{8}
NQBr	2.2×10^{-3}	1.5×10^{5}

A preliminary analysis of the binding rate constants indicates that they are of larger magnitude than the diffusion constants. This suggests that the transport of redox mediators into the active site is the rate-determining step in the overall process. This analysis was recently used in comparing values of these two independent processes[168].

The diffusion rate constants were compared with the bimolecular rate constant of the mediator-GOx electron transfer process, k_{ET} (determined in Chapter 2). As illustrated in Figure 3.6B, the log of bimolecular rate constants exhibit a relatively stronger correlation with the diffusion constants (R^2=0.76) than with log of binding constants (R^2 = 0.16). This observation suggests that the electron transfer kinetics are strongly influenced by diffusion rates than the binding kinetics. Consequently, transport of redox mediators emerges as the overall rate-limiting step in electron transport, irrespective of the driving force of redox mediators (redox potential). This result also aligns with studies that concluded the possibility of enzyme-ligand interactions being transport-limited.[169] Ultimately, this study addresses a longstanding question posed by the Saveant group[153] decades ago regarding the rate-limiting step of similar processes.

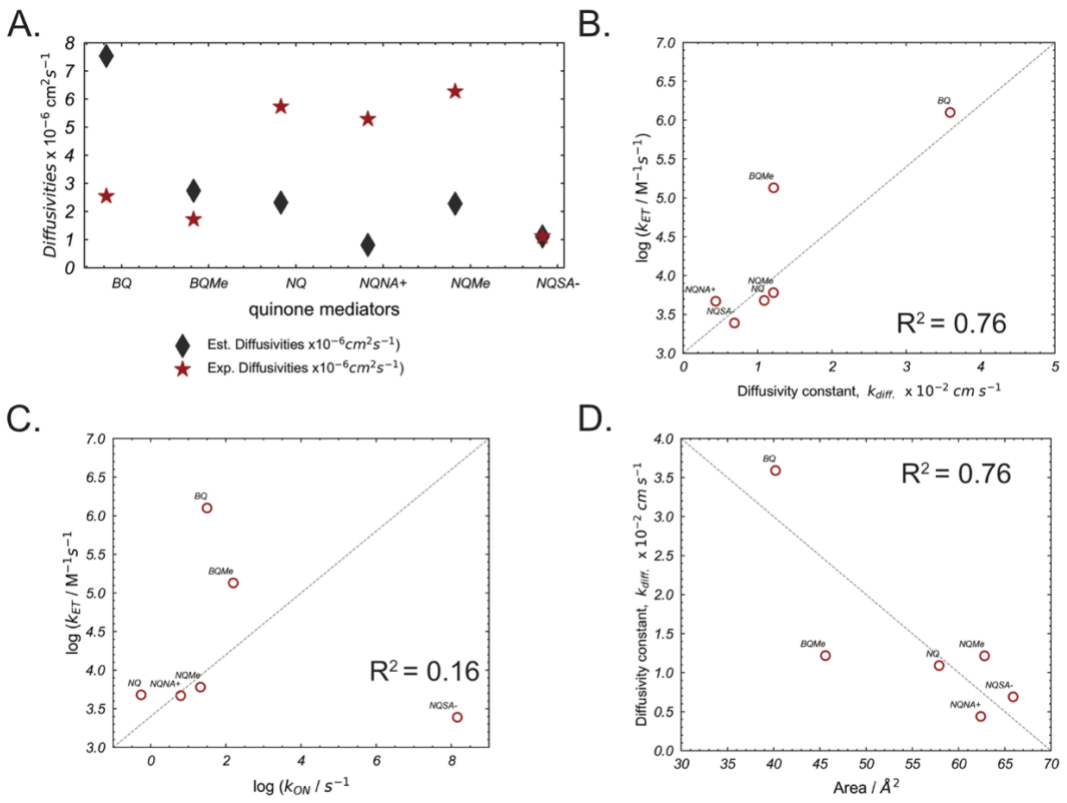

Figure 3.6 A comparison of rate constants with various parameters. (A) illustrates a relationship of experimental and computationally estimated diffusivities, indicating generally higher experimental diffusivities for naphthoquinones compared to computationally determined values. (B) the diffusivity coefficients are compared with the bimolecular rate constant. (C) showcases the comparison between the binding rate constant and the bimolecular rate constant. (D) shows the comparison between the surface area of mediators and the diffusivity rate constants.

Comparing the surface area with diffusion constants reveals that benzoquinones exhibit higher diffusivities because of their smaller areas as depicted in Figure 3.6D. These compounds represent ideal mediators for use as they can achieve high transport rates and consequently high electron transfer rates. Moreover, these mediators are unique, as their redox potential is relatively low, making them promising candidates for biofuel and biosensor applications due to their low overpotential.

3.4.4 Rate Constant Analysis

We calculated the rate constant of electron transfer based on the predicted distances by molecular docking. This rate constant was estimated following an approximation made by the Kano group.[170]

The rate of electron transfer in mediators can be broadly classified into two regimes: a free energy-dependent regime known as the Linear Free Energy Relationship (LFER) and a non-linear free energy relationship (non-LFER), as expressed in equation 3.3.

(3.3) $$\frac{1}{k_2} = \frac{1}{k_{LFER}} + \frac{1}{k_{non-LFER}}$$

where k_{LFER} represents the rate constant governed by the standard Gibbs energy change (ΔG°) of the reaction as expressed in equation 3.4.

(3.4) $$k_{LFER} = k_{LFER}^\circ exp\left(-\frac{\alpha \Delta G^\circ}{RT}\right)$$

and α ($0 < \alpha < 1$) is a proportionality constant in LFER, k°_{LFER} is the rate constant at $\Delta G^\circ = 0$ and $k^\circ_{non\text{-}LFER}$ is independent of $E^{\circ\prime}$ or (ΔG°).

Assuming that $k^\circ_{LFER,}$ which is dependent on ΔG° is the same for all quinone redox mediators in the library due to approximately similar redox potentials, the limiting constant in the overall electron transfer process is $k^\circ_{non\text{-}LFER.}$ This constant is proportional to the closest distance between the mediator electron center and the active site FAD. This constant also depends on the diffusion rate constant, k_{diff}. The diffusion dependent rate constant can be expressed by equation 3.5.

(3.5) $$k_{diff} = 4\pi N \rho_E \rho_E (D_E + D_M)(r_E + r_M)$$

where N, ρ, r and D are Avogadro's number, ratio of the active domain area against the total surface of reactants, radius and diffusivities of the enzyme and redox mediators, respectively. In a diffusion-controlled reaction, the mediator is assumed to be able to access the redox center of the enzyme. However, in this case were the mediators access the redox center of the enzyme, there is direct overlap of orbital or hopping of electron at those short distances. The logarithmic

value of the electron transfer rate is proportional to the closest distance between redox mediator and the active site of the enzyme with a proportionality constant, β, approximated to 12 nm^{-1} for organic mediators.[81,170] The $k^\circ_{non\text{-}LFER}$ becomes identical to k_{diff}. With these assumptions, $k^\circ_{non\text{-}LFER}$ for both systems can be expressed in equation 3.5 as follows:

(3.5) $$k_{non-LFER} = k_{diff}{}^\circ exp(-\beta d)$$

where d is the distance of redox mediator binding. Using a theoretical k_{diff} between 10^9 ~ 10^{10} $M^{-1}s^{-1}$ for all redox mediators, the $k_{non\text{-}LFER}$ was calculated using equation 3.5. These values are presented in Figure 3.7 for all redox mediators.

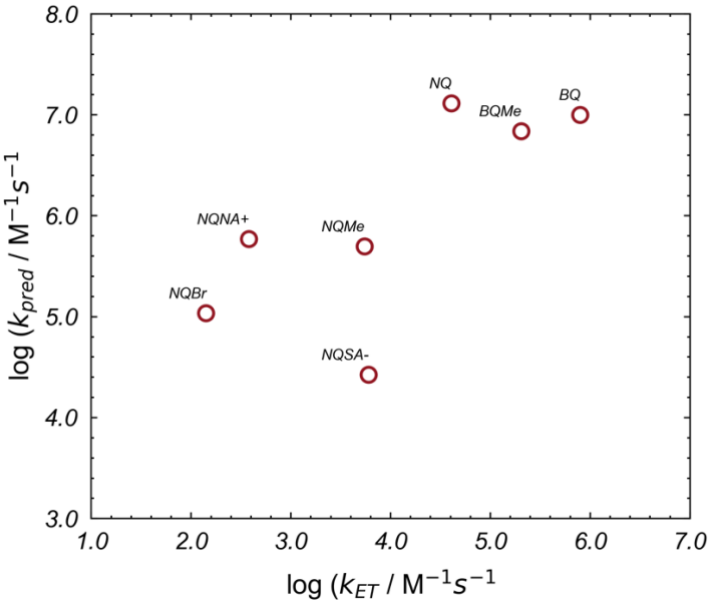

Figure 3.7 illustrates a comparison between the rate constants calculated using predicted binding distances and experimental data. The correlation coefficient R^2 is 0.53 indicating a weak correlation between the two sets of data.

The absence of a linear correlation between the two rate constants indicates that the overall bimolecular rate constant is not influenced by electron transfer but most by molecular transport rates. Comparing the magnitudes, the calculated electron transfer rates are higher than the experimental values suggesting that they are not a limiting factor. These findings support the conclusion that transport rates are the limiting factors in the overall electron transfer process.

3.5 Conclusion

The objective of this study was to examine the pivotal role of redox mediator size in controlling electron transfer rates in mediated enzymatic electrocatalysis, particularly within the context of glucose oxidase (GOx). A detailed analysis of GOx active site tunnel was performed to guide computational experiments. A combination of computational simulations, including molecular docking, steered molecular dynamics (SMD), and umbrella sampling (US), transport and binding kinetics of various quinone redox mediators within the GOx active site tunnel was investigated.

The findings indicated that the surface area of redox mediators significantly influences their transport rates within the active site tunnel, not necessarily the binding kinetics. Smaller mediators such as benzoquinones exhibited higher diffusivities compared to larger naphthoquinones obviously because of their few favorable interactions inside the GOx tunnel. Furthermore, the binding rate constants obtained from our simulations suggest that the transport of redox mediators into the active site is the rate-determining step in the overall electron transfer process. These insights provide valuable guidance for the design of more efficient redox mediator systems for mediated enzymatic catalysis. By understanding the interplay between redox mediator size, transport kinetics, and binding affinity, researchers can tailor the properties of redox mediators to optimize electron transfer rates and enhance the efficiency of enzymatic catalytic reactions. Additionally, our study contributes to addressing longstanding questions in the field regarding the rate-limiting steps of electron transport processes, providing clarity on the factors that govern these complex phenomena.

Chapter 4: Influence of Active Site Tunnel Radius on Quinone-Modified Redox Mediator Interaction with Glucose Oxidase and Glucose Dehydrogenase cofactors.

4.1 Abstract

Mediated bioelectrocatalysis has enabled biological energy production and biosensing systems with enzymatic biofuel Cells (EFCs) and biosensors emerging as pioneering technologies. Glucose oxidase (GOx) is pivotal in glucose-oxidizing EFCs while glucose dehydrogenase (FAD-GDH) has been employed to a lesser extent. While direct electron transfer has not been demonstrated in FAD-GDH and GOx, redox mediators such as quinone-based redox polymer have been utilized to enable electron transfer with these oxidoreductases. Although GOx has demonstrated successful mediated electron transfer with various redox mediators, limitations are still reported with quinone-based polymers. Quinone-functionalized compounds integrated into linear polyethyleneimine (LPEI) offer promising mediators for FAD-GDH and GOx as they exhibit ideal redox mediator physicoelectrochemical properties (i.e. low redox potential, easy to tune structures, and less toxic) unlike their counterparts. However, studies have shown that FAD-GDH exhibits bioelectrocatalytic activity with quinone-modified redox polymers, but GOx unexpectedly does not despite similar chemical properties of both systems. To uncover insights into the difference in electrochemical activity between quinone modified LPEI (NQ-LPEI) and GOx as compared to with FAD-GDH, we show our computational efforts from a combined molecular docking and dynamics studies, and MoleOnline analysis. Docking simulations predicted that a representative quinone modified redox polymer, NQ-A binds closer to the cofactor of FAD-GDH (3.06 Å away) than GOx (10.9 Å away). This distance predicts an exponential dependence of biomolecular rate constants between redox mediator and enzyme cofactor. Molecular Dynamics confirmed stable binding positions of the NQ-A/FAD-GDH and NQ-A/GOx complexes where residues interacting with NQ-A were identified to be ASN 93 and ARG 501 in NQ-A/GOx, and THR 333 and HIS 510 in NQ-A/FAD-GDH system. The larger active site tunnel radius in FAD-GDH enables NQ-A to approach the FAD-GDH cofactor for efficient electron transfer, while the tunnel

of GOx smaller radius hinders mediator passage to access the cofactor. Residues acting as "molecular gates" were found to govern the size of the active site opening in both systems with TYR 53 and ARG 501 identified in NQ-A/FAD-GDH and TYR 68 and ARG 512 in NQ-A/GOx system. Biomolecular rate constant (k_{ET}) approximations revealed NQ-A/FAD-GDH complex has a rate constant 12,100 times that of NQ-A/GOx which makes the k_{ET} for NQ-A/GOx to be practically zero. This underscores the inability of GOx to effectively transfer electrons with quinone-modified redox mediators. This study provided quantitative insights into why FAD-GDH interacts effectively with quinone-modified redox polymers compared to GOx. These findings guide the rational design of redox species tailored to enhance quinone-mediated GOx-mediated bioelectrocatalysis.

4.2 Introduction

Mediated bioelectrocatalysis has enabled a dramatic increase in use of enzyme based-bioelectrochemical technologies spanning enzymatic biofuel cells (EFCs),[2–4,6,45,171–174] implantable enzymatic power devices[3,5,7,12–15,47,172,175] and biosensors.[11–14,47,175–177] Recently, these technologies have been attracting significant research attention due to their promising prospects on both the bioenergy and sensing markets.[8,155,178] In most of these biotechnologies, bioelectrodes are assembled by direct or indirect interface of glucose oxidase (GOx) which serves as the biocatalyst which facilitates the oxidation of glucose. GOx is often referred to as the enzyme “Ferrari" of these modern bioelectrochemical systems due to its favorable catalytic properties including high selectivity and turnover rates.[26] By contrast, glucose dehydrogenase (FAD-GDH) is also utilized in supporting the enzymatic oxidation of glucose. Studies have established that due to the deep active site pockets of these oxidoreductases (approximately 20 ~ 23 Å),[151] direct electron transfer with electrode surfaces during bioelectrocatalysis is unattainable and that necessitates the use of redox mediators to facilitate mediated electron exchange.[151] Despite the concerted efforts in rational mediator design for these oxidoreductases shown in the past decades, GOx has been found inactive when immobilized with quinone-based polymers, a redox

mediator which exhibits ideal electrochemical properties especially for biofuel and biosensor electrode development. The inactivity of this functionalized redox mediator significantly hinders the full utilization of GOx potential. This challenge underscores the need to understand why GOx functions effectively with free diffusion mediators, particularly quinones, but remains inactive when coupled with a polymer-backbone. Addressing this knowledge gap is imperative for guiding the development of functional redox mediator polymers specifically tailored to enhance GOx-mediated bioelectrocatalysis.

Among the families of redox mediators tailored for FAD-GDH and GOx such as osmium complexes[179,180], ferrocenes[33,43,49,152,181], and ruthenium[83] functionalized derivatives, quinone-functionalized compounds have been experimentally studied as promising alternatives due to their low redox potential and the ability to fine tune their structure to achieve desired electrochemical properties.[50,51,182] These mediators are integrated into a polymer backbone commonly linear polyethyleneimine (LPEI), forming wired immobilized systems connected by spacer linkers[49] made from carbon chains which afford segmental mobility of mediators as shown in Scheme 4.1. These quinone-based mediators have garnered attention for their suitability to both enzymatic systems. Notably, their key electrochemical properties such as low onset potential and high catalytic current densities are qualities typically considered mutually exclusive in such applications.[8,173] Moreover, the tunability of quinone moieties allows for precise adjustments to achieve optimal current densities in diverse bioelectrocatalytic platforms.

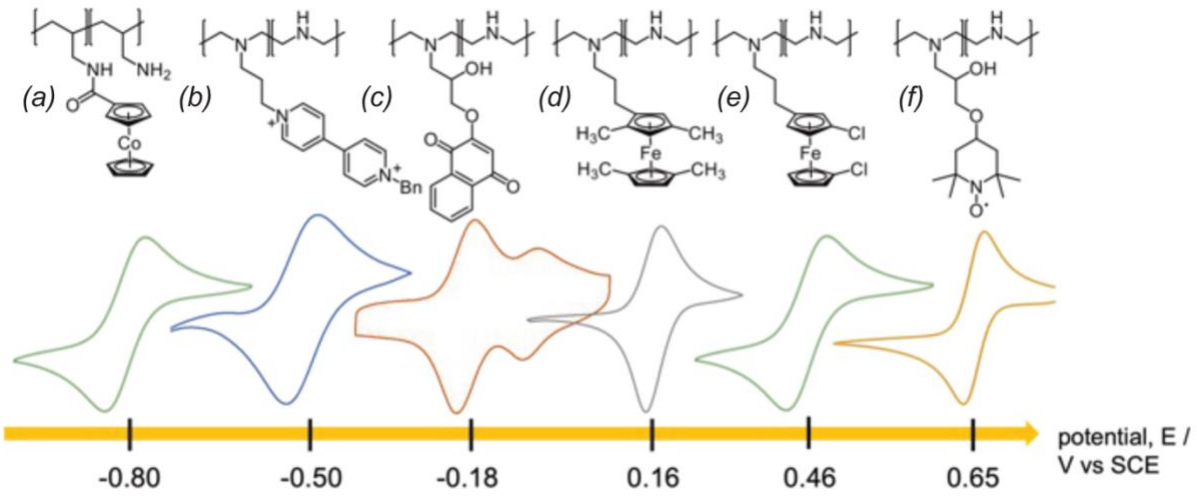

Scheme 4.1 Commonly studied redox polymers including ferrocenes derivatives, pyridiniums, quinones, TEMPO with their corresponding redox potential vs SCE. Quinones are considered ideal redox mediators with GOx (~0.3 V vs. SCE) because of their low potential (~0.18 vs. SCE) which results in high current densities in bioelectrocatalysis applications.[49]

In efforts to advance the application of quinone-modified redox polymers, the Minteer group synthesized a rationally designed quinone derivative. The redox polymer, namely 1,2-naphthoquinone-modified linear polyethyleneimine (NQ-LPEI) redox hydrogel, labeled (c) in Scheme 4.1, was covalently immobilized at the EFC bioanode. Electrochemical measurements of mediated bioelectrocatalytic rates with both FAD-GDH and GOx were conducted at the carbon electrode.[183] The FAD-dependent FAD-GDH mediated by the quinone functionalized LPEI exhibited an open circuit potential (OCP) of 0.864 V and delivered a maximum power density of 2.3 mW^{-2} at 0.55 V.[183] These findings demonstrated a notable possibility of utilizing these mediated systems, signaling a step closer to fully leveraging quinone-modified glucose-oxidizing bioanodes.

Both these oxidoreductases have been extensively studied revealing that they possess similar physicoelectrochemical properties including the presence of the same FAD cofactor and comparable molecular weights (~160kD).[184,185] In addition, both enzymes have shown effective mediated electron transfers with quinone free redox mediators during glucose oxidation. Despite

these similarities in properties, the same quinone redox polymer exhibited no bioelectrocatalytic activity with GOx as shown in Figure 4.1. Nonetheless, it is worth noting that FAD-GDH is insensitive to O_2, but GOx has recognized it as its native exogenous mediator. This phenomenon promoted a further investigation to uncover unexplored structural and mechanistic insights into the behavior of GOx in relation to polymeric functionalized redox mediators.

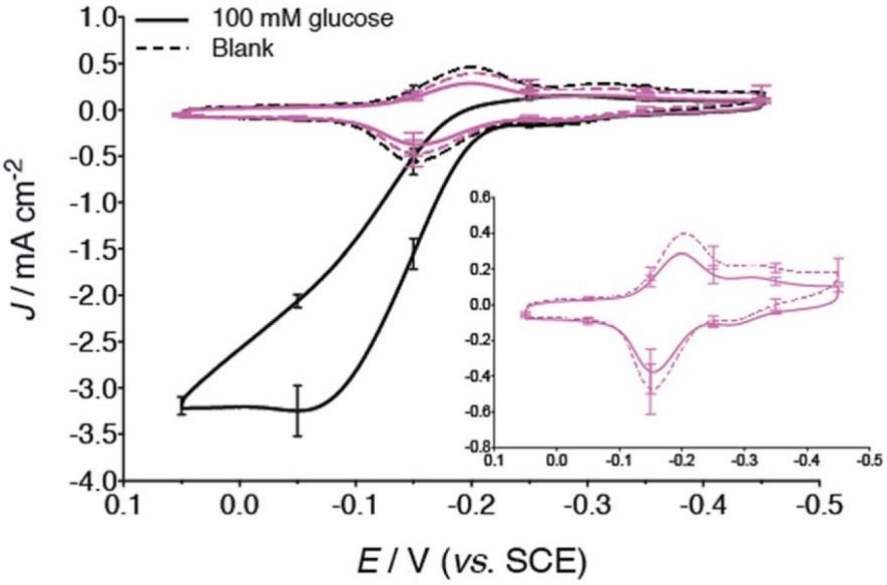

Figure 4.1 Bioelectrocatalysis experiments of FAD-GDH and GOx mediated by NQ-LPEI in the presence and absence of 100 mM glucose. The small CV to the right shows GOx exhibiting no activity upon addition of 100 mM glucose. The bioelectrochemical experiments were performed at pH 6.5 (citrate/phosphate buffer, 0.2 M) and at a scan rate of 10 mV s^{-1}.[183]

Previous research in electron transfer of biological systems similar to oxidoreductase-mediator system highlighted the importance of establishing optimal distances (<14 Å) between the donor and acceptor for efficient electron transfer to occur.[186,187] Thus, investigating how the dynamic architecture of the active sites in FAD-GDH and GOx influences these binding distances between quinone-modified redox mediators and the FAD cofactors is imperative for understanding and optimizing electron transfer processes. Specifically, we hypothesize that the dynamic behavior and size of the active site tunnel radius in GOx hinders the passage of NQ-modified polymer relative to FAD-GDH. This hypothesis is proposed aiming to quantitatively explore the

differences in the active site tunnel architectures and rationalize their impact on bioelectrocatalytic activity between the two enzymes as reported by the Minteer group.[183]

Investigating these types of questions is complex when relying solely on experimental methods. This work aims to advance the understanding of these redox polymers by employing computational methods introduced in Chapter 3. We adopt a comprehensive approach involving molecular docking, molecular dynamics, and MoleOnline analysis on a system comprising of carefully designed NQ-modified species and oxidoreductases (FAD-GDH and GOx). A quinone redox mediator functionalized with a polymer backbone model is employed as representative NQ-LPEI in GOx mediated electrodes. Using an integrated computational approach, we aim to explore the behavior of this redox polymer when interacting with both oxidoreductases.

Molecular docking is a valuable technique for predicting binding sites between receptors and ligands. In our study, the receptors are the oxidoreductase enzymes, and the ligands are the redox mediators. Previous studies have successfully utilized this method to identify binding sites for redox mediators, polymer chains, and substrates. For example, Holtmann's group screened redox mediators for P450 monooxygenases and calculated associated electron transfers based on predicted positions.[188] Additionally, molecular docking has been employed to investigate complex structures of GOx, revealing structures positioned between catalytic residues. [189–192]

Molecular dynamics is utilized to relax the oxidoreductases and simulate the free energies of the oxidoreductase complexes as the system evolves towards equilibrium.[84] Additionally, the time-dependent changes in the active site tunnels of the oxidoreductases as they approach equilibrium is also analyzed. MoleOnline[193] is a useful tool in characterizing the radii along the tunnel length and computing associated parameters. Finally, to relate computational experiments to physical experiments, rate constant comparisons are conducted using data from both methods for each system.

4.3 Methods

4.3.1 DFT Optimization of Redox Polymer

All geometry optimization and DFT free energy calculations were conducted using Gaussian 09, utilizing the B3LYP level of theory, 6-31+G (d,p) basis set, and CPCM (water) solvation model. The quinone redox polymer underwent optimization, and the resulting structure was converted into PDB format for use in subsequent simulations.

4.3.2 Molecular Dynamics

Two molecular dynamics (MD) experiments were performed using the Gromacs package, version 4.0.2. The structures of each protein were obtained from the Protein Data Bank (PDB), with 4YNT used for FAD-GDH and 1CF3 for GOx. The first MD experiment involved relaxing the structure for 10 ns, followed by a second experiment to confirm the docking positions of the oxidoreductase-redox mediator complexes for another 10 ns. In both simulations, the protein structures were placed into a cubic box side length 10.26 nm totaling to a volume of 1080.33 nm. The simulation box was solvated with simple point charge (SPC) water molecules and 100 mM NaCl was added to neutralize counterions. The system underwent preparatory steps which includes the steepest descents energy minimization and equilibration. Two equilibration steps were performed - first, a 50 ps simulation under the constant volume (NVT) ensemble, followed by a constant pressure (NPT) ensemble simulation for 50 ps at 1.0 bar, maintaining a temperature of 310 K using the Berendsen weak coupling method. Subsequently, MD production was performed for 10 ns. During this data collection period, the Nosé-Hoover thermostat was employed to control temperature, while the Parrinello-Rahman barostat regulated pressure isotropically at 1.0 bar.[166] Replicates were performed for each type of simulation. Trajectories were extracted from the enzyme-only simulation for molecular docking and from the enzyme-complex for distance analysis. The trajectories were converted into PDB files for analysis using MoleOnline and ChimeraX.

4.3.3 Docking Simulations

Autodock Vina[194] was employed for docking simulations with an energy range, exhaustiveness, and number of modes set to 5, 160, and 60, respectively. The search box dimensions were set at 126 Å, 90 Å, and 114 Å for FAD-GDH, and 126 Å, 122 Å, and 126 Å for GOx. The center coordinates for FAD-GDH were 50.584 Å, 48.413 Å, and 48.176 Å, while for GOx, they were 50.323 Å, 40.369 Å, and 47.802 Å. A total of 300 simulations were performed for each enzyme-mediator system.

4.3.4 Radii Determination

The PDB structures requiring analysis were obtained and uploaded to the MoleOnline server.[193] Initial search coordinates were determined, mainly those of the N5 atom of the FAD cofactor. The jobs of each oxidoreductase structure under analysis were independently submitted, and the results were downloaded in various forms of information.

4.4 Results and Discussion

4.4.1 Redox Mediator Selection

Directly using the quinone modified LPEI redox polymer in simulations poses challenges, particularly regarding convergence. These challenges stem from factors such as the chain length of repeated polymeric units with varied conformational freedom, and extended simulation times. To simplify simulations and approximate the behavior of the quinone-modified LPEI chain units (with an average molecular weight of 91 g/mol per unit), a representative modified 1,2-naphthoquinone with an adamantane bulky group substituted at position 4 (molecular weight of 601.87 g/mol) was selected for the study. This species approximates to 6 quinone-modified LPEI chain units and can mimic controlled behavior of a real LPEI redox polymer. These adamantane groups add LPEI-like bulkiness and flexibility. We reasoned that while this group may not fit into the active site of both oxidoreductases, it could serve to anchor the attached redox quinone, similar to the role observed in experiments with LPEI as illustrated in Scheme 4.2.

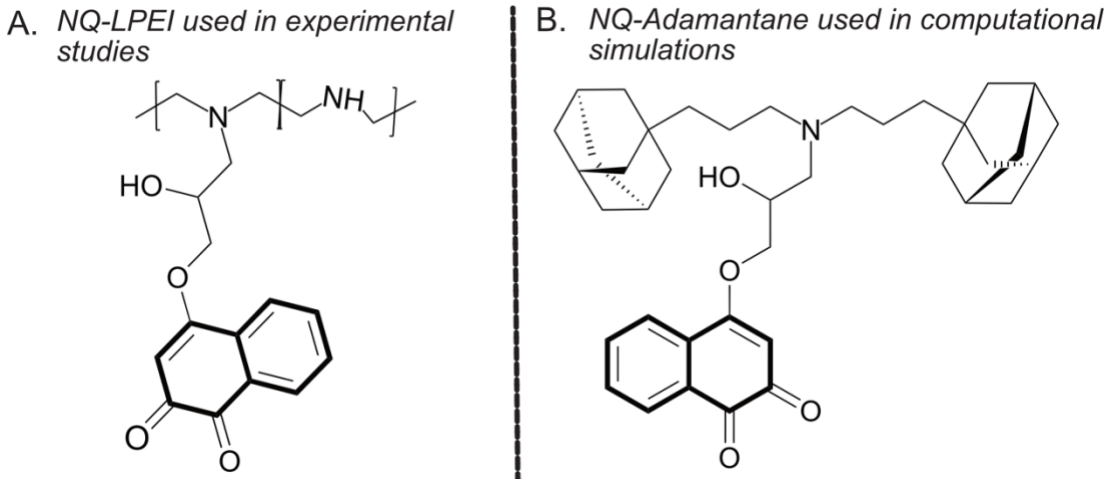

Scheme 4.2 A representative of the polymeric structure of 1,2-naphthoquinone modified redox species. In (A) a LPEI – quinone modified employed in bioelectrocatalysis experiments while (B) shows the 1,2-naphthoquinone – adamantane (NQ-A) modified mediators used in computational simulations.

4.4.2 Molecular docking and Molecular Dynamics

Several initial preparatory steps were performed on the oxidoreductases and NQ-A structures for docking simulations. First, the NQ-A redox species was optimized through Density Functional Theory calculations (DFT) to obtain the ground state electron configuration as described above. Subsequently, the PDB structures of the oxidoreductases (4YNT: FAD-GDH and 1CF3: GOx) were subjected to a 10 ns molecular dynamics simulation for relaxation. This involved solvating with water and neutralizing charges. This step is crucial to ensure that the proteins adopted the most favorable conformation in a solution-like environment.

To verify that the oxidoreductases had reached equilibrium in the simulated environment, the Root Mean Square Deviation (RMSD) was computed. RMSD values indicate the deviation of atomic positions in a molecular structure until adiabatic equilibrium is achieved (lowest energy complex), providing insights into structural stability over time.[195] As depicted in Figure 4.2, the RMSD values for FAD-GDH and GOx were observed to converge at 0.13 and 0.10 nm, respectively. This convergence suggests that both proteins had reached equilibrium at the specified simulation timescale, indicating that they were suitable for subsequent docking simulations.

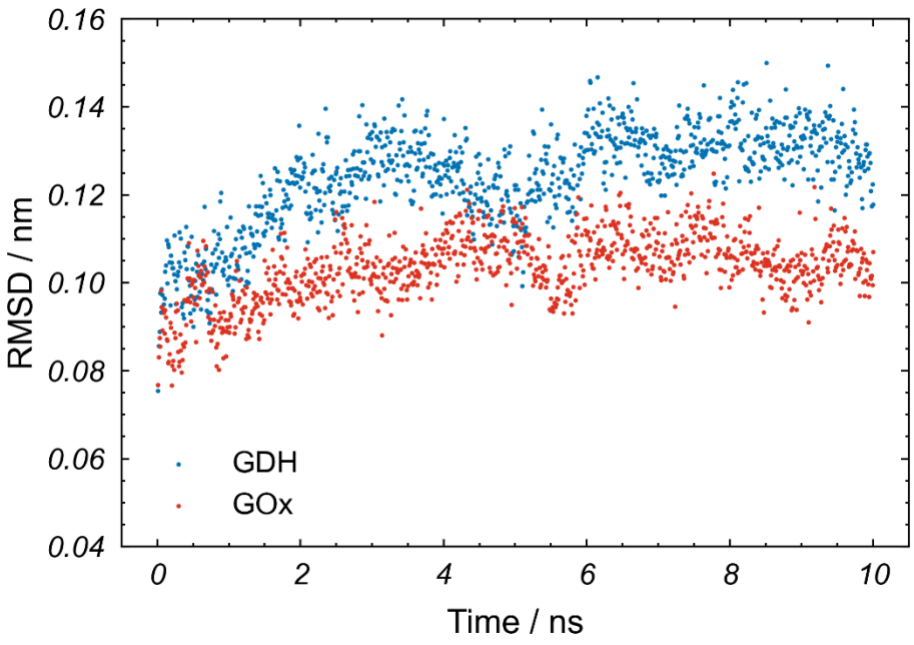

Figure 4.2 The RMSD of oxidoreductases FAD-GDH and GOx shown their stability after 4 ns of MD. The equilibrium ensures proteins have assume a solution like behavior.

Following these steps, Autodock Vina[194] was employed to predict the binding positions and affinities of NQ-A to both oxidoreductases active sites. The most favorable binding sites located close to the FAD cofactor for both enzymes were determined and are shown in Scheme 4.3. A preliminary assessment of the docking results indicates that the redox species NQ-A binds more closely to FAD-GDH (3.06 Å or 0.306 nm) than to FAD-GOx (10.9 Å or 1.09 nm). Both the NQ-A/FAD-GDH and NQ-A/GOx complexes exhibit relatively similar affinities, with binding energies of -8.0 kcal/mol and -8.1 kcal/mol, respectively. Binding is primarily dictated by a spectrum of molecular interaction forces, spanning hydrogen bonding to Van der Waals forces. The most favorable interactions typically occur within the active site, facilitated by catalytic residues. However, in cases where the redox mediator cannot be accommodated within the active site, in the GOx case, favorable interactions may also be established at the protein surface.

Given that the primary objective of this study was to elucidate why quinone functionalized redox polymers do not function with GOx, these initial docking findings suggest that the observed inactivity may be attributed to a difference in these distances. The difference in distances is crucial

for predicting the likelihood of successful orbital wavefunction overlap and efficient electron transfer.[68,74] This assessment aligns with a previous study where cobalt sepulchrate and methylviolgen were computationally screened against P450 monooxygenases to identify suitable mediators for electrochemically driven P450 catalyzed reactions. It was found that redox mediators with predicted binding distances higher than 8 Å between the redox mediator electron center and the active site resulted in no measurable mediated catalysis, emphasizing the importance of the distance between cofactors for electron transfer with redox mediators.[188]

Quinones are known to favor inner sphere electron transfer mechanisms, and their ability to transfer electrons diminishes over longer distances (electron hopping).[11,72,196] Therefore, based on this widely accepted theory of quinone electron transfer, it can be inferred that NQ-A is situated more favorably for efficient electron transfer in FAD-GDH than in GOx.

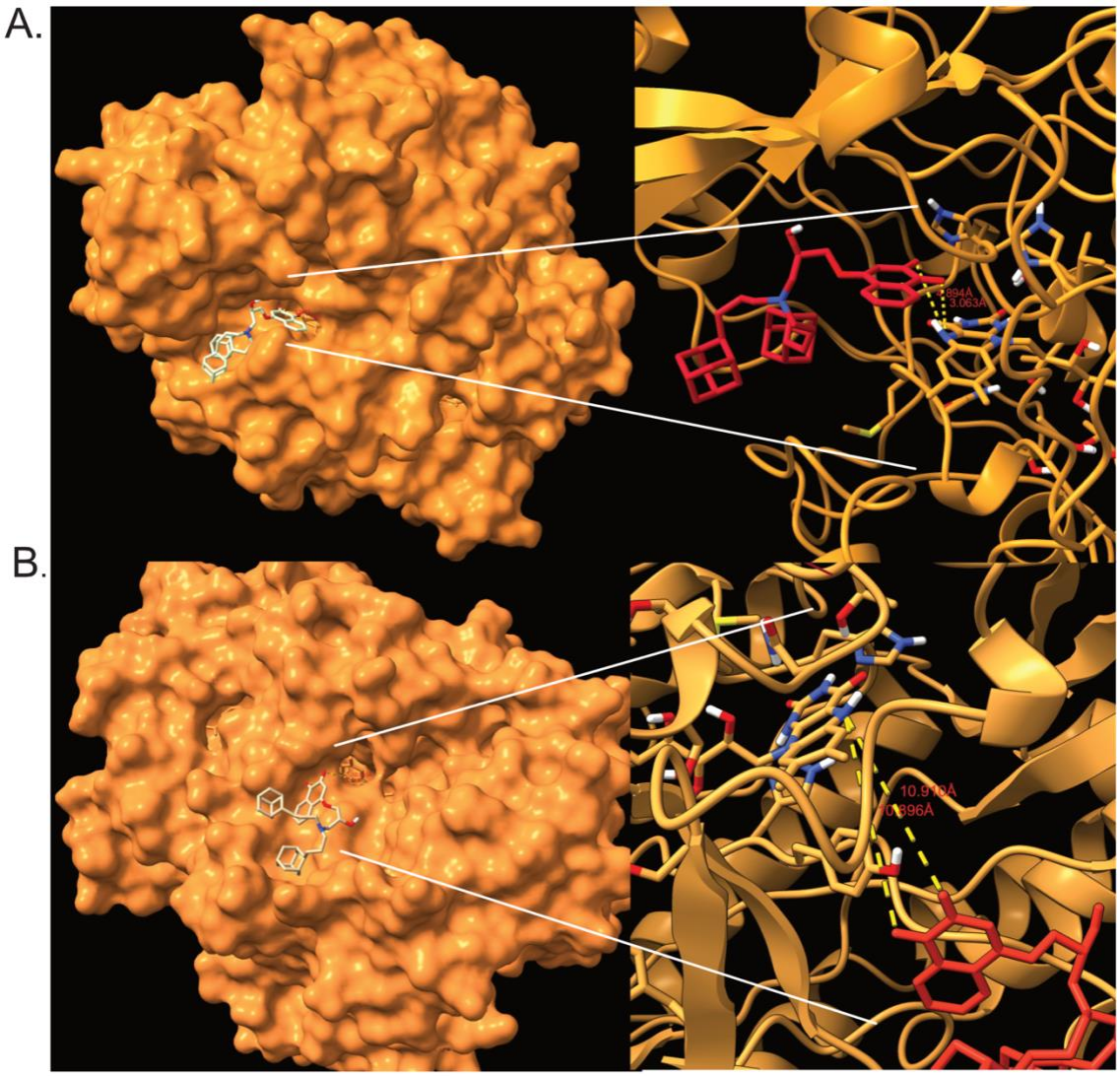

Scheme 4.3 Molecular docking simulations predictions of NQ-A on FAD-GDH and GOx oxidoreductases. NQ-A electron centers are predicted to be 3.06 Å away from the FAD cofactor as shown in (A) while 10.9 Å away from FAD cofactor in (B). This difference in NQ-A/GOx distances may be attributed to absence of mediated bioelectrocatalytic activity.

We examined the specific residues located at entrance of these oxidoreductase tunnel from the molecular docking results. For FAD-GDH, we identified residues TYR 53 and ARG 501 located at the tunnel entrance working as “molecular gates” that govern the passage of redox mediators as illustrated in Scheme 4.4. These residues are separated by 5.1 Å providing a width possible for the redox mediator to enter.

However, in the case of GOx, the residues situated at the entrance are TRY 68 and ARG 512 which work as "molecular gates." They are only 3.6 Å apart, approximately 30% smaller than in FAD-GDH. It seems that ARG 501 in FAD-GDH possesses much more flexibility than ARG 512 in GOx, allowing the entrance of the redox mediators during mediated bioelectrocatalysis. This difference in “molecular gate” size offers another explanation for why the redox polymer fits into the FAD-GDH tunnel but not into GOx, thereby enabling an appropriate distance for electron exchange between redox centers.

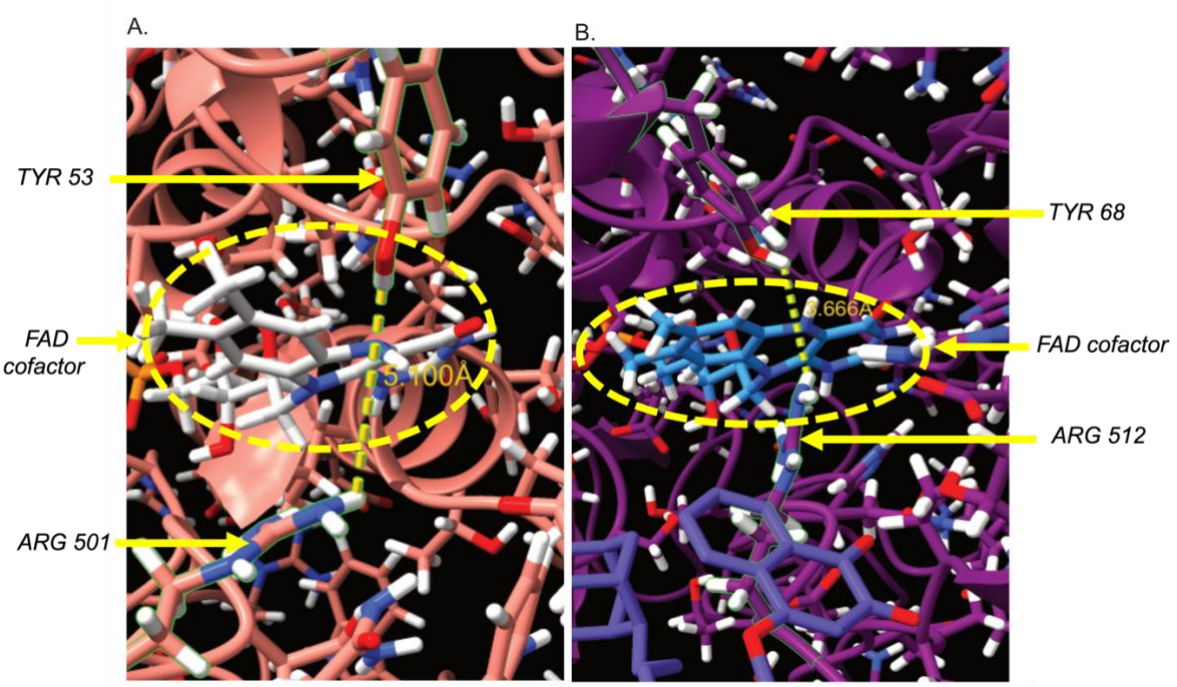

Scheme 4.4 illustrates the residues serving as entrances in both oxidoreductases. In (A) residues TYR 53 and ARG 501 are shown separated by 5.1 Å. In (B) residues TYR 68 and ARG 512 are shown to be 3.7 Å apart indicating a 30% difference in "molecular gate" size.

4.4.3 Molecular Dynamics of Enzyme-Complexes

To confirm that the NQ-A binding position remains stable and predominant in solution for both oxidoreductases, a separate molecular dynamics simulation of the enzyme-complex was conducted. In this experiment, it was hypothesized that the distance between the FAD cofactor and the redox mediator should be roughly maintained as the complex approaches equilibrium over a 10 ns period of molecular dynamics. This same approach was used in confirming the

binding stability of the GOx-glucose complex.[178] Figure 4.3 illustrates the distance dependence over the simulation timescale.

Figure 4.3 illustrates that the docking simulations and molecular dynamics distances of both complexes converge, suggesting that the binding positions are stable and likely even under a solution-like environment. The initial distances of the redox polymer do not exactly align with the starting distances in Scheme 4.3 due to pre-molecular dynamics steps applied to the complexes such as minimization, NVT, and NPT equilibration, which shifted their positions. However, the NQ-A/FAD-GDH complex distances between electron centers are maintained around 6 Å (1 to 3 Å higher than predicted by docking simulations), occasionally drifting to 4 Å. In contrast, the NQ-A/GOx complex drifts away (approximately 5 Å) from the predicted docking position. These variations throughout the simulation period are expected, as the NQ-A in GOx possesses the freedom to move because it's bound at the active site entrance unlike in FAD-GDH where the redox polymer is bound within the tunnel. This experiment confirms the close binding of the redox species to the FAD cofactor in FAD-GDH enables electron transfer, while in GOx, the distance is farther, reducing the likelihood of electron transfer occurring.

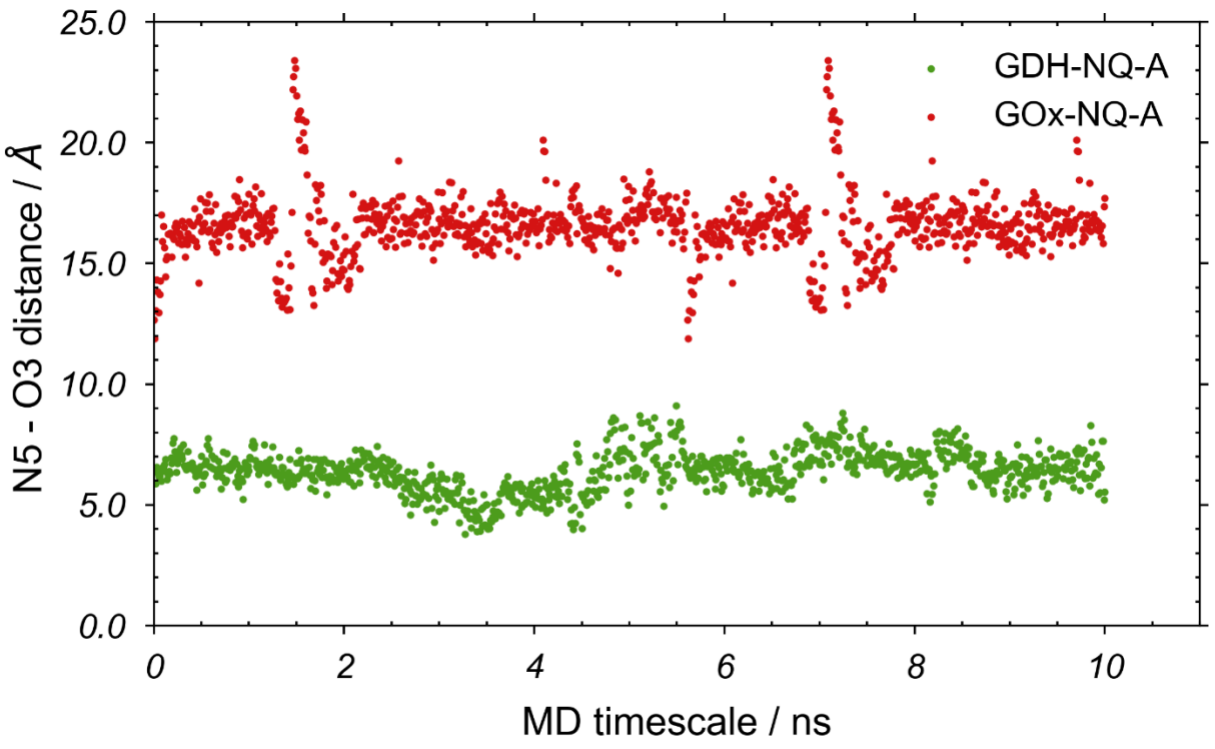

Figure 4.3 Results of a 10 ns MD simulation of the oxidoreductases-NQ-A complexes, depicting the distances between the center of mass (COM) of N5 and O3 of 1,2-naphthoquinone-A. In the graph, red represents distance variations of the NQ-A/GOx complex, while green represents the NQ-A/FAD-GDH complex. The NQ-A/FAD-GDH complex maintains distances around 6 Å between electron centers (1 to 3 Å higher than predicted by docking simulations). The NQ-A/GOx complex exhibits distances fluctuating around 16 Å.

Upon examining the binding sites, we observed that NQ-A primarily engages in hydrogen bonding with residues ASN 93 and ARG 501 as depicted in Scheme 4.5. These residues anchor the redox polymer at approximately 3.9 Å enabling orbital overlap between electron centers and subsequent electron transfer. However, in GOx hydrogen bonding contacts occur between residues THR 333 and His 510, although at a greater distance of 10.9 Å from the cofactor. It is noteworthy that these contacts in GOx do not impede the mediator from entering the active site; rather, they represent stable binding interactions after the mediator has been sterically hindered from entering the active site tunnel.

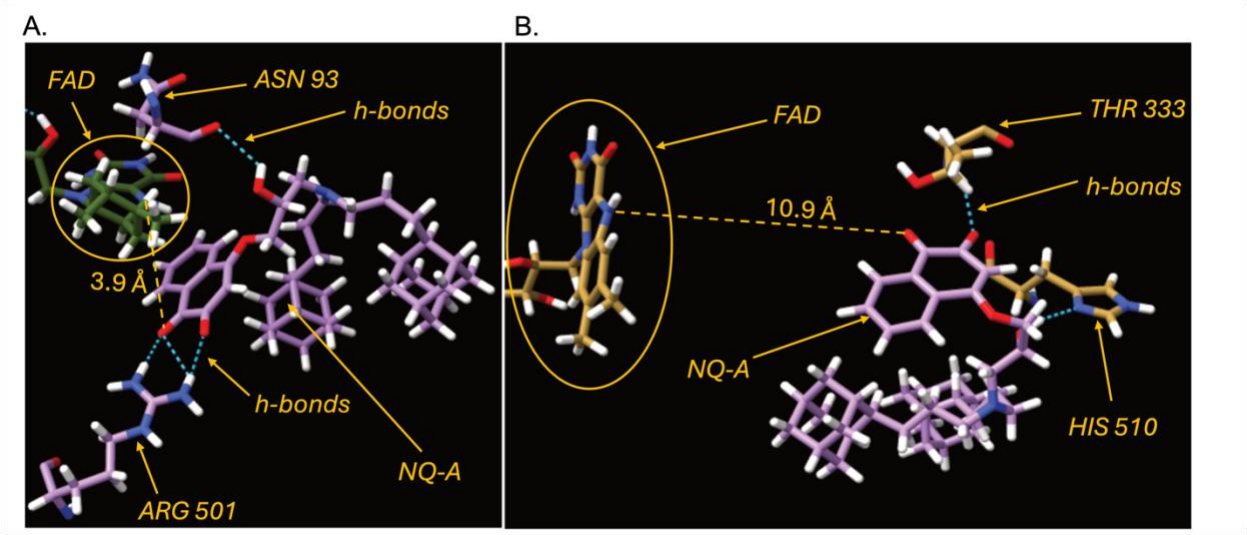

Scheme 4.5 illustrates enzyme contacts. In A, NQ-A/FAD-GDH binds within the active site tunnel, positioned 3.9 Å away from the N5 of the FAD cofactor. Hydrogen bonds form between residues ASN 93 and ARG 501. In B, NQ-A/GOx contacts occur between THR 333 and HIS 510, located at 10.9 Å from the cofactor.

4.4.4 Characterization of Oxidoreductases Molecular Tunnels

To facilitate electron transfer from quinones to the cofactors of oxidoreductases, the active sites of these enzymes need to be sufficiently open. If these active sites are closed or too narrow, the diffusion of the redox mediator can be sterically hindered. We further investigated the role of these dynamics in allowing the passage of redox mediators and subsequently controlling the observed differences in distances between the NQ-A/FAD-GDH and NQ-A/GOx complexes. We hypothesized that this disparity in distance might be correlated with the size of the active site tunnels in both enzymes. To test this hypothesis, we analyzed 20 trajectories for each oxidoreductase, ranging from 0 to 10 ns of molecular dynamics simulations using MoleOnline. Additionally, we sought to determine whether there are any instances where the radius may be sufficiently large to allow the passage of redox mediators for GOx.

MoleOnline searched the active site tunnel starting with coordinates of N5 of both enzymes – GDH and GOx. The radii of the tunnel of the crystal structure of both enzymes and the average radii obtained from of 20 trajectories are plotted in Figure 4.4 for FAD-GDH and GOx, respectively.

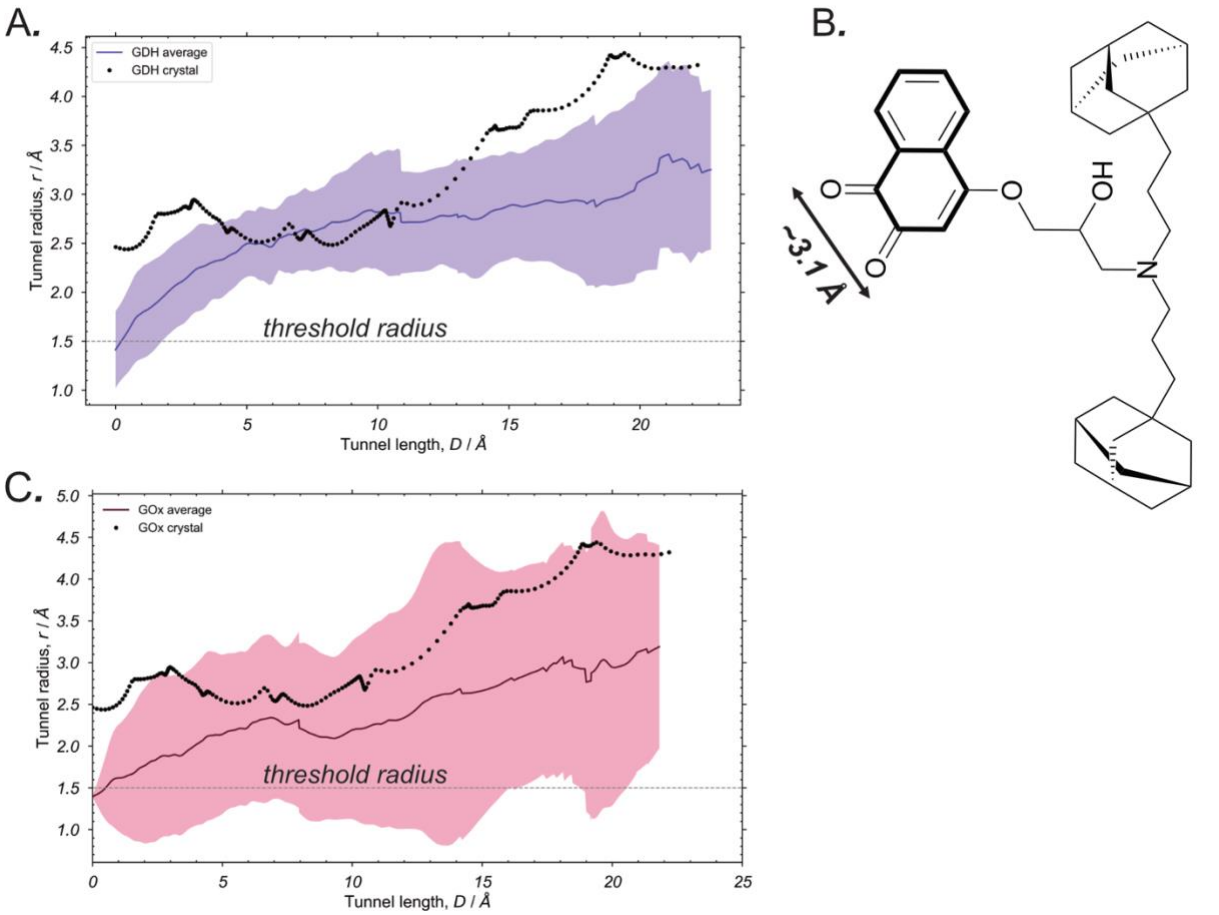

Figure 4.4 Variation in tunnel radii among oxidoreductases. The tunnels of both (FAD-GDH) and (GOx) are examined before (crystal structure) and through the 10 ns of MD. The radius of the GOx tunnel is markedly smaller than that of GDH, and NQ-A encounters steric hindrance in accessing the FAD cofactor, remaining at 10.9 Å. Panel B illustrates the minimum approach dimension of NQ-A in comparison to the tunnel radii in both A and B. The fluctuations shown by the shaded are depict the time-dependent changes in tunnel radii across all enzymes during 10 ns of MD. Both enzymes exhibit changes in radii, potentially regulating mediator movement into the active site.

From the tunnel visualization, it is apparent that FAD-GDH has a significantly larger radius than GOx both before and after equilibrium at 10 ns of MD. The electron transfer process in redox mediators is governed by a combination of driving force and mediator size[28], which dictates the ability to diffuse into the active site. With an approach width of ~ 3.1 Å, NQ-A has a higher probability to accessing the tunnel in GDH than in GOx. This phenomenon explains why NQ-A redox species is predicted to bind to the cofactor in FAD-GDH while being unable to bind closer

to the cofactor in GOx. This further illustrates why NQ-LPEI cannot access the active site of GOx in solution but can in that of FAD-GDH resulting in no bioelectrocatalysis activity.

Moreover, the active site entrances fluctuate as demonstrated by variation in radii opening for both enzymes in Figure 4.4. The fluctuation in FAD-GDH is more pronounced above the threshold line than those for GOx. This reinforces the idea that the radius of GOx may not open enough to allow the redox polymer to approach the FAD cofactor closely, leaving the distance relatively large and insufficient for short-range electron transfer suitable for quinone redox mediators.

4.4.5 A Comparison Computationally of Approximated Rate constants

The rate constants were approximated based on the distances obtained from MD-molecular docking studies. This approximation follows a similar approach to that used by the Kano group[170] from chapter 3.

A similar derivation is used where the rate of electron transfer in mediators is broadly classified into two regimes: a free energy-dependent regime known as the Linear Free Energy Relationship (LFER) and a non-linear free energy relationship (non-LFER), as expressed in equation 3.3.

(3.3) $$\frac{1}{k_2} = \frac{1}{k_{LFER}} + \frac{1}{k_{non-LFER}}$$

where k_{LFER} represents the rate constant governed by the standard Gibbs energy change (ΔG°) of the reaction as expressed in equation 3.4.

(3.4) $$k_{LFER} = k_{LFER}^\circ exp\left(-\frac{\alpha \Delta G^\circ}{RT}\right)$$

and α ($0 < \alpha < 1$) is a proportionality constant in LFER, k°_{LFER} is the rate constant at $\Delta G^\circ = 0$ and $k^\circ_{non\text{-}LFER}$ is independent of $E^{\circ\prime}$ or (ΔG°).

Assuming that k°_{LFER}, which is dependent on ΔG° is the same for both NQ-A/FAD-GDH and NQ-A/GOx due to their similar redox potential, the limiting constant in the overall electron transfer process is $k^\circ_{non\text{-}LFER}$ which is proportional to the closest distance between the mediator

electron center and the active site FAD. This constant also depends on the diffusion rate constant, k_{diff}. The diffusion dependent rate constant can be expressed by equation 3.5.

(3.5) $k_{diff} = 4\pi N \rho_E \rho_E (D_E + D_M)(r_E + r_M)$

where N, ρ, r and D are Avogadro's number, ratio of the active domain area against the total surface of reactants, radius and diffusivities of the enzyme and redox mediators, respectively. In a diffusion-controlled reaction, the mediator is assumed to be able to access the redox center of the enzyme. However, in this case were one of the mediators loosely access the redox center of the enzyme, there is absence of direct overlap of orbital, but hopping of electron at those short distance assumed by NQ-A/FAD-GDH can be possible. In that case, the logarithmic value of the electron transfer rate is proportional to the closest distance between redox mediator and the active site of the enzyme with a proportionality constant, β, approximated to 12 nm^{-1} for organic mediators.[81,170] The $k^\circ_{non\text{-}LFER}$ becomes identical to k_{diff}. With these assumptions, $k^\circ_{non\text{-}LFER}$ can be expressed for both NQ-A/FAD-GDH (1) and NQ-A/GOx (2) in equation 4.1 and 4.2.

(4.1) $k_{non-\mathrm{LFER}(1)} = \mathrm{k_{diff}}^\circ \exp(-\beta \mathrm{d}(1))$

(4.2) $\mathrm{k_{non-LFER(2)}} = \mathrm{k_{diff}}^\circ \exp(-\beta \mathrm{d}(2))$

Dividing (4.1) by (4.2) gives the ratio of $k^\circ_{non\text{-}LFER}$ of NQ-A/FAD-GDH (1) to NQ-A/GOx (2) and 3.06 and 10.9 Å is substituted for center-to-center distances of NQ-A/FAD-GDH and NQ-A/GOx

(4.3) $\frac{\mathrm{k_{non-LFER(1)}}}{\mathrm{k_{non-LFER(2)}}} = \frac{\exp(-0.306\times12)}{\exp(-1.09\times12)} = 12100$

A comparison of these two systems reveals that NQ-A/FAD-GDH has a rate constant approximately 12,100 times that of NQ-A/GOx at the predicted center to center distances of 3.06 and 10.9 Å. Evaluating these ratios at various distances sampled by NQ-A in NQ-A/GOx bound complexes as depicted in Figure 4.5, it becomes apparent that the ratio basically approaches infinity for any incremental increase in the center-to-center separation. This emphasizes the rate constant dependence on distance. Moreover, this indicates that the activity of NQ-LPEI/GOx is practically zero at the computationally predicted distances. Given the considerable fluctuations of

this in real solution, the activity of NQ-LPEI/GOx is impossible to observe as reported by the Minteer group.[183]

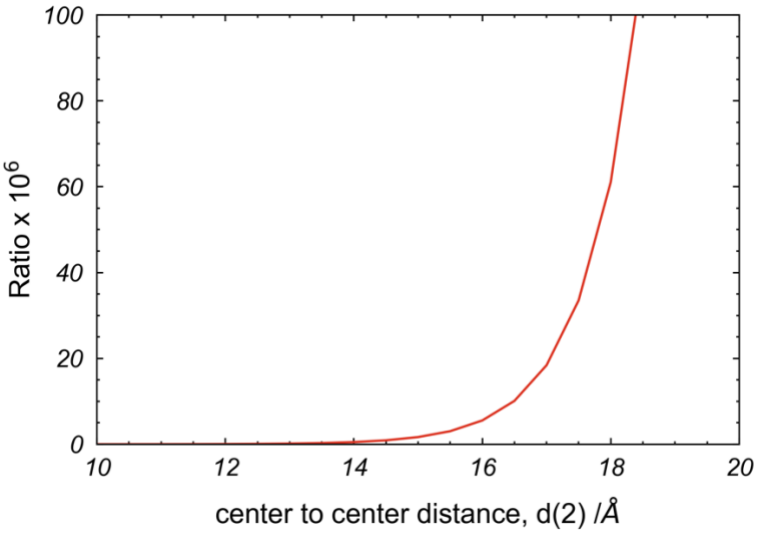

Figure 4.5 The center-to-center distance dependence in NQ-A/GOx complexes as compared to the rate constant ratios calculated by dividing equations (4) and (5) at a constant center-to-center distance in NQ-A/GDH-FAD complexes but varying that of NQ-A/GOx complexes.

4.5 Conclusion

This study aimed to quantitatively investigate why glucose dehydrogenase (FAD-GDH) interacts effectively with a rationally designed modified 1,2-naphthoquinone-LPEI, while glucose oxidase (GOx) remains inactive with the same mediator during bioelectrocatalysis despite their comparable physicoelectrochemical properties. A multilevel computational simulation approach was employed spanning molecular docking, and molecular dynamics to explore this phenomenon. Molecular dynamics served two purposes: simulating the systems to achieve a solution-like environment and ensuring the binding conformation of the oxidoreductase complexes is maintained as the system evolves to equilibrium. MoleOnline was utilized for tunnel radius measurements and visualization.

In this study, molecular docking predicted the binding sites of a representative quinone-modified polymer, NQ-A, to be 3.06 Å and 10.9 Å for GDH and GOx, respectively, from the FAD cofactor. Molecular dynamics confirmed that these binding positions are the most favorable, even

when the system is at equilibrium in a solution-like environment. Furthermore, residues interacting with NQ-A via hydrogen bonding were identified including ASN 93 and ARG 501 in NQ-A/GOx, and THR 333 and HIS 510 in NQ-A/FAD-GDH system. The tunnel radius of the two enzymes was compared, revealing that FAD-GDH has a relatively larger radius than GOx.

Comparative analysis of the tunnel radius of the two enzymes revealed that FAD-GDH has a relatively larger radius than GOx. Residues acting as "molecular gates" were found to govern the size of the active site opening in both systems with TYR 53 and ARG 501 identified in NQ-A/FAD-GDH and TYR 68 and ARG 512 in NQ-A/GOx system. This larger radius in GDH allows for the entrance of the redox polymer, minimizing the distance for electron transfer, whereas in GOx, it prevents the passage of redox mediators, hindering their entrance. The difference in donor-acceptor distances results in FAD-GDH exhibiting rapid electron transfer rates with the quinone-modified redox polymer, while GOx remains inactive.

Utilizing the predicted distances, the electron transfer rate constants for both systems were estimated. The approximations indicated that NQ-A/FAD-GDH system has a rate constant approximately 12,100 times higher than that of NQ-A/GOx which goes to infinity at any further distance. This renders NQ-A/GOx essentially inactive aligning with previous reports. Molecular dynamics simulations elucidated the time-dependent dynamics of the active site tunnel, revealing significant changes in enzyme radius over time, which are crucial for redox mediator diffusion into the active site. Overall, this study highlights the potential of computational investigation in exploring gaps and identifying bottlenecks in electron transfer within mediated systems. Such insights are invaluable for refining mediator design strategies.

Chapter 5: Conclusion and Future Directions.

5.1 Summary

This thesis has showcased efforts to advance the design of redox mediators for enzymatically catalyzed reactions. A structured approach has been demonstrated wherein structure-function relationships are elucidated to comprehend the influence of molecular structure on controlling the activity of redox mediators. Utilizing a model involving glucose oxidase (GOx) and quinone mediators, this thesis has illustrated that the design of mediators for such mediated biological systems can be approached from a molecular engineering perspective. In addition to focusing on the structural features of redox mediators, this study has investigated specific interactions within the active site of GOx. It is acknowledged that mediators undergo processes such as approaching the active site, transport inside the active site, and binding at specific positions. The GOx active site was characterized using computational tools, shedding light on its structure-function relationship within the tunnel to comprehend specific mediator interactions with the catalysts. Leveraging this platform, the analysis was extended to a system involving glucose dehydrogenase (FAD-GDH) and GOx to understand why a quinone-modified mediator function with FAD-GDH but not with GOx. While this work has showcased some achievements in this subject, further research is necessary to deepen our understanding of these mediated – bioelectrocatalytic systems.

5.2 Future Directions

5.2.1 Proposed Polymer Modified Redox Mediator

A separate molecular dynamics study was conducted on a systematically substituted 1,2-naphthoquinone with a sulfonate group at all positions. These simulations were performed for all the mediators shown in Figure 5.1A, wherein an imaginary spring with a constant force was employed to pull the molecule through the active site channel of glucose oxidase. The distance-time profiles of each mediator were recorded and compared, as depicted in Figure 5.1B. It was

observed that the orientation of redox mediators is crucial, and substitution at positions 5 or 6 provides the most ideal geometry for approaching the active site of GOx redox mediators.

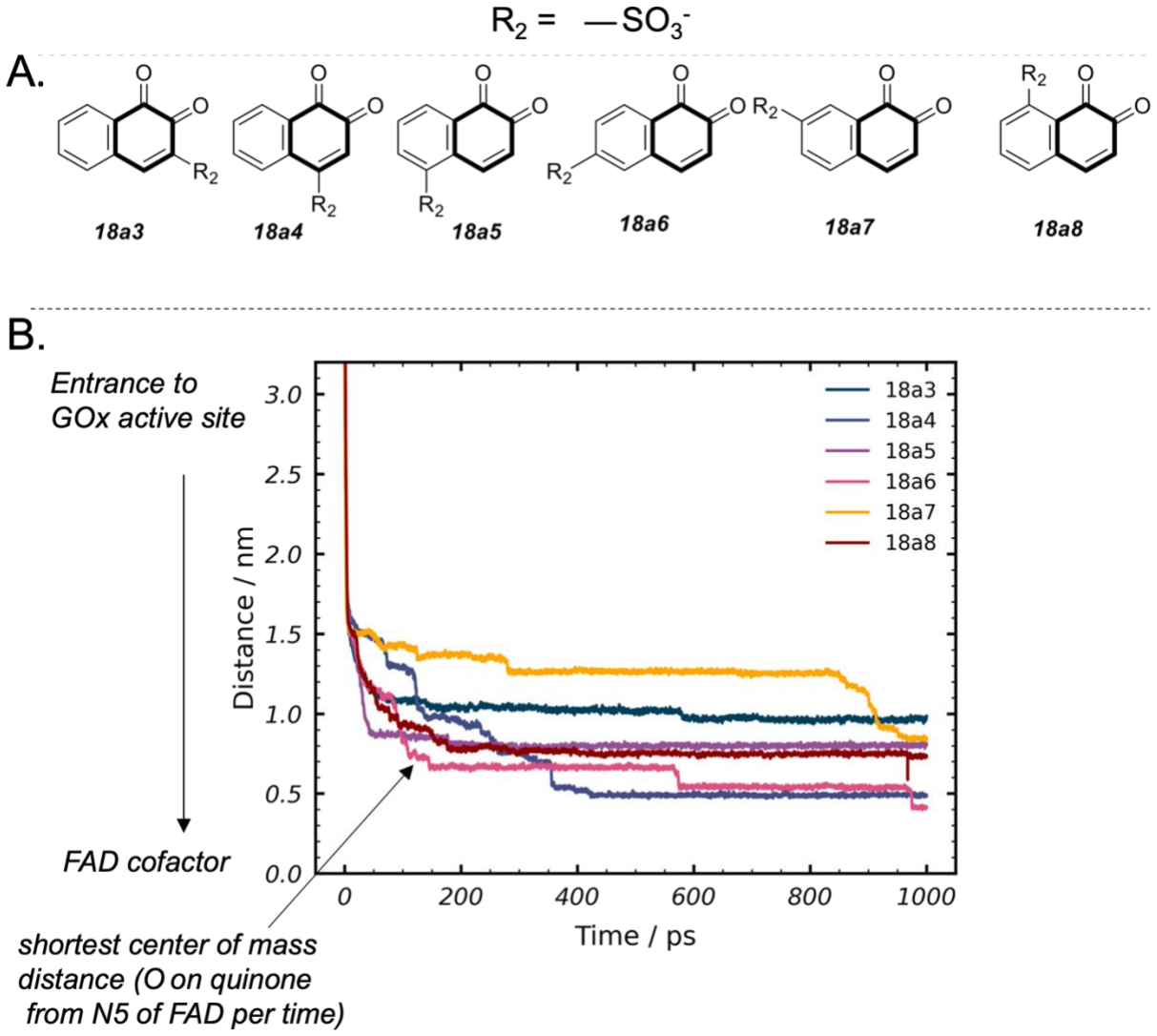

Figure 5.1 The results of the Steered Molecular Dynamics (SMD) study showing distance-time profiles of systematically substituted quinones. The quinone substituted at position 6 demonstrates the furthest distance reached to the FAD cofactor within the specified period.

With this knowledge, we developed a novel compound named 6-NQ-A, which is a 1,2-naphthoquinone substituted at position 6 by adamantane group. The redox mediator was optimized and subjected to molecular docking against GOx as shown in Scheme 5.1. Simulation results indicated that 6-NQ-A binds approximately 3.2 Å away from N5 of FAD of GOx, suggesting a favorable distance conducive to rapid electron transfer, potentially comparable to or even

surpassing that observed in FAD-GDH. With a high degree of confidence, it can be inferred that if 1,2-naphthoquinone substituted at position 6 modified with LPEI proves effective, it could facilitate high electron transfer rates, thereby rendering GOx-quinone-mediated bioanodes practically viable.

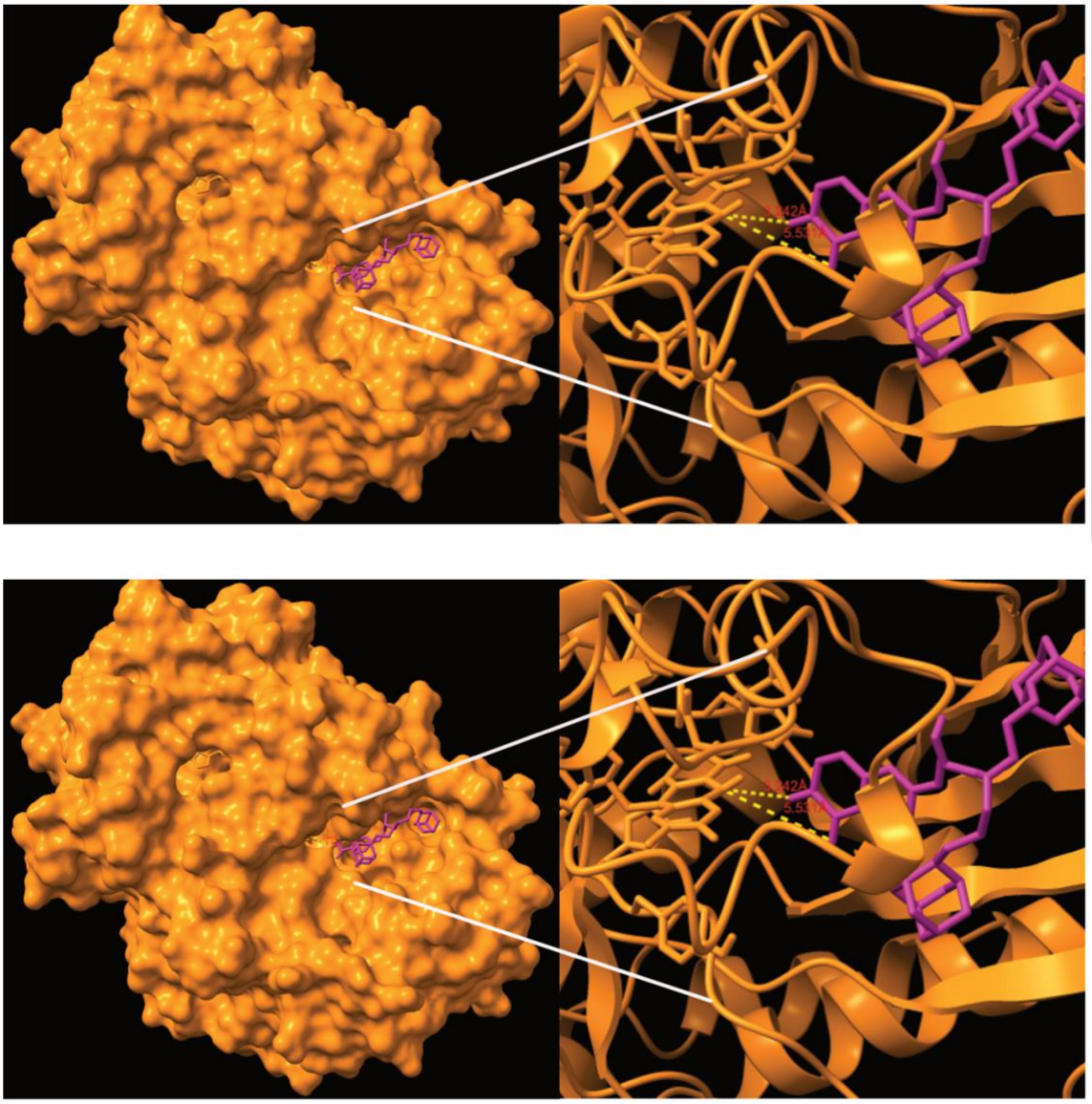

Scheme 5.1 Molecular docking simulations predicting the position of 6-NQ-A on GOx, with the electron centers of 6-NQ-A anticipated to be approximately 3.2 Å away from the FAD cofactor, as depicted. This optimal distance suggests a conducive environment for facilitating mediated bioelectrocatalytic activity.

The findings of this preliminary investigation indicate that substituting at position 6 notably enhances the ability of 6-NQ-A to diffuse through the active site, surpassing quinone substitutions at other positions (as depicted in Scheme 5.1). This observation suggests that attaching the linker chain at position 6 could effectively orient the redox mediator within the active site, potentially facilitating electron transfer with GOx.

This presents an opportunity to advance these research areas further through additional experiments, involving the synthesis of the 6-NQ-LPEI redox polymer and subsequent physical testing. It is highly probable that this system will demonstrate bioelectrocatalytic activity for biofuel electrodes.

5.2.2 Mediator Design for Other Oxidoreductases

This thesis demonstrated an effective approach for designing mediators for GOx using parameterized modeling. This methodology can also be applied to design mediators for other systems, such as Nitrogenase or Hydrogenases. These enzymes hold significant potential as environmentally friendly alternatives for nitrogen reduction to value-added products like ammonia. Currently, the mediators for these systems remain unknown. Employing a similar approach can aid in identifying the structural features that mediators must possess to efficiently exchange electrons with the cofactors.

As demonstrated in Chapter 3, employing computational approaches to investigate rate-limiting steps can inform mediator design as well, allowing researchers to assess the feasibility of a mediator of interest before investing time in its synthesis and application.

Overall, there is still more work needed to develop fully effective mediated enzymatic systems that meet the output requirements of next generation biosensors and biofuels.

REFERENCES

(1) Chen, H.; Dong, F.; Minteer, S. D. The Progress and Outlook of Bioelectrocatalysis for the Production of Chemicals, Fuels and Materials. *Nature Catalysis*. Nature Research March 1, 2020, pp 225–244. https://doi.org/10.1038/s41929-019-0408-2.

(2) Atanassov, P.; Banta, S.; Barton, S. C.; Cooney, M.; Liaw, B. Y.; Mukerjee, S.; Apblett, C. Enzymatic Biofuel Cells. *Electrochem Soc Interface* **2007**, *16* (2), 28–31. https://doi.org/10.1149/2.F04072IF.

(2) Cinquin, P.; Gondran, C.; Giroud, F.; Mazabrard, S.; Pellissier, A.; Boucher, F.; Alcaraz, J.-P.; Gorgy, K.; Lenouvel, F.; Mathé, S.; Porcu, P.; Cosnier, S. A Glucose BioFuel Cell Implanted in Rats. *PLoS One* **2010**, *5* (5), e10476. https://doi.org/10.1371/journal.pone.0010476.

(4) Gomez, C.; Shipovskov, S.; Ferapontova, E. E. Peroxidase Biocathodes for a Biofuel Cell Development. *Journal of Renewable and Sustainable Energy* **2010**, *2* (1), 13103. https://doi.org/10.1063/1.3298136/284545.

(5) Barton, S. C.; Gallaway, J.; Atanassov, P. Enzymatic Biofuel Cells for Implantable and Microscale Devices. *Chem Rev* **2004**, *104* (10), 4867–4886. https://doi.org/10.1021/cr020719k.

(6) Jeon, W. Y.; Lee, J. H.; Dashnyam, K.; Choi, Y. B.; Kim, T. H.; Lee, H. H.; Kim, H. W.; Kim, H. H. Performance of a Glucose-Reactive Enzyme-Based Biofuel Cell System for Biomedical Applications. *Sci Rep* **2019**, *9* (1). https://doi.org/10.1038/s41598-019-47392-1.

(7) Bollella, P.; Lee, I.; Blaauw, D.; Katz, E. A Microelectronic Sensor Device Powered by a Small Implantable Biofuel Cell. *ChemPhysChem* **2020**, *21* (1), 120–128. https://doi.org/10.1002/cphc.201900700.

(8) Kavanagh, P.; Leech, D. Mediated Electron Transfer in Glucose Oxidising Enzyme Electrodes for Application to Biofuel Cells: Recent Progress and Perspectives. *Physical Chemistry Chemical Physics*. April 14, 2013, pp 4859–4869. https://doi.org/10.1039/c3cp44617d.

(9) Ruff, A.; Conzuelo, F.; Schuhmann, W. Bioelectrocatalysis as the Basis for the Design of Enzyme-Based Biofuel Cells and Semi-Artificial Biophotoelectrodes. *Nature Catalysis*. Nature Research March 1, 2020, pp 214–224. https://doi.org/10.1038/s41929-019-0381-9.

(10) Hyun, K.; Kang, S.; Kwon, Y. Performance Evaluation of Glucose Oxidation Reaction Using Biocatalysts Adopting Different Quinone Derivatives and Their Utilization in Enzymatic Biofuel Cells. *Korean Journal of Chemical Engineering* **2019**, *36* (3), 500–504. https://doi.org/10.1007/s11814-018-0218-2.

(11) Ikeda, T.; Kano, K. An Electrochemical Approach to the Studies of Biological Redox Reactions and Their Applications to Biosensors, Bioreactors, and Biofuel Cells. *J Biosci Bioeng* **2001**, *92* (1), 9–18. https://doi.org/10.1016/S1389-1723(01)80191-2.

(12) Wang, J. Electrochemical Glucose Biosensors. *Chem Rev* **2008**, *108* (2), 814–825. https://doi.org/10.1021/cr068123a.

(13) Christwardana, M.; Ji, J.; Chung, Y.; Kwon, Y. Highly Sensitive Glucose Biosensor Using New Glucose Oxidase Based Biocatalyst. *Korean Journal of Chemical Engineering* **2017**, *34* (11), 2916–2921. https://doi.org/10.1007/s11814-017-0224-9.

(14) Ghica, M. E.; Brett, C. M. A. A Glucose Biosensor Using Methyl Viologen Redox Mediator on Carbon Film Electrodes. *Anal Chim Acta* **2005**, *532* (2), 145–151. https://doi.org/10.1016/j.aca.2004.10.058.

(15) Park, T. M.; Iwuoha, E. I.; Smyth, M. R.; MacCraith, B. D. Sol-Gel-Based Amperometric Glucose Biosensor Incorporating an Osmium Redox Polymer as Mediator. *Analytical Communications* **1996**, *33* (8), 271–273. https://doi.org/10.1039/AC9963300271.

(16) Martinez, C. M.; Alvarez, L. H. Application of Redox Mediators in Bioelectrochemical Systems. *Biotechnology Advances*. Elsevier Inc. September 1, 2018, pp 1412–1423. https://doi.org/10.1016/j.biotechadv.2018.05.005.

(17) Hickey, D. P.; Gaffney, E. M.; Minteer, S. D. Electrometabolic Pathways: Recent Developments in Bioelectrocatalytic Cascades. *Top Curr Chem* **2018**, *376* (6). https://doi.org/10.1007/s41061-018-0221-4.

(18) Milton, R. D.; Wang, T.; Knoche, K. L.; Minteer, S. D. Tailoring Biointerfaces for Electrocatalysis. *Langmuir* **2016**, *32* (10), 2291–2301. https://doi.org/10.1021/acs.langmuir.5b04742.

(19) Milton, R. D.; Minteer, S. D. Direct Enzymatic Bioelectrocatalysis: Differentiating between Myth and Reality. *J R Soc Interface* **2017**, *14* (131). https://doi.org/10.1098/rsif.2017.0253.

(20) FREW, J. E.; HILL, H. A. O. Direct and Indirect Electron Transfer between Electrodes and Redox Proteins. *Eur J Biochem* **1988**, *172* (2), 261–269. https://doi.org/10.1111/j.1432-1033.1988.tb13882.x.

(21) Léger, C.; Bertrand, P. Direct Electrochemistry of Redox Enzymes as a Tool for Mechanistic Studies. *Chemical Reviews*. July 2008, pp 2379–2438. https://doi.org/10.1021/cr0680742.

(22) Mazurenko, I.; Hitaishi, V. P.; Lojou, E. Recent Advances in Surface Chemistry of Electrodes to Promote Direct Enzymatic Bioelectrocatalysis. *Current Opinion in Electrochemistry*. Elsevier B.V. February 1, 2020, pp 113–121. https://doi.org/10.1016/j.coelec.2019.11.004.

(23) Sosna, M.; Bonamore, A.; Gorton, L.; Boffi, A.; Ferapontova, E. E. Direct Electrochemistry and Os-Polymer-Mediated Bioelectrocatalysis of NADH Oxidation by Escherichia Coli Flavohemoglobin at Graphite Electrodes. *Biosens Bioelectron* **2013**, *42* (1), 219–224. https://doi.org/10.1016/j.bios.2012.10.094.

(24) Degani, Y.; Heller, Adam. Direct Electrical Communication between Chemically Modified Enzymes and Metal Electrodes. I. Electron Transfer from Glucose Oxidase to Metal Electrodes via Electron Relays, Bound Covalently to the Enzyme. *J Phys Chem* **1987**, *91* (6), 1285–1289. https://doi.org/10.1021/j100290a001.

(25) Léger, C.; Bertrand, P. Direct Electrochemistry of Redox Enzymes as a Tool for Mechanistic Studies. *Chemical Reviews*. July 2008, pp 2379–2438. https://doi.org/10.1021/cr0680742.

(26) Bauer, J. A.; Zámocká, M.; Majtán, J.; Bauerová-Hlinková, V. Glucose Oxidase, an Enzyme “Ferrari”: Its Structure, Function, Production and Properties in the Light of Various Industrial and Biotechnological Applications. *Biomolecules*. MDPI March 1, 2022. https://doi.org/10.3390/biom12030472.

(27) Chen, H.; Simoska, O.; Lim, K.; Grattieri, M.; Yuan, M.; Dong, F.; Seok Lee, Y.; Beaver, K.; Weliwatte, S.; M. Gaffney, E.; D. Minteer, S. Fundamentals, Applications, and Future Directions of Bioelectrocatalysis. *Chem Rev* **2020**, *120* (23), 12903–12993. https://doi.org/10.1021/acs.chemrev.0c00472.

(28) Mtemeri, L.; Hickey, D. P. Model-Driven Design of Redox Mediators: Quantifying the Impact of Quinone Structure on Bioelectrocatalytic Activity with Glucose Oxidase. *J Phys Chem B* **2023**. https://doi.org/10.1021/acs.jpcb.3c03740.

(29) Anson, C. W.; Stahl, S. S. Mediated Fuel Cells: Soluble Redox Mediators and Their Applications to Electrochemical Reduction of O2 and Oxidation of H2, Alcohols, Biomass, and Complex Fuels. *Chemical Reviews*. American Chemical Society April 22, 2020, pp 3749–3786. https://doi.org/10.1021/acs.chemrev.9b00717.

(30) Uchimiya, M.; Stone, A. T. Reversible Redox Chemistry of Quinones: Impact on Biogeochemical Cycles. *Chemosphere*. Elsevier Ltd 2009, pp 451–458. https://doi.org/10.1016/j.chemosphere.2009.07.025.

(31) Leskovac, V.; Trivić, S.; Wohlfahrt, G.; Kandrač, J.; Peričin, D. Glucose Oxidase from Aspergillus Niger: The Mechanism of Action with Molecular Oxygen, Quinones, and One-Electron Acceptors. *International Journal of Biochemistry and Cell Biology*. Elsevier Ltd 2005, pp 731–750. https://doi.org/10.1016/j.biocel.2004.10.014.

(32) Sarewicz, M.; Osyczka, A. ELECTRONIC CONNECTION BETWEEN THE QUINONE AND CYTOCHROME C REDOX POOLS AND ITS ROLE IN REGULATION OF MITOCHONDRIAL ELECTRON TRANSPORT AND REDOX SIGNALING Sarewicz M, Osyczka A. Electronic Connection Between the Quinone and Cytochrome c Redox Pools and Its. *Physiol Rev* **2015**, *95*, 219–243. https://doi.org/10.1152/physrev.00006.2014.-Mi.

(33) E. G. Cass, A.; Davis, Graham.; D. Francis, G.; Allen O. Hill, H.; J. Aston, W.; John. Higgins, I.; V. Plotkin, E.; D. L. Scott, L.; P. F. Turner, A. Ferrocene-Mediated Enzyme Electrode for Amperometric Determination of Glucose. *Anal Chem* **2002**, *56* (4), 667–671. https://doi.org/10.1021/ac00268a018.

(34) Ohara, T. J.; Rajagopalan, R.; Heller, A. *Glucose Electrodes Based on Cross-Linked [Os(Bpy)2Cl]+/2+ Complexed Poly(1-Vlnyllmidazole) Films*; 1993; Vol. 65. https://pubs.acs.org/sharingguidelines.

(35) Flexer, V.; Ielmini, M. V.; Calvo, E. J.; Bartlett, P. N. Extracting Kinetic Parameters for Homogeneous [Os(Bpy)2ClPyCOOH]+ Mediated Enzyme Reactions from Cyclic Voltammetry and Simulations. *Bioelectrochemistry* **2008**, *74* (1), 201–209. https://doi.org/10.1016/j.bioelechem.2008.08.001.

(36) Hickey, D. P.; Cai, R.; Yang, Z. Y.; Grunau, K.; Einsle, O.; Seefeldt, L. C.; Minteer, S. D. Establishing a Thermodynamic Landscape for the Active Site of Mo-Dependent

Nitrogenase. *J Am Chem Soc* **2019**, *141* (43), 17150–17157. https://doi.org/10.1021/jacs.9b06546.

(37) Rutledge, H. L.; Tezcan, F. A. Electron Transfer in Nitrogenase. *Chem Rev* **2020**. https://doi.org/10.1021/acs.chemrev.9b00663.

(38) Ruth, J. C.; Spormann, A. M. Enzyme Electrochemistry for Industrial Energy Applications - A Perspective on Future Areas of Focus. *ACS Catalysis*. American Chemical Society May 21, 2021, pp 5951–5967. https://doi.org/10.1021/acscatal.1c00708.

(39) Nakashima, Y.; Mizoshita, N.; Tanaka, H.; Nakaoki, Y. Amphiphilic Polymer Mediators Promoting Electron Transfer on Bioanodes with PQQ-Dependent Glucose Dehydrogenase. *Langmuir* **2016**, *32* (49), 12986–12994. https://doi.org/10.1021/acs.langmuir.6b03145.

(40) Tsuruoka, N.; Sadakane, T.; Hayashi, R.; Tsujimura, S. Bimolecular Rate Constants for FAD-Dependent Glucose Dehydrogenase from Aspergillus Terreus and Organic Electron Acceptors. *Int J Mol Sci* **2017**, *18* (3). https://doi.org/10.3390/ijms18030604.

(41) Babanova, S.; Matanovic, I.; Chavez, M. S.; Atanassov, P. Role of Quinones in Electron Transfer of PQQ-Glucose Dehydrogenase Anodes - Mediation or Orientation Effect. *J Am Chem Soc* **2015**, *137* (24), 7754–7762. https://doi.org/10.1021/jacs.5b03053.

(42) Butler, J.; Hoey, B. M. *The One-Electron Reduction Potential of Several Substrates Can Be Related to Their Reduction Rates by Cytochrome P-450 Reductase*; 1993.

(43) Forrow, N. J.; Sanghera, G. S.; Walters, S. J. The Influence of Structure in the Reaction of Electrochemically Generated Ferrocenium Derivatives with Reduced Glucose Oxidase. *Journal of the Chemical Society, Dalton Transactions* **2002**, No. 16, 3187–3194. https://doi.org/10.1039/b204702k.

(44) Calabrese Barton, S.; Kim, H.-H.; Binyamin, G.; Zhang, Y.; Heller, A. Electroreduction of O 2 to Water on the “Wired” Laccase Cathode †. **2001**. https://doi.org/10.1021/jp012488b.

(45) Cinquin, P.; Gondran, C.; Giroud, F.; Mazabrard, S.; Pellissier, A. A Glucose BioFuel Cell Implanted in Rats. *PLoS One* **2010**, *5* (5), 10476. https://doi.org/10.1371/journal.pone.0010476.

(46) Edelman, P. G.; Wang, J.; Kaku, T.; Karan, H. J.; Okamoto, Y.; Heller, A.; Degani, Y.; Gregg, B. *Electrical Communication between Electrodes and Enzymes Mediated by Redox Hydrogels*; UTC, 1992; Vol. 487. https://pubs.acs.org/sharingguidelines.

(47) Martinkova, P.; Pohanka, M. Biosensors for Blood Glucose and Diabetes Diagnosis: Evolution, Construction, and Current Status. *Anal Lett* **2015**, *48* (16), 2509–2532. https://doi.org/10.1080/00032719.2015.1043661.

(48) Minteer, S. D. *Enzyme Stabilization and Immobilization*; Minteer, S. D., Ed.; Methods in Molecular Biology; Springer New York: New York, NY, 2017; Vol. 1504. https://doi.org/10.1007/978-1-4939-6499-4.

(49) Hickey, D. P. *Enzyme Stabilization and Immobilization*; Minteer, S. D., Ed.; Methods in Molecular Biology; Springer New York: New York, NY, 2017; Vol. 1504. https://doi.org/10.1007/978-1-4939-6499-4.

(50) Janda, P.; Weber, J. *Quinone-Mediated Glucose Oxidase Electrode with the Enzyme Immobilized in Polypyrrole*; Elsevier Sequoia S.A, 1991; Vol. 300.

(51) Janda, P.; Weber, J. *Quinone-Mediated Glucose Oxidase Electrode with the Enzyme Immobilized in Polypyrrole*; Elsevier Sequoia S.A, 1991; Vol. 300.

(52) Limoges, B.; Savéant, J. M. Catalysis by Immobilized Redox Enzymes. Diagnosis of Inactivation and Reactivation Effects through Odd Cyclic Voltammetric Responses. *Journal of Electroanalytical Chemistry* **2004**, *562* (1), 43–52. https://doi.org/10.1016/j.jelechem.2003.07.035.

(53) Gallaway, J. W.; Barton, S. A. C. Kinetics of Redox Polymer-Mediated Enzyme Electrodes. *J Am Chem Soc* **2008**, *130* (26), 8527–8536. https://doi.org/10.1021/ja0781543.

(54) Tripathi, A. K.; Joy, M. E.; Choudhury, D.; Das, R.; Neergat, M. Kinetics of V 5+ /V 4+ Redox Reaction—Butler-Volmer and Marcus Models . *J Electrochem Soc* **2021**, *168* (11), 110548. https://doi.org/10.1149/1945-7111/ac39d9.

(55) Huz3, T.-W.; Wong, K.-Y.; Shiu, K.-K. *Kinetics of O-Benzoquinone Mediated Oxidation of Glucose by Glucose Oxidase at Edge Plane Pyrolytic Graphite Electrode*; 1995.

(56) Huz3, T.-W.; Wong, K.-Y.; Shiu, K.-K. *Kinetics of O-Benzoquinone Mediated Oxidation of Glucose by Glucose Oxidase at Edge Plane Pyrolytic Graphite Electrode*; 1995.

(57) Bartlett, P. N.; Pratt, K. F. E. Theoretical Treatment of Diffusion and Kinetics in Amperometric Immobilized Enzyme Electrodes Part I: Redox Mediator Entrapped within the Film. *Journal of Electroanalytical Chemistry* **1995**, *397* (1–2), 61–78. https://doi.org/10.1016/0022-0728(95)04236-7.

(58) Elgrishi, N.; J. Rountree, K.; D. McCarthy, B.; S. Rountree, E.; T. Eisenhart, T.; L. Dempsey, J. A Practical Beginner's Guide to Cyclic Voltammetry. *J Chem Educ* **2017**, *95* (2), 197–206. https://doi.org/10.1021/acs.jchemed.7b00361.

(59) Heineman, W. R.; Kissinger, P. T. Analytical Electrochemistry: Methodology and Applications of Dynamic Techniques. *Anal Chem* **1978**, *50* (5), 166–175. https://doi.org/10.1021/ac50028a020.

(60) Mirceski, V.; Gulaboski, R.; Lovric, M.; Bogeski, I.; Kappl, R.; Hoth, M. Square-Wave Voltammetry: A Review on the Recent Progress. *Electroanalysis* **2013**, *25* (11), 2411–2422. https://doi.org/10.1002/elan.201300369.

(61) De Souza, D.; Codognoto, L.; Malagutti, A. R.; Toledo, R. A.; Pedrosa, V. A.; Oliveira, R. T. S.; Mazo, L. H.; Avaca, L. A.; Machado, S. A. S. Square Wave Voltammetry. Second Part: Applications. *Quim Nova* **2004**, *27* (5), 790–797. https://doi.org/10.1590/S0100-40422004000500019.

(62) De Souza, D.; Machado, S. A. S.; Avaca, L. A. Square Wave Voltammetry. Part I: Theoretical Aspects. *Quim Nova* **2003**, *26* (1), 81–89. https://doi.org/10.1590/S0100-40422003000100015.

(63) Eccles, G. N. Recent Advances in Pulse Cyclic and Square-Wave Cyclic Voltammetric Analysis. *Crit Rev Anal Chem* **1991**, *22* (5), 345–380. https://doi.org/10.1080/10408349108051639.

(64) Mirceski, V.; Gulaboski, R.; Lovric, M.; Bogeski, I.; Kappl, R.; Hoth, M. Square-Wave Voltammetry: A Review on the Recent Progress. *Electroanalysis* **2013**, *25* (11), 2411–2422. https://doi.org/10.1002/ELAN.201300369.

(65) Gibson, Q. H.; Swoboda, B. E. P.; Massey, V. Kinetics and Mechanism of Action of Glucose Oxidase. *Journal of Biological Chemistry* **1964**, *239* (11), 3927–3934. https://doi.org/10.1016/S0021-9258(18)91224-X.

(66) Tao, Z.; Raffel, R. A.; Souid, A.-K.; Goodisman, J. Kinetic Studies on Enzyme-Catalyzed Reactions: Oxidation of Glucose, Decomposition of Hydrogen Peroxide and Their Combination. *Biophys J* **2009**, *96* (7), 2977–2988. https://doi.org/10.1016/j.bpj.2008.11.071.

(67) Bard, A. J. Elements of Molecular and Biomolecular Electrochemistry: An Electrochemical Approach to Electron Transfer Chemistry By Jean-Michel Savéant (Université de Paris 7, Denis Diderot). J. Wiley & Sons, Inc.: Hoboken, NJ. 2006. Xviii + 486 Pp. $135. ISBN 0-471-44573-8. *J Am Chem Soc* **2007**, *129* (1), 242–242. https://doi.org/10.1021/ja069754p.

(68) Marcus, R. A.; Sutin, N. Electron Transfers in Chemistry and Biology. *Biochimica et Biophysica Acta (BBA) - Reviews on Bioenergetics* **1985**, *811* (3), 265–322. https://doi.org/10.1016/0304-4173(85)90014-X.

(69) Turró, C.; Zaleski, J. M.; Karabatsos, Y. M.; Nocera, D. G. *Bimolecular Electron Transfer in the Marcus Inverted Region*; 1996. https://pubs.acs.org/sharingguidelines.

(70) Henstridge, M. C.; Laborda, E.; Rees, N. V.; Compton, R. G. Marcus-Hush-Chidsey Theory of Electron Transfer Applied to Voltammetry: A Review. *Electrochim Acta* **2012**, *84*, 12–20. https://doi.org/10.1016/j.electacta.2011.10.026.

(71) Bard AJ, F. L. *Electrochemical Methods. Fundamental and Applications*; 2001.

(72) Matsumoto, R.; Kano, K.; Ikeda, T. Theory of Steady-State Catalytic Current of Mediated Bioelectrocatalysis. *Journal of Electroanalytical Chemistry* **2002**, *535* (1–2), 37–40. https://doi.org/10.1016/S0022-0728(02)01159-2.

(73) An, D.; Petrović, P.; Frank, D.; Caroline, S.; Kamerlin, L.; Hoffmann, K.; Strodel, B. Shuffling Active Site Substate Populations Affects Catalytic Activity: The Case of Glucose Oxidase. **2017**. https://doi.org/10.1021/acscatal.7b01575.

(74) Clegg, A. D.; Rees, N. V.; Klymenko, O. V.; Coles, B. A.; Compton, R. G. Experimental Validation of Marcus Theory for Outer-Sphere Heterogeneous Electron-Transfer Reactions: The Oxidation of Substituted 1,4-Phenylenediamines. *ChemPhysChem* **2004**, *5* (8), 1234–1240. https://doi.org/10.1002/cphc.200400128.

(75) Taylor, N. B.; Kassal, I. Generalised Marcus Theory for Multi-Molecular Delocalised Charge Transfer. *Chem Sci* **2018**, *9* (11), 2942–2951. https://doi.org/10.1039/c8sc00053k.

(76) Turró, C.; Zaleski, J. M.; Karabatsos, Y. M.; Nocera, D. G. *Bimolecular Electron Transfer in the Marcus Inverted Region*; 1996. https://pubs.acs.org/sharingguidelines.

(77) Turró, C.; Zaleski, J. M.; Karabatsos, Y. M.; Nocera, D. G. Bimolecular Electron Transfer in the Marcus Inverted Region. *J Am Chem Soc* **1996**, *118* (25), 6060–6067. https://doi.org/10.1021/JA960575P/ASSET/IMAGES/LARGE/JA960575PF00007.JPEG.

(78) Butler, J. A. V. Studies in Heterogeneous Equilibria. Part II.—The Kinetic Interpretation of the Nernst Theory of Electromotive Force. *Trans. Faraday Soc.* **1924**, *19* (March), 729–733. https://doi.org/10.1039/TF9241900729.

(79) Hamelers, H. V. M.; Ter Heijne, A.; Stein, N.; Rozendal, R. A.; Buisman, C. J. N. Butler-Volmer-Monod Model for Describing Bio-Anode Polarization Curves. **2010**. https://doi.org/10.1016/j.biortech.2010.06.156.

(80) Armstrong, F. A.; Camba, R.; Heering, H. A.; Hirst, J.; Jeuken, L. J. C.; Jones, A. K.; Le′ger, C.; McEvoy, J. P. Fast Voltammetric Studies of the Kinetics and Energetics of Coupled Electron-Transfer Reactions in Proteins. *Faraday Discuss* **2000**, *116*, 191–203. https://doi.org/10.1039/b002290j.

(81) Vazquez-Duhalt, R.; Aguila, S. A.; Arrocha, A. A.; Ayala, M. QM/MM Molecular Modeling and Marcus Theory in the Molecular Design of Electrodes for Enzymatic Fuel Cells. *ChemElectroChem* **2014**, *1* (3), 496–513. https://doi.org/10.1002/celc.201300096.

(82) Fraser, D. M.; Zakeeruddin, S. M.; Grätzel, M. Towards Mediator Design: II. Optimization of Mediator Global Charge for the Mediation of Glucose Oxidase of Aspergillus Niger. *Journal of Electroanalytical Chemistry* **1993**, *359* (1–2), 125–139. https://doi.org/10.1016/0022-0728(93)80405-7.

(83) Zakeeruddin, S. M.; Fraser, D. M.; Nazeeruddin, M.-K.; Grätzel, M. Towards Mediator Design: Characterization of Tris-(4,4′-Substituted-2,2′-Bipyridine) Complexes of Iron(II), Ruthenium(II) and Osmium(II) as Mediators for Glucose Oxidase of Aspergillus Niger and Other Redox Proteins. *Journal of Electroanalytical Chemistry* **1992**, *337* (1–2), 253–283. https://doi.org/10.1016/0022-0728(92)80542-C.

(84) Choi, J. M.; Kim, H.-S. Structure-Guided Rational Design of the Substrate Specificity and Catalytic Activity of an Enzyme; 2020; pp 181–202. https://doi.org/10.1016/bs.mie.2020.04.050.

(85) Hosseinzadeh, P.; Lu, Y. Design and Fine-Tuning Redox Potentials of Metalloproteins Involved in Electron Transfer in Bioenergetics. *Biochim Biophys Acta Bioenerg* **2016**, *1857* (5), 557–581. https://doi.org/10.1016/j.bbabio.2015.08.006.

(86) Kulys, J. J.; Čénas, N. K. Oxidation of Glucose Oxidase from Penicillium Vitale by One- and Two-Electron Acceptors. *Biochimica et Biophysica Acta (BBA) - Protein Structure and Molecular Enzymology* **1983**, *744* (1), 57–63. https://doi.org/10.1016/0167-4838(83)90340-0.

(87) Cherkasov, A.; Muratov, E. N.; Fourches, D.; Varnek, A.; Baskin, I. I.; Cronin, M.; Dearden, J.; Gramatica, P.; Martin, Y. C.; Todeschini, R.; Consonni, V.; Kuz'Min, V. E.; Cramer, R.; Benigni, R.; Yang, C.; Rathman, J.; Terfloth, L.; Gasteiger, J.; Richard, A.; Tropsha, A. QSAR Modeling: Where Have You Been? Where Are You Going To? *Journal of Medicinal Chemistry*. American Chemical Society June 26, 2014, pp 4977–5010. https://doi.org/10.1021/jm4004285.

(88) Rasulev, B. F.; Abdullaev, N. D.; Syrov, V. N.; Leszczynski, J. A Quantitative Structure-Activity Relationship (QSAR) Study of the Antioxidant Activity of Flavonoids. *QSAR Comb Sci* **2005**, *24* (9), 1056–1065. https://doi.org/10.1002/qsar.200430013.

(89) Rhodes, Z.; Simoska, O.; Dantanarayana, A.; Stevenson, K. J.; Minteer, S. D. Using Structure-Function Relationships to Understand the Mechanism of Phenazine-Mediated Extracellular Electron Transfer in Escherichia Coli. *iScience* **2021**, *24* (9). https://doi.org/10.1016/j.isci.2021.103033.

(90) Nieh, C. H.; Tsujimura, S.; Shirai, O.; Kano, K. Electrostatic and Steric Interaction between Redox Polymers and Some Flavoenzymes in Mediated Bioelectrocatalysis. *Journal of Electroanalytical Chemistry* **2013**, *689*, 26–30. https://doi.org/10.1016/j.jelechem.2012.11.023.

(91) Yang, J.-H.; Kim, H. T.; Kim, H. A Cyclodextrin-Based Approach for Selective Detection of Catecholamine Hormone Mixtures. *Micro and Nano Systems Letters* **2014**, *2* (1), 1. https://doi.org/10.1186/s40486-014-0001-z.

(92) Kingsley, L. J.; Lill, M. A. Substrate Tunnels in Enzymes: Structure-Function Relationships and Computational Methodology. *Proteins: Structure, Function and Bioinformatics*. John Wiley and Sons Inc. April 1, 2015, pp 599–611. https://doi.org/10.1002/prot.24772.

(93) Ströhle, F. W.; Cekic, S. Z.; Magnusson, A. O.; Schwaneberg, U.; Roccatano, D.; Schrader, J.; Holtmann, D. A Computational Protocol to Predict Suitable Redox Mediators for Substitution of NAD(P)H in P450 Monooxygenases. *J Mol Catal B Enzym* **2013**, *88*, 47–51. https://doi.org/10.1016/j.molcatb.2012.11.010.

(94) Ding, Y.; Li, Y.; Yu, G. Exploring Bio-Inspired Quinone-Based Organic Redox Flow Batteries: A Combined Experimental and Computational Study. *Chem* **2016**, *1* (5), 790–801. https://doi.org/10.1016/j.chempr.2016.09.004.

(95) Do, P. C.; Lee, E. H.; Le, L. Steered Molecular Dynamics Simulation in Rational Drug Design. *J Chem Inf Model* **2018**, *58* (8), 1473–1482. https://doi.org/10.1021/ACS.JCIM.8B00261/ASSET/IMAGES/LARGE/CI-2018-00261D_0001.JPEG.

(96) De Vivo, M.; Masetti, M.; Bottegoni, G.; Cavalli, A. Role of Molecular Dynamics and Related Methods in Drug Discovery. **2016**. https://doi.org/10.1021/acs.jmedchem.5b01684.

(97) De Vivo, M.; Masetti, M.; Bottegoni, G.; Cavalli, A. Role of Molecular Dynamics and Related Methods in Drug Discovery. *Journal of Medicinal Chemistry*. American Chemical Society May 12, 2016, pp 4035–4061. https://doi.org/10.1021/acs.jmedchem.5b01684.

(98) Xiang, T. X.; Anderson, B. D. Liposomal Drug Transport: A Molecular Perspective from Molecular Dynamics Simulations in Lipid Bilayers. *Adv Drug Deliv Rev* **2006**, *58* (12–13), 1357–1378. https://doi.org/10.1016/J.ADDR.2006.09.002.

(99) Patel, H. M.; Noolvi, M. N.; Sharma, P.; Jaiswal, V.; Bansal, S.; Lohan, S.; Kumar, S. S.; Abbot, V.; Dhiman, S.; Bhardwaj, V. Quantitative Structure-Activity Relationship (QSAR) Studies as Strategic Approach in Drug Discovery. *Medicinal Chemistry Research* **2014**, *23* (12), 4991–5007. https://doi.org/10.1007/s00044-014-1072-3.

(100) Zhao, Y. H.; Abraham, M. H.; Zissimos, A. M. Fast Calculation of van Der Waals Volume as a Sum of Atomic and Bond Contributions and Its Application to Drug Compounds. *Journal of Organic Chemistry* **2003**, *68* (19), 7368–7373. https://doi.org/10.1021/jo034808o.

(101) Kingsley, L. J.; Lill, M. A. Substrate Tunnels in Enzymes: Structure–Function Relationships and Computational Methodology. *Proteins: Structure, Function, and Bioinformatics* **2015**, *83* (4), 599–611. https://doi.org/10.1002/PROT.24772.

(102) Torres, P. H. M.; Sodero, A. C. R.; Jofily, P.; Silva-Jr, F. P. Key Topics in Molecular Docking for Drug Design. *Int J Mol Sci* **2019**, *20* (18), 4574. https://doi.org/10.3390/ijms20184574.

(103) Thomsen, R.; Christensen, M. H. MolDock: A New Technique for High-Accuracy Molecular Docking. **2006**. https://doi.org/10.1021/jm051197e.

(104) Meyer, M.; Wohlfahrt, G.; Knäblein, J.; Schomburg, D. *Aspects of the Mechanism of Catalysis of Glucose Oxidase: A Docking, Molecular Mechanics and Quantum Chemical Study*; KLUWER/ESCOM, 1998; Vol. 12.

(105) Peng, Y.; Yang, Y.; Li, L.; Jia, Z.; Cao, W.; Alexov, E. DFMD: Fast and Effective DelPhiForce Steered Molecular Dynamics Approach to Model Ligand Approach Toward a Receptor: Application to Spermine Synthase Enzyme. *Front Mol Biosci* **2019**, *6*. https://doi.org/10.3389/fmolb.2019.00074.

(106) Hickey, D. P.; Schiedler, D. A.; Matanovic, I.; Doan, P. V.; Atanassov, P.; Minteer, S. D.; Sigman, M. S. Predicting Electrocatalytic Properties: Modeling Structure–Activity Relationships of Nitroxyl Radicals. *J Am Chem Soc* **2015**, *137* (51), 16179–16186. https://doi.org/10.1021/jacs.5b11252.

(107) Robinson, S. G.; Sigman, M. S. Integrating Electrochemical and Statistical Analysis Tools for Molecular Design and Mechanistic Understanding. *Acc Chem Res* **2020**, *53* (2), 289–299. https://doi.org/10.1021/acs.accounts.9b00527.

(108) Trott, O.; Olson, A. J. AutoDock Vina: Improving the Speed and Accuracy of Docking with a New Scoring Function, Efficient Optimization, and Multithreading. *J Comput Chem* **2010**, *31* (2), 455–461. https://doi.org/10.1002/jcc.21334.

(109) Spitaleri, A.; Decherchi, S.; Cavalli, A.; Rocchia, W. Fast Dynamic Docking Guided by Adaptive Electrostatic Bias: The MD-Binding Approach. *J Chem Theory Comput* **2018**, *14* (3), 1727–1736. https://doi.org/10.1021/acs.jctc.7b01088.

(110) Gumbart, J. Exploring Substrate Diffusion in Channels Using Biased Molecular Dynamics Simulations. In *Membrane Protein Structure and Dynamics*; Humana Press, 2012; pp 337–350. https://doi.org/10.1007/978-1-62703-023-6_19.

(111) Patel, J. S.; Berteotti, A.; Ronsisvalle, S.; Rocchia, W.; Cavalli, A. Steered Molecular Dynamics Simulations for Studying Protein-Ligand Interaction in Cyclin-Dependent Kinase 5. *J Chem Inf Model* **2014**, *54* (2), 470–480. https://doi.org/10.1021/ci4003574.

(112) Ramírez, C. L.; Martí, M. A.; Roitberg, A. E. Steered Molecular Dynamics Methods Applied to Enzyme Mechanism and Energetics. In *Methods in Enzymology*; Academic Press Inc., 2016; Vol. 578, pp 123–143. https://doi.org/10.1016/bs.mie.2016.05.029.

(113) Xiao, B. L.; Ning, Y. N.; Niu, N. N.; Li, D.; Moosavi-Movahedi, A. A.; Sheibani, N.; Hong, J. Steered Molecular Dynamic Simulations of Conformational Lock of Cu, Zn-Superoxide Dismutase. *Sci Rep* **2019**, *9* (1). https://doi.org/10.1038/s41598-019-40892-0.

(114) Chen, L. Y. Free-Energy Landscape of Glycerol Permeation through Aquaglyceroporin GlpF Determined from Steered Molecular Dynamics Simulations. *Biophys Chem* **2010**, *151* (3), 178–180. https://doi.org/10.1016/J.BPC.2010.05.014.

(115) Milton, R. D.; Minteer, S. D. Direct Enzymatic Bioelectrocatalysis: Differentiating between Myth and Reality. *J R Soc Interface* **2017**, *14* (131), 20170253. https://doi.org/10.1098/rsif.2017.0253.

(116) Heller, A. Electrical Connection of Enzyme Redox Centers to Electrodes. *J Phys Chem* **1992**, *96* (9), 3579–3587. https://doi.org/10.1021/j100188a007.

(117) Page, C. C.; Moser, C. C.; Chen, X.; Dutton, P. L. Natural Engineering Principles of Electron Tunnelling in Biological Oxidation–Reduction. *Nature* **1999**, *402* (6757), 47–52. https://doi.org/10.1038/46972.

(118) Kavanagh, P.; Leech, D. Mediated Electron Transfer in Glucose Oxidising Enzyme Electrodes for Application to Biofuel Cells: Recent Progress and Perspectives. *Physical Chemistry Chemical Physics*. April 14, 2013, pp 4859–4869. https://doi.org/10.1039/c3cp44617d.

(119) Milton, R. D.; Hickey, D. P.; Abdellaoui, S.; Lim, K.; Wu, F.; Tan, B.; Minteer, S. D. Rational Design of Quinones for High Power Density Biofuel Cells. *Chem Sci* **2015**, *6* (8), 4867–4875. https://doi.org/10.1039/C5SC01538C.

(120) Zakeeruddin, S. M.; Fraser, D. M.; Nazeeruddin, M. K.; Grätzel, M. Towards Mediator Design: Characterization of Tris-(4,4′-Substituted-2,2′-Bipyridine) Complexes of Iron(II), Ruthenium(II) and Osmium(II) as Mediators for Glucose Oxidase of Aspergillus Niger and Other Redox Proteins. *Journal of Electroanalytical Chemistry* **1992**, *337* (1–2), 253–283. https://doi.org/http://dx.doi.org/10.1016/0022-0728(92)80542-C.

(121) Hernández-Padilla, G.; Cruz-Ramírez, M.; Rebolledo-Chávez, J. P. F.; Ocampo-Hernández, J.; Mendoza, A.; Tenorio, F. J.; Ramírez, L. D.; Ortiz-Frade, L. The Role of Molecular Interaction between GOD and Metal Complexes on Redox Mediation Processes. *J Mol Struct* **2021**, *1245*. https://doi.org/10.1016/j.molstruc.2021.131026.

(122) Patel, H. M.; Noolvi, M. N.; Sharma, P.; Jaiswal, V.; Bansal, S.; Lohan, S.; Kumar, S. S.; Abbot, V.; Dhiman, S.; Bhardwaj, V. Quantitative Structure-Activity Relationship (QSAR) Studies as Strategic Approach in Drug Discovery. *Medicinal Chemistry Research* **2014**, *23* (12), 4991–5007. https://doi.org/10.1007/s00044-014-1072-3.

(123) Hickey, D. P.; Schiedler, D. A.; Matanovic, I.; Doan, P. V.; Atanassov, P.; Minteer, S. D.; Sigman, M. S. Predicting Electrocatalytic Properties: Modeling Structure–Activity Relationships of Nitroxyl Radicals. *J Am Chem Soc* **2015**, *137* (51), 16179–16186. https://doi.org/10.1021/jacs.5b11252.

(124) Brethomé, A. v.; Fletcher, S. P.; Paton, R. S. Conformational Effects on Physical-Organic Descriptors: The Case of Sterimol Steric Parameters. *ACS Catal* **2019**, *9* (3), 2313–2323. https://doi.org/10.1021/acscatal.8b04043.

(125) Leskovac, V.; Trivić, S.; Wohlfahrt, G.; Kandrač, J.; Peričin, D. Glucose Oxidase from Aspergillus Niger: The Mechanism of Action with Molecular Oxygen, Quinones, and One-Electron Acceptors. *International Journal of Biochemistry and Cell Biology*. Elsevier Ltd 2005, pp 731–750. https://doi.org/10.1016/j.biocel.2004.10.014.

(126) Janda, P.; Weber, J. Quinone-Mediated Glucose Oxidase Electrode with the Enzyme Immobilized in Polypyrrole. *J Electroanal Chem Interfacial Electrochem* **1991**, *300* (1–2), 119–127. https://doi.org/10.1016/0022-0728(91)85388-6.

(127) Ikeda, T.; Kano, K. An Electrochemical Approach to the Studies of Biological Redox Reactions and Their Applications to Biosensors, Bioreactors, and Biofuel Cells. *J Biosci Bioeng* **2001**, *92* (1), 9–18. https://doi.org/10.1016/S1389-1723(01)80191-2.

(128) Sarewicz, M.; Osyczka, A. Electronic Connection between the Quinone and Cytochrome c Redox Pools and Its Role in Regulation of Mitochondrial Electron Transport and Redox Signaling. *Physiol Rev* **2015**, *95* (1), 219–243. https://doi.org/10.1152/physrev.00006.2014.

(129) Wendlandt, A. E.; Stahl, S. S. Quinone-Catalyzed Selective Oxidation of Organic Molecules. *Angewandte Chemie International Edition* **2015**, *54* (49), 14638–14658. https://doi.org/10.1002/anie.201505017.

(130) Čėnas, N.; Anusevičius, Ž.; Nivinskas, H.; Misevičiene, L.; Šarlauskas, J. Structure-Activity Relationships in Two-Electron Reduction of Quinones. *Methods Enzymol* **2004**, *382* (1970), 258–277. https://doi.org/10.1016/S0076-6879(04)82015-9.

(131) Newman, D. K.; Kolter, R. A Role for Excreted Quinones in Extracellular Electron Transfer. *Nature* **2000**, *405* (6782), 94–97. https://doi.org/10.1038/35011098.

(132) Battaglini, F.; Koutroumanis, M.; English, A. M.; Mikkelsen, S. R. Targeting Glucose Oxidase at Aspartate and Glutamate Residues with Organic Two-Electron Redox Mediators. *Bioconjug Chem* **1994**, *5* (5), 430–435. https://doi.org/10.1021/bc00029a009.

(133) Butler, J.; Hoey, B. M. The One-Electron Reduction Potential of Several Substrates Can Be Related to Their Reduction Rates by Cytochrome P-450 Reductase. *Biochimica et Biophysica Acta (BBA) - Protein Structure and Molecular Enzymology* **1993**, *1161* (1), 73–78. https://doi.org/10.1016/0167-4838(93)90198-Z.

(134) Nieh, C. H.; Tsujimura, S.; Shirai, O.; Kano, K. Electrostatic and Steric Interaction between Redox Polymers and Some Flavoenzymes in Mediated Bioelectrocatalysis. *Journal of Electroanalytical Chemistry* **2013**, *689*, 26–30. https://doi.org/10.1016/j.jelechem.2012.11.023.

(135) Frisch, M. J.; Trucks, G. W.; Schlegel, H. B.; Scuseria, G. E.; Robb, M. A.; Cheeseman, J. R.; Scalmani, G.; Barone, V.; Mennucci, B.; Petersson, G. A.; Nakatsuji, H.; Caricato, M.; Li, X.; Hratchian, H. P.; Izmaylov, A. F.; Bloino, J.; Zheng, G.; Sonnenberg, J. L.; Hada, M.; Ehara, M.; Toyota, K.; Fukuda, R.; Hasegawa, J.; Ishida, M.; Nakajima, T.; Honda, Y.; Kitao, O.; Nakai, H.; Vreven, T.; Montgomery Jr., J. A.; Peralta, J. E.; Ogliaro, F.; Bearpark, M. J.; Heyd, J.; Brothers, E. N.; Kudin, K. N.; Staroverov, V. N.; Kobayashi, R.; Normand, J.; Raghavachari, K.; Rendell, A. P.; Burant, J. C.; Iyengar, S. S.; Tomasi, J.; Cossi, M.; Rega, N.; Millam, N. J.; Klene, M.; Knox, J. E.; Cross, J. B.; Bakken, V.; Adamo, C.; Jaramillo, J.; Gomperts, R.; Stratmann, R. E.; Yazyev, O.; Austin, A. J.; Cammi, R.; Pomelli, C.; Ochterski, J. W.; Martin, R. L.; Morokuma, K.; Zakrzewski, V. G.; Voth, G. A.; Salvador, P.; Dannenberg, J. J.; Dapprich, S.; Daniels, A. D.; Farkas, Ã.; Foresman, J. B.; Ortiz, J. v; Cioslowski, J.; Fox, D. J. Gaussian 09. Gaussian, Inc.: Wallingford, CT, USA 2009.

(136) Huynh, M. T.; Anson, C. W.; Cavell, A. C.; Stahl, S. S.; Hammes-Schiffer, S. Quinone 1 E- and 2 e-/2 H+ Reduction Potentials: Identification and Analysis of Deviations from Systematic Scaling Relationships. *J Am Chem Soc* **2016**, *138* (49), 15903–15910. https://doi.org/10.1021/jacs.6b05797.

(137) Savéant, J. M.; Su, K. B. Homogeneous Redox Catalysis of Electrochemical Reaction. Part VI. Zone Diagram Representation of the Kinetic Regimes. *Journal of Electroanalytical Chemistry* **1984**, *171* (1–2), 341–349. https://doi.org/10.1016/0022-0728(84)80125-4.

(138) Limoges, B.; Moiroux, J.; Savéant, J. M. Kinetic Control by the Substrate and/or the Cosubstrate in Electrochemically Monitored Redox Enzymatic Homogeneous Systems. Catalytic Responses in Cyclic Voltammetry. *Journal of Electroanalytical Chemistry* **2002**, *521* (1–2), 1–7. https://doi.org/10.1016/S0022-0728(02)00657-5.

(139) Kano, K.; Ikeda, T. Fundamentals and Practices of Mediated Bioelectrocatalysis. *Analytical Sciences* **2000**, *16* (10), 1013–1021. https://doi.org/10.2116/analsci.16.1013.

(140) Silverstein, T. P. Marcus Theory: Thermodynamics CAN Control the Kinetics of Electron Transfer Reactions. *J Chem Educ* **2012**, *89* (9), 1159–1167. https://doi.org/10.1021/ed1007712.

(141) Ohnishi, T.; Yamazaki, H.; Iyanagi, T.; Nakamura, T.; Yamazaki, I. One-Electron-Transfer Reactions in Biochemical Systems II. The Reaction of Free Radicals Formed in the Enzymic Oxidation. *Biochimica et Biophysica Acta (BBA) - Bioenergetics* **1969**, *172* (3), 357–369. https://doi.org/10.1016/0005-2728(69)90132-7.

(142) Marcus, R. A.; Sutin, N. Electron Transfers in Chemistry and Biology. *Biochimica et Biophysica Acta (BBA) - Reviews on Bioenergetics* **1985**, *811* (3), 265–322. https://doi.org/http://dx.doi.org/10.1016/0304-4173(85)90014-X.

(143) Turró, C.; Zaleski, J. M.; Karabatsos, Y. M.; Nocera, D. G. Bimolecular Electron Transfer in the Marcus Inverted Region. *J Am Chem Soc* **1996**, *118* (25), 6060–6067. https://doi.org/10.1021/JA960575P.

(144) Rees, N. v; Clegg, A. D.; Klymenko, O. v; Coles, B. A.; Compton, R. G. Marcus Theory for Outer-Sphere Heterogeneous Electron Transfer: Predicting Electron-Transfer Rates for Quinones. *J Phys Chem B* **2004**, *108* (34), 13047–13051. https://doi.org/10.1021/jp040382l.

(145) Robinson, S. G.; Sigman, M. S. Integrating Electrochemical and Statistical Analysis Tools for Molecular Design and Mechanistic Understanding. *Acc Chem Res* **2020**, *53* (2), 289–299. https://doi.org/10.1021/acs.accounts.9b00527.

(146) Forrow, N. J.; Walters, S. J. Transition Metal Half-Sandwich Complexes as Redox Mediators to Glucose Oxidase. *Biosens Bioelectron* **2004**, *19* (7), 763–770. https://doi.org/10.1016/j.bios.2003.08.011.

(147) Bourbonnais, R.; Leech, D.; Paice, M. G. Electrochemical Analysis of the Interactions of Laccase Mediators with Lignin Model Compounds. *Biochim Biophys Acta Gen Subj* **1998**, *1379* (3), 381–390. https://doi.org/10.1016/S0304-4165(97)00117-7.

(148) Wohlfahrt, G.; Trivić, S.; Zeremski, J.; Peričin, D.; Leskovac, V. The Chemical Mechanism of Action of Glucose Oxidase from Aspergillus Niger. *Mol Cell Biochem* **2004**, *260* (1), 69–83. https://doi.org/10.1023/B:MCBI.0000026056.75937.98.

(149) Clark, I. A.; Cowden, W. B.; Hunt, N. H. Free Radical-Induced Pathology. *Med Res Rev* **1985**, *5* (3), 297–332. https://doi.org/10.1002/MED.2610050303.

(150) Lowe, H. J.; Clark, W. M.; Hemmerich, P.; Veeger, C.; Wood, H. C. S.; Janik, B.; Elving, P. J.; Williams, R. F.; Bruice, T. C.; Shinkai, S. S.; Eberlein, G.; Stankovich, M. T.; Shopfer, L. M.; Massey, V.; Ghisla, S. *Molecular Recognition of Artificial Single-Electron Acceptor Cosubstrates by Glucose Oxidase?*; 1993; Vol. 115. https://pubs.acs.org/sharingguidelines.

(151) Bauer, J. A.; Zámocká, M.; Majtán, J.; Bauerová-Hlinková, V. Glucose Oxidase, an Enzyme "Ferrari": Its Structure, Function, Production and Properties in the Light of Various Industrial and Biotechnological Applications. *Biomolecules* **2022**, *12* (3), 472. https://doi.org/10.3390/biom12030472.

(152) Forrow, N. J.; Sanghera, G. S.; Walters, S. J. The Influence of Structure in the Reaction of Electrochemically Generated Ferrocenium Derivatives with Reduced Glucose Oxidase. *Journal of the Chemical Society, Dalton Transactions* **2002**, No. 16, 3187–3194. https://doi.org/10.1039/b204702k.

(153) Anicet, N.; Anne, A.; Bourdillon, C.; Demaille, C.; Moiroux, J.; Savéant, J. M. Electrochemical Approach to the Dynamics of Molecular Recognition of Redox Enzyme Sites by Artificial Cosubstrates in Solution and in Integrated Systems. *Faraday Discuss* **2000**, *116*, 269–279. https://doi.org/10.1039/b001392g.

(154) Bourdillon, C.; Demaille, C.; Moiroux, J.; Saveant, J. M. New Insights into the Enzymic Catalysis of the Oxidation of Glucose by Native and Recombinant Glucose Oxidase Mediated by Electrochemically Generated One-Electron Redox Cosubstrates. *J Am Chem Soc* **1993**, *115* (1), 1–10. https://doi.org/10.1021/ja00054a001.

(155) Wohlfahrt, G.; Trivi‹, S.; Zeremski, J.; Peric, D.; Leskovac, V. The Chemical Mechanism of Action of Glucose Oxidase from Aspergillus Niger. *Mol Cell Biochem* **2004**, *260*, 69–83.

(156) Battaglini, F.; Koutroumanis, M.; English, A. M.; Mikkelsen, S. R. *Targeting Glucose Oxidase at Aspartate and Glutamate Residues with Organic Two-Electron Redox Mediators*; 1994; Vol. 5. https://pubs.acs.org/sharingguidelines.

(157) Shoichet, B. K.; Leach, A. R.; Kuntz, I. D. Ligand Solvation in Molecular Docking. *Proteins: Structure, Function and Genetics* **1999**, *34* (1), 4–16. https://doi.org/10.1002/(SICI)1097-0134(19990101)34:1<4::AID-PROT2>3.0.CO;2-6.

(158) Macchiarulo, A.; Nobeli, I.; Thornton, J. M. Ligand Selectivity and Competition between Enzymes in Silico. *Nature Biotechnology*. August 2004, pp 1039–1045. https://doi.org/10.1038/nbt999.

(159) Noh, S. Y.; Notman, R. Comparison of Umbrella Sampling and Steered Molecular Dynamics Methods for Computing Free Energy Profiles of Aromatic Substrates through Phospholipid Bilayers. *Journal of Chemical Physics* **2020**, *153* (3). https://doi.org/10.1063/5.0016114/1062418.

(160) Ferreira, M. F.; Franca, E. F.; Leite, F. L. Unbinding Pathway Energy of Glyphosate from the EPSPs Enzyme Binding Site Characterized by Steered Molecular Dynamics and Potential of Mean Force. *J Mol Graph Model* **2017**, *72*, 43–49. https://doi.org/10.1016/j.jmgm.2016.11.010.

(161) Mills, M.; Andricioaei, I. An Experimentally Guided Umbrella Sampling Protocol for Biomolecules. *Journal of Chemical Physics* **2008**, *129* (11). https://doi.org/10.1063/1.2976440.

(162) Kosztin, I.; Barz, B.; Janosi, L. Calculating Potentials of Mean Force and Diffusion Coefficients from Nonequilibrium Processes without Jarzynski's Equality. **2006**. https://doi.org/10.1063/1.2166379.

(163) Schenter, G. K.; Garrett, B. C.; Truhlar, D. G. Generalized Transition State Theory in Terms of the Potential of Mean Force. *Journal of Chemical Physics* **2003**, *119* (12), 5828–5833. https://doi.org/10.1063/1.1597477.

(164) You, W.; Tang, Z.; Chang, C. E. A. Potential Mean Force from Umbrella Sampling Simulations: What Can We Learn and What Is Missed? *J Chem Theory Comput* **2019**, *15* (4), 2433–2443. https://doi.org/10.1021/acs.jctc.8b01142.

(165) Grayson, P.; Tajkhorshid, E.; Schulten, K. *Mechanisms of Selectivity in Channels and Enzymes Studied with Interactive Molecular Dynamics*; 2003; Vol. 85.

(166) Lemkul, J. A.; Bevan, D. R. Assessing the Stability of Alzheimer's Amyloid Protofibrils Using Molecular Dynamics. *J Phys Chem B* **2010**, *114* (4), 1652–1660. https://doi.org/10.1021/jp9110794.

(167) Hecht, H. J.; Kalisz, H. M.; Hendle, J.; Schmid, R. D.; Schomburg, D. Crystal Structure of Glucose Oxidase from Aspergillus Niger Refined at 2·3 Å Reslution. *J Mol Biol* **1993**, *229* (1), 153–172. https://doi.org/10.1006/jmbi.1993.1015.

(168) Yoon, T.; Park, W.; Kim, Y.; Na, S. Electric Field-Mediated Regulation of Enzyme Orientation for Efficient Electron Transfer at the Bioelectrode Surface: A Molecular Dynamics Study. *Appl Surf Sci* **2023**, *608*. https://doi.org/10.1016/J.APSUSC.2022.155124.

(169) Wade, R. C.; Gabdoulline, R. R.; Lu¨demannlu¨demann, S. K.; Lounnas, V. *Colloquium Paper This Paper Was Presented at the Colloquium ' 'Computational Biomolecular Science*; 1998; Vol. 95.

(170) Okumura, N.; Abo, T.; Tsujimura, S.; Kano, K. Kinetic Studies of Electron Transfer between PQQ-Dependent Soluble Glucose Dehydrogenase and Mediators. *ECS Meeting Abstracts* **2006**, *MA2006-01* (13), 556–556. https://doi.org/10.1149/MA2006-01/13/556.

(171) Himmel, M. E.; Ding, S. Y.; Johnson, D. K.; Adney, W. S.; Nimlos, M. R.; Brady, J. W.; Foust, T. D. Biomass Recalcitrance: Engineering Plants and Enzymes for Biofuels Production. *Science*. February 9, 2007, pp 804–807. https://doi.org/10.1126/science.1137016.

(172) Cinquin, P.; Gondran, C.; Giroud, F.; Mazabrard, S.; Pellissier, A.; Boucher, F.; Alcaraz, J. P.; Gorgy, K.; Lenouvel, F.; Mathé, S.; Porcu, P.; Cosnier, S. A Glucose BioFuel Cell Implanted in Rats. *PLoS One* **2010**, *5* (5). https://doi.org/10.1371/journal.pone.0010476.

(173) Milton, R. D.; Hickey, D. P.; Abdellaoui, S.; Lim, K.; Wu, F.; Tan, B.; Minteer, S. D. Rational Design of Quinones for High Power Density Biofuel Cells. *Chem Sci* **2015**, *6* (8), 4867–4875. https://doi.org/10.1039/c5sc01538c.

(174) Jeon, W.-Y.; Lee, J.-H.; Dashnyam, K.; Choi, Y.-B.; Kim, T.-H.; Lee, H.-H.; Kim, H.-W.; Kim, H.-H. Performance of a Glucose-Reactive Enzyme-Based Biofuel Cell System for Biomedical Applications. https://doi.org/10.1038/s41598-019-47392-1.

(175) Ghica, M. E.; Brett, C. M. A. A Glucose Biosensor Using Methyl Viologen Redox Mediator on Carbon Film Electrodes. *Anal Chim Acta* **2005**, *532* (2), 145–151. https://doi.org/10.1016/j.aca.2004.10.058.

(176) Rahman, M. M.; Umar, A.; Sawada, K. Development of Amperometric Glucose Biosensor Based on Glucose Oxidase Co-Immobilized with Multi-Walled Carbon Nanotubes at Low Potential. *Sens Actuators B Chem* **2009**, *137* (1), 327–333. https://doi.org/10.1016/j.snb.2008.10.060.

(177) Mcneil, C. J.; Cooper, J. M.; Al Spoors, J. *Amperometric Enzyme Electrode for Determination of Theophylline in Serum*; 1992; Vol. 7.

(178) Witt, S.; Wohlfahrt, G.; Schomburg, D.; Hecht, H.-J. R.; Kalisz, H. M. *Conserved Arginine-516 of Penicillium Amagasakiense Glucose Oxidase Is Essential for the Efficient Binding of β-D-Glucose*; 2000; Vol. 347.

(179) Flexer, V.; Mano, N. Wired Pyrroloquinoline Quinone Soluble Glucose Dehydrogenase Enzyme Electrodes Operating at Unprecedented Low Redox Potential. *Anal Chem* **2014**, *86* (5), 2465–2473. https://doi.org/10.1021/ac403334w.

(180) Hasan, K.; Patil, S. A.; Leech, D.; Hägerhäll, C.; Gorton, L. Electrochemical Communication between Microbial Cells and Electrodes via Osmium Redox Systems. In *Biochemical Society Transactions*; 2012; Vol. 40, pp 1330–1335. https://doi.org/10.1042/BST20120120.

(181) Saleem, M.; Yu, H.; Wang, L.; Zain-ul-Abdin; Khalid, H.; Akram, M.; Abbasi, N. M.; Huang, J. Review on Synthesis of Ferrocene-Based Redox Polymers and Derivatives and Their Application in Glucose Sensing. *Anal Chim Acta* **2015**, *876*, 9–25. https://doi.org/10.1016/j.aca.2015.01.012.

(182) Takada, K.; Gopalan, P.; Ober, C. K.; Abruña, H. D. Synthesis, Characterization, and Redox Reactivity of Novel Quinone-Containing Polymer. *Chemistry of Materials* **2001**, *13* (9), 2928–2932. https://doi.org/10.1021/cm010159q.

(183) Milton, R. D.; Hickey, D. P.; Abdellaoui, S.; Lim, K.; Wu, F.; Tan, B.; Minteer, S. D. Rational Design of Quinones for High Power Density Biofuel Cells. *Chem Sci* **2015**, *6* (8), 4867–4875. https://doi.org/10.1039/c5sc01538c.

(184) Yoshida, H.; Sakai, G.; Mori, K.; Kojima, K.; Kamitori, S.; Sode, K. Structural Analysis of Fungus-Derived FAD Glucose Dehydrogenase. *Sci Rep* **2015**, *5* (1), 13498. https://doi.org/10.1038/srep13498.

(185) Okuda-Shimazaki, J.; Yoshida, H.; Sode, K. FAD Dependent Glucose Dehydrogenases-Discovery and Engineering of Representative Glucose Sensing Enzymes. **2019**. https://doi.org/10.1016/j.bioelechem.2019.107414.

(186) Page, C. C.; Moser, C. C.; Chen, X.; Dutton, P. L. *Natural Engineering Principles of Electron Tunnelling in Biological Oxidation±reduction*; 1999; Vol. 402. www.nature.com.

(187) Moser, C. C.; Keske, J. M.; Warncke, K.; Farid, R. S.; Dutton, P. L. Nature of Biological Electron Transfer. *Nature* **1992**, *355* (6363), 796–802. https://doi.org/10.1038/355796a0.

(188) Ströhle, F. W.; Cekic, S. Z.; Magnusson, A. O.; Schwaneberg, U.; Roccatano, D.; Schrader, J.; Holtmann, D. A Computational Protocol to Predict Suitable Redox Mediators for Substitution of NAD(P)H in P450 Monooxygenases. *J Mol Catal B Enzym* **2013**, *88*, 47–51. https://doi.org/10.1016/j.molcatb.2012.11.010.

(189) Hernández-Padilla, G.; Cruz-Ramírez, M.; Rebolledo-Chávez, J. P. F.; Ocampo-Hernández, J.; Mendoza, A.; Tenorio, F. J.; Ramírez, L. D.; Ortiz-Frade, L. The Role of Molecular Interaction between GOD and Metal Complexes on Redox Mediation Processes. *J Mol Struct* **2021**, *1245*. https://doi.org/10.1016/j.molstruc.2021.131026.

(190) Szefler, B.; Diudea, M. V.; Putz, M. V.; Grudzinski, I. P. Molecular Dynamic Studies of the Complex Polyethylenimine and Glucose Oxidase. *Int J Mol Sci* **2016**, *17* (11). https://doi.org/10.3390/ijms17111796.

(191) Meyer, M.; Wohlfahrt, G.; Knäblein, J.; Schomburg, D. *Aspects of the Mechanism of Catalysis of Glucose Oxidase: A Docking, Molecular Mechanics and Quantum Chemical Study*; KLUWER/ESCOM, 1998; Vol. 12.

(192) Arango Gutierrez, E.; Wallraf, A. M.; Balaceanu, A.; Bocola, M.; Davari, M. D.; Meier, T.; Duefel, H.; Schwaneberg, U. How to Engineer Glucose Oxidase for Mediated Electron Transfer. *Biotechnol Bioeng* **2018**, *115* (10), 2405–2415. https://doi.org/10.1002/bit.26785.

(193) Pravda, L.; Sehnal, D.; Toušek, D.; Navrátilová, V.; Bazgier, V.; Berka, K.; Vařeková, R. S.; Koča, J.; Otyepka, M. MOLEonline: A Web-Based Tool for Analyzing Channels, Tunnels and Pores (2018 Update). *Nucleic Acids Res* **2018**, *46* (W1), W368–W373. https://doi.org/10.1093/nar/gky309.

(194) Trott, O.; Olson, A. J. AutoDock Vina: Improving the Speed and Accuracy of Docking with a New Scoring Function, Efficient Optimization, and Multithreading. *J Comput Chem* **2010**, *31* (2), 455–461. https://doi.org/10.1002/jcc.21334.

(195) Merlino, A.; Mazzarella, L.; Carannante, A.; Fiore, A. Di; Donato, A. Di; Notomista, E.; Sica, F. The Importance of Dynamic Effects on the Enzyme Activity. *Journal of Biological Chemistry* **2005**, *280* (18), 17953–17960. https://doi.org/10.1074/jbc.M501339200.

(196) Kano-2006-Electron Transfer Kinetics between PQQ-Dependent Soluble Glucose Dehydrogenase and Mediators.

(197) Huynh, M. T.; Anson, C. W.; Cavell, A. C.; Stahl, S. S.; Hammes-Schiffer, S. Quinone 1 E- and 2 e-/2 H+ Reduction Potentials: Identification and Analysis of Deviations from Systematic Scaling Relationships. *J Am Chem Soc* **2016**, *138* (49), 15903–15910. https://doi.org/10.1021/jacs.6b05797.

APPENDIX

6.1 Diffusivities

Table 6.1 Catalytic current density (j_{max}), diffusivity, D_M, bimolecular rate constant, k, and the natural log of k for all quinone mediators. Values of j_{max}, k and log of k are reported as averages with standard deviations, where n = 3.

Quinone mediator	j_{max} ($\mu A\ cm^{-2}$)	j_{max} ($\mu A\ cm^{-2}$) error (+/-)	$D_M \times 10^{-6}$ ($cm^2 s^{-1}$)	k ($M^{-1}s^{-1}$)	log (k_{ave} ($M^{-1}s^{-1}$))	log (k_{ave} ($M^{-1}s^{-1}$)) error (+/-)
1	207	12	5.7	4.0×10^{4}	4.61	0.03
2	33	4	6.1	9.5×10^{2}	2.98	0.11
3	4.4	0.4	1.8	5.9×10^{1}	1.77	0.08
4	11	1	2.2	2.9×10^{2}	2.46	0.06
5	2.8	0.4	0.4	1.1×10^{2}	2.03	0.13
6	3.5	0.6	2.6	2.5×10^{1}	1.41	0.05
7	2.6	0.3	0.2	2.2×10^{2}	2.35	0.09
8	15	2	4.8	2.7×10^{2}	2.43	0.04
9	36	3	1.1	6.1×10^{3}	3.79	0.03
10	615	53	2.6	8.0×10^{5}	5.90	0.03
11	568	62	5.3	3.3×10^{5}	5.52	0.04
12	191	31	1.1	1.9×10^{5}	5.27	0.11
13	257	22	1.7	2.1×10^{5}	5.31	0.03
14	67	4	1.7	1.4×10^{4}	4.15	0.02
15	25	3	2.2	1.5×10^{3}	3.18	0.04
16	34	4	0.6	1.1×10^{4}	4.04	0.10
17	7	0	0.9	3.0×10^{2}	2.48	0.05
18	711	12	1.6	1.7×10^{6}	6.23	0.01
19	651	44	1.3	1.8×10^{6}	6.25	0.06
20	754	6	1.3	2.3×10^{6}	6.36	0.00
21	699	54	3.4	7.7×10^{5}	5.89	0.02
22	640	26	1.3	1.7×10^{6}	6.23	0.02
23	12	1	0.2	4.6×10^{3}	3.66	0.02
24	82	6	0.4	9.2×10^{4}	4.96	0.04
25	78	6	0.1	2.3×10^{5}	5.35	0.02

6.2 Optimization and Energy Calculation

All geometry optimization and DFT free energy calculations were performed in Gaussian 09 using the B3LYP level of theory, 6-31+G (d,p) basis set and CPCM (water) solvation model. The free energy of all the charged states required in the calculation of the $2e^-/2H^+$ reduction potential was obtained, and the respective redox potential were calculated as described previously. An example input file is show below:

opt=tight freq=noraman ub3lyp/3-21+g geom=connectivity

6.3 Calculated Redox Potential Determination

A previously reported analysis method was adopted for calculating the redox potential of all compounds.[197] First, a reference reaction was selected from the redox reactions of model compound 1. Then, the reaction of interest, for example, of compound 2 which undergo the first electron reduction from $[2]^0$ to $[2]^-$ via a step with associated free energy, ΔG_r°, is used to demonstrate the calculations as given below.

$[2]^0$	+	e^-	→	$[2]^-$				$-FE^\circ$
$[1]^-_{ref}$			→	$[1]^0_{ref}$	+	e^-		FE°_{ref}
$[1]^-_{ref}$	+	$[2]^0$	→	$[1]^0_{ref}$	+	$[2]^-$		ΔG_r°

The reduction potential for compound 2 can then be calculated using equation 6.1

(6.1) $$E^0 = -\frac{\Delta G_r^0}{F} + E^0_{ref}$$

where E^0_{ref} is the reduction potential of the reference compound 1 experimentally determined. The reference reaction was used to calculate pK_a values using the analysis below

$[2H]^+$			→	$[2]^0$	+	H^+	$\ln(10)\,RTpK_a$
$[1]^0_{ref}$	+	H^+	→	$[1H]^+_{ref}$			$-\ln(10)\,RTpK_{a,ref}$
$[1]^0_{ref}$	+	$[2H]^+$	→	$[1H]^+_{ref}$	+	$[2]^0$	ΔG_r^0

where pKa of the oxidation event of the compound 2 is expressed as

(6.2) $$pK_a([2H]^+) = \frac{\Delta G_r^0}{\ln(10)RT} + pK_{a,ref}$$

Table 6.2 The experimental and calculated potentials of quinones vs SCE.

Quinone mediator	Exp. $E°_{Q/QH2}$	Calc. $E°_{Q/QH2}$
1	-0.09	-0.06
2	-0.16	-0.11
3	-0.18	-0.24
4	-0.19	-0.10
5	-0.19	-0.10
6	-0.27	-0.40
7	-0.32	-0.25
8	-0.22	-0.24
9	0.02	0.11
10	0.08	0.03
11	0.08	0.14
12	0.11	0.15
13	0.01	-0.06
14	-0.05	-0.20
15	-0.04	-0.09
16	-0.09	-0.11
17	0.05	0.05
18	0.15	0.13
19	0.11	0.11
20	0.11	0.11
21	0.09	0.09
22	0.18	0.18
23	0.12	0.12
24	0.08	0.08
25	0.17	0.17

6.3 Multivariate Linear Regression

Multivariate linear regression analysis was performed using MATLAB. Without restricting the number of parameters, one model was identified to correlate strongly to the training set of quinones,

(6.3) $\log k = 0.068E°_{Q/QH_2} + 0.15V + 0.13\mu - 1.10A + 0.67D_c - 0.51B_1 + 0.08AB_2 + 0.16AB_5$

$R^2 = 0.99$ and p-value of 4.75×10^{-12}

Where $E°_{Q/QH2}$ is the redox potential, A is the molecular area, m is dipole moment, D_c is collision diameter, and B_1, B_2 and B_5 are Sterimol parameters. Despite the strong correlation, this model was disregarded because the large number of parameters required represent an overfit relative to the size of the dataset used. When the number of parameters was limited, several models were found that include the redox potential and a descriptor of the overall molecular size, specifically projected molecular area (included in the primary text), and molecular volume, V (based on the van der Waals radii). The model representing the volume correlation is shown below.

(6.4) $\log k = 0.71E°_{Q/QH_2} - 0.53V$

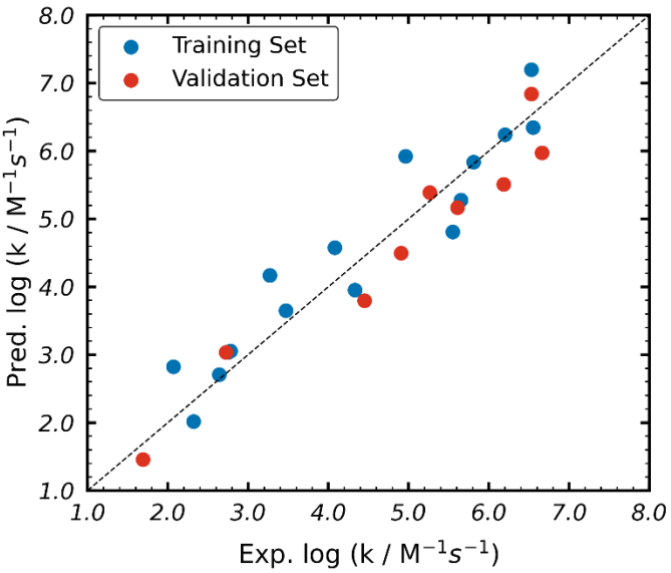

Figure 6.1 Log plot of experimental versus predicted bimolecular rate constants for the reaction of all quinone mediators studied with GOx (R^2 = 0.89).

It should be noted that CV analysis of mediators 17 and 25 (Figure 6.23 and Figure 6.31 below) reveals deviation from electrochemically reversible behavior on the timescale of bioelectrocatalytic measurements (i.e., 5 mV s^{-1}). This is likely due to reactivity of the corresponding electrochemically reduced species with either solvent or various forms of 17 or 25 present in solution, and both are consistent with EC type mechanisms in the absence of GOx or glucose. Upon addition of GOx and glucose, CV analysis of both mediators reveals a shift in the reactivity of both mediators from an EC to a catalytic EC' reaction. This suggests that the rates of the ambient chemical reactions are slower than the reaction between each mediator and GOx. To ensure that error in the rate constants of 17 and 25 were sufficiently small to include in modelling efforts, the QSAR model described in equation 18 was recalculated excluding 17 and 25. The resulting correlation, shown in Figure 6.2, retains the same parameter coefficients and exhibits a similar R^2 (R^2 = 0.91).

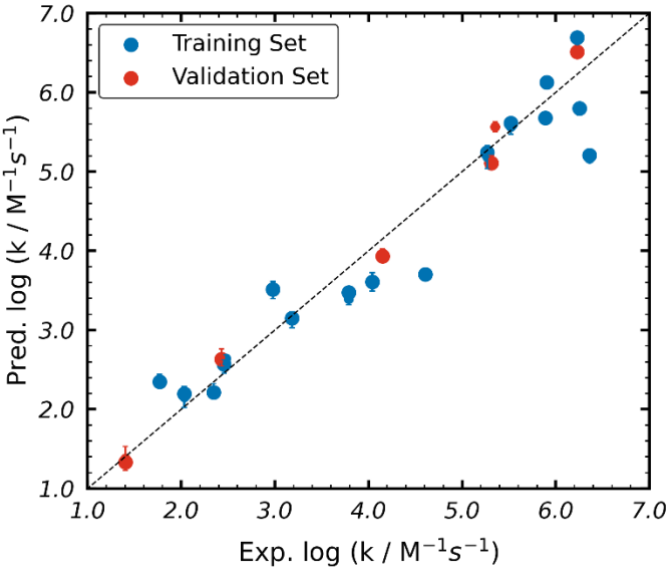

Figure 6.2 Log plot of experimental versus predicted bimolecular rate constants for the reaction of all quinone mediators studied (excluding 17 and 25) with GOx (R^2 = 0.91).

6.4 Stopped Flow Spectrophotometry Analysis

6.4.1 Initial Rate Analysis

The order of reaction with respect to the amount of mediator and GOx was determined from the Stopped – Flow Spectrophotometry data from initial rate analysis. A representative UV-Vis of 1mM reduced GOx with 1 mM 1 is shown in Figure 6.3 for increasing time intervals. The spectra for different concentrations were analyzed at 370 nm wavelengths to obtain absorbance and time values for each concentration of enzyme and quinone used respectively as shown in Figure 6.4.

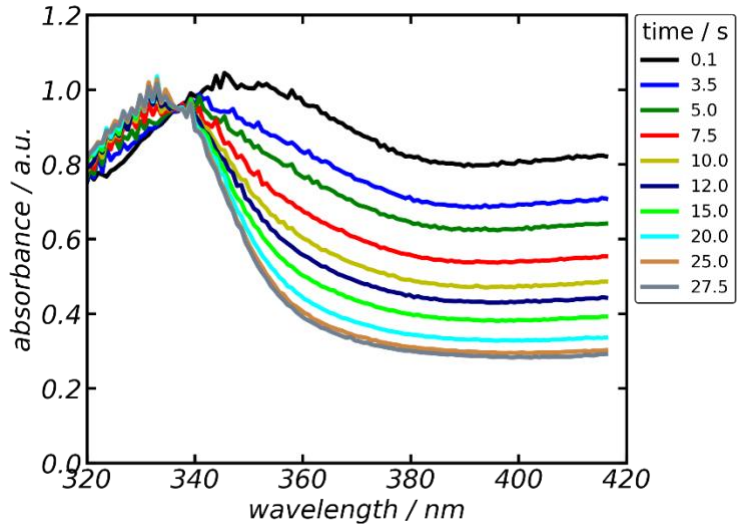

Figure 6.3 Representative spectra of 1 mM 1 with 1 mM reduced GOx dissolved in 100 mM phosphate buffer at pH 7 and room temperature showing normalized absorbance values as a function of wavelength and time.

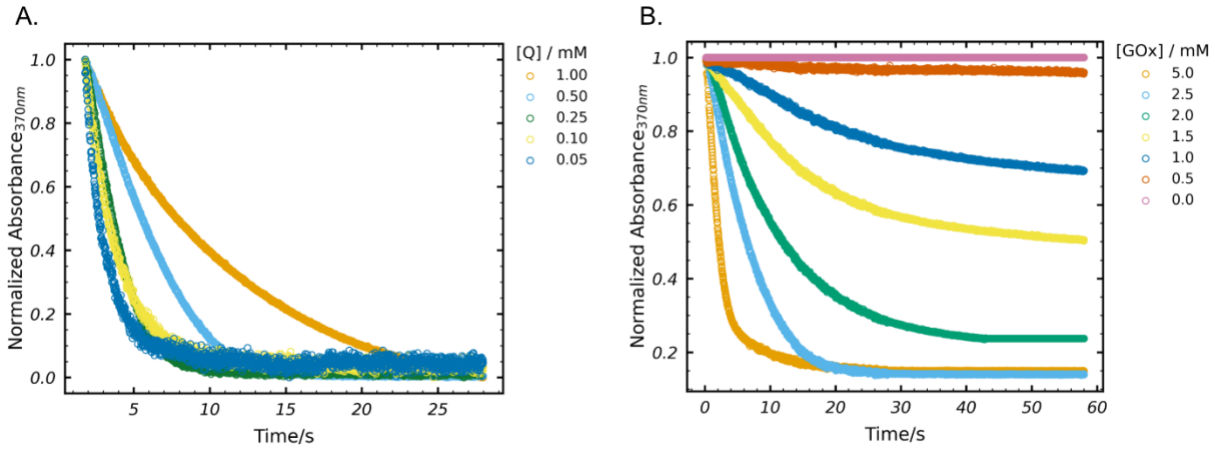

Figure 6.4 Plots of the normalized absorbance at 370 nm as a function of time (A) 100:1 glucose/GOx (1 mM with respect to glucose) with increasing concentration of 1, and (B) 1 mM of 1 reacted with different concentrations of glucose/GOx (concentrations are of glucose in a 100:1 glucose/GOx mixture).

Initial rate analysis was performed using the absorbance from the first 1000 ms after injection. The reaction rate order was determined from the linear relationship between concentration and reaction rate, shown in Figure 6.5.

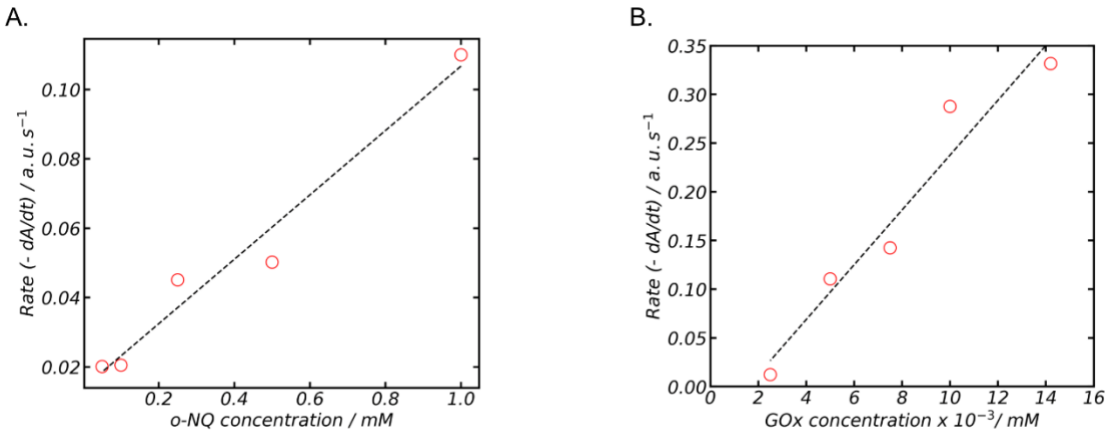

Figure 6.5 The plots represent the initial rate analysis of a constant concentration of GOx reacted with increasing concentration of the 1 (A) and vice versa in (B). 3.2 Stoichiometry Ratios.

For mediator-enzyme stoichiometry, the full reaction was analyzed by stopped-flow spectrophotometry. Data for the reaction with 1 and glucose/GOx is shown above and of 16 with glucose/GOx is shown in Figure 6.6. The remaining quinone concentration was analyzed against the quinone equivalents to determine the stoichiometric ratios.

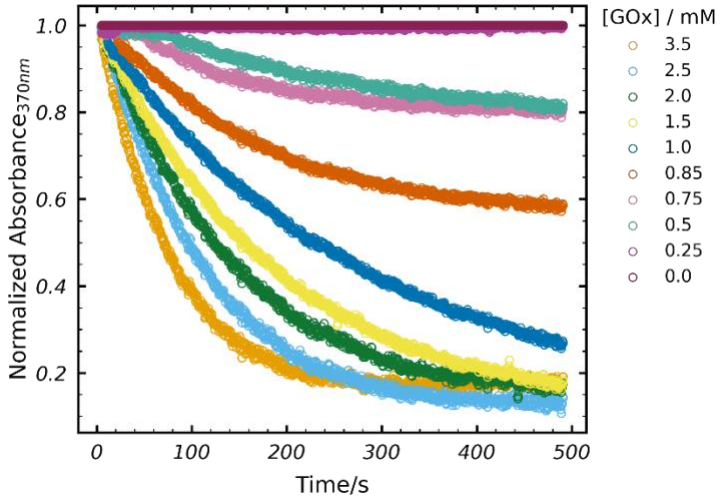

Figure 6.6 Plot of the normalized absorbance at 370 nm as a function of time for the reaction of 1 mM 16 with increasing concentrations of glucose/GOx mixture.

6.5. Electrochemical Experiments: Cyclic, Square-Wave Voltammetry and Scan Rate Study 1,2-Naphthoquinone (1)

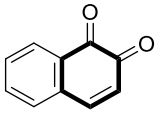

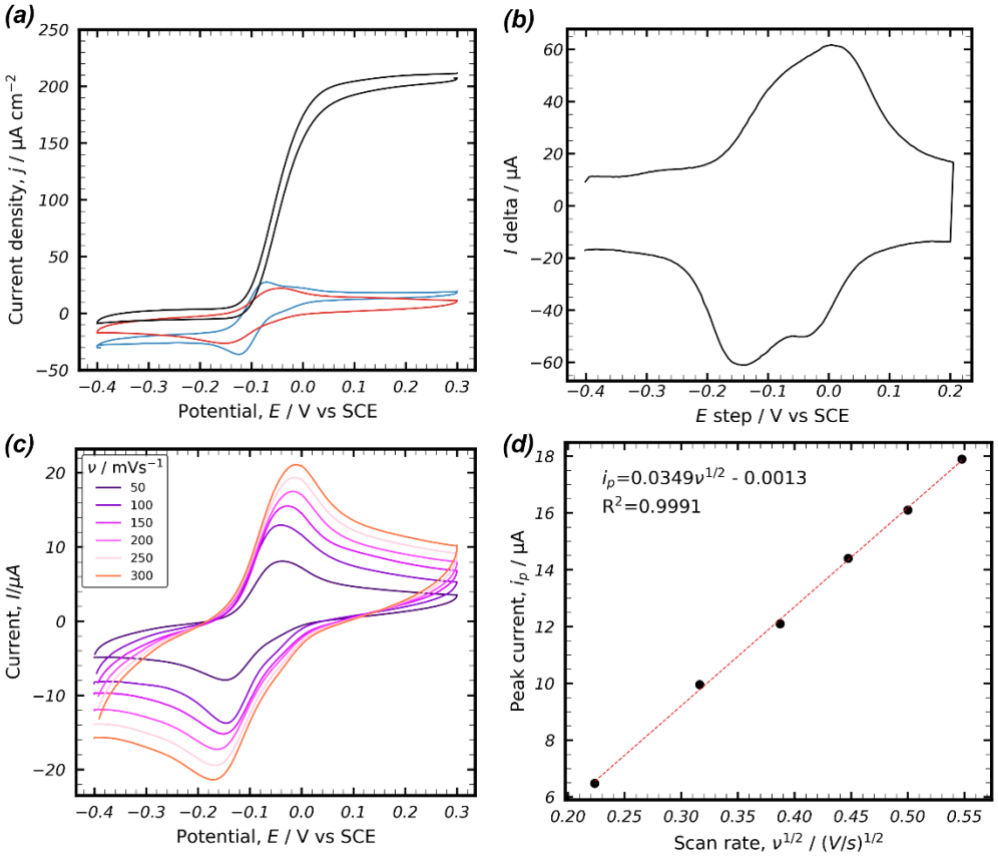

Figure 6.7 (a) CVs showing the catalytic current density of the glucose oxidase-1 mediated system. The CV in (blue) is 0.5 mM 1, (red) with 10 μM glucose oxidase and (black) with 100 mM glucose in 100mM phosphate buffer at pH 7 and 5mV/s scan rate. (b) shows the SWV of 0.5 mM 1 showing peak reduction (E_1) and oxidation potential (E_2). The pulse height, width, and step height of 10 mV, 1 ms and -5 mV, respectively. (c) describes the scan rate dependence study and (d) shows the correlation between the square root of scan rate and the respective peak potentials.

1,4-Naphthoquinone (2)

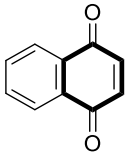

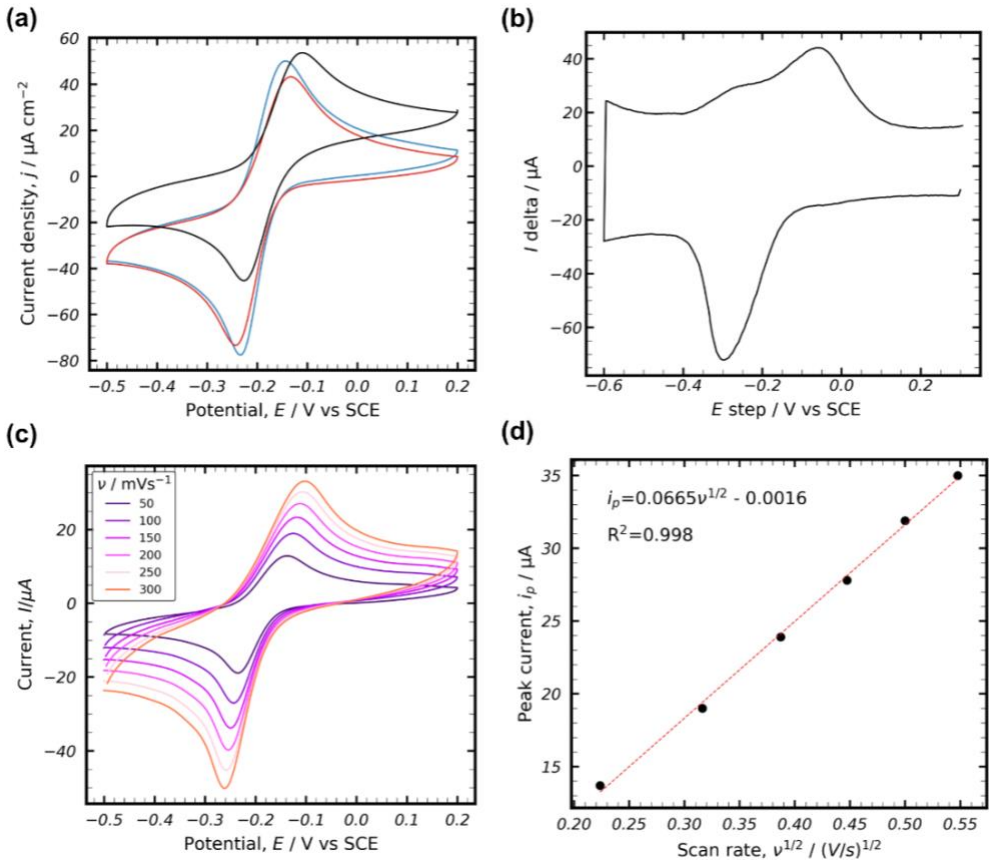

Figure 6.8 (a) A CV showing the catalytic current density of the glucose oxidase-2 mediated system. The CV in (blue) is 0.5 mM 2, (red) with 10µM glucose oxidase and (black) with 100 mM glucose in 100mM phosphate buffer at pH 7 and 5mV/s scan rate. (b) shows the SWV of 0.5 mM 2 showing peak reduction (E_1) and oxidation potential (E_2). The pulse height, width, and step height of 10 mV, 1 ms and -5 mV, respectively. (c) describes the scan rate dependence study and (d) shows the correlation between the square root of scan rate and the respective peak potentials.

2-Methyl-1,4-naphthoquinone (3)

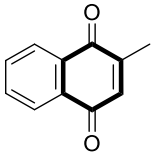

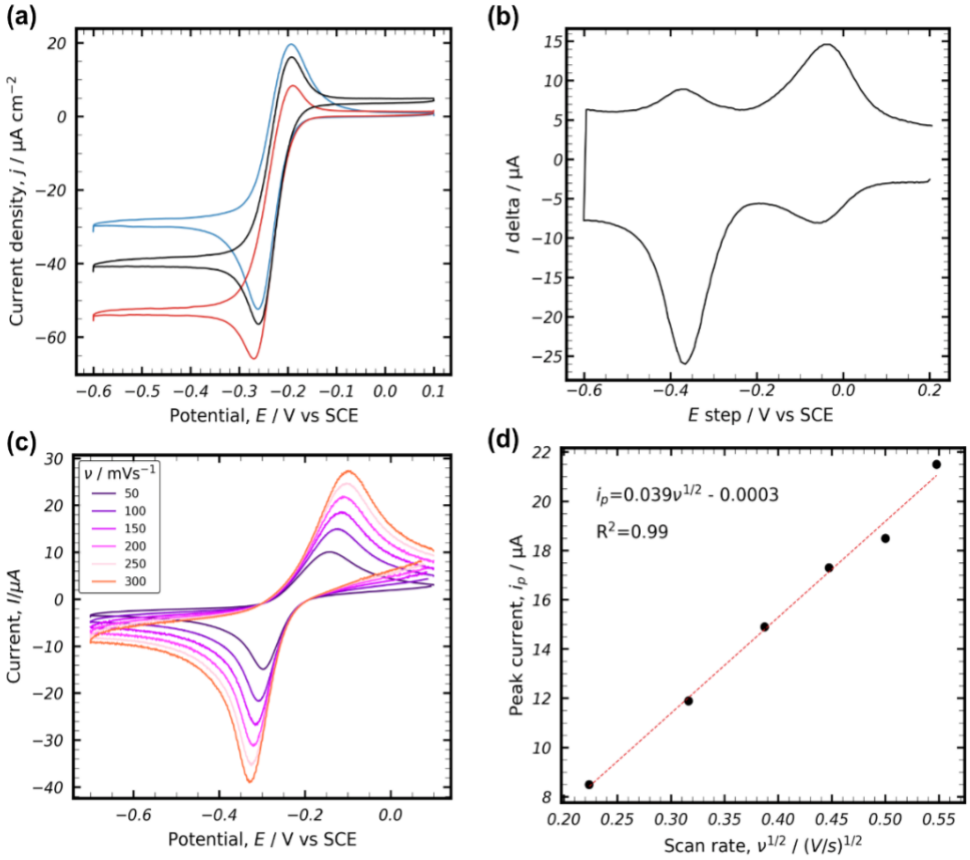

Figure 6.9 a. A CV showing the catalytic current density of the glucose oxidase-3 mediated system. The CV in (blue) is 0.5 mM 3, (red) with 10μM glucose oxidase and (black) with 100 mM glucose in 100mM phosphate buffer at pH 7 and 5mV/s scan rate. (b) shows the SWV of 0.5 mM 3 showing peak reduction (E_1) and oxidation potential (E_2). The pulse height, width, and step height of 10 mV, 5 ms and -5 mV, respectively. (c) describes the scan rate dependence study and (d) shows the correlation between the square root of scan rate and the respective peak potentials.

2,3-Dichloro-1,4-naphthoquinone (4)

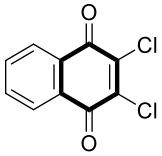

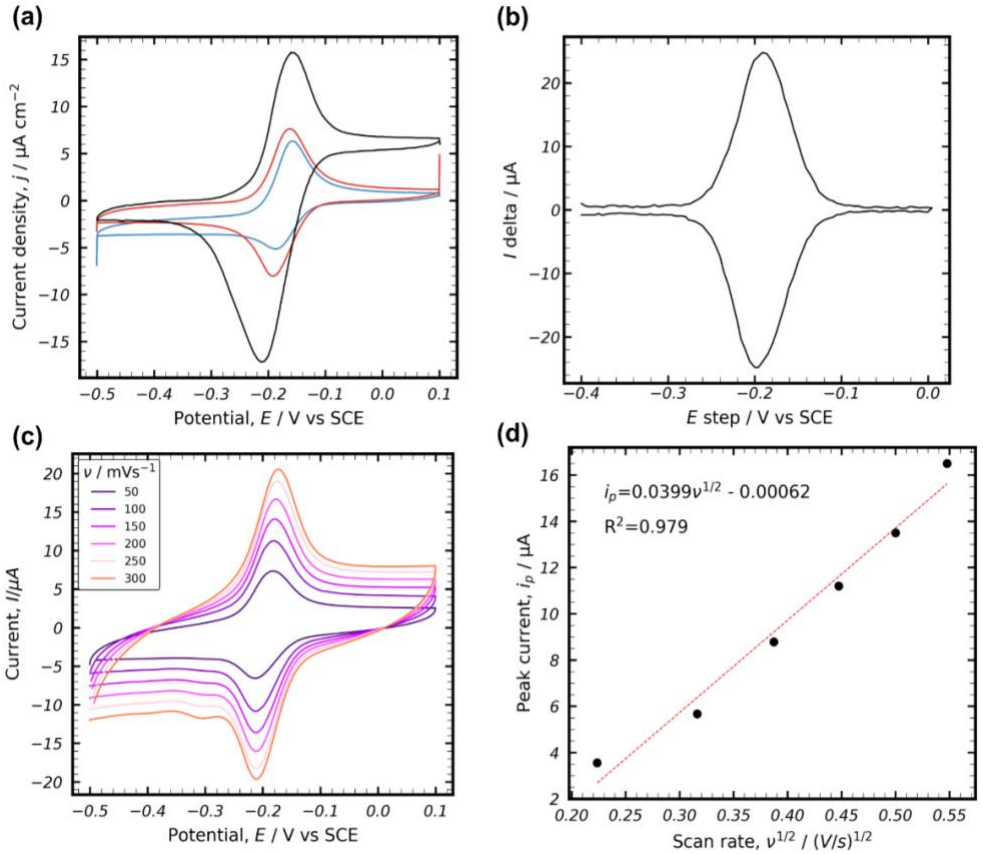

Figure 6.10 (a) A CV showing the catalytic current density of the glucose oxidase-4 mediated system. The CV in (blue) is 0.5 mM 4, (red) with 10µM glucose oxidase and (black) with 100 mM glucose in 100mM phosphate buffer at pH 7 and 5mV/s scan rate. (b) shows the SWV of 0.5 mM 4 showing peak reduction (E_1) and oxidation potential (E_2). The pulse height, width, and step height of 20 mV, 20 ms and 5 mV, respectively. (c) describes the scan rate dependence study and (d) shows the correlation between the square root of scan rate and the respective peak potentials.

2,3-Dibromo-1,4-naphthoquinone (5)

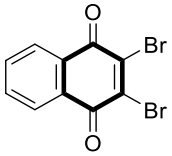

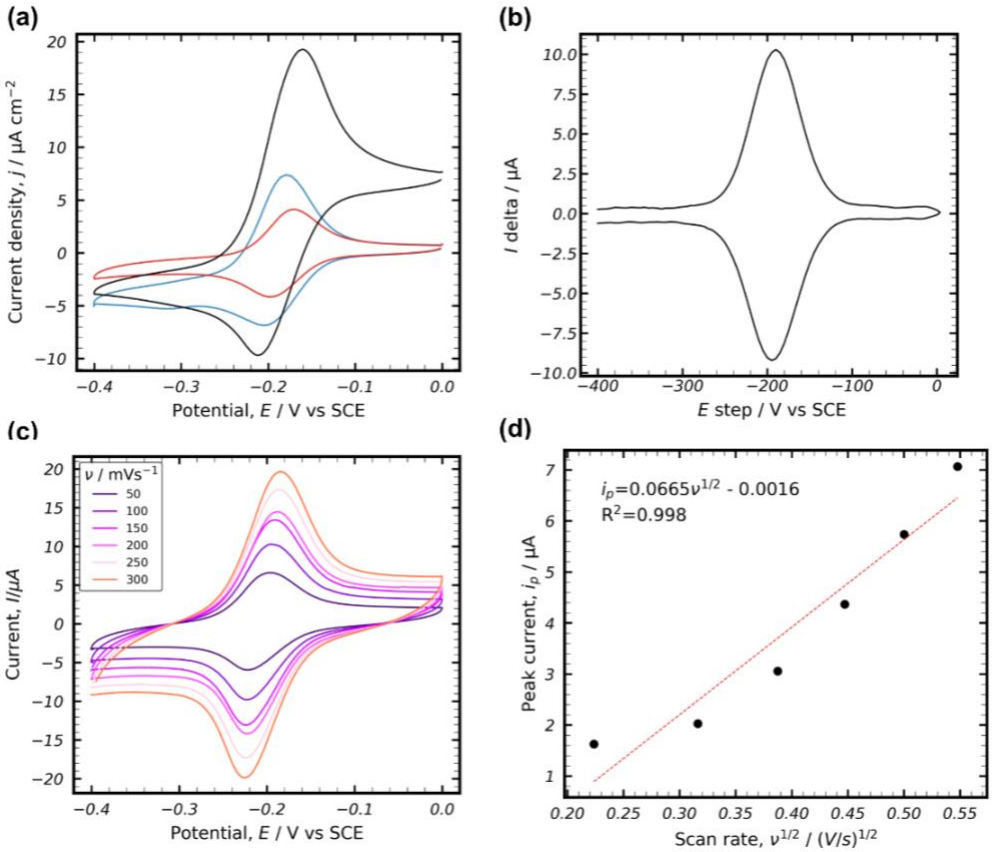

Figure 6.11 (a) A CV showing the catalytic current density of the glucose oxidase-5 mediated system. The CV in (blue) is 0.5 mM 5, (red) with 10μM glucose oxidase and (black) with 100 mM glucose in 100mM phosphate buffer at pH 7 and 5mV/s scan rate. (b) shows the SWV of 0.5 mM 5 showing peak reduction (E_1) and oxidation potential (E_2). The pulse height, width, and step height of 10 mV, 20 ms and 5 mV, respectively. (c) describes the scan rate dependence study and (d) shows the correlation between the square root of scan rate and the respective peak potentials.

2-Methoxy-1,4-naphthoquinone (6)

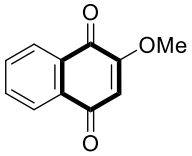

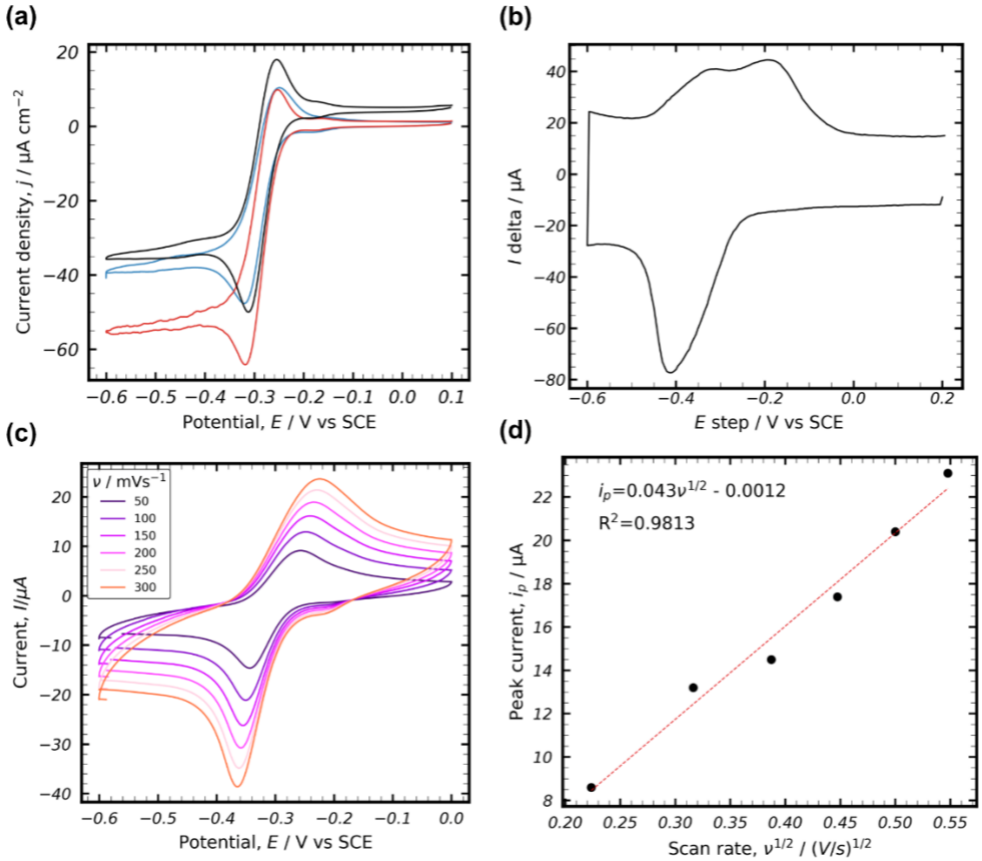

Figure 6.12 (a) A CV showing the catalytic current density of the glucose oxidase-6 mediated system. The CV in (blue) is 0.5 mM 6, (red) with 10µM glucose oxidase and (black) with 100 mM glucose in 100mM phosphate buffer at pH 7 and 5mV/s scan rate. (b) shows the SWV of 0.5 mM 6 showing peak reduction (E_1) and oxidation potential (E_2). The pulse height, width, and step height of 10 mV, 20 ms and 5 mV, respectively. (c) describes the scan rate dependence study and (d) shows the correlation between the square root of scan rate and the respective peak potentials.

5,8-Hydroxy-1,4-naphthoquinone (7)

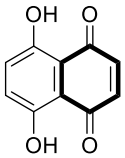

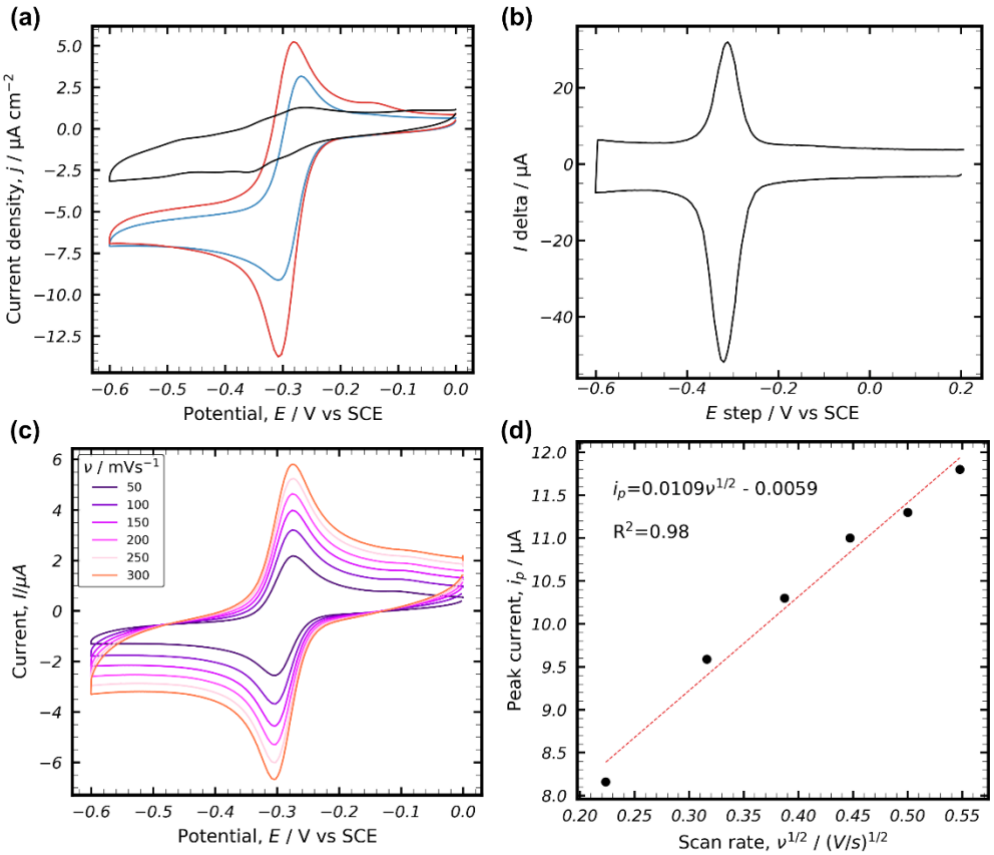

Figure 6.13 (a) A CV showing the catalytic current density of the glucose oxidase-7 mediated system. The CV in (blue) is 0.5 mM 7, (red) with 10µM glucose oxidase and (black) with 100 mM glucose in 100mM phosphate buffer at pH 7 and 5mV/s scan rate. (b) shows the SWV of 0.5 mM 7 showing peak reduction (E_1) and oxidation potential (E_2). The pulse height, width, and step height of 10 mV, 5 ms and - 5 mV, respectively. (c) describes the scan rate dependence study and (d) shows the correlation between the square root of scan rate and the respective peak potentials.

5-Hydroxy-1,4-naphthoquinone (8)

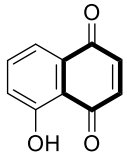

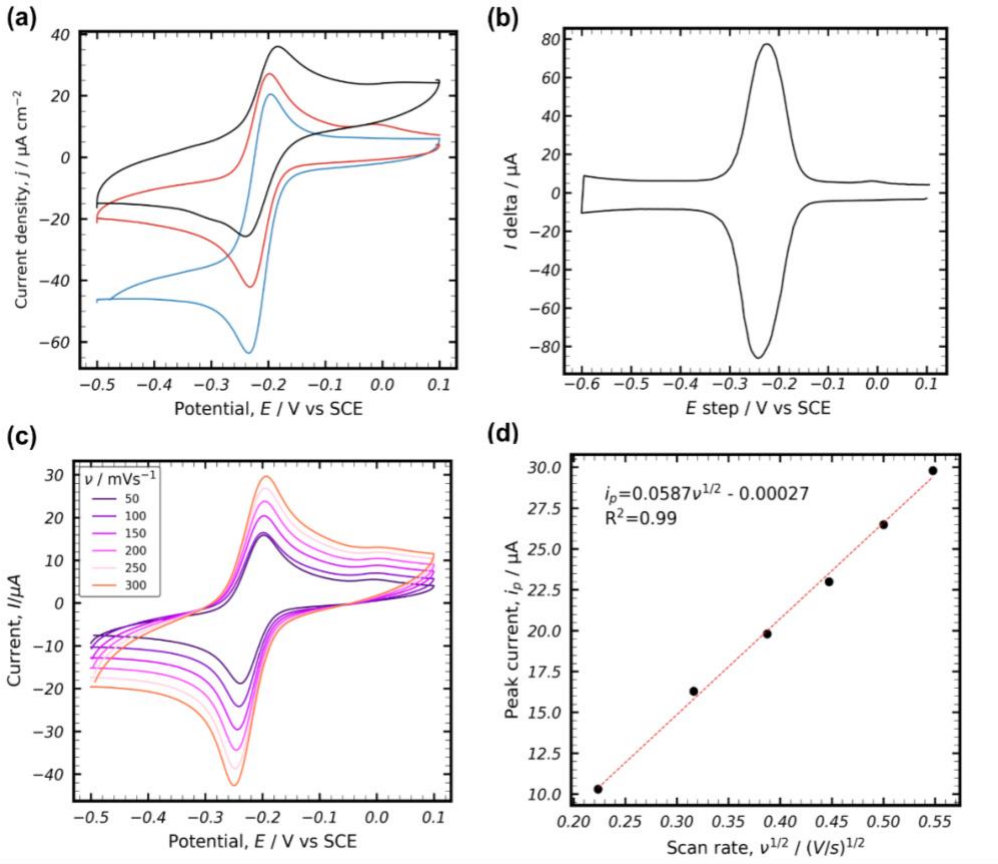

Figure 6.14 (a). A CV showing the catalytic current density of the glucose oxidase-8 system. The CV in (blue) is 0.5 mM 8, (red) with 10μM glucose oxidase and (black) with 100 mM glucose in 100mM phosphate buffer at pH 7 and 5mV/s scan rate. (b) shows the SWV of 0.5 mM 8 showing peak reduction (E_1) and oxidation potential (E_2). The pulse height, width, and step height of 10 mV, 5 ms and - 5 mV, respectively. (c) describes the scan rate dependence study and (d) shows the correlation between the square root of scan rate and the respective peak potentials.

1,2-Naphthoquinone-4-sulfonate (9)

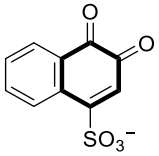

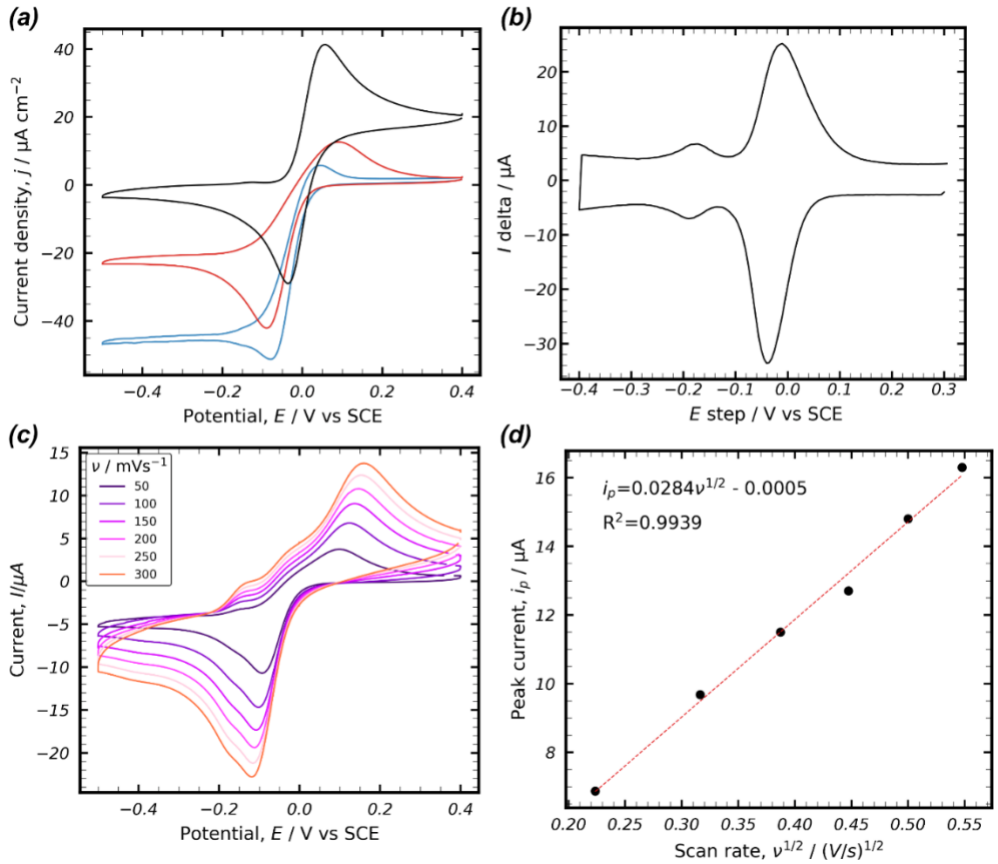

Figure 6.15 (a) A CV showing the catalytic current density of the glucose oxidase-9 mediated system. The CV in (blue) is 0.5 mM 9, (red) with 10µM glucose oxidase and (black) with 100 mM glucose in 100mM phosphate buffer at pH 7 and 5mV/s scan rate. (b) shows the SWV of 0.5 mM 9 showing peak reduction (E_1) and oxidation potential (E_2). The pulse height, width, and step height of 10 mV, 5 ms and - 5 mV, respectively. (c) describes the scan rate dependence study and (d) shows the correlation between the square root of scan rate and the respective peak potentials.

1,4-Benzoquinone (10)

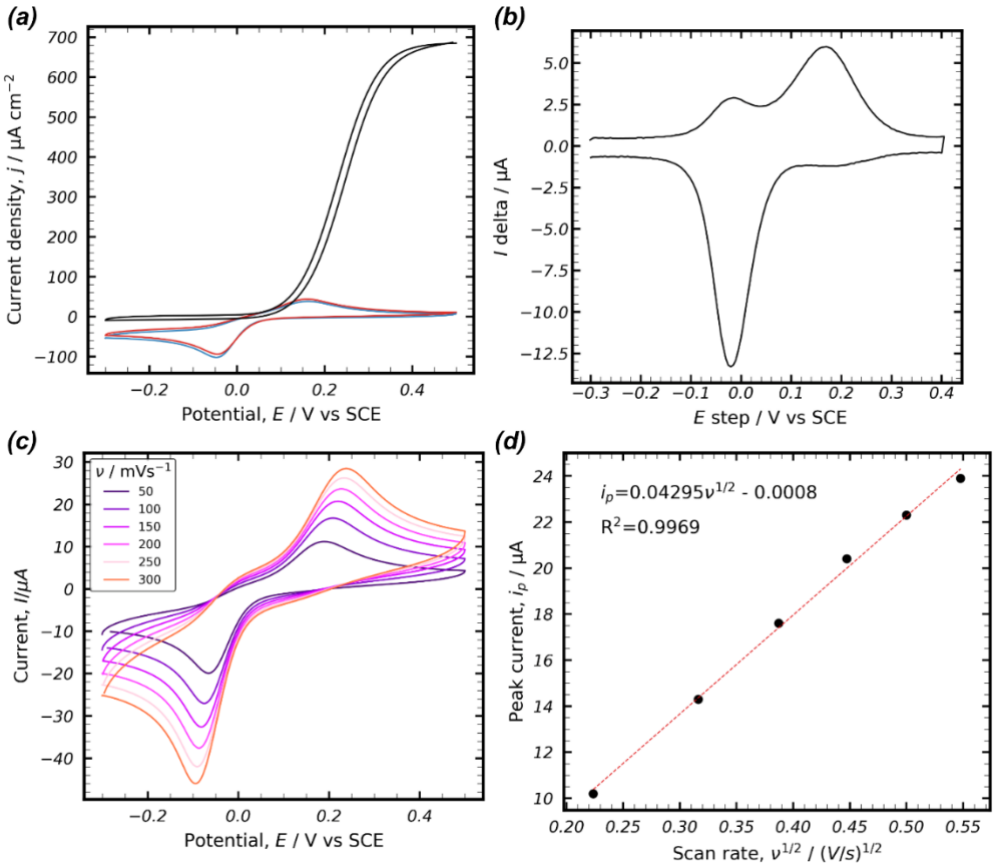

Figure 6.16 (a) A CV showing the catalytic current density of the glucose oxidase-10 mediated system. The CV in (blue) is 0.5 mM 10, (red) with 10 µM glucose oxidase and (black) with 100 mM glucose in 100mM phosphate buffer at pH 7 and 5mV/s scan rate. (b) shows the SWV of 0.5 mM 10 showing peak reduction (E_1) and oxidation potential (E_2). The pulse height, width, and step height of 10 mV, 5 ms and - 5 mV, respectively. (c) describes the scan rate dependence study and (d) shows the correlation between the square root of scan rate and the respective peak potentials.

2,6-Dichloro-1,4-benzoquinone (11)

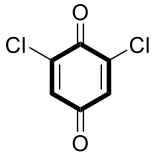

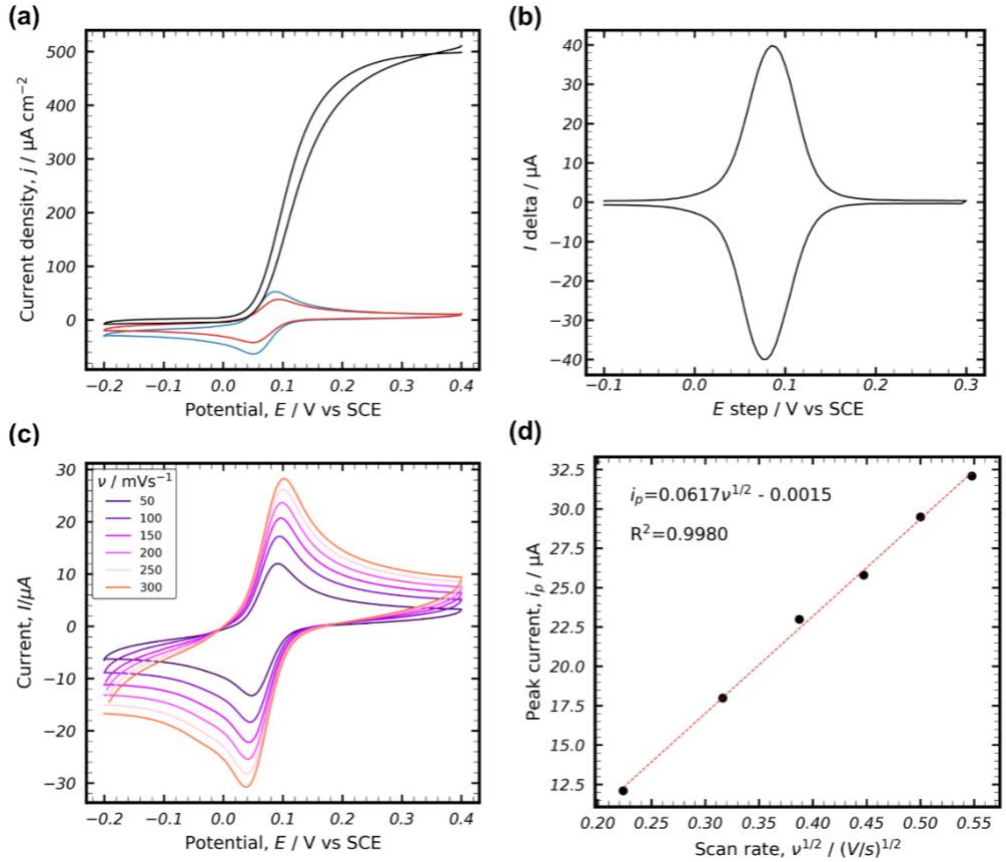

Figure 6.17 (a) A CV showing the catalytic current density of the glucose oxidase-11 mediated system. The CV in (blue) is 0.5 mM 11, (red) with 10µM glucose oxidase and (black) with 100 mM glucose in 100mM phosphate buffer at pH 7 and 5mV/s scan rate. (b) shows the SWV of 0.5 mM 11 showing peak reduction (E_1) and oxidation potential (E_2). The pulse height, width, and step height of 10 mV, 5 ms and - 5 mV, respectively. (c) describes the scan rate dependence study and (d) shows the correlation between the square root of scan rate and the respective peak potentials.

2,5-Dibromo-1,4-benzoquinone (12)

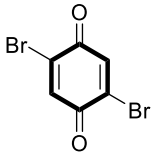

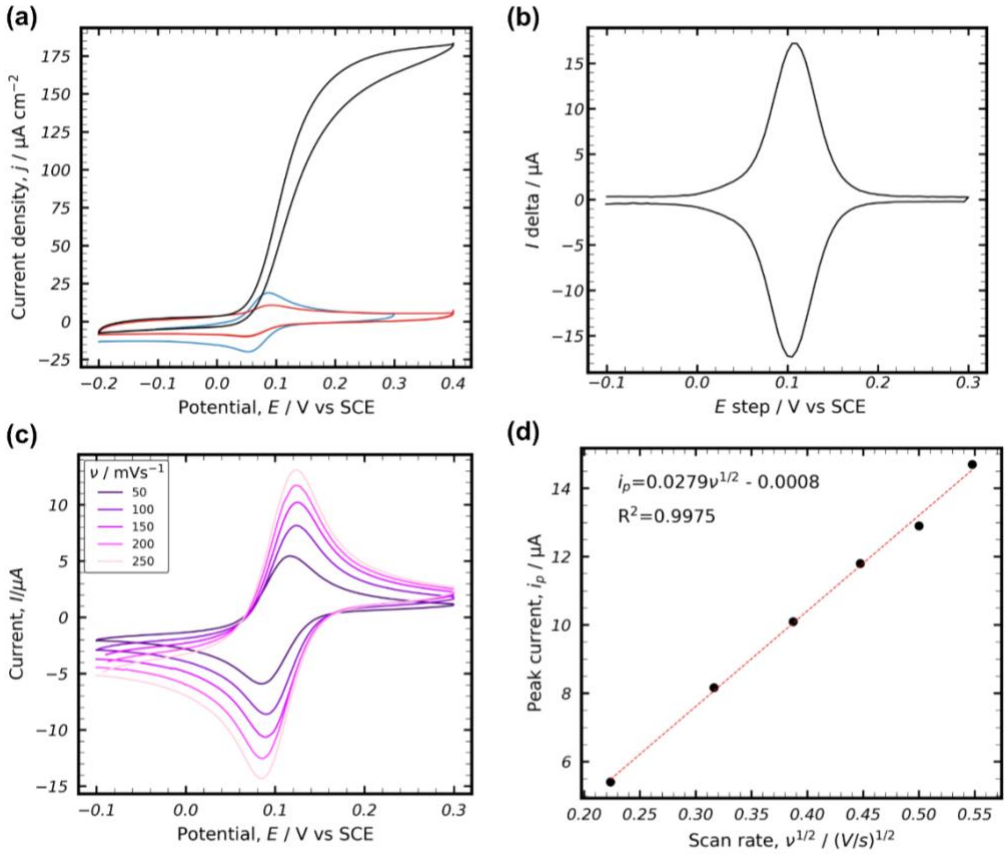

Figure 6.18 (a) A CV showing the catalytic current density of the glucose oxidase-12 mediated system. The CV in (blue) is 0.5 mM 12, (red) with 10μM glucose oxidase and (black) with 100 mM glucose in 100mM phosphate buffer at pH 7 and 5mV/s scan rate. (b) shows the SWV of 0.5 mM 12 showing peak reduction (E_1) and oxidation potential (E_2). The pulse height, width, and step height of 10 mV, 20 ms and 5 mV, respectively. (c) describes the scan rate dependence study and (d) shows the correlation between the square root of scan rate and the respective peak potentials.

2-Methyl-1,4-benzoquinone (13)

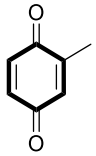

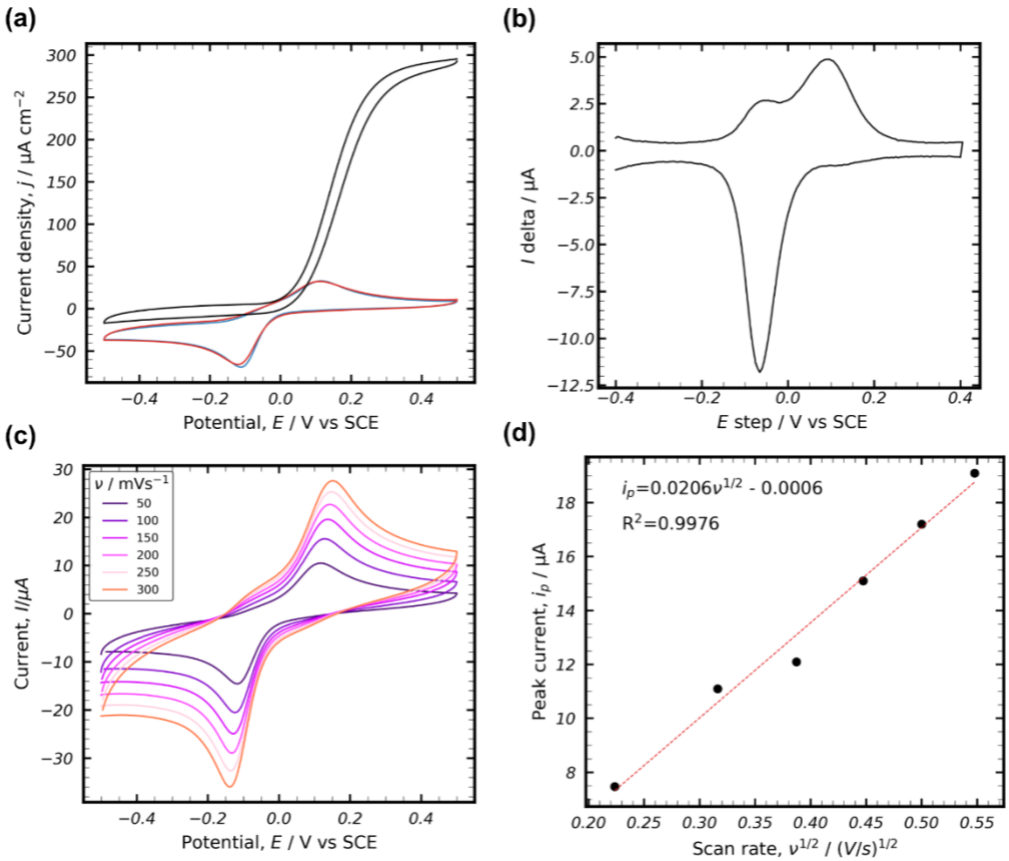

Figure 6.19 (a) A CV showing the catalytic current density of the glucose oxidase-2-methyl-13 mediated system. The CV in (blue) is 0.5 mM 13, (red) with 10µM glucose oxidase and (black) with 100 mM glucose in 100mM phosphate buffer at pH 7 and 5mV/s scan rate. (b) shows the SWV of 0.5 mM 13 showing peak reduction (E_1) and oxidation potential (E_2). The pulse height, width, and step height of 10 mV, 20 ms and 5 mV, respectively. (c) describes the scan rate dependence study and (d) shows the correlation between the square root of scan rate and the respective peak potentials.

2,6-Dimethyl-1,4-benzoquinone (14)

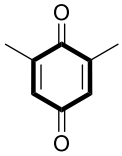

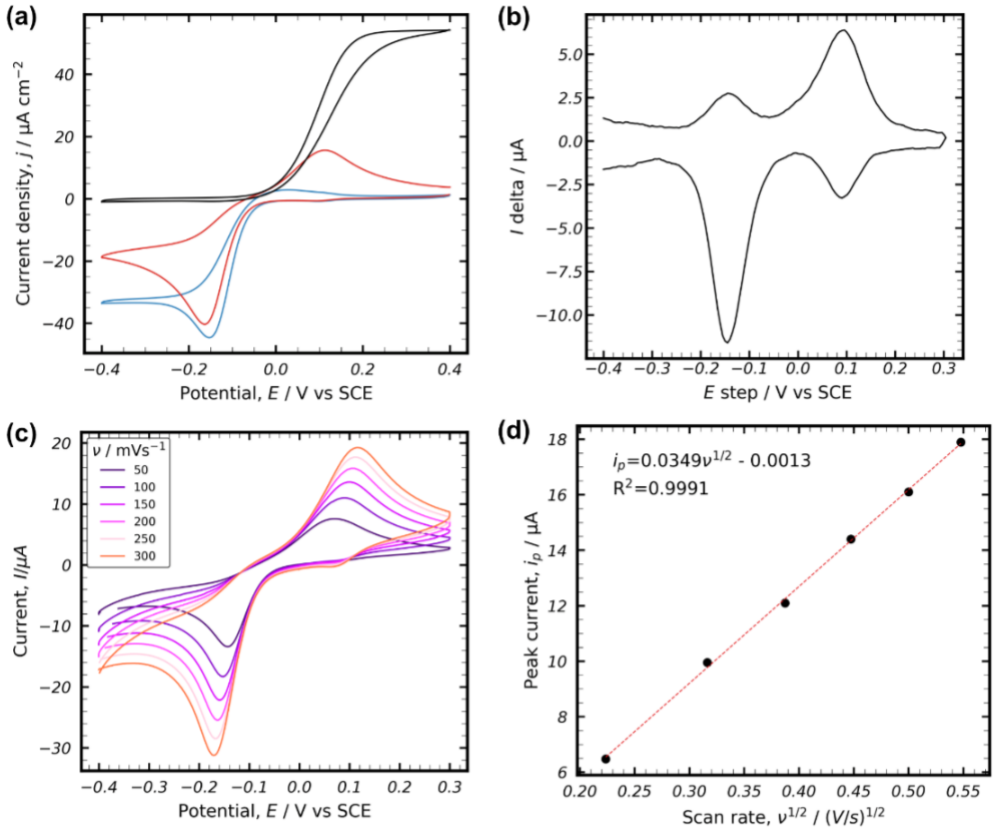

Figure 6.20 (a) A CV showing the catalytic current density of the glucose oxidase-14 mediated system. The CV in (blue) is 0.5 mM 14, (red) with 10μM glucose oxidase and (black) with 100 mM glucose in 100mM phosphate buffer at pH 7 and 5mV/s scan rate. (b) shows the SWV of 0.5 mM 14 showing peak reduction (E_1) and oxidation potential (E_2). The pulse height, width, and step height of 10 mV, 10 ms and -5 mV, respectively. (c) describes the scan rate dependence study and (d) shows the correlation between the square root of scan rate and the respective peak potentials.

2,3-Dimethoxy-5-methyl-1,4-benzoquinone (15)

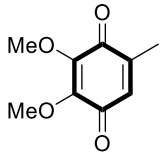

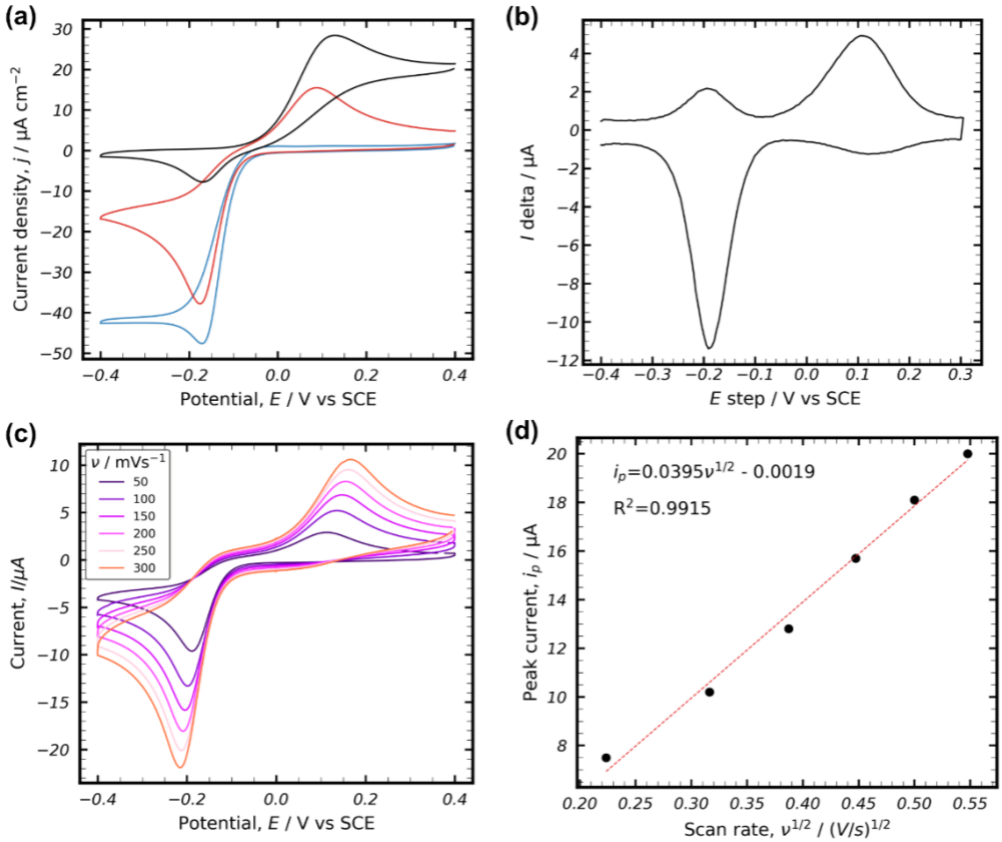

Figure 6.21 (a) A CV showing the catalytic current density of the glucose oxidase-15 mediated system. The CV in (blue) is 0.5 mM 15, (red) with 10μM glucose oxidase and (black) with 100 mM glucose in 100mM phosphate buffer at pH 7 and 5mV/s scan rate. (b) shows the SWV of 0.5 mM 15 showing peak reduction (E_1) and oxidation potential (E_2). The pulse height, width, and step height of 10 mV, 10 ms and -5 mV, respectively. (c) describes the scan rate dependence study and (d) shows the correlation between the square root of scan rate and the respective peak potentials.

2,6-Dimethoxy-1,4-benzoquinone (16)

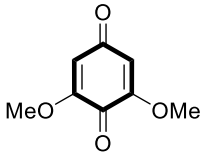

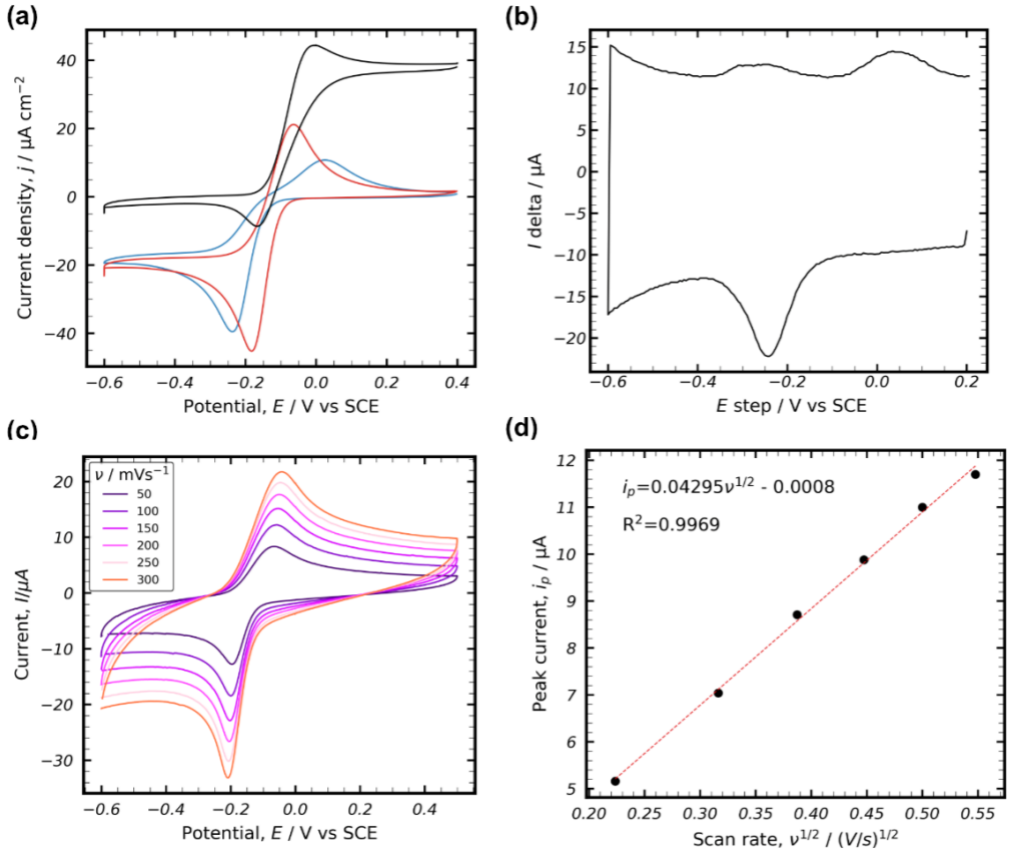

Figure 6.22 (a) A CV showing the catalytic current density of the glucose oxidase-16 mediated system. The CV in (blue) is 0.5 mM 16, (red) with 10µM glucose oxidase and (black) with 100 mM glucose in 100mM phosphate buffer at pH 7 and 5mV/s scan rate. (b) shows the SWV of 0.5 mM 2,6-dimethoxy-16 showing peak reduction (E_1) and oxidation potential (E_2). The pulse height, width, and step height of 10 mV, 1 ms and -5 mV, respectively. (c) describes the scan rate dependence study and (d) shows the correlation between the square root of scan rate and the respective peak potentials.

3,5-Di-tertbutyl-1,2-benzoquinone (17)

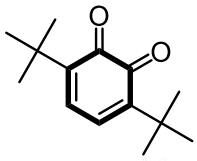

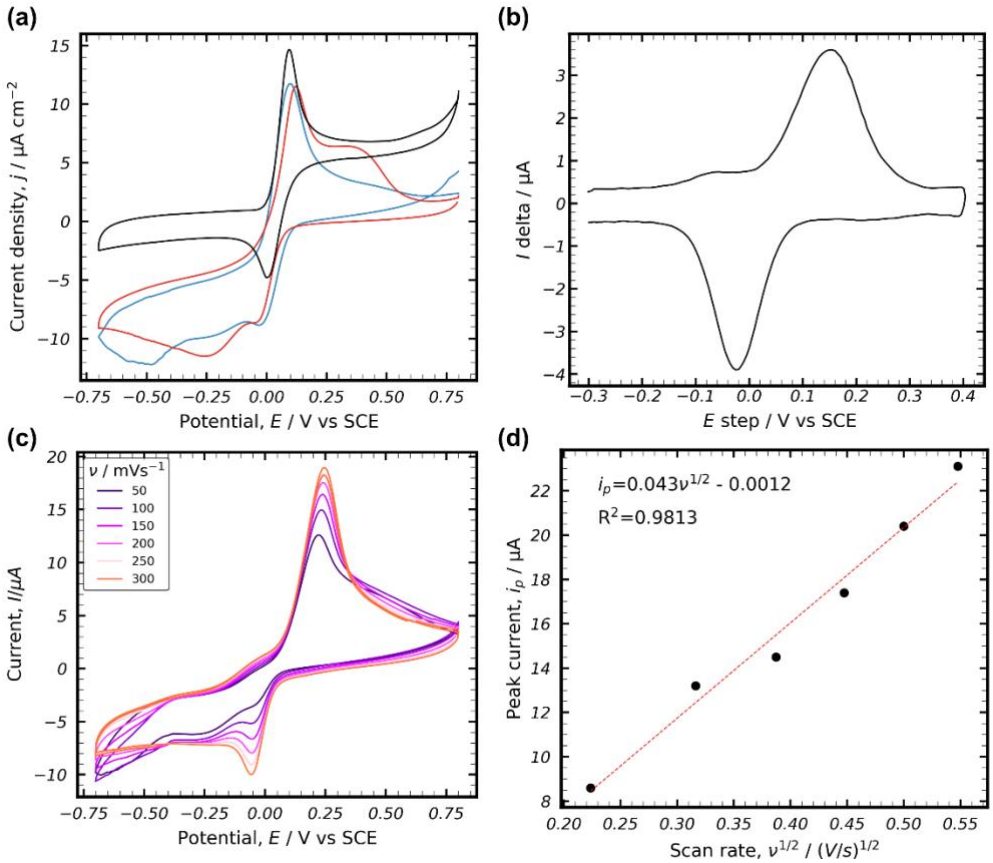

Figure 6.23 (a) A CV showing the catalytic current density of the glucose oxidase-17 system. The CV in (blue) is 0.5 mM 17, (red) with 10µM glucose oxidase and (black) with 100 mM glucose in 100mM phosphate buffer at pH 7 and 5mV/s scan rate. (b) shows the SWV of 0.5 mM 17 showing peak reduction (E_1) and oxidation potential (E_2). The pulse height, width, and step height of 10 mV, 20 ms and 5 mV, respectively. (c) describes the scan rate dependence study and (d) shows the correlation between the square root of scan rate and the respective peak potentials.

Catechol (18)

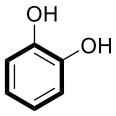

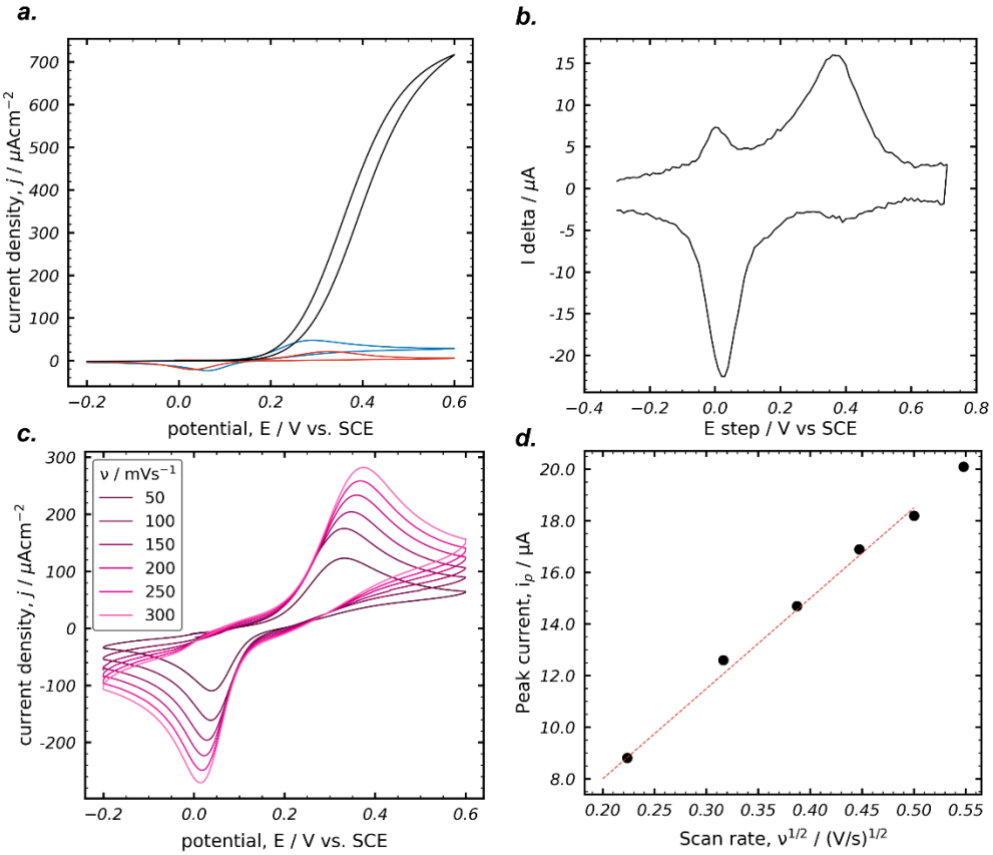

Figure 6.24 (a) A CV showing the catalytic current density of the glucose oxidase-18 system. The CV in (blue) is 0.5 mM 18, (red) with 10μM glucose oxidase and (black) with 100 mM glucose in 100mM phosphate buffer at pH 7 and 5mV/s scan rate. (b) shows the SWV of 0.5 mM 18 showing peak reduction (E_1) and oxidation potential (E_2). The pulse height, width, and step height of 10 mV, 20 ms and 5 mV, respectively. (c) describes the scan rate dependence study and (d) shows the correlation between the square root of scan rate and the respective peak potentials.

4-Methylcatechol (19)

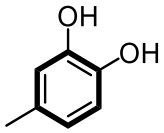

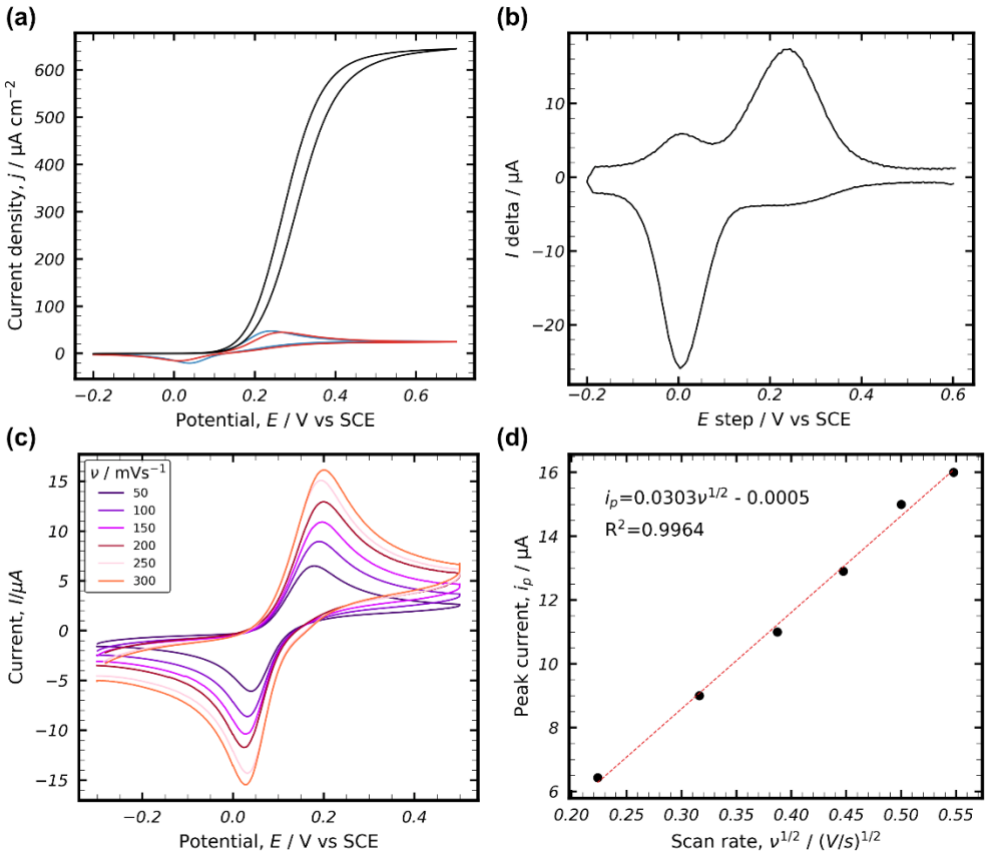

Figure 6.25 (a) A CV showing the catalytic current density of the glucose oxidase-19 mediated system. The CV in (blue) is 0.5 mM 19, (red) with 10µM glucose oxidase and (black) with 100 mM glucose in 100mM phosphate buffer at pH 7 and 5mV/s scan rate. (b) shows the SWV of 0.5 mM 19 showing peak reduction (E_1) and oxidation potential (E_2). The pulse height, width, and step height of 10 mV, 5 ms and 5 mV, respectively. (c) describes the scan rate dependence study and (d) shows the correlation between the square root of scan rate and the respective peak potentials.

4-Ethylcatechol (20)

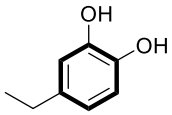

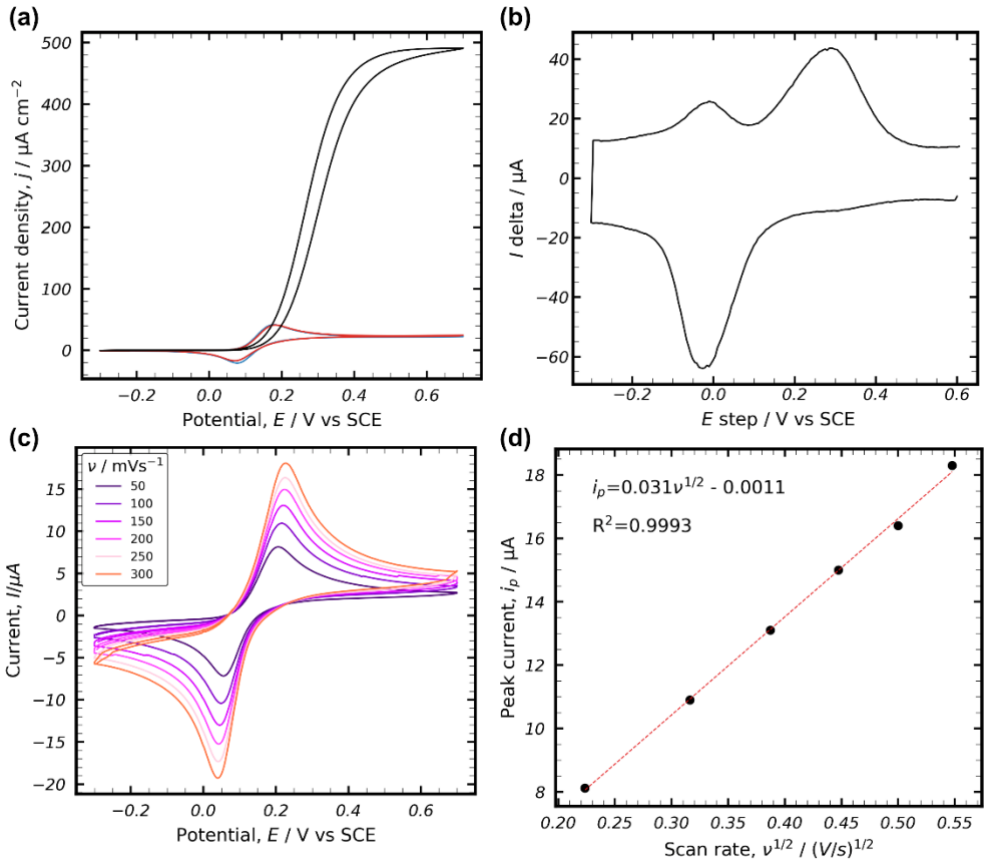

Figure 6.26 (a) A CV showing the catalytic current density of the glucose oxidase-20 mediated system. The CV in (blue) is 0.5 mM 20, (red) with 10µM glucose oxidase and (black) with 100 mM glucose in 100mM phosphate buffer at pH 7 and 5mV/s scan rate. (b) shows the SWV of 0.5 mM 20 showing peak reduction (E_1) and oxidation potential (E_2). The pulse height, width, and step height of 10 mV, 1 ms and -5 mV, respectively. (c) describes the scan rate dependence study and (d) shows the correlation between the square root of scan rate and the respective peak potentials.

3-Bromocatechol (21)

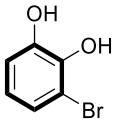

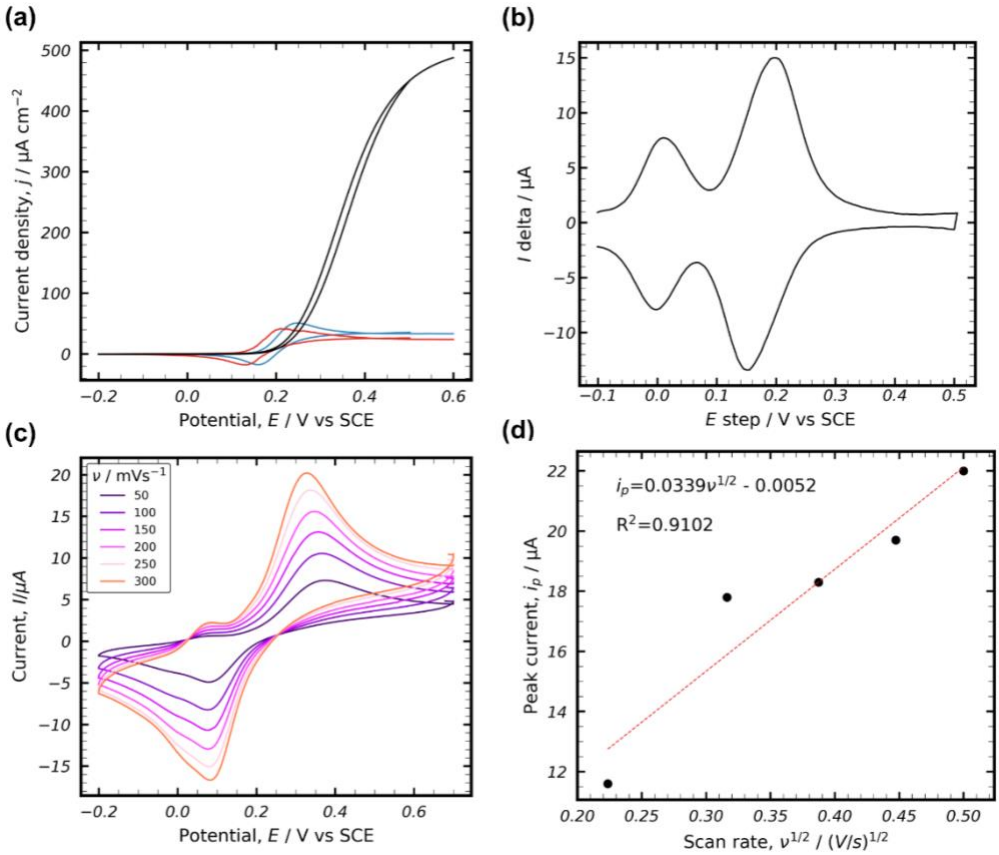

Figure 6.27 (a) A CV showing the catalytic current density of the glucose oxidase-21 mediated system. The CV in (blue) is 0.5 mM 21, (red) with 10µM glucose oxidase and (black) with 100 mM glucose in 100mM phosphate buffer at pH 7 and 5mV/s scan rate. (b) shows the SWV of 0.5 mM 21 showing peak reduction (E_1) and oxidation potential (E_2). The pulse height, width, and step height of 10 mV, 1 ms and -5 mV, respectively. (c) describes the scan rate dependence study and (d) shows the correlation between the square root of scan rate and the respective peak potentials.

3-Fluorocatechol (22)

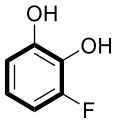

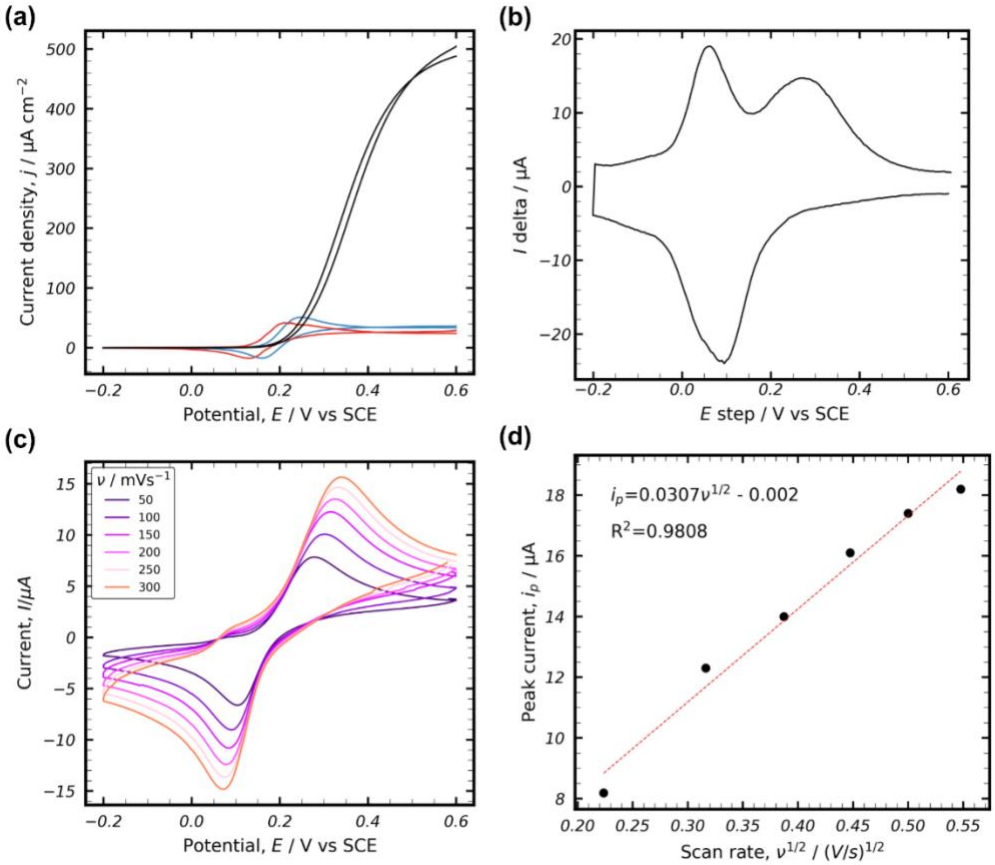

Figure 6.28 (a) A CV showing the catalytic current density of the glucose oxidase-22 mediated system. The CV in (blue) is 0.5 mM 22, (red) with 10μM glucose oxidase and (black) with 100 mM glucose in 100mM phosphate buffer at pH 7 and 5mV/s scan rate. (b) shows the SWV of 0.5 mM 22 showing peak reduction (E_1) and oxidation potential (E_2). The pulse height, width, and step height of 10 mV, 20 ms and 5 mV, respectively. (c) describes the scan rate dependence study and (d) shows the correlation between the square root of scan rate and the respective peak potentials.

3,4,5-Trihydroxybenzoic acid (23)

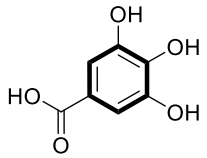

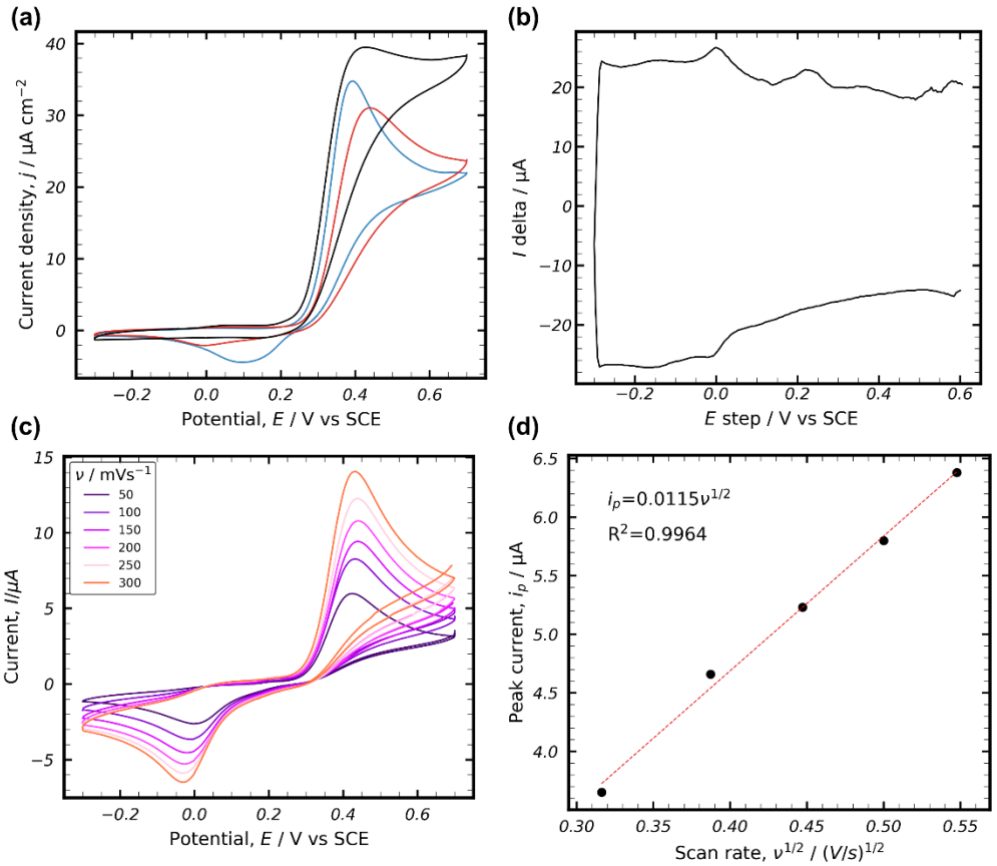

Figure 6.29 (a) A CV showing the catalytic current density of the glucose oxidase-23 mediated system. The CV in (blue) is 0.5 mM 23, (red) with 10μM glucose oxidase and (black) with 100 mM glucose in 100mM phosphate buffer at pH 7 and 5mV/s scan rate. (b) shows the SWV of 0.5 mM 23 showing peak reduction (E_1) and oxidation potential (E_2). The pulse height, width, and step height of 10 mV, 20 ms and 5 mV, respectively. (c) describes the scan rate dependence study and (d) shows the correlation between the square root of scan rate and the respective peak potentials.

3,4-Dihydroxyphenylacetic acid (24)

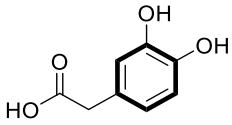

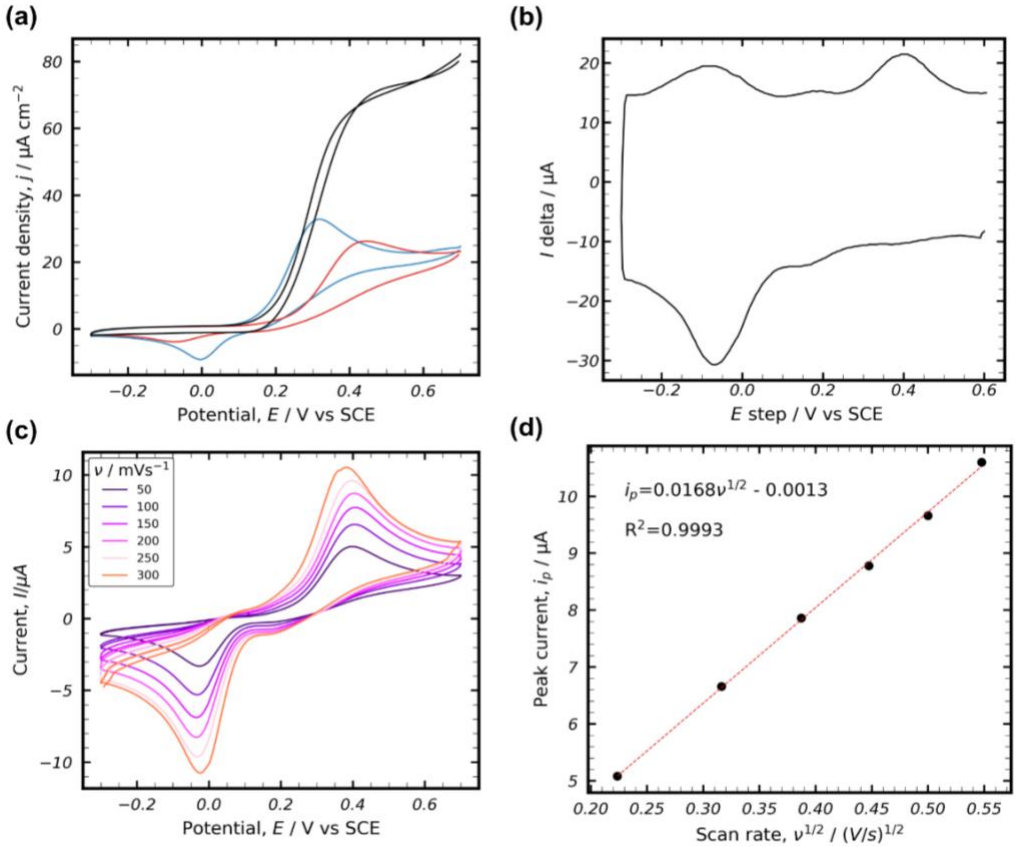

Figure 6.30 (a) A CV showing the catalytic current density of the glucose oxidase-24 mediated system. The CV in (blue) is 0.5 mM 24, (red) with 10μM glucose oxidase and (black) with 100 mM glucose in 100mM phosphate buffer at pH 7 and 5mV/s scan rate. (b) shows the SWV of 0.5 mM 24 showing peak reduction (E_1) and oxidation potential (E_2). The pulse height, width, and step height of 10 mV, 5 ms and -5 mV, respectively. (c) describes the scan rate dependence study and (d) shows the correlation between the square root of scan rate and the respective peak potentials.

3,4-Dihydroxy-DL-phenylalanine (25)

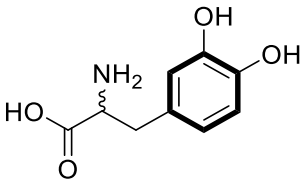

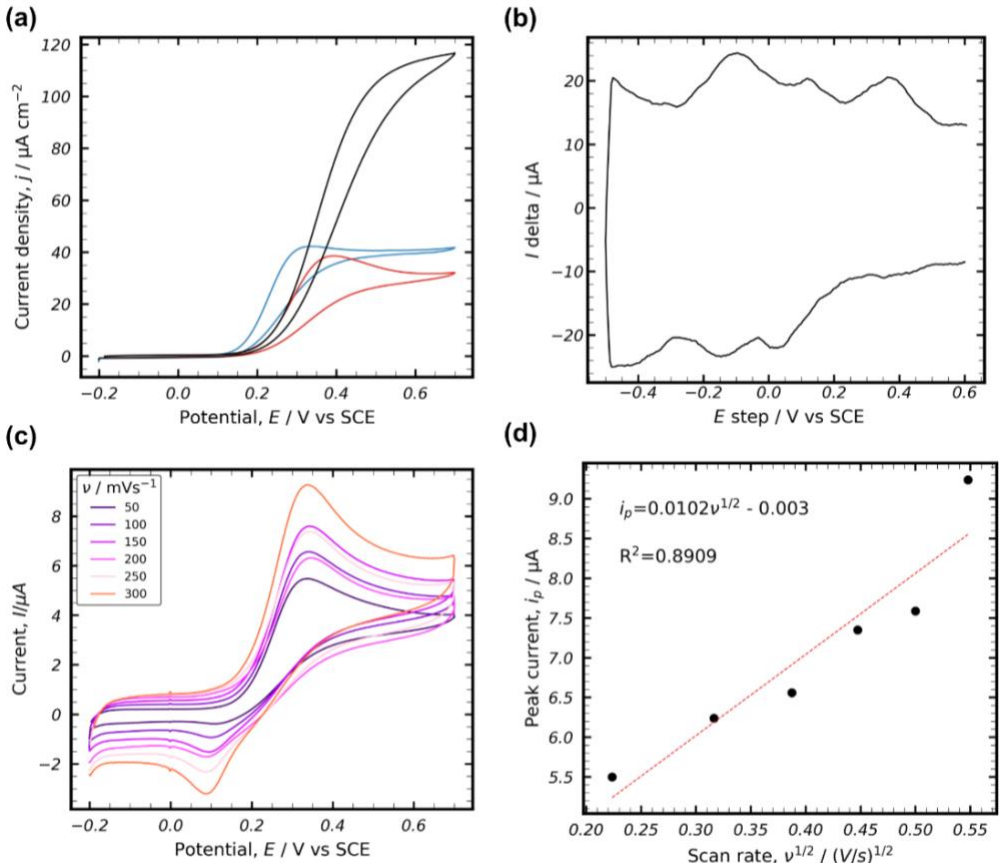

Figure 6.31 (a) A CV showing the catalytic current density of the glucose oxidase-25 mediated system. The CV in (blue) is 0.5 mM 25, (red) with 10µM glucose oxidase and (black) with 100 mM glucose in 100mM phosphate buffer at pH 7 and 5mV/s scan rate. (b) shows the SWV of 0.5 mM 25 showing peak reduction (E_1) and oxidation potential (E_2). The pulse height, width, and step height of 10 mV, 20 ms and 5 mV, respectively. (c) describes the scan rate dependence study and (d) shows the correlation between the square root of scan rate and the respective peak potentials.

6.6 Multivariate Regression Analysis Input Data

Table 6.3 Input parameters used in training the QSAR model.

Quinone Mediator	log(k/ $M^{-1}s^{-1}$)	$E°_{Q/QH2}$ V vs. SCE	HOMO	LUMO	Dipole Moment (Debye)	Electroneg.
1	4.61	-0.06	-0.255	-0.154	9.491	0.205
2	2.98	-0.11	-0.279	-0.148	2.065	0.213
3	1.77	-0.24	-0.279	-0.125	1.608	0.202
4	2.46	-0.10	-0.283	-0.141	4.891	0.212
5	2.03	-0.10	-0.278	-0.140	4.415	0.209
6	1.41	-0.40	-0.267	-0.125	0.089	0.196
7	2.35	-0.25	-0.255	-0.168	7.309	0.211
8	2.43	-0.24	-0.260	-0.144	4.530	0.202
9	3.79	0.11	-0.253	-0.154	12.539	0.203
10	5.90	0.03	-0.292	-0.163	0.000	0.228
11	5.52	0.15	-0.295	-0.155	1.190	0.225
12	5.27	0.15	-0.286	-0.154	0.000	0.220
13	5.31	-0.06	-0.283	-0.160	1.056	0.221
14	4.15	-0.20	-0.208	-0.151	1.698	0.179
15	3.18	-0.09	-0.258	-0.135	4.188	0.197
16	4.04	-0.11	-0.260	-0.130	0.164	0.195
17	2.48	0.05	-0.258	-0.137	9.149	0.197
18	6.23	0.13	-0.257	-0.167	8.046	0.222
19	6.25	0.11	-0.269	-0.195	9.156	0.232
20	6.36	0.11	-0.258	-0.166	9.412	0.212
21	5.89	0.09	-0.260	-0.179	7.858	0.219
22	6.23	0.18	-0.274	-0.207	7.930	0.241
23	3.66	0.12	-0.262	-0.187	9.318	0.225
24	4.96	0.08	-0.266	-0.173	3.583	0.219
25	5.35	0.17	-0.254	-0.163	10.920	0.209

Table 6.3 (cont'd).

Quinone Mediator	Electrophilicity	Polarizability (a)	Electron Energy	Collision Diameter (Å)		
				A	B	C
1	0.41	178.09	-535.15	3.37	7.93	9.78
2	0.35	170.77	-535.16	9.50	3.37	8.17
3	0.26	189.12	-574.48	3.37	7.93	9.78
4	0.32	211.45	-1454.33	3.49	8.18	10.45
5	0.32	237.33	-5677.41	8.18	10.74	3.85
6	0.27	197.53	-649.69	7.91	4.39	1.60
7	0.51	194.72	-685.60	3.37	9.51	8.81
8	0.35	181.88	-610.38	3.37	8.16	9.71
9	0.42	229.68	-1158.53	9.35	9.25	5.15
10	0.40	104.40	-381.49	3.37	7.21	7.70
11	0.43	141.49	-1300.67	3.49	8.67	8.06
12	0.37	167.51	-5523.73	3.85	9.25	7.69
13	0.40	121.86	-710.00	8.57	4.32	6.93
14	0.56	139.05	-460.14	4.43	8.54	8.17
15	0.32	169.80	-649.86	4.70	8.72	9.83
16	0.29	153.57	-610.56	10.82	4.63	7.97
17	0.32	236.82	-696.02	10.74	7.83	7.83
18	0.49	99.94	-600.79	3.46	7.34	7.90
19	0.72	119.32	-420.80	4.33	8.75	7.01
20	0.48	135.22	-460.12	10.08	7.29	4.44
21	0.59	133.05	-2952.60	3.85	7.85	8.21
22	0.87	100.05	-480.71	3.37	7.94	7.21
23	0.67	137.14	-645.29	3.37	9.02	8.08
24	0.52	143.12	-609.38	5.90	6.17	10.09
25	0.48	171.71	-704.06	5.71	12.10	6.81

Table 6.3 (cont'd).

Quinone mediator	Molecular Area Å^2	Distance Å	Volume Å^3	Surface Area Å^2	Sterimol Parameters for C2					
					B1	B2	B3	B4	B5	L
1	57.9	2.8	135.1	151.0	1.52	1.52	1.52	1.52	1.52	3.04
2	57.9	3.7	134.7	150.3	1.10	1.10	1.10	1.10	1.10	2.20
3	63.2	4.8	151.3	166.0	1.70	1.93	2.02	2.12	2.13	3.40
4	66.2	5.1	181.4	190.0	1.75	1.75	1.75	1.75	1.75	3.50
5	69.5	7.3	222.8	216.0	1.83	1.83	1.83	1.83	1.83	3.66
6	66.2	2.8	159.9	175.4	1.52	1.52	2.47	3.11	3.14	4.37
7	63.8	3.3	151.2	164.9	1.10	1.10	1.10	1.10	1.10	2.20
8	60.8	3.7	143.2	157.6	1.10	1.10	1.10	1.10	1.10	2.20
9	65.9	5.9	179.1	179.1	1.52	1.52	1.52	1.52	1.52	3.04
10	40.2	3.4	91.3	111.2	1.10	1.10	1.10	1.10	1.10	2.20
11	48.7	3.8	139.2	154.8	1.75	1.75	1.75	1.75	1.75	3.50
12	52.2	3.5	183.1	186.7	1.83	1.83	1.83	1.83	1.83	3.66
13	45.6	3.4	107.2	126.9	1.70	1.94	2.01	2.12	2.13	3.40
14	50.9	3.7	123.5	142.3	1.10	1.10	1.10	1.10	1.10	2.20
15	61.6	4.6	160.1	175.6	1.52	1.52	2.62	3.14	3.17	4.35
16	56.8	4.9	141.5	161.4	1.52	1.52	2.62	3.14	3.17	4.35
17	70.5	7.9	224.9	223.2	1.52	1.52	1.52	1.52	1.52	3.04
18	40.3	49.3	183.6	167.4	1.52	1.52	1.52	1.52	3.04	1.52
19	45.6	2.8	107.4	127.5	1.52	1.52	1.52	1.52	1.52	3.04
20	50.8	3.7	123.2	143.0	1.52	1.52	1.52	1.52	1.52	3.04
21	46.2	5.1	137.9	149.2	1.52	1.52	1.52	1.52	1.52	3.04
22	40.7	2.9	95.3	115.3	1.52	1.52	1.52	1.52	1.52	3.04
23	53.3	5.0	128.6	148.5	1.52	1.52	1.52	1.52	1.52	3.04
24	50.4	3.7	138.0	156.2	1.52	1.52	1.52	1.52	1.52	3.04
25	49.3	3.5	167.4	183.6	1.52	1.52	1.52	1.52	1.52	3.04

Table 6.3 (cont'd).

Quinone mediator	Sterimol Parameters C3 B1	B2	B3	B4	B5	L	C4 B1	B2	B3	B4	B5	L
1	1.10	1.10	1.10	1.10	1.10	2.20	1.10	1.10	1.10	1.10	1.10	2.20
2	1.10	1.10	1.10	1.10	1.10	2.20	1.52	1.52	1.52	1.52	1.52	3.04
3	1.10	1.10	1.10	1.10	1.10	2.20	1.52	1.52	1.52	1.52	1.52	3.04
4	1.75	1.75	1.75	1.75	1.75	3.50	1.52	1.52	1.52	1.52	1.52	3.04
5	1.83	1.83	1.83	1.83	1.83	3.66	1.52	1.52	1.52	1.52	1.52	3.04
6	1.10	1.10	1.10	1.10	1.10	2.20	1.52	1.52	1.52	1.52	1.52	3.04
7	1.10	1.10	1.10	1.10	1.10	2.20	1.52	1.52	1.52	1.52	1.52	3.04
8	1.10	1.10	1.10	1.10	1.10	2.20	1.52	1.52	1.52	1.52	1.52	3.04
9	1.10	1.10	1.10	1.10	1.10	2.20	2.24	2.76	2.77	2.96	2.96	3.72
10	1.10	1.10	1.10	1.10	1.10	2.20	1.52	1.52	1.52	1.52	1.52	3.04
11	1.10	1.10	1.10	1.10	1.10	2.20	1.52	1.52	1.52	1.52	1.52	3.04
12	1.10	1.10	1.10	1.10	1.10	2.20	1.52	1.52	1.52	1.52	1.52	3.04
13	1.10	1.10	1.10	1.10	1.10	2.20	1.52	1.52	1.52	1.52	1.52	3.04
14	1.70	1.95	2.02	2.12	2.12	3.40	1.52	1.52	1.52	1.52	1.52	3.04
15	1.52	1.52	2.56	3.15	3.17	4.36	1.52	1.52	1.52	1.52	1.52	3.04
16	1.52	1.52	2.56	3.15	3.17	4.36	1.52	1.52	1.52	1.52	1.52	3.04
17	2.86	3.13	3.28	3.28	3.29	4.46	1.10	1.10	1.10	1.10	1.10	2.20
18	1.47	1.47	1.47	1.47	1.47	1.47	1.10	1.10	1.10	1.10	1.10	2.20
19	1.10	1.10	1.10	1.10	1.10	2.20	1.10	1.10	1.10	1.10	1.10	2.20
20	1.10	1.10	1.10	1.10	1.10	2.20	1.70	1.98	1.99	3.06	3.24	4.58
21	1.83	1.83	1.83	1.83	1.83	3.66	1.10	1.10	1.10	1.10	1.10	2.20
22	1.47	1.47	1.47	1.47	1.47	2.94	1.10	1.10	1.10	1.10	1.10	2.20
23	1.52	1.52	1.52	1.93	2.01	3.04	1.10	1.10	1.10	1.10	1.10	2.20
24	1.10	1.10	1.10	1.10	1.10	2.20	1.70	2.26	2.27	3.89	3.98	4.86
25	1.10	1.10	1.10	1.10	1.10	2.20	1.70	2.79	3.23	4.17	4.44	6.56

Table 6.3 (cont'd).

Quinone mediator	Sterimol parameters C5 B1	B2	B3	B4	B5	L	C6 B1	B2	B3	B4	B5	L
1	1.70	1.89	3.04	3.91	4.47	4.59	1.70	1.89	3.04	3.91	4.47	4.59
2	1.70	1.94	2.04	4.45	4.47	4.59	1.70	2.00	2.46	4.30	4.47	4.59
3	1.70	1.89	3.04	3.91	4.47	4.59	1.70	1.89	3.04	3.91	4.47	4.59
4	1.70	1.97	2.04	4.44	4.46	4.58	1.70	1.88	3.09	3.86	4.46	4.58
5	1.70	1.92	2.92	4.01	4.46	4.58	1.70	1.73	2.05	4.46	4.46	4.58
6	1.70	1.91	2.96	3.98	4.47	4.59	1.70	1.99	2.55	4.25	4.46	4.58
7	1.70	1.72	2.69	5.47	5.47	4.58	1.70	2.06	2.67	5.42	5.47	4.58
8	1.70	1.80	2.05	5.44	5.44	4.58	1.70	1.88	2.69	4.48	4.49	4.59
9	1.70	1.77	2.04	4.49	4.49	4.60	1.70	1.78	2.05	4.47	4.47	4.59
10	1.10	1.10	1.10	1.10	1.10	2.20	1.10	1.10	1.10	1.10	1.10	2.20
11	1.10	1.10	1.10	1.10	1.10	2.20	1.75	1.75	1.75	1.75	1.75	3.50
12	1.83	1.83	1.83	1.83	1.83	3.66	1.10	1.10	1.10	1.10	1.10	2.20
13	1.10	1.10	1.10	1.10	1.10	2.20	1.10	1.10	1.10	1.10	1.10	2.20
14	1.70	1.95	2.02	2.12	2.12	3.40	1.10	1.10	1.10	1.10	1.10	2.20
15	1.10	1.10	1.10	1.10	1.10	2.20	1.70	1.98	2.00	2.12	2.13	3.40
16	1.10	1.10	1.10	1.10	1.10	2.20	1.70	1.98	2.00	2.12	2.13	3.40
17	2.87	3.17	3.27	3.30	3.31	4.48	1.10	1.10	1.10	1.10	1.10	2.20
18	1.10	1.10	1.10	1.10	1.10	2.20	2.20	1.10	1.10	1.10	1.10	2.20
19	1.70	1.95	2.02	2.12	2.13	3.40	1.10	1.10	1.10	1.10	1.10	2.20
20	1.10	1.10	1.10	1.10	1.10	2.20	1.10	1.10	1.10	1.10	1.10	2.20
21	1.10	1.10	1.10	1.10	1.10	2.20	1.10	1.10	1.10	1.10	1.10	2.20
22	1.10	1.10	1.10	1.10	1.10	2.20	1.10	1.10	1.10	1.10	1.10	2.20
23	1.70	1.70	2.53	2.75	2.76	4.29	1.10	1.10	1.10	1.10	1.10	2.20
24	1.10	1.10	1.10	1.10	1.10	2.20	1.10	1.10	1.10	1.10	1.10	2.20
25	1.10	1.10	1.10	1.10	1.10	2.20	1.10	1.10	1.10	1.10	1.10	2.20

6.7 Geometry Optimized Coordinates

Table 6.4 Geometry Optimized Coordinates of the library of quinones: 1,2-NQ (1).

Q				$Q^{\cdot-}$			
Atom	X	Y	Z	Atom	X	Y	Z
C	-3.0352	0.3621	0.0000	C	3.0465	0.3256	0.0000
C	-2.0051	1.3092	0.0000	C	2.0464	1.2886	0.0000
C	-0.6652	0.9011	0.0000	C	0.6801	0.9231	0.0000
C	-0.3685	-0.4849	0.0000	C	0.3313	-0.4624	0.0000
C	-1.4047	-1.4247	0.0000	C	1.3676	-1.4236	0.0000
C	-2.7374	-1.0036	0.0000	C	2.7027	-1.0426	0.0000
H	-4.0690	0.6929	0.0000	H	4.0907	0.6250	0.0000
H	-2.2415	2.3690	0.0000	H	2.3066	2.3446	0.0000
C	0.4109	1.8893	0.0000	C	-0.3652	1.9105	0.0000
C	1.0434	-0.9289	0.0000	C	-1.0751	-0.8900	0.0000
H	-3.5375	-1.7367	0.0000	H	3.4840	-1.7978	0.0000
C	2.1532	0.1715	0.0000	C	-2.1228	0.1664	0.0000
C	1.7254	1.5651	0.0000	C	-1.6854	1.5458	0.0000
H	2.5006	2.3247	0.0000	H	-2.4666	2.3030	0.0000
O	1.3806	-2.1046	0.0000	O	-1.3876	-2.1179	0.0000
H	-1.1576	-2.4811	0.0000	H	1.0929	-2.4735	0.0000
O	3.3303	-0.1758	0.0000	O	-3.3599	-0.1335	0.0000
H	0.1170	2.9359	0.0000	H	-0.0853	2.9615	0.0000
Q^{2-}				QH^{-}			
C	3.0610	0.2978	0.0000	C	-3.0900	0.2184	0.0000
C	2.0818	1.2719	0.0000	C	-2.1440	1.2256	0.0000
C	0.6928	0.9475	0.0000	C	-0.7517	0.9385	0.0000
C	0.2984	-0.4513	0.0000	C	-0.3285	-0.4444	0.0000
C	1.3447	-1.4254	0.0000	C	-1.3313	-1.4650	0.0000
C	2.6815	-1.0766	0.0000	C	-2.6720	-1.1411	0.0000
H	4.1126	0.5749	0.0000	H	-4.1491	0.4601	0.0000
H	2.3627	2.3249	0.0000	H	-2.4565	2.2681	0.0000
C	-0.3199	1.9292	0.0000	C	0.2414	1.9548	0.0000
C	-1.0882	-0.8684	0.0000	C	1.0504	-0.7185	0.0000
H	3.4481	-1.8487	0.0000	H	-3.4185	-1.9314	0.0000
C	-2.1081	0.1783	0.0000	C	2.0515	0.2839	0.0000
C	-1.6581	1.5348	0.0000	C	1.5893	1.6415	0.0000
H	-2.4371	2.2991	0.0000	H	2.3362	2.4330	0.0000
O	-1.4082	-2.1370	0.0000	O	1.5195	-2.0175	0.0000
H	1.0529	-2.4718	0.0000	H	-1.0192	-2.5051	0.0000
O	-3.3920	-0.0993	0.0000	O	3.3051	-0.0834	0.0000
H	-0.0523	2.9850	0.0000	H	-0.0750	2.9960	0.0000
				H	2.4939	-1.8761	0.0000

Table 6.4 (cont'd).

QH_2			
C	-3.1111	0.2361	-0.0117
C	-2.1653	1.2404	-0.0211
C	-0.7750	0.9420	-0.0082
C	-0.3636	-0.4357	0.0063
C	-1.3619	-1.4506	0.0298
C	-2.7023	-1.1208	0.0186
H	-4.1688	0.4810	-0.0216
H	-2.4715	2.2831	-0.0361
C	0.2145	1.9642	0.0000
C	1.0297	-0.7209	-0.0027
H	-3.4501	-1.9079	0.0395
C	1.9667	0.2985	0.0064
C	1.5558	1.6512	0.0125
H	2.3169	2.4250	0.0159
O	1.5414	-2.0055	0.0366
H	-1.0746	-2.4968	0.0713
O	3.3070	0.0225	0.0028
H	-0.1013	3.0033	-0.0047
H	1.0207	-2.6078	-0.5136
H	3.4158	-0.9419	-0.0446

Table 6.5 Geometry Optimized Coordinates of the library of quinones:1,4-NQ (2).

Q				$Q^{\cdot-}$			
Atom	X	Y	Z	Atom	X	Y	Z
C	0.0000	0.6998	2.6829	C	0.0000	2.6686	-0.7049
C	0.0000	1.4004	1.4753	C	0.0000	1.4653	-1.3969
C	0.0000	0.7062	0.2603	C	0.0000	0.2304	-0.7128
C	0.0000	-0.7062	0.2603	C	0.0000	0.2304	0.7128
C	0.0000	-1.4004	1.4753	C	0.0000	1.4653	1.3969
C	0.0000	-0.6998	2.6829	C	0.0000	2.6686	0.7049
H	0.0000	1.2431	3.6225	H	0.0000	3.6096	-1.2483
H	0.0000	2.4849	1.4621	H	0.0000	1.4493	-2.4821
C	0.0000	1.4578	-1.0261	C	0.0000	-1.0353	-1.4703
C	0.0000	-1.4578	-1.0261	C	0.0000	-1.0353	1.4703
H	0.0000	-2.4849	1.4621	H	0.0000	1.4493	2.4821
H	0.0000	-1.2431	3.6225	H	0.0000	3.6096	1.2483
C	0.0000	-0.6723	-2.2832	C	0.0000	-2.2411	0.6912
C	0.0000	0.6723	-2.2832	C	0.0000	-2.2411	-0.6912
H	0.0000	-1.2467	-3.2048	H	0.0000	-3.1811	1.2387
H	0.0000	1.2467	-3.2048	H	0.0000	-3.1811	-1.2387
O	0.0000	-2.6894	-1.0669	O	0.0000	-1.0506	2.7448
O	0.0000	2.6894	-1.0669	O	0.0000	-1.0506	-2.7448
Q^{2-}				QH^{-}			
C	0.0000	2.6591	-0.7094	C	-2.7417	0.4345	0.0000
C	0.0000	1.4555	-1.3938	C	-1.6240	1.2517	0.0000
C	0.0000	0.2019	-0.7242	C	-0.3102	0.7235	0.0000
C	0.0000	0.2019	0.7242	C	-0.1501	-0.7076	0.0000
C	0.0000	1.4555	1.3938	C	-1.3156	-1.5284	0.0000
C	0.0000	2.6591	0.7094	C	-2.5810	-0.9727	0.0000
H	0.0000	3.6004	-1.2547	H	-3.7385	0.8676	0.0000
H	0.0000	1.4390	-2.4803	H	-1.7266	2.3326	0.0000
C	0.0000	-1.0374	-1.4918	C	0.8467	1.6297	0.0000
C	0.0000	-1.0374	1.4918	C	1.1623	-1.2536	0.0000
H	0.0000	1.4390	2.4803	H	-1.1938	-2.6069	0.0000
H	0.0000	3.6004	1.2547	H	-3.4557	-1.6182	0.0000
C	0.0000	-2.2083	0.7096	C	2.2568	-0.4114	0.0000
C	0.0000	-2.2083	-0.7096	C	2.1107	0.9943	0.0000
H	0.0000	-3.1658	1.2328	H	3.2592	-0.8390	0.0000
H	0.0000	-3.1658	-1.2328	H	3.0011	1.6193	0.0000
O	0.0000	-1.0373	2.8099	O	1.2735	-2.6448	0.0000
O	0.0000	-1.0373	-2.8099	O	0.6915	2.9159	0.0000
				H	2.2100	-2.8844	0.0000

QH_2

Table 6.5 (cont'd).

C	0.0000	-0.7082	2.6838
C	-0.0001	-1.4044	1.4917
C	0.0000	-0.7173	0.2475
C	0.0000	0.7173	0.2475
C	0.0001	1.4044	1.4917
C	0.0000	0.7082	2.6838
H	-0.0001	-1.2476	3.6264
H	-0.0001	-2.4887	1.4897
C	0.0000	-1.4097	-1.0020
C	0.0000	1.4097	-1.0020
H	0.0001	2.4887	1.4897
H	0.0001	1.2476	3.6264
C	0.0000	0.7087	-2.1881
C	0.0000	-0.7087	-2.1881
H	0.0000	1.2387	-3.1366
H	0.0000	-1.2387	-3.1366
O	0.0001	2.7842	-0.9424
O	-0.0001	-2.7842	-0.9424
H	0.0001	3.1522	-1.8373
H	-0.0001	-3.1522	-1.8373

Table 6.6 Geometry Optimized Coordinates of the library of quinones: 2-methyl-1,4-NQ (3).

Q				$Q^{\cdot-}$			
Atom	X	Y	Z	Atom	X	Y	Z
C	-3.1330	0.0029	0.0000	C	-3.1204	-0.0328	0.0000
C	-2.1581	1.0024	0.0000	C	-2.1613	0.9704	0.0000
C	-0.8021	0.6590	0.0000	C	-0.7838	0.6618	0.0000
C	-0.4208	-0.6988	0.0000	C	-0.3783	-0.7039	0.0000
C	-1.4043	-1.6948	0.0000	C	-1.3710	-1.7092	0.0000
C	-2.7559	-1.3451	0.0000	C	-2.7206	-1.3855	0.0000
H	-4.1843	0.2730	0.0000	H	-4.1767	0.2220	0.0000
H	-2.4359	2.0509	0.0000	H	-2.4519	2.0162	0.0000
C	0.2422	1.7206	0.0000	C	0.2219	1.7365	0.0000
C	1.0198	-1.0813	0.0000	C	1.0464	-1.0768	0.0000
H	-1.1000	-2.7358	0.0000	H	-1.0492	-2.7457	0.0000
H	-3.5145	-2.1214	0.0000	H	-3.4694	-2.1730	0.0000
C	2.0500	0.0068	0.0000	C	2.0114	0.0010	0.0000
C	1.6557	1.2991	0.0000	C	1.5950	1.3231	0.0000
H	2.3828	2.1068	0.0000	H	2.3380	2.1190	0.0000
O	1.3716	-2.2611	0.0000	O	1.4077	-2.2994	0.0000
O	-0.0481	2.9204	0.0000	O	-0.1153	2.9671	0.0000
C	3.4888	-0.4125	0.0000	C	3.4761	-0.3535	0.0000
H	3.7105	-1.0283	-0.8783	H	3.7401	-0.9564	-0.8774
H	3.7105	-1.0283	0.8783	H	3.7401	-0.9564	0.8774
H	4.1484	0.4574	0.0000	H	4.0979	0.5463	0.0000
Q^{2-}				QH^{-}			
C	-3.1123	-0.0780	0.0000	C	3.1136	-0.0954	0.0000
C	-2.1672	0.9337	0.0000	C	2.1755	0.9186	0.0000
C	-0.7709	0.6676	0.0000	C	0.7787	0.6304	0.0000
C	-0.3352	-0.7138	0.0000	C	0.3509	-0.7454	0.0000
C	-1.3344	-1.7266	0.0000	C	1.3470	-1.7539	0.0000
C	-2.6870	-1.4325	0.0000	C	2.6974	-1.4508	0.0000
H	-4.1735	0.1613	0.0000	H	4.1734	0.1465	0.0000
H	-2.4765	1.9753	0.0000	H	2.4941	1.9563	0.0000
C	0.1894	1.7594	0.0000	C	-0.2109	1.6450	0.0000
C	1.0716	-1.0793	0.0000	C	-1.0662	-1.1154	0.0000
H	-0.9949	-2.7586	0.0000	H	1.0104	-2.7862	0.0000
H	-3.4223	-2.2345	0.0000	H	3.4384	-2.2460	0.0000
C	1.9834	0.0031	0.0000	C	-1.9974	-0.0407	0.0000
C	1.5384	1.3531	0.0000	C	-1.5501	1.3014	0.0000
H	2.2937	2.1421	0.0000	H	-2.2961	2.0971	0.0000
O	1.4554	-2.3419	0.0000	O	-1.4339	-2.3596	0.0000
O	-0.1900	3.0226	0.0000	O	0.2276	2.9710	0.0000

Table 6.6 (cont'd).

C	3.4667	-0.2886	0.0000	C	-3.4749	-0.3458	0.0000
H	3.7710	-0.8784	-0.8764	H	-3.7689	-0.9385	0.8770
H	3.7710	-0.8785	0.8764	H	-3.7689	-0.9385	-0.8769
H	4.0525	0.6376	0.0000	H	-4.0702	0.5736	0.0000
				H	-0.5426	3.5554	0.0000
QH_2							
C	-3.1205	-0.1349	-0.0011				
C	-2.2027	0.8947	-0.0019				
C	-0.8062	0.6293	-0.0007				
C	-0.3473	-0.7331	0.0004				
C	-1.3264	-1.7674	0.0030				
C	-2.6757	-1.4793	0.0019				
H	-4.1843	0.0827	-0.0021				
H	-2.5354	1.9266	-0.0033				
C	0.1605	1.6751	0.0002				
C	1.0579	-0.9890	-0.0009				
H	-1.0287	-2.8126	0.0078				
H	-3.3992	-2.2889	0.0041				
C	1.9806	0.0451	0.0005				
C	1.5075	1.3824	0.0015				
H	2.2337	2.1919	0.0025				
C	3.4613	-0.2450	0.0005				
H	3.7524	-0.8348	-0.8762				
H	3.7543	-0.8259	0.8826				
H	4.0395	0.6823	-0.0045				
O	-0.3227	2.9636	-0.0002				
H	0.4147	3.5900	-0.0002				
O	1.5676	-2.2702	-0.0006				
H	0.8598	-2.9266	-0.0251				

Table 6.7 Geometry Optimized Coordinates of the library of quinones: 2,3-dichloro-1,4-NQ (4).

Q				$Q^{\cdot -}$			
Atom	X	Y	Z	Atom	X	Y	Z
C	-3.7392	0.6995	0.0000	C	-3.7234	0.7043	0.0000
C	-2.5319	1.4004	0.0000	C	-2.5208	1.3972	0.0000
C	-1.3182	0.7042	0.0000	C	-1.2889	0.7094	0.0000
C	-1.3182	-0.7042	0.0000	C	-1.2889	-0.7094	0.0000
C	-2.5319	-1.4004	0.0000	C	-2.5208	-1.3972	0.0000
C	-3.7392	-0.6995	0.0000	C	-3.7234	-0.7043	0.0000
H	-4.6782	1.2435	0.0000	H	-4.6637	1.2480	0.0000
H	-2.5184	2.4844	0.0000	H	-2.5037	2.4817	0.0000
C	-0.0448	1.4677	0.0000	C	-0.0329	1.4797	0.0000
C	-0.0448	-1.4677	0.0000	C	-0.0329	-1.4797	0.0000
H	-2.5184	-2.4844	0.0000	H	-2.5037	-2.4817	0.0000
H	-4.6782	-1.2435	0.0000	H	-4.6638	-1.2480	0.0000
C	1.2323	-0.6769	0.0000	C	1.1816	-0.6950	0.0000
C	1.2323	0.6769	0.0000	C	1.1816	0.6950	0.0000
O	-0.0129	-2.6917	0.0000	O	-0.0280	-2.7427	0.0000
O	-0.0129	2.6917	-0.0001	O	-0.0280	2.7427	0.0000
Cl	2.6889	-1.6060	0.0000	Cl	2.6881	-1.5952	0.0000
Cl	2.6889	1.6060	0.0000	Cl	2.6881	1.5952	0.0000
Q^{2-}				QH^{-}			
C	-3.7129	0.7079	0.0000	C	-3.7075	-0.7543	0.0101
C	-2.5100	1.3935	0.0000	C	-2.5012	-1.4330	0.0296
C	-1.2612	0.7183	0.0000	C	-1.2640	-0.7470	0.0158
C	-1.2612	-0.7183	0.0000	C	-1.2696	0.6855	-0.0120
C	-2.5100	-1.3935	0.0000	C	-2.5235	1.3614	-0.0448
C	-3.7129	-0.7079	0.0000	C	-3.7138	0.6589	-0.0327
H	-4.6535	1.2535	0.0000	H	-4.6454	-1.3023	0.0216
H	-2.4907	2.4790	0.0000	H	-2.4728	-2.5173	0.0536
C	-0.0282	1.5029	0.0000	C	-0.0163	-1.5227	0.0144
C	-0.0282	-1.5029	0.0000	C	-0.0334	1.3949	0.0005
H	-2.4907	-2.4790	0.0000	H	-2.5457	2.4456	-0.0947
H	-4.6535	-1.2535	0.0000	H	-4.6572	1.1972	-0.0613
C	1.1404	-0.7147	0.0000	C	1.1519	0.6796	0.0023
C	1.1404	0.7147	0.0000	C	1.1697	-0.7370	-0.0043
O	-0.0462	-2.8046	0.0000	O	-0.0244	-2.8014	0.0243
O	-0.0462	2.8046	0.0000	Cl	2.6655	1.5841	0.0142
Cl	2.6909	-1.5915	0.0000	Cl	2.7076	-1.6035	-0.0274
Cl	2.6909	1.5915	0.0000	O	-0.0019	2.7816	-0.0511
				H	-0.5654	3.1479	0.6458
QH_2							
C	3.70609	0.70757	0.00000				

Table 6.7 (cont'd).

C	2.5148	1.4051	0.0000
C	1.2739	0.7146	0.0000
C	1.2739	-0.7146	0.0000
C	2.5148	-1.4051	0.0000
C	3.7061	-0.7076	0.0000
H	4.6482	1.2471	0.0000
H	2.5115	2.4889	0.0000
C	0.0308	1.4186	0.0000
C	0.0308	-1.4186	0.0000
H	2.5115	-2.4889	0.0000
H	4.6482	-1.2471	0.0000
C	-1.1562	-0.7117	0.0000
C	-1.1562	0.7117	0.0000
Cl	-2.6648	-1.6047	0.0000
Cl	-2.6648	1.6047	0.0000
O	0.0912	-2.7795	0.0000
H	-0.8052	-3.1518	0.0000
O	0.0912	2.7795	0.0000
H	-0.8052	3.1518	0.0000

Table 6.8 Geometry Optimized Coordinates of the library of quinones: 2,3 -dibromo-1,4-NQ (5).

Q				Q^{-}			
Atom	X	Y	Z	Atom	X	Y	Z
C	-4.4386	0.6995	-0.0001	C	-4.4213	0.7042	-0.0001
C	-3.2310	1.3994	0.0001	C	-3.2184	1.3962	0.0001
C	-2.0172	0.7037	0.0000	C	-1.9867	0.7088	0.0000
C	-2.0172	-0.7037	-0.0002	C	-1.9867	-0.7088	-0.0002
C	-3.2310	-1.3994	-0.0004	C	-3.2184	-1.3962	-0.0004
C	-4.4386	-0.6995	-0.0003	C	-4.4213	-0.7042	-0.0004
H	-5.3772	1.2440	0.0000	H	-5.3614	1.2485	0.0000
H	-3.2168	2.4834	0.0003	H	-3.2005	2.4807	0.0003
C	-0.7450	1.4671	0.0002	C	-0.7316	1.4790	0.0002
C	-0.7450	-1.4671	-0.0003	C	-0.7316	-1.4790	-0.0003
H	-3.2168	-2.4834	-0.0006	H	-3.2005	-2.4807	-0.0006
H	-5.3772	-1.2440	-0.0005	H	-5.3614	-1.2485	-0.0005
C	0.5299	-0.6756	-0.0001	C	0.4815	-0.6936	-0.0001
C	0.5299	0.6756	0.0002	C	0.4815	0.6936	0.0002
O	-0.7185	-2.6915	-0.0005	O	-0.7310	-2.7414	-0.0005
O	-0.7185	2.6915	0.0005	O	-0.7310	2.7414	0.0005
Br	2.1072	-1.6968	-0.0002	Br	2.1048	-1.6887	-0.0002
Br	2.1072	1.6968	0.0004	Br	2.1048	1.6887	0.0004
	-4.4386	0.6995	-0.0001	C	-4.4213	0.7042	-0.0001
Q^{2-}				QH^{-}			
C	-4.4106	-0.7077	0.0001	C	4.4035	-0.7430	0.0000
C	-3.2073	-1.3924	-0.0001	C	3.2005	-1.4273	0.0000
C	-1.9591	-0.7175	0.0000	C	1.9595	-0.7478	0.0000
C	-1.9591	0.7175	0.0002	C	1.9653	0.6832	0.0000
C	-3.2073	1.3924	0.0004	C	3.2126	1.3684	0.0000
C	-4.4106	0.7077	0.0003	C	4.4059	0.6713	0.0000
H	-5.3508	-1.2539	0.0001	H	5.3433	-1.2882	0.0000
H	-3.1870	-2.4778	-0.0003	H	3.1771	-2.5120	0.0000
C	-0.7267	-1.5036	-0.0002	C	0.7153	-1.5289	0.0000
C	-0.7267	1.5036	0.0003	C	0.7307	1.3926	0.0000
H	-3.1870	2.4778	0.0006	H	3.2132	2.4529	0.0000
H	-5.3508	1.2539	0.0005	H	5.3479	1.2130	0.0000
C	0.4399	0.7136	0.0001	C	-0.4478	0.6718	0.0000
C	0.4399	-0.7136	-0.0002	C	-0.4679	-0.7445	0.0000
O	-0.7498	-2.8038	-0.0005	O	0.7318	-2.8093	0.0000
Br	2.1062	1.6820	0.0002	Br	-2.0782	1.6815	0.0000
Br	2.1062	-1.6820	-0.0004	Br	-2.1287	-1.6889	0.0000
O	-0.7498	2.8038	0.0006	O	0.7936	2.7709	0.0000
				H	-0.1104	3.1255	0.0000
QH_2							

Table 6.8 (cont'd).

C	4.3917	-0.7074	0.0000
C	3.2000	-1.4041	0.0000
C	1.9593	-0.7141	0.0000
C	1.9593	0.7141	0.0000
C	3.2000	1.4041	0.0000
C	4.3917	0.7074	0.0000
H	5.3335	-1.2475	0.0000
H	3.1966	-2.4878	0.0000
C	0.7167	-1.4188	0.0000
C	0.7167	1.4188	0.0000
H	3.1966	2.4878	0.0000
H	5.3335	1.2475	0.0000
C	-0.4687	0.7105	0.0000
C	-0.4687	-0.7105	0.0000
Br	-2.0992	1.6878	0.0000
Br	-2.0992	-1.6878	0.0000
O	0.7828	2.7791	0.0000
H	-0.1157	3.1503	0.0000
O	0.7828	-2.7791	0.0000
H	-0.1157	-3.1503	0.0000

Table 6.9 Geometry Optimized Coordinates of the library of quinones: 2-methoxy-1,4-NQ (6).

Q				$Q^{\cdot-}$			
Atom	X	Y	Z	Atom	X	Y	Z
C	3.4666	0.2133	0.0003	C	-3.3995	-0.4981	0.0000
C	2.4143	1.1322	0.0003	C	-2.6241	0.6541	0.0000
C	1.0905	0.6843	0.0002	C	-1.2161	0.5848	0.0000
C	0.8225	-0.7001	0.0000	C	-0.5799	-0.6889	0.0000
C	1.8816	-1.6164	0.0000	C	-1.3875	-1.8496	0.0000
C	3.2006	-1.1606	0.0001	C	-2.7726	-1.7609	0.0000
H	4.4926	0.5678	0.0003	H	-4.4837	-0.4277	0.0000
H	2.6075	2.1993	0.0001	H	-3.0857	1.6365	0.0000
C	-0.0342	1.6691	-0.0001	C	-0.4085	1.8183	0.0000
C	-0.5753	-1.2019	-0.0001	C	0.8853	-0.8343	0.0000
H	1.6604	-2.6781	-0.0002	H	-0.8950	-2.8166	0.0000
H	4.0189	-1.8736	0.0000	H	-3.3743	-2.6659	0.0000
C	-1.6775	-0.1715	-0.0001	C	1.6375	0.4062	0.0000
C	-1.4036	1.1597	-0.0001	C	1.0065	1.6450	0.0000
H	-2.1856	1.9094	-0.0001	H	1.6265	2.5377	0.0000
O	-0.8482	-2.3972	-0.0003	O	1.4321	-1.9860	0.0000
O	0.1844	2.8869	-0.0004	O	-0.9560	2.9702	0.0000
O	-2.8898	-0.7298	0.0000	O	3.0050	0.4794	0.0000
C	-4.0444	0.1295	0.0004	C	3.8675	-0.6692	0.0000
H	-4.0540	0.7546	0.8981	H	4.8763	-0.2503	0.0000
H	-4.0543	0.7550	-0.8970	H	3.7174	-1.2831	-0.8898
H	-4.9033	-0.5392	0.0005	H	3.7174	-1.2831	0.8898
Q^{2-}				QH^{-}			
C	-3.3947	-0.5205	0.0000	C	-3.4706	0.1375	0.0000
C	-2.6240	0.6310	0.0000	C	-2.4530	1.0776	0.0000
C	-1.2063	0.5941	0.0000	C	-1.0888	0.7043	0.0000
C	-0.5442	-0.6942	0.0000	C	-0.7592	-0.6995	0.0000
C	-1.3686	-1.8568	0.0000	C	-1.8250	-1.6500	0.0000
C	-2.7511	-1.7852	0.0000	C	-3.1449	-1.2419	0.0000
H	-4.4805	-0.4576	0.0000	H	-4.5108	0.4515	0.0000
H	-3.0949	1.6103	0.0000	H	-2.6794	2.1398	0.0000
C	-0.4349	1.8280	0.0000	C	-0.0396	1.7293	0.0000
C	0.9028	-0.8529	0.0000	C	0.5967	-1.0931	0.0000
H	-0.8695	-2.8215	0.0000	H	-1.5812	-2.7078	0.0000
H	-3.3441	-2.6976	0.0000	H	-3.9386	-1.9851	0.0000
C	1.6039	0.3761	0.0000	C	1.5945	-0.1258	0.0000
C	0.9586	1.6404	0.0000	C	1.2964	1.2506	0.0000
H	1.6001	2.5210	0.0000	H	2.0953	1.9838	0.0000
O	1.4591	-2.0501	0.0000	O	-0.3290	2.9893	0.0000
O	-1.0084	3.0118	0.0000	O	2.8772	-0.6436	0.0000

Table 6.9 (cont'd).

O	2.9984	0.5201	0.0000	C	3.9869	0.2546	0.0000
C	3.8884	-0.5953	0.0001	H	4.8784	-0.3734	0.0000
H	4.8910	-0.1549	0.0000	H	3.9845	0.8869	0.8948
H	3.7626	-1.2211	-0.8869	H	3.9845	0.8868	-0.8948
H	3.7625	-1.2210	0.8870	O	0.9170	-2.4498	0.0000
				H	1.8845	-2.5119	0.0000

QH_2

C	-3.3959	-0.3623	-0.1829
C	-2.5665	0.7385	-0.1263
C	-1.1591	0.5885	-0.0015
C	-0.5947	-0.7322	0.0661
C	-1.4837	-1.8430	0.0061
C	-2.8466	-1.6652	-0.1157
H	-4.4694	-0.2319	-0.2788
H	-2.9791	1.7399	-0.1764
C	-0.2870	1.7152	0.0617
C	0.8200	-0.8835	0.1968
H	-1.1044	-2.8603	0.0540
H	-3.4999	-2.5311	-0.1606
C	1.6305	0.2397	0.2421
C	1.0743	1.5391	0.1797
H	1.7504	2.3879	0.2284
O	2.9948	0.1316	0.4156
C	3.7265	-0.3144	-0.7424
H	4.7770	-0.3347	-0.4482
H	3.5911	0.3885	-1.5723
H	3.4075	-1.3157	-1.0450
O	1.4340	-2.1092	0.2936
H	0.7888	-2.8238	0.2187
O	-0.8752	2.9545	-0.0037
H	-0.1975	3.6439	0.0336

Table 6.10 Geometry Optimized Coordinates of the library of quinones: 5,8-hydroxy-1,4-NQ (7).

Q				$Q^{\cdot-}$			
Atom	X	Y	Z	Atom	X	Y	Z
C	-0.68792	-2.45251	0.00000	C	0.69937	-2.44127	0.00000
C	-1.41068	-1.23134	0.00000	C	1.41099	-1.23792	0.00000
C	-0.71383	-0.01100	0.00000	C	0.71448	-0.00126	0.00000
C	0.71383	-0.01100	0.00000	C	-0.71448	-0.00126	0.00000
C	1.41068	-1.23134	0.00000	C	-1.41099	-1.23792	0.00000
C	0.68792	-2.45251	0.00000	C	-0.69937	-2.44127	0.00000
H	-1.24489	-3.38345	0.00000	H	1.24971	-3.37730	0.00000
C	-1.44722	1.25027	0.00000	C	1.45125	1.25559	0.00000
C	1.44722	1.25027	0.00000	C	-1.45125	1.25559	0.00000
H	1.24489	-3.38345	0.00000	H	-1.24971	-3.37730	0.00000
C	0.67402	2.50407	0.00000	C	-0.69109	2.46673	0.00000
C	-0.67402	2.50407	0.00000	C	0.69108	2.46673	0.00000
H	1.24728	3.42590	0.00000	H	-1.24395	3.40240	0.00000
H	-1.24728	3.42590	0.00000	H	1.24394	3.40240	0.00000
O	2.70073	1.28512	0.00000	O	-2.74490	1.26235	0.00001
O	-2.70073	1.28512	0.00000	O	2.74490	1.26235	0.00000
O	2.75154	-1.29120	0.00000	O	-2.77025	-1.26128	-0.00001
H	3.07937	-0.35074	0.00000	H	-3.04049	-0.28490	-0.00002
O	-2.75154	-1.29120	0.00000	O	2.77025	-1.26128	0.00000
H	-3.07937	-0.35074	0.00000	H	3.04049	-0.28490	0.00001
Q^{2-}				QH^{-}			
C	0.7107	-2.4334	0.0000	C	-0.7804	-2.4337	0.0000
C	1.4164	-1.2418	0.0000	C	-1.4541	-1.2242	0.0000
C	0.7171	0.0123	0.0000	C	-0.7231	0.0123	0.0000
C	-0.7171	0.0123	0.0000	C	0.7237	-0.0023	0.0000
C	-1.4164	-1.2418	0.0000	C	1.3707	-1.2827	0.0000
C	-0.7107	-2.4334	0.0000	C	0.6302	-2.4490	0.0000
H	1.2559	-3.3741	0.0000	H	-1.3419	-3.3629	0.0000
C	1.4578	1.2552	0.0000	C	-1.4708	1.2589	0.0000
C	-1.4578	1.2552	0.0000	C	1.3962	1.2607	0.0000
H	-1.2559	-3.3741	0.0000	H	1.1510	-3.4046	0.0000
C	-0.7095	2.4365	0.0000	C	0.6690	2.4370	0.0000
C	0.7095	2.4365	0.0000	C	-0.7389	2.4509	0.0000
H	-1.2441	3.3855	0.0000	H	1.2070	3.3841	0.0000
H	1.2441	3.3855	0.0000	H	-1.2737	3.3967	0.0000
O	-2.7989	1.2281	0.0000	O	-2.7953	1.2381	0.0000
O	2.7989	1.2281	0.0000	O	2.7555	-1.3378	0.0000
O	-2.7853	-1.2271	0.0000	H	3.0200	-2.2683	0.0001
H	-3.0059	-0.1929	0.0000	O	-2.8123	-1.1949	0.0000
O	2.7853	-1.2271	0.0000	H	-3.0304	-0.1613	0.0000

Table 6.10 (cont'd).

H	3.0059	-0.1930	0.0000	O	2.7863	1.2975	0.0000
				H	3.0590	2.2255	0.0000
QH_2							
C	-0.7068	2.4359	0.0000				
C	-1.3934	1.2479	0.0000				
C	-0.7254	-0.0195	0.0000				
C	0.7254	-0.0195	0.0000				
C	1.3934	1.2479	0.0000				
C	0.7068	2.4359	0.0000				
H	-1.2451	3.3803	0.0000				
C	-1.4177	-1.2703	0.0000				
C	1.4176	-1.2703	0.0000				
H	1.2451	3.3803	0.0000				
C	0.6994	-2.4539	0.0000				
C	-0.6995	-2.4539	0.0000				
H	1.2523	-3.3873	0.0000				
H	-1.2524	-3.3873	0.0000				
O	2.7805	1.2296	0.0000				
H	3.1308	2.1293	0.0001				
O	-2.7804	1.2296	0.0000				
H	-3.1308	2.1293	0.0000				
O	2.7799	-1.3868	0.0000				
H	3.1863	-0.5056	0.0000				
O	-2.7799	-1.3868	0.0000				
H	-3.1863	-0.5056	0.0000				

Table 6.11 Geometry Optimized Coordinates of the library of quinones: 5-hydroxy-1,4-NQ (8).

Q				$Q^{\cdot-}$			
Atom	X	Y	Z	Atom	X	Y	Z
C	-1.4099	-2.3266	0.0000	C	-1.1942	-2.4362	0.0000
C	-0.0184	-2.1287	0.0000	C	0.1626	-2.1262	0.0000
C	0.4936	-0.8364	0.0000	C	0.5847	-0.7829	0.0000
C	-0.3804	0.2829	0.0000	C	-0.3872	0.2601	0.0000
C	-1.7787	0.0658	0.0000	C	-1.7707	-0.0851	0.0000
C	-2.2834	-1.2489	0.0000	C	-2.1655	-1.4237	0.0000
H	-1.8082	-3.3362	0.0000	H	-1.5117	-3.4755	0.0000
H	0.6629	-2.9717	0.0000	H	0.9147	-2.9073	0.0000
C	1.9692	-0.6205	0.0000	C	2.0235	-0.4528	0.0000
C	0.1541	1.6450	0.0000	C	0.0139	1.6625	0.0000
H	-3.3586	-1.3931	0.0000	H	-3.2251	-1.6610	0.0000
C	1.6192	1.8270	0.0000	C	1.4133	1.9470	0.0000
C	2.4605	0.7777	0.0000	C	2.3637	0.9443	0.0000
H	1.9752	2.8527	0.0000	H	1.7102	2.9928	0.0000
H	3.5384	0.9067	0.0000	H	3.4223	1.1924	0.0000
O	-2.6569	1.0842	0.0000	O	-2.7121	0.8901	0.0000
H	-2.1286	1.9244	0.0000	H	-2.1822	1.7578	0.0000
O	-0.5932	2.6468	0.0000	O	-0.8756	2.6039	0.0000
O	2.7705	-1.5568	0.0000	O	2.9137	-1.3616	0.0000
Q^{2-}				QH^{-}			
C	2.0421	1.5967	0.0000	C	0.9011	2.5814	0.0076
C	1.7980	0.2109	0.0000	C	-0.4007	2.1162	0.0092
C	0.4094	-0.2343	0.0000	C	-0.6832	0.7279	0.0064
C	-0.6609	0.7248	0.0000	C	0.4058	-0.2159	0.0079
C	-0.3422	2.1117	0.0000	C	1.7441	0.3069	-0.0058
C	0.9799	2.5274	0.0000	C	1.9802	1.6700	-0.0024
H	3.0754	1.9378	0.0000	H	1.1054	3.6488	0.0104
C	0.1046	-1.6327	0.0000	H	-1.2429	2.7996	0.0106
C	-2.0623	0.2944	0.0000	C	-2.0851	0.2807	-0.0066
H	-1.1601	2.8246	0.0000	C	0.0974	-1.6064	0.0151
H	1.2118	3.5919	0.0000	H	3.0084	2.0203	-0.0114
C	-2.2749	-1.1006	0.0000	C	-1.2139	-2.0345	0.0139
C	-1.2160	-2.0429	0.0000	C	-2.2851	-1.1210	-0.0110
H	-3.3032	-1.4598	0.0000	H	-1.4188	-3.1036	0.0318
H	-1.4370	-3.1092	0.0000	H	-3.3061	-1.4949	-0.0224
O	-3.0357	1.1682	0.0000	O	2.8377	-0.5246	-0.0260
O	1.1327	-2.5583	0.0000	H	2.5111	-1.4489	-0.0319
O	2.7751	-0.6788	0.0000	O	1.1647	-2.5325	0.0824
H	1.9708	-1.9667	0.0000	O	-3.0548	1.1342	-0.0151
				H	0.9990	-3.2694	-0.5217

Table 6.11 (cont'd).

QH_2			
C	0.8362	-2.5958	0.0000
C	-0.4501	-2.0947	0.0000
C	-0.6680	-0.6922	0.0000
C	0.4522	0.2115	0.0000
C	1.7705	-0.3562	0.0000
C	1.9474	-1.7297	0.0000
H	1.0014	-3.6692	0.0000
H	-1.3047	-2.7600	0.0000
C	-1.9912	-0.1497	0.0000
C	0.1874	1.6166	0.0000
H	2.9595	-2.1217	0.0000
C	-1.1000	2.1013	0.0000
C	-2.1997	1.2112	0.0000
H	-1.2783	3.1730	0.0000
H	-3.2096	1.6119	0.0000
O	2.9006	0.4117	0.0000
H	2.6528	1.3552	0.0000
O	1.2852	2.4601	0.0000
H	1.0176	3.3898	0.0000
O	-3.0204	-1.0611	0.0000
H	-3.8698	-0.5977	0.0000

Table 6.12 Geometry Optimized Coordinates of the library of quinones: 1,2-NQ-4-sulfonate (9).

Q				$Q^{\cdot-}$			
Atom	X	Y	Z	Atom	X	Y	Z
C	0.3319	-1.7232	0.0000	C	0.2708	1.7034	-0.0155
C	0.6466	-0.4069	0.0000	C	0.6453	0.3850	-0.0065
C	-0.3679	0.6647	0.0000	C	-0.3416	-0.6763	-0.0059
C	-1.7460	0.3152	0.0000	C	-1.7245	-0.3073	0.0066
C	-2.1669	-1.1030	0.0000	C	-2.1569	1.0999	0.0174
C	-1.0511	-2.1826	0.0000	C	-1.1043	2.1430	-0.0188
H	1.0095	2.3234	0.0000	H	1.0282	-2.3490	-0.0290
H	1.1106	-2.4774	0.0000	H	1.0335	2.4751	-0.0205
C	-0.0304	2.0263	0.0000	C	-0.0135	-2.0539	-0.0186
C	-2.7304	1.3107	0.0000	C	-2.7071	-1.3224	0.0053
C	-2.3751	2.6598	0.0000	C	-2.3603	-2.6649	-0.0097
C	-1.0239	3.0109	0.0000	C	-1.0005	-3.0301	-0.0216
H	-3.7728	1.0108	0.0000	H	-3.7487	-1.0184	0.0145
H	-3.1430	3.4264	0.0000	H	-3.1320	-3.4296	-0.0134
H	-0.7335	4.0568	0.0000	H	-0.7181	-4.0791	-0.0341
O	-3.3368	-1.4613	0.0000	O	-3.3815	1.4100	0.0520
O	-1.3618	-3.3694	0.0000	O	-1.3976	3.3811	-0.0462
S	2.4310	0.0157	0.0000	S	2.4220	0.0125	0.0086
O	3.1500	-1.2888	0.0000	O	3.1234	1.3348	0.0143
O	2.6312	0.8084	1.2495	O	2.6989	-0.7801	-1.2354
O	2.6312	0.8084	-1.2495	O	2.6745	-0.7780	1.2590
Q^{2-}				QH^{-}			
C	0.2158	1.6996	-0.0238	C	-0.1990	-1.7015	0.0000
C	0.6455	0.3659	-0.0170	C	-0.6520	-0.3924	0.0000
C	-0.3090	-0.6845	-0.0122	C	0.2562	0.7121	0.0000
C	-1.7112	-0.3042	0.0083	C	1.6730	0.4108	0.0000
C	-2.1619	1.0765	0.0212	C	2.0878	-0.9333	0.0000
C	-1.1432	2.1201	-0.0239	C	1.1935	-2.0275	0.0000
H	1.0537	-2.3696	-0.0458	H	-1.1891	2.3234	0.0000
H	0.9692	2.4824	-0.0325	H	-0.9184	-2.5134	0.0000
C	0.0098	-2.0769	-0.0275	C	-0.1332	2.0816	0.0000
C	-2.6848	-1.3474	0.0100	C	2.6107	1.4903	0.0000
C	-2.3405	-2.6840	-0.0077	C	2.1865	2.8009	0.0000
C	-0.9677	-3.0526	-0.0268	C	0.7990	3.1011	0.0000
H	-3.7285	-1.0476	0.0244	H	3.6704	1.2553	0.0000
H	-3.1118	-3.4510	-0.0098	H	2.9147	3.6078	0.0000
H	-0.6846	-4.1026	-0.0430	H	0.4686	4.1361	0.0000
O	-3.4285	1.3634	0.0598	O	3.4236	-1.2665	0.0000
O	-1.4549	3.3946	-0.0516	O	1.6794	-3.2383	0.0000
S	2.4125	0.0414	0.0110	S	-2.4475	-0.1308	0.0000

Table 6.12 (cont'd).

O	3.0990	1.3801	0.0043	O	-3.0705	-1.4943	0.0000
O	2.7607	-0.7640	-1.2171	O	-2.7728	0.6421	-1.2467
O	2.7218	-0.7303	1.2708	O	-2.7728	0.6422	1.2467
				H	3.3842	-2.2508	0.0000
QH_2							
C	-0.1982	-1.6661	0.0000				
C	-0.6665	-0.3674	0.0000				
C	0.2413	0.7384	0.0000				
C	1.6529	0.4595	0.0000				
C	2.0978	-0.8910	0.0000				
C	1.1846	-1.9302	0.0000				
H	-1.2244	2.3338	0.0000				
H	-0.9077	-2.4875	0.0000				
C	-0.1666	2.1035	0.0000				
C	2.5836	1.5358	0.0000				
C	2.1464	2.8428	0.0000				
C	0.7586	3.1266	0.0000				
H	3.6440	1.3090	0.0000				
H	2.8656	3.6565	0.0000				
H	0.4197	4.1584	0.0000				
O	3.4419	-1.1388	0.0000				
O	1.7167	-3.1993	0.0000				
S	-2.4670	-0.1313	0.0000				
O	-3.0504	-1.5089	0.0000				
O	-2.7871	0.6353	-1.2468				
O	-2.7871	0.6352	1.2468				
H	3.5807	-2.0994	0.0000				
H	1.0202	-3.8703	0.0000				

Table 6.13 Geometry Optimized Coordinates of the library of quinones: 1,4-BQ (10).

Q				$Q^{\cdot-}$			
Atom	X	Y	Z	Atom	X	Y	Z
C	0.0000	1.2713	0.6723	C	0.0000	1.2277	0.6869
C	0.0000	0.0000	1.4381	C	0.0000	0.0000	1.4560
C	0.0000	-1.2713	0.6723	C	0.0000	-1.2277	0.6869
C	0.0000	-1.2713	-0.6723	C	0.0000	-1.2277	-0.6869
C	0.0000	0.0000	-1.4381	C	0.0000	0.0000	-1.4560
C	0.0000	1.2713	-0.6723	C	0.0000	1.2277	-0.6869
H	0.0000	2.1881	1.2538	H	0.0000	2.1635	1.2417
O	0.0000	0.0000	-2.6698	O	0.0000	0.0000	-2.7347
O	0.0000	0.0000	2.6698	O	0.0000	0.0000	2.7347
H	0.0000	2.1881	-1.2538	H	0.0000	2.1635	-1.2417
H	0.0000	-2.1881	-1.2538	H	0.0000	-2.1635	-1.2417
H	0.0000	-2.1881	1.2538	H	0.0000	-2.1635	1.2417
Q^{2-}				QH^{-}			
C	0.0000	1.1945	0.7023	C	-0.6337	1.2178	0.0000
C	0.0000	0.0000	1.4818	C	-1.3558	0.0212	0.0000
C	0.0000	-1.1945	0.7023	C	-0.6594	-1.1905	0.0000
C	0.0000	-1.1945	-0.7023	C	0.7401	-1.2070	0.0000
C	0.0000	0.0000	-1.4818	C	1.5268	-0.0101	0.0000
C	0.0000	1.1945	-0.7023	C	0.7637	1.2038	0.0000
H	0.0000	2.1487	1.2324	H	-1.1726	2.1630	0.0000
O	0.0000	0.0000	-2.8068	O	2.8306	-0.0226	0.0000
O	0.0000	0.0000	2.8068	H	1.3058	2.1478	0.0000
H	0.0000	2.1487	-1.2324	H	1.2608	-2.1628	0.0000
H	0.0000	-2.1487	-1.2324	H	-1.2091	-2.1313	0.0000
H	0.0000	-2.1487	1.2324	O	-2.7504	0.0942	0.0000
				H	-3.1168	-0.8005	0.0000
QH_2							
C	0.0000	0.6974	1.2206				
C	0.0000	1.4008	0.0106				
C	0.0000	0.6997	-1.1980				
C	0.0000	-0.6997	-1.1980				
C	0.0000	-1.4008	0.0106				
C	0.0000	-0.6974	1.2206				
H	0.0000	1.2466	2.1569				
H	0.0000	-1.2466	2.1569				
H	0.0000	-1.2360	-2.1432				
H	0.0000	1.2360	-2.1432				
O	0.0000	2.7770	0.0754				
H	0.0000	3.1528	-0.8162				
O	0.0000	-2.7770	0.0754				

Table 6.13 (cont'd).

H	0.0000	-3.1528	-0.8162

Table 6.14 Geometry Optimized Coordinates of the library of quinones: 2,6-dichloro-1,4-BQ (11).

Q				$Q^{\cdot-}$			
Atom	X	Y	Z	Atom	X	Y	Z
C	1.2725	1.2633	0.0000	C	1.2306	1.2671	0.0000
C	0.0000	2.0191	0.0000	C	0.0000	2.0297	0.0000
C	-1.2725	1.2633	0.0000	C	-1.2306	1.2671	0.0000
C	-1.2713	-0.0801	0.0000	C	-1.2145	-0.1014	0.0000
C	0.0000	-0.8794	0.0000	C	0.0000	-0.9085	0.0000
C	1.2713	-0.0801	0.0000	C	1.2145	-0.1014	0.0000
H	2.1881	1.8439	0.0000	H	2.1671	1.8152	0.0000
H	-2.1881	1.8439	0.0000	H	-2.1671	1.8152	0.0000
O	0.0000	3.2488	0.0000	O	0.0000	3.3015	0.0000
O	0.0000	-2.0968	0.0000	O	0.0000	-2.1694	0.0000
Cl	-2.7418	-0.9982	0.0000	Cl	-2.7428	-0.9824	0.0000
Cl	2.7418	-0.9982	0.0000	Cl	2.7428	-0.9824	0.0000
	1.2725	1.2633	0.0000	C	1.2306	1.2671	0.0000
Q^{2-}				QH^{-}			
C	1.1981	1.2747	0.0000	C	1.2136	1.3083	0.0021
C	0.0000	2.0502	0.0000	C	0.0000	2.0785	0.0041
C	-1.1981	1.2747	0.0000	C	-1.2136	1.3083	0.0021
C	-1.1696	-0.1214	0.0000	C	-1.1876	-0.0789	-0.0038
C	0.0000	-0.9450	0.0000	C	0.0000	-0.8288	-0.0018
C	1.1696	-0.1214	0.0000	C	1.1876	-0.0789	-0.0038
H	2.1542	1.7918	0.0000	H	2.1633	1.8334	0.0043
H	-2.1542	1.7918	0.0000	H	-2.1633	1.8334	0.0043
O	0.0000	3.3633	0.0000	O	0.0000	3.3663	0.0084
O	0.0000	-2.2456	0.0000	Cl	-2.7283	-0.9577	-0.0043
Cl	-2.7496	-0.9705	0.0000	Cl	2.7283	-0.9577	-0.0043
Cl	2.7496	-0.9705	0.0000	O	0.0000	-2.2104	-0.0900
				H	0.0000	-2.6039	0.7952
QH_2							
C	1.2705	1.2062	-0.0001				
C	0.0959	1.9638	-0.0001				
C	-1.1485	1.3285	0.0000				
C	-1.1972	-0.0617	0.0000				
C	-0.0410	-0.8582	0.0001				
C	1.1887	-0.1855	-0.0001				
H	2.2429	1.6867	-0.0001				
H	-2.0600	1.9143	-0.0001				
Cl	-2.7584	-0.8738	-0.0001				
Cl	2.6682	-1.1273	0.0000				
O	-0.0586	-2.2179	0.0001				
H	-0.9769	-2.5334	0.0005				

Table 6.14 (cont'd).

O	0.0979	3.3330	0.0002
H	1.0043	3.6726	0.0002

Table 6.15 Geometry Optimized Coordinates of the library of quinones: 2,5-dibromo-1,4-BQ (12).

Q				$Q^{\cdot-}$			
Atom	X	Y	Z	Atom	X	Y	Z
C	-1.24436	0.71890	0.00000	C	0.08571	1.40131	0.00000
C	-1.23053	-0.76011	0.00000	C	-1.23186	0.79788	0.00000
C	0.10794	-1.43425	0.00000	C	-1.23186	-0.65571	-0.00001
C	1.24436	-0.71890	0.00000	C	-0.08571	-1.40131	0.00000
C	1.23053	0.76011	0.00000	C	1.23186	-0.79788	0.00000
C	-0.10794	1.43425	0.00000	C	1.23186	0.65571	-0.00001
H	-2.22575	1.17960	0.00000	H	0.12108	2.48564	0.00000
H	2.22575	-1.17960	0.00000	H	-0.12108	-2.48564	0.00000
O	2.27783	1.39439	0.00000	O	2.28533	-1.50016	0.00000
O	-2.27783	-1.39439	0.00000	O	-2.28533	1.50016	0.00000
Br	-0.10794	3.31290	0.00000	Br	2.92891	1.52821	0.00000
Br	0.10794	-3.31290	0.00000	Br	-2.92891	-1.52821	0.00000

Q^{2-}				QH^{-}			
C	1.1854	0.7100	0.0002	C	0.6188	1.2199	0.0000
C	-0.0061	1.4995	0.0000	C	-0.7754	1.1435	0.0000
C	-1.1766	0.6847	0.0001	C	-1.3500	-0.1314	0.0000
C	-1.1854	-0.7100	0.0002	C	-0.5853	-1.2909	0.0000
C	0.0061	-1.4995	0.0000	C	0.8500	-1.2691	0.0000
C	1.1766	-0.6847	0.0001	C	1.3898	0.0622	0.0000
H	2.1322	1.2429	0.0002	H	1.0876	2.1983	0.0000
H	-2.1322	-1.2429	0.0002	H	-1.0706	-2.2615	0.0000
O	-0.0061	-2.8046	-0.0001	O	1.5582	-2.3425	0.0000
O	0.0061	2.8046	-0.0001	Br	3.2975	0.2504	0.0000
Br	2.8898	-1.5872	0.0000	Br	-3.2678	-0.2587	0.0000
Br	-2.8898	1.5872	0.0000	O	-1.4959	2.3222	0.0000
				H	-2.4434	2.1106	0.0000

QH_2			
C	0.5895	1.2668	0.0000
C	-0.8028	1.1591	0.0000
C	-1.3766	-0.1202	0.0000
C	-0.5895	-1.2668	0.0000
C	0.8028	-1.1591	0.0000
C	1.3766	0.1202	0.0000
H	1.0412	2.2519	0.0000
H	-1.0412	-2.2519	0.0000
Br	3.2732	0.2730	0.0000
Br	-3.2732	-0.2730	0.0000
O	-1.5276	2.3149	0.0000
H	-2.4769	2.1059	0.0000

Table 6.15 (cont'd).

O	1.52759	-2.31490	0.00000
H	2.47686	-2.10589	0.00000

Table 6.16 Geometry Optimized Coordinates of the library of quinones: 2-methyl-1,4-BQ (13).

Q				$Q^{\cdot-}$			
Atom	X	Y	Z	Atom	X	Y	Z
C	0.7987	-0.7135	-0.0001	C	-0.7728	0.6938	-0.0001
C	1.0249	0.7692	0.0001	C	-1.0718	-0.7357	0.0002
C	-0.1540	1.6704	0.0000	C	0.0585	-1.6380	-0.0004
C	-1.4055	1.1833	-0.0004	C	1.3575	-1.1913	-0.0005
C	-1.6439	-0.2813	0.0000	C	1.6692	0.2211	0.0003
C	-0.4700	-1.1772	-0.0007	C	0.5361	1.1218	-0.0001
O	-2.7921	-0.7332	0.0007	O	2.8749	0.6507	0.0004
O	2.1642	1.2351	0.0002	O	-2.2747	-1.1687	0.0006
H	-0.6855	-2.2422	-0.0012	H	0.7590	2.1877	-0.0002
H	0.0576	2.7353	0.0002	H	-0.1627	-2.7033	-0.0007
H	-2.2827	1.8230	-0.0007	H	2.1899	-1.8919	-0.0009
C	2.0081	-1.5979	0.0002	C	-1.9248	1.6644	-0.0003
H	1.7205	-2.6510	-0.0012	H	-1.5680	2.6984	-0.0009
H	2.6321	-1.3983	-0.8776	H	-2.5665	1.5183	-0.8774
H	2.6303	-1.4001	0.8797	H	-2.5662	1.5192	0.8772
Q^{2-}				QH^{-}			
C	-0.7569	0.6790	0.0000	C	-0.7892	0.6914	-0.0001
C	-1.1215	-0.7087	0.0000	C	-1.1746	-0.6977	0.0000
C	-0.0230	-1.6130	0.0000	C	-0.0965	-1.6362	-0.0001
C	1.3210	-1.2007	0.0000	C	1.2492	-1.2525	0.0000
C	1.6977	0.1716	0.0000	C	1.5851	0.1007	0.0000
C	0.5927	1.0748	0.0000	C	0.5637	1.0568	0.0000
O	2.9599	0.5795	0.0000	O	-2.4262	-1.0681	0.0001
O	-2.3851	-1.1119	0.0000	H	0.8251	2.1157	-0.0001
H	0.8195	2.1436	-0.0001	H	-0.3479	-2.6954	-0.0002
H	-0.2492	-2.6811	-0.0001	H	2.0381	-2.0018	-0.0001
H	2.1123	-1.9529	0.0000	C	-1.8649	1.7481	-0.0001
C	-1.8495	1.7229	0.0000	H	-1.4347	2.7552	-0.0010
H	-1.4307	2.7357	-0.0006	H	-2.5206	1.6564	-0.8760
H	-2.5066	1.6287	-0.8757	H	-2.5194	1.6577	0.8769
H	-2.5059	1.6295	0.8764	O	2.9390	0.4479	0.0000
				H	3.02051	1.41115	0.00033
QH_2							
C	-0.7298	0.7407	-0.0001				
C	-1.0818	-0.6204	0.0000				
C	-0.0976	-1.6119	-0.0001				
C	1.2565	-1.2668	-0.0001				
C	1.6210	0.0802	-0.0001				
C	0.6320	1.0699	-0.0001				
H	0.9197	2.1190	0.0000				

Table 6.16 (cont'd).

H	-0.3846	-2.6605	-0.0001
H	2.0229	-2.0352	0.0000
C	-1.7954	1.8081	0.0000
H	-1.3480	2.8052	-0.0004
H	-2.4443	1.7225	-0.8790
H	-2.4437	1.7230	0.8796
O	2.9674	0.3787	0.0001
H	3.0958	1.3376	0.0003
O	-2.4290	-0.9201	-0.0001
H	-2.5540	-1.8793	0.0014

Table 6.17 Geometry Optimized Coordinates of the library of quinones: 2,6-dimethyl-1,4-BQ (14).

Q				$Q^{\cdot-}$			
Atom	X	Y	Z	Atom	X	Y	Z
C	0.0000	-1.0264	-1.2678	C	1.0331	-1.2262	0.0000
C	0.0000	-1.7831	0.0000	C	1.7973	0.0000	0.0000
C	0.0000	-1.0264	1.2678	C	1.0331	1.2262	0.0000
C	0.0000	0.3223	1.2962	C	-0.3437	1.2478	0.0000
C	0.0000	1.0772	0.0000	C	-1.0991	0.0000	0.0000
C	0.0000	0.3223	-1.2962	C	-0.3437	-1.2478	0.0000
H	0.0000	-1.6176	-2.1794	H	1.5946	-2.1592	0.0000
H	0.0000	-1.6176	2.1794	H	1.5946	2.1592	0.0000
O	-0.0001	2.3071	0.0000	O	-2.3776	0.0000	0.0000
O	0.0000	-3.0191	0.0000	O	3.0787	0.0000	0.0000
C	0.0000	1.1281	-2.5600	C	-1.1114	-2.5445	0.0000
C	0.0000	1.1281	2.5600	C	-1.1114	2.5445	0.0000
H	-0.8785	1.7810	-2.6020	H	-1.7648	-2.6206	0.8773
H	0.0000	0.4769	-3.4362	H	-0.4323	-3.4021	0.0000
H	0.8785	1.7809	-2.6020	H	-1.7649	-2.6206	-0.8773
H	-0.8785	1.7810	2.6020	H	-1.7648	2.6206	0.8773
H	0.0000	0.4769	3.4362	H	-0.4323	3.4021	0.0000
H	0.8785	1.7809	2.6020	H	-1.7649	2.6206	-0.8773
Q^{2-}				QH^{-}			
C	0.0000	-1.0435	1.1945	C	0.9933	-1.2051	-0.0151
C	0.0000	-1.8187	0.0000	C	1.6986	0.0000	-0.0127
C	0.0000	-1.0435	-1.1945	C	0.9933	1.2051	-0.0151
C	0.0000	0.3640	-1.2122	C	-0.4066	1.2269	-0.0019
C	0.0000	1.1245	0.0000	C	-1.1615	0.0000	0.0065
C	0.0000	0.3640	1.2122	C	-0.4066	-1.2268	-0.0019
H	0.0000	-1.5791	2.1468	H	1.5493	-2.1417	-0.0255
H	0.0000	-1.5791	-2.1468	H	1.5493	2.1417	-0.0255
O	0.0000	2.4510	0.0000	O	-2.4637	0.0000	0.0185
O	0.0000	-3.1467	0.0000	C	-1.1530	-2.5380	-0.0006
C	0.0000	1.1010	2.5319	C	-1.1530	2.5380	-0.0006
C	0.0000	1.1010	-2.5319	H	-1.8049	-2.6328	0.8777
H	0.8756	1.7568	2.6367	H	-0.4615	-3.3874	-0.0035
H	0.0000	0.4021	3.3764	H	-1.8107	-2.6321	-0.8749
H	-0.8756	1.7568	2.6367	H	-1.8049	2.6328	0.8777
H	0.8756	1.7568	-2.6367	H	-0.4615	3.3874	-0.0035
H	0.0000	0.4021	-3.3764	H	-1.8107	2.6321	-0.8749
H	-0.8756	1.7568	-2.6367	O	3.1083	0.0000	-0.0823
				H	3.4729	0.0001	0.8132
QH_2							
C	0.9744	-1.2594	0.0000				

Table 6.17 (cont'd).

C	1.7319	-0.0878	0.0000
C	1.0957	1.1559	0.0000
C	-0.3026	1.2445	0.0000
C	-1.0476	0.0545	0.0000
C	-0.4255	-1.2060	0.0000
H	1.4805	-2.2204	0.0000
H	1.6862	2.0695	0.0000
C	-1.2482	-2.4738	0.0000
C	-1.0016	2.5816	0.0000
H	-1.8937	-2.5443	0.8853
H	-0.6011	-3.3538	0.0000
H	-1.8937	-2.5443	-0.8853
H	-1.6463	2.6941	0.8792
H	-0.2769	3.3996	0.0000
H	-1.6463	2.6941	-0.8792
O	3.1057	-0.2181	0.0000
H	3.5202	0.6560	0.0000
O	-2.4233	0.1897	0.0000
H	-2.8470	-0.6791	0.0000

Table 6.18 Geometry Optimized Coordinates of the library of quinones: 2,3-dimethoxy-5-methyl-1,4-BQ (15).

Q				$Q^{\cdot-}$			
Atom	X	Y	Z	Atom	X	Y	Z
C	-0.9309	-1.8665	0.1263	C	-0.9492	-1.8236	0.1154
C	0.5088	-1.6313	-0.1025	C	0.4698	-1.6646	-0.0942
C	0.9885	-0.2204	-0.2358	C	0.9420	-0.2979	-0.2790
C	0.0891	0.8003	-0.2620	C	0.0593	0.7649	-0.3000
C	-1.3766	0.5285	-0.1500	C	-1.3791	0.5793	-0.1410
C	-1.8412	-0.8739	0.1108	C	-1.8452	-0.7792	0.0972
H	-1.2151	-2.9026	0.2854	H	-1.2994	-2.8416	0.2751
O	-2.1883	1.4431	-0.2734	O	-2.1842	1.5653	-0.2105
O	1.2961	-2.5748	-0.1882	O	1.2681	-2.6606	-0.1194
C	-3.3110	-1.0826	0.3117	C	-3.3225	-0.9968	0.2972
H	-3.8730	-0.7341	-0.5612	H	-3.8979	-0.6355	-0.5634
H	-3.6697	-0.5027	1.1690	H	-3.6930	-0.4443	1.1692
H	-3.5331	-2.1381	0.4796	H	-3.5451	-2.0578	0.4420
O	0.4912	2.0695	-0.5184	O	0.5367	2.0316	-0.5635
C	0.2836	3.0514	0.5255	C	0.4782	2.9475	0.5422
H	0.6507	3.9928	0.1172	H	0.8455	3.9052	0.1675
H	0.8667	2.7778	1.4104	H	1.1266	2.6034	1.3576
H	-0.7748	3.1392	0.7758	H	-0.5482	3.0588	0.9018
C	3.2388	-0.3597	0.5781	C	3.1540	-0.3029	0.5942
H	4.2229	-0.1020	0.1875	H	4.1680	-0.1177	0.2337
H	3.1858	-1.4283	0.7895	H	3.0684	-1.3329	0.9499
H	3.0337	0.2230	1.4815	H	2.9244	0.3961	1.4081
O	2.3024	0.0123	-0.4633	O	2.2803	-0.0731	-0.5233
Q^{2-}				QH^{-}			
C	-0.8779	-1.8290	0.1148	C	-0.8343	-1.8622	0.1185
C	0.5201	-1.6704	-0.0950	C	0.5636	-1.6675	-0.0923
C	0.9237	-0.3132	-0.2937	C	0.9554	-0.2966	-0.2880
C	0.0001	0.7517	-0.3143	C	0.0145	0.7438	-0.3136
C	-1.4095	0.5709	-0.1432	C	-1.3538	0.4803	-0.1315
C	-1.8134	-0.7795	0.0950	C	-1.7865	-0.8329	0.0954
H	-1.2363	-2.8466	0.2829	H	-1.1721	-2.8844	0.2817
O	-2.2655	1.5757	-0.2035	O	1.4213	-2.6465	-0.1099
O	1.3709	-2.6829	-0.1068	C	-3.2571	-1.1317	0.2998
C	-3.2816	-1.0715	0.3037	H	-3.8656	-0.8406	-0.5674
H	-3.8898	-0.7603	-0.5570	H	-3.6707	-0.6133	1.1760
H	-3.6913	-0.5328	1.1697	H	-3.4122	-2.2022	0.4574
H	-3.4509	-2.1423	0.4649	O	0.4272	2.0412	-0.5849
O	0.4906	2.0359	-0.5787	C	0.5428	2.8808	0.5717
C	0.4701	2.9040	0.5552	H	0.85685	3.8639	0.2136

Table 6.18 (cont'd).

H	0.8148	3.8853	0.2145	H	1.2978	2.4876	1.2633
H	1.1498	2.5386	1.3382	H	-0.4183	2.9704	1.0896
H	-0.5448	2.9896	0.9577	C	3.1636	-0.1840	0.5742
C	3.1154	-0.1837	0.5989	H	4.1719	0.0496	0.2226
H	4.1405	0.0109	0.2685	H	3.1181	-1.2223	0.9150
H	3.0416	-1.2028	0.9925	H	2.9043	0.4925	1.3997
H	2.8503	0.5377	1.3852	O	2.2839	0.0198	-0.5392
O	2.2708	-0.0230	-0.5416	O	-2.2245	1.5672	-0.1969
				H	-3.1233	1.2665	-0.0103

QH_2

C	-0.7633	-1.8785	0.1116
C	0.5805	-1.5658	-0.0885
C	0.9657	-0.2287	-0.2857
C	-0.0189	0.7741	-0.3048
C	-1.3734	0.4384	-0.1262
C	-1.7587	-0.8917	0.0958
H	-1.0501	-2.9154	0.2691
C	-3.2125	-1.2527	0.2950
H	-3.8252	-0.9868	-0.5762
H	-3.6449	-0.7505	1.1701
H	-3.3231	-2.3280	0.4516
O	0.3480	2.0711	-0.5797
C	0.3111	2.9749	0.5409
H	0.6157	3.9488	0.1543
H	1.0143	2.6527	1.3170
H	-0.6981	3.0416	0.9571
C	3.1608	0.0384	0.5956
H	4.1456	0.3323	0.2287
H	3.2048	-0.9765	1.0010
H	2.8363	0.7370	1.3749
O	2.2765	0.1023	-0.5392
O	-2.2772	1.4751	-0.1903
H	-3.1737	1.1467	-0.0379
O	1.5729	-2.5183	-0.1102
H	1.1888	-3.3932	0.0431

Table 6.19 Geometry Optimized Coordinates of the library of quinones: 2,6-dimethoxy-1,4-BQ (16).

Q				$Q^{\cdot-}$			
Atom	X	Y	Z	Atom	X	Y	Z
C	0.7987	-0.7135	-0.0001	C	-0.7728	0.6938	-0.0001
C	1.0249	0.7692	0.0001	C	-1.0718	-0.7357	0.0002
C	-0.1540	1.6704	0.0000	C	0.0585	-1.6380	-0.0004
C	-1.4055	1.1833	-0.0004	C	1.3575	-1.1913	-0.0005
C	-1.6439	-0.2813	0.0000	C	1.6692	0.2211	0.0003
C	-0.4700	-1.1772	-0.0007	C	0.5361	1.1218	-0.0001
O	-2.7921	-0.7332	0.0007	O	2.8749	0.6507	0.0004
O	2.1642	1.2351	0.0002	O	-2.2747	-1.1687	0.0006
H	-0.6855	-2.2422	-0.0012	H	0.7590	2.1877	-0.0002
H	0.0577	2.7353	0.0002	H	-0.1627	-2.7033	-0.0007
H	-2.2827	1.8230	-0.0007	H	2.1899	-1.8919	-0.0009
C	2.0081	-1.5979	0.0002	C	-1.9248	1.6644	-0.0003
H	1.7205	-2.6510	-0.0012	H	-1.5680	2.6984	-0.0009
H	2.6321	-1.3983	-0.8776	H	-2.5665	1.5183	-0.8774
H	2.6303	-1.4001	0.8797	H	-2.5662	1.5192	0.8772
Q^{2-}				QH^{-}			
C	-0.7569	0.6790	0.0000	C	-0.7892	0.6914	-0.0001
C	-1.1215	-0.7087	0.0000	C	-1.1746	-0.6977	0.0000
C	-0.0230	-1.6130	0.0000	C	-0.0965	-1.6362	-0.0001
C	1.3210	-1.2007	0.0000	C	1.2492	-1.2525	0.0000
C	1.6977	0.1716	0.0000	C	1.5851	0.1007	0.0000
C	0.5927	1.0748	0.0000	C	0.5637	1.0568	0.0000
O	2.9599	0.5795	0.0000	O	-2.4262	-1.0681	0.0001
O	-2.3851	-1.1119	0.0000	H	0.8251	2.1157	-0.0001
H	0.8195	2.1436	-0.0001	H	-0.3479	-2.6954	-0.0002
H	-0.2492	-2.6811	-0.0001	H	2.0381	-2.0018	-0.0001
H	2.1123	-1.9529	0.0000	C	-1.8649	1.7481	-0.0001
C	-1.8495	1.7229	0.0000	H	-1.4347	2.7552	-0.0010
H	-1.4307	2.7357	-0.0006	H	-2.5206	1.6564	-0.8760
H	-2.5066	1.6287	-0.8757	H	-2.5194	1.6577	0.8769
H	-2.5059	1.6295	0.8764	O	2.9390	0.4479	0.00003
				H	3.0205	1.4112	0.00033
QH_2							
C	-0.7298	0.7407	-0.0001				
C	-1.0818	-0.6204	0.0000				
C	-0.0976	-1.6119	-0.0001				
C	1.25645	-1.2668	-0.0001				
C	1.62104	0.0802	-0.0001				
C	0.6320	1.0699	-0.0001				

Table 6.19 (cont'd).

H	0.9197	2.1190	0.0000
H	-0.3846	-2.6605	-0.0001
H	2.0229	-2.0352	0.0000
C	-1.7954	1.8081	0.0000
H	-1.3480	2.8052	-0.0004
H	-2.4443	1.7225	-0.8790
H	-2.4437	1.7230	0.8796
O	2.9674	0.3787	0.0001
H	3.0958	1.3376	0.0003
O	-2.4290	-0.9201	-0.0001
H	-2.5540	-1.8793	0.0014

Table 6.20 Geometry Optimized Coordinates of the library of quinones: 3,5-di-tert-butyl-1,2-BQ (17).

Q				$Q^{\cdot-}$			
Atom	X	Y	Z	Atom	X	Y	Z
C	1.10425	-0.12371	0.00000	C	1.08973	-0.11289	0.00000
C	1.23894	1.35503	0.00000	C	1.25116	1.33953	-0.00001
C	-0.06952	2.21570	0.00000	C	0.01207	2.18119	0.00000
C	-1.34867	1.52989	-0.00001	C	-1.26471	1.52220	0.00000
C	-1.40856	0.17313	0.00000	C	-1.38939	0.14810	0.00000
C	-0.16056	-0.61711	0.00000	C	-0.18965	-0.63957	0.00000
O	2.30716	1.95182	0.00000	O	2.38632	1.91231	-0.00001
O	0.03925	3.43954	0.00001	O	0.10044	3.45287	0.00001
H	-0.28929	-1.69125	0.00000	H	-0.30638	-1.71614	0.00000
C	2.35987	-1.00877	0.00000	C	2.33558	-1.02375	0.00000
C	3.20342	-0.72111	-1.26895	C	3.18712	-0.75521	-1.26673
C	3.20341	-0.72112	1.26896	C	3.18712	-0.75520	1.26673
C	2.00089	-2.50797	-0.00001	C	1.97413	-2.52401	0.00001
H	2.62649	-0.93303	-2.17602	H	2.61535	-0.99146	-2.17234
H	3.53950	0.31663	-1.30499	H	3.49803	0.28967	-1.31485
H	4.08724	-1.36860	-1.27296	H	4.08250	-1.38949	-1.26097
H	2.62648	-0.93305	2.17603	H	2.61536	-0.99144	2.17234
H	4.08724	-1.36860	1.27297	H	4.08250	-1.38947	1.26096
H	3.53950	0.31662	1.30500	H	3.49803	0.28968	1.31485
H	2.92487	-3.09459	-0.00001	H	2.89672	-3.11518	0.00001
H	1.42892	-2.79473	0.88912	H	1.39942	-2.81055	0.88783
H	1.42892	-2.79472	-0.88914	H	1.39942	-2.81056	-0.88781
C	-2.72639	-0.60631	0.00000	C	-2.74982	-0.57352	0.00000
C	-2.78820	-1.49824	1.26778	C	-2.86743	-1.46444	1.26223
C	-3.95467	0.32250	-0.00001	C	-3.93695	0.40924	0.00000
C	-2.78820	-1.49824	-1.26778	C	-2.86743	-1.46444	-1.26223
H	-1.97157	-2.22447	1.31139	H	-2.07830	-2.22133	1.30422
H	-2.75245	-0.88880	2.17678	H	-2.80353	-0.85905	2.17344
H	-3.72895	-2.05873	1.26971	H	-3.83159	-1.98672	1.26847
H	-3.98248	0.96166	-0.88854	H	-3.93351	1.05170	-0.88704
H	-4.86505	-0.28465	-0.00001	H	-4.87732	-0.15266	0.00000
H	-3.98249	0.96166	0.88853	H	-3.93351	1.05170	0.88704
H	-3.72895	-2.05873	-1.26971	H	-3.83159	-1.98673	-1.26847
H	-2.75243	-0.88882	-2.17678	H	-2.80353	-0.85905	-2.17344
H	-1.97157	-2.22448	-1.31137	H	-2.07831	-2.22134	-1.30422
H	-2.23129	2.15772	-0.00001	H	-2.13305	2.17354	0.00000
Q^{2-}				QH^{-}			
C	1.10376	-0.10979	0.00000	C	1.07848	-0.18558	0.00000
C	1.25447	1.31567	0.00000	C	1.17959	1.20498	0.00000

Table 6.20 (cont'd).

C	0.02170	2.13344	0.00000	C	0.03862	2.07769	0.00000
C	-1.22306	1.46319	0.00000	C	-1.23299	1.47129	0.00000
C	-1.36642	0.05574	0.00000	C	-1.38582	0.06962	0.00000
C	-0.19166	-0.69996	0.00000	C	-0.23434	-0.72898	0.00000
O	2.42257	1.91672	0.00000	O	0.28170	3.36935	0.00000
O	0.08974	3.44826	0.00000	H	-0.34143	-1.80375	0.00000
H	-0.26605	-1.77944	0.00000	C	2.33249	-1.08788	0.00000
C	2.36095	-1.01653	0.00000	C	3.18229	-0.80875	-1.26488
C	3.21525	-0.74377	-1.26351	C	3.18229	-0.80876	1.26488
C	3.21525	-0.74377	1.26351	C	1.98297	-2.59057	0.00000
C	2.03215	-2.52580	0.00000	H	2.61217	-1.04405	-2.17149
H	2.65993	-1.02256	-2.16851	H	3.48906	0.23818	-1.31511
H	3.46911	0.31666	-1.32094	H	4.08391	-1.43419	-1.26310
H	4.14177	-1.33523	-1.24534	H	2.61217	-1.04406	2.17149
H	2.65992	-1.02256	2.16851	H	4.08390	-1.43420	1.26310
H	4.14177	-1.33523	1.24535	H	3.48907	0.23818	1.31511
H	3.46910	0.31666	1.32095	H	2.90940	-3.17604	-0.00001
H	2.96735	-3.09973	0.00000	H	1.40927	-2.87949	0.88733
H	1.46198	-2.82578	0.88679	H	1.40926	-2.87948	-0.88733
H	1.46197	-2.82577	-0.88679	C	-2.80828	-0.53404	0.00000
C	-2.77608	-0.57258	0.00000	C	-3.57776	-0.06449	1.25962
C	-3.56317	-0.12196	1.25691	C	-3.57776	-0.06450	-1.25962
C	-3.56318	-0.12195	-1.25690	C	-2.80382	-2.07600	0.00000
C	-2.74375	-2.11447	0.00000	H	-3.06904	-0.39562	2.17243
H	-3.05488	-0.45071	2.17127	H	-3.66188	1.02589	1.29875
H	-3.65789	0.96762	1.30036	H	-4.59301	-0.48030	1.26736
H	-4.57510	-0.54859	1.25955	H	-3.06904	-0.39562	-2.17242
H	-3.05488	-0.45070	-2.17126	H	-4.59301	-0.48030	-1.26735
H	-4.57510	-0.54859	-1.25954	H	-3.66188	1.02589	-1.29876
H	-3.65790	0.96763	-1.30035	H	-3.83539	-2.44587	0.00000
H	-3.76741	-2.50783	-0.00001	H	-2.30599	-2.48276	-0.88697
H	-2.23528	-2.51033	-0.88619	H	-2.30599	-2.48277	0.88698
H	-2.23529	-2.51033	0.88618	H	-2.10137	2.12626	0.00000
H	-2.10894	2.10016	0.00000	O	2.37654	1.89694	0.00000
				H	2.03831	2.82958	0.00000

QH_2

C	1.05444	-0.18478	0.00459
C	1.18410	1.21837	0.00521
C	0.05150	2.04321	-0.00342
C	-1.23314	1.50414	-0.00889
C	-1.40893	0.11633	0.00104
C	-0.25726	-0.69053	0.01147

Table 6.20 (cont'd).

H	-0.38898	-1.76383	0.01757
C	2.28268	-1.12517	-0.00621
C	3.15310	-0.85690	-1.26141
C	3.12034	-0.94200	1.28666
C	1.87333	-2.61323	-0.05377
H	2.57912	-1.06066	-2.17178
H	3.51388	0.17250	-1.32142
H	4.02613	-1.51897	-1.25702
H	2.51047	-1.14100	2.17366
H	3.96329	-1.64134	1.28682
H	3.55207	0.05789	1.41084
H	2.77732	-3.23027	-0.07765
H	1.29402	-2.91075	0.82616
H	1.28927	-2.84779	-0.94928
C	-2.80470	-0.53953	0.00189
C	-2.96739	-1.41390	1.26952
C	-3.94008	0.50298	-0.00763
C	-2.96118	-1.43052	-1.25490
H	-2.21774	-2.20979	1.31438
H	-2.87098	-0.80754	2.17709
H	-3.95698	-1.88549	1.27941
H	-3.90413	1.13800	-0.89947
H	-4.90707	-0.01101	-0.00658
H	-3.90834	1.14950	0.87608
H	-3.95051	-1.90270	-1.26322
H	-2.86080	-0.83602	-2.16986
H	-2.21096	-2.22652	-1.28582
H	-2.06967	2.19251	-0.01322
O	2.37603	1.92898	-0.03584
H	3.08341	1.45947	0.42395
O	0.20189	3.40765	-0.00449
H	1.15295	3.59987	0.04714

Table 6.21 Geometry Optimized Coordinates of the library of quinones: catechol (18).

Q				$Q^{\cdot-}$			
Atom	X	Y	Z	Atom	X	Y	Z
C	0	-0.7326	1.7771	C	0.0000	-0.7129	1.8104
C	0	-1.4588	0.6362	C	0.0000	-1.4123	0.6218
C	0	-0.7838	-0.6649	C	0.0000	-0.7514	-0.6600
C	0	0.7838	-0.6649	C	0.0000	0.7514	-0.6600
C	0	1.4588	0.6362	C	0.0000	1.4123	0.6218
C	0	0.7326	1.7771	C	0.0000	0.7129	1.8104
H	0	-1.2343	2.7401	H	0.0000	-1.2469	2.7574
H	0	-2.5440	0.6385	H	0.0000	-2.5002	0.6153
H	0	2.5440	0.6385	H	0.0000	2.5002	0.6153
H	0	1.2343	2.7401	H	0.0000	1.2469	2.7574
O	0	1.3813	-1.7336	O	0.0000	1.4037	-1.7508
O	0	-1.3813	-1.7336	O	0.0000	-1.4037	-1.7508
Q^{2-}				QH^{-}			
C	0.0000	-0.6969	1.8468	C	1.8863	0.6618	0.0000
C	0.0000	-1.3847	0.6112	C	0.6906	1.4027	0.0000
C	0.0000	-0.7408	-0.6538	C	-0.5717	0.7610	0.0000
C	0.0000	0.7408	-0.6538	C	-0.5461	-0.6765	0.0000
C	0.0000	1.3847	0.6112	C	0.6280	-1.4108	0.0000
C	0.0000	0.6969	1.8468	C	1.8682	-0.7355	0.0000
H	0.0000	-1.2564	2.7816	H	2.8380	1.1893	0.0000
H	0.0000	-2.4765	0.6053	H	0.7199	2.4909	0.0000
H	0.0000	2.4765	0.6053	H	0.5844	-2.4979	0.0000
H	0.0000	1.2564	2.7816	H	2.7946	-1.3030	0.0000
O	0.0000	1.4198	-1.7765	O	-1.7909	-1.2673	0.0000
O	0.0000	-1.4198	-1.7765	O	-1.7450	1.3399	0.0000
				H	-2.3815	-0.4759	0.0000
QH_2							
C	1.8831	0.7349	0.0000				
C	0.6538	1.4069	0.0000				
C	-0.5342	0.6780	0.0000				
C	-0.5021	-0.7276	0.0000				
C	0.7223	-1.3933	0.0000				
C	1.9162	-0.6619	0.0000				
H	2.8051	1.3075	0.0000				
H	0.6181	2.4932	0.0000				
H	0.7282	-2.4790	0.0000				
H	2.8660	-1.1873	0.0000				
O	-1.6678	-1.4494	0.0000				
O	-1.7931	1.2340	0.0000				
H	-2.4173	-0.8332	0.0000				

Table 6.21 (cont'd).

H	-1.7477	2.2003	0.0000

Table 6.22 Geometry Optimized Coordinates of the library of quinones: 4-methylcatechol (19).

Q				$Q^{\cdot-}$			
Atom	X	Y	Z	Atom	X	Y	Z
C	-0.9830	-1.3089	0.0000	C	-1.0178	-1.3068	0.0000
C	-1.4858	0.0790	0.0000	C	-1.5049	0.0401	0.0000
C	-0.6184	1.1245	0.0000	C	-0.5918	1.0771	0.0000
C	0.8239	0.9144	0.0000	C	0.8352	0.8754	0.0000
C	1.3405	-0.5620	0.0000	C	1.3303	-0.5396	0.0000
C	0.3299	-1.6235	0.0000	C	0.3328	-1.5796	0.0000
H	-1.7257	-2.1022	-0.0001	H	-1.7351	-2.1250	0.0000
H	-0.9673	2.1529	0.0000	H	-0.9374	2.1096	0.0000
H	0.6787	-2.6513	0.0000	H	0.6903	-2.6074	0.0000
O	1.6419	1.8296	0.0000	O	1.6499	1.8526	0.0000
O	2.5454	-0.7807	0.0001	O	2.5761	-0.8011	0.0000
C	-2.9736	0.2643	0.0000	C	-2.9939	0.2926	0.0000
H	-3.4168	-0.2191	-0.8793	H	-3.4733	-0.1540	-0.8803
H	-3.2515	1.3197	0.0000	H	-3.2177	1.3630	0.0000
H	-3.4168	-0.2191	0.8794	H	-3.4733	-0.1540	0.8803
Q^{2-}				QH^{-}			
C	-1.0548	-1.3074	0.0000	C	-1.0985	-1.3036	0.0000
C	-1.5291	0.0029	0.0000	C	-1.5543	0.0185	0.0000
C	-0.5729	1.0481	0.0000	C	-0.5703	1.0303	0.0000
C	0.8336	0.8584	0.0000	C	0.7887	0.7369	0.0000
C	1.3250	-0.5397	0.0000	C	1.2935	-0.6138	0.0000
C	0.3402	-1.5565	0.0000	C	0.2717	-1.6073	0.0000
H	-1.7536	-2.1445	0.0000	H	-1.8216	-2.1184	0.0000
H	-0.9246	2.0828	0.0000	H	-0.8801	2.0769	0.0000
H	0.6952	-2.5894	0.0000	H	0.5919	-2.6482	0.0000
O	1.6679	1.8717	0.0000	O	1.7419	1.7487	0.0000
O	2.6117	-0.8093	0.0000	O	2.5659	-0.8823	0.0000
C	-3.0115	0.3179	0.0000	C	-3.0268	0.3679	0.0000
H	-3.6109	-0.5999	0.0000	H	-3.6434	-0.5370	0.0000
H	-3.3126	0.9048	-0.8798	H	-3.3112	0.9590	-0.8808
H	-3.3126	0.9048	0.8798	H	-3.3112	0.9590	0.8808
				H	1.2897	2.6037	0.0000
QH_2							
C	-1.1098	-1.3152	0.0000				
C	-1.5847	0.0002	0.0000				
C	-0.6416	1.0424	0.0000				
C	0.7290	0.7865	0.0000				
C	1.1924	-0.5426	0.0000				
C	0.2658	-1.5830	0.0000				
H	-1.8107	-2.1450	0.0000				

Table 6.22 (cont'd).

H	-0.9796	2.0770	0.0000
H	0.6198	-2.6112	0.0000
C	-3.0648	0.3097	0.0000
H	-3.6589	-0.6083	0.0000
H	-3.3511	0.8952	-0.8815
H	-3.3511	0.8952	0.8816
O	2.5531	-0.7377	0.0000
H	2.7452	-1.6860	0.0000
O	1.6755	1.7814	0.0000
H	1.2394	2.6454	0.0000

Table 6.23 Geometry Optimized Coordinates of the library of quinones: 4-ethylcatechol (19).

Q				$Q^{\cdot-}$			
Atom	X	Y	Z	Atom	X	Y	Z
C	-1.0283	0.3648	0.0000	C	-1.0412	0.4108	0.0003
C	-0.4244	-0.8521	0.0002	C	-0.3908	-0.8079	0.0002
C	1.0278	-0.9783	0.0001	C	1.0460	-0.9376	0.0003
C	1.8728	0.3371	0.0000	C	1.8555	0.3220	-0.0002
C	1.1348	1.6023	-0.0001	C	1.1248	1.5635	0.0001
C	-0.2149	1.5976	0.0001	C	-0.2514	1.6074	0.0004
H	-0.9905	-1.7773	0.0001	H	-0.9510	-1.7391	0.0001
H	1.7103	2.5226	-0.0001	H	1.7080	2.4822	0.0002
H	-0.7542	2.5414	0.0003	H	-0.7605	2.5695	0.0006
O	3.0957	0.2704	0.0000	O	3.1283	0.2874	-0.0010
O	1.6123	-2.0580	-0.0001	O	1.6133	-2.0768	0.0006
C	-2.5211	0.5655	-0.0001	C	-2.5528	0.5573	0.0003
C	-3.3873	-0.6931	0.0000	C	-3.3709	-0.7364	-0.0008
H	-2.7667	1.1918	-0.8705	H	-2.8393	1.1634	-0.8714
H	-3.2048	-1.3090	-0.8868	H	-3.1625	-1.3463	-0.8867
H	-3.2047	-1.3087	0.8870	H	-3.1625	-1.3478	0.8840
H	-4.4447	-0.4141	0.0000	H	-4.4408	-0.5044	-0.0007
H	-2.7667	1.1921	0.8701	H	-2.8395	1.1621	0.8728
Q^{2-}				QH^{-}			
C	-1.0773	0.2061	-0.3295	C	1.1072	-0.1872	-0.3388
C	-0.2330	-0.9306	-0.2691	C	0.2310	0.9170	-0.2683
C	1.1709	-0.8858	-0.0650	C	-1.1349	0.7627	-0.0563
C	1.7846	0.4512	0.1061	C	-1.7546	-0.5282	0.1046
C	0.9106	1.5637	0.0354	C	-0.8399	-1.6196	0.0258
C	-0.4848	1.4597	-0.1781	C	0.5359	-1.4563	-0.1879
H	-0.6772	-1.9220	-0.3903	H	0.6319	1.9254	-0.3860
H	1.3589	2.5527	0.1506	H	-1.2542	-2.6209	0.1348
H	-1.0934	2.3636	-0.2255	H	1.1730	-2.3387	-0.2403
O	3.0771	0.5887	0.3045	O	-3.0325	-0.6700	0.2970
O	1.9012	-1.9768	-0.0307	C	2.5978	0.0099	-0.5280
C	-2.5749	0.0501	-0.5180	C	3.3543	0.3618	0.7679
C	-3.3372	-0.3731	0.7537	H	2.7781	0.8058	-1.2637
H	-2.7801	-0.6929	-1.3031	H	2.9708	1.2899	1.2070
H	-2.9703	-1.3347	1.1304	H	3.2416	-0.4323	1.5149
H	-3.2081	0.3680	1.5515	H	4.4257	0.4973	0.5762
H	-4.4126	-0.4762	0.5594	H	3.0314	-0.9049	-0.9521
H	-2.9953	0.9995	-0.8767	O	-1.9826	1.8637	0.0044
				H	-1.4583	2.6674	-0.1170
QH_2							
C	1.1414	-0.1506	-0.3454				

Table 6.23 (cont'd).

C	0.2798	0.9559	-0.2646
C	-1.0911	0.8006	-0.0561
C	-1.6351	-0.4894	0.0774
C	-0.7891	-1.5949	-0.0043
C	0.5849	-1.4285	-0.2142
H	0.6813	1.9624	-0.3691
H	-1.2098	-2.5931	0.0920
H	1.2218	-2.3065	-0.2780
C	2.6324	0.0461	-0.5311
C	3.3848	0.2777	0.7930
H	2.8088	0.9004	-1.1959
H	3.0113	1.1702	1.3069
H	3.2616	-0.5758	1.4686
H	4.4565	0.4150	0.6114
H	3.0523	-0.8338	-1.0324
O	-1.9607	1.8608	0.0224
H	-1.4736	2.6897	-0.0886
O	-2.9915	-0.5873	0.2779
H	-3.2415	-1.5189	0.3549

Table 6.24 Geometry Optimized Coordinates of the library of quinones: 3-bromo-1,2-benzenediol (21).

Q				$Q^{\cdot-}$			
Atom	X	Y	Z	Atom	X	Y	Z
C	-1.6331	1.9159	0.0000	C	-1.5874	1.9520	0.0000
C	-0.2026	1.6154	0.0000	C	-0.1964	1.6513	0.0000
C	0.2659	0.3480	0.0000	C	0.2177	0.3385	0.0000
C	-0.6706	-0.7939	0.0000	C	-0.6901	-0.7848	0.0000
C	-2.2054	-0.4478	0.0000	C	-2.1594	-0.4398	0.0000
C	-2.5906	0.9618	0.0000	C	-2.5325	0.9510	0.0000
H	-1.9097	2.9656	0.0000	H	-1.8922	2.9949	0.0000
H	0.4867	2.4528	0.0000	H	0.5290	2.4578	0.0000
H	-3.6491	1.1980	0.0000	H	-3.5946	1.1817	0.0000
O	-0.3256	-1.9615	0.0000	O	-0.3099	-1.9875	0.0000
O	-3.0047	-1.3727	0.0000	O	-3.0214	-1.3677	0.0000
Br	2.1124	-0.0440	0.0000	Br	2.0942	-0.0515	0.0000
Q^{2-}				QH^{-}			
C	-1.5455	1.9902	0.0000	C	1.4818	2.0514	0.0000
C	-0.1873	1.6903	0.0000	C	0.1306	1.7072	0.0000
C	0.1807	0.3291	0.0000	C	-0.2434	0.3557	0.0000
C	-0.6995	-0.7792	0.0000	C	0.6885	-0.7085	0.0000
C	-2.1488	-0.4247	0.0000	C	2.0656	-0.2836	0.0000
C	-2.4976	0.9491	0.0000	C	2.4647	1.0405	0.0000
H	-1.8713	3.0289	0.0000	H	1.7741	3.0971	0.0000
H	0.5691	2.4686	0.0000	H	-0.6332	2.4783	0.0000
H	-3.5607	1.1908	0.0000	H	3.5233	1.2867	0.0000
O	-0.3098	-2.0170	0.0000	O	0.4466	-1.9826	0.0000
O	-3.0488	-1.3699	0.0000	O	2.9687	-1.3202	0.0000
Br	2.0891	-0.0606	0.0000	Br	-2.1111	-0.0945	0.0000
				H	2.3760	-2.1084	0.0000

QH_2			
C	-1.50533	2.04582	0.00000
C	-0.14302	1.74317	0.00000
C	0.25104	0.40377	0.00001
C	-0.68766	-0.62890	0.00000
C	-2.05633	-0.30262	0.00000
C	-2.46480	1.02855	0.00000
H	-1.82136	3.08385	0.00000
H	0.60254	2.52965	0.00000
H	-3.52605	1.25374	0.00000
Br	2.09850	-0.06496	0.00000
O	-2.99490	-1.29748	0.00000
H	-2.54730	-2.15861	0.00000

Table 6.24 (cont'd).

O	-0.39137	-1.96246	0.00000
H	0.57149	-2.09416	0.00000

Table 6.25 Geometry Optimized Coordinates of the library of quinones: 3-fluoro-1,2-benzenediol (22).

Q				$Q^{\cdot-}$			
Atom	X	Y	Z	Atom	X	Y	Z
C	0.3623	1.9772	0.0000	C	0.2363	2.0142	0.0000
C	-0.9995	1.4426	-0.0000	C	-1.0631	1.4262	0.0000
C	-1.2142	0.1147	-0.0000	C	-1.1650	0.0611	0.0000
C	-0.1123	-0.8620	0.0000	C	-0.0492	-0.8507	0.0000
C	1.3376	-0.2608	-0.0000	C	1.3087	-0.2091	0.0000
C	1.4671	1.1961	0.0000	C	1.3704	1.2331	0.0000
H	0.4629	3.0577	0.0000	H	0.3179	3.0973	0.0000
H	-1.8394	2.1290	-0.0000	H	-1.9581	2.0400	0.0000
H	2.4686	1.6121	0.0000	H	2.3585	1.6861	0.0000
O	2.2838	-1.0353	-0.0000	O	2.3520	-0.9302	-0.0000
O	-0.2848	-2.0681	0.0000	O	-0.2029	-2.1077	0.0000
F	-2.4589	-0.4020	-0.0000	F	-2.4155	-0.5076	-0.0000
Q^{2-}				QH^{-}			
C	0.1067	2.0481	0.0000	C	0.3052	2.0520	0.0000
C	-1.1325	1.4051	0.0000	C	-1.0010	1.5453	0.0000
C	-1.1267	0.0041	0.0000	C	-1.1187	0.1569	0.0000
C	-0.0023	-0.8474	0.0000	C	-0.0505	-0.7246	0.0000
C	1.3016	-0.1449	0.0000	C	1.3033	-0.2280	0.0000
C	1.2865	1.2781	0.0000	C	1.4133	1.2003	0.0000
H	0.1613	3.1349	0.0000	H	0.4571	3.1287	0.0000
H	-2.0749	1.9461	0.0000	H	-1.8825	2.1762	0.0000
H	2.2551	1.7793	0.0000	H	2.4182	1.6168	0.0000
O	2.4216	-0.8212	0.0000	O	2.3195	-1.0261	0.0000
O	-0.1019	-2.1534	0.0000	O	-0.2489	-2.0927	0.0000
F	-2.3888	-0.6136	0.0000	F	-2.3850	-0.4132	0.0000
				H	-1.2022	-2.2639	0.0000
QH_2							
C	-0.1045	2.0921	0.0000				
C	-1.2899	1.3491	0.0000				
C	-1.1862	-0.0343	0.0000				
C	0.0336	-0.7036	0.0000				
C	1.2112	0.0604	0.0000				
C	1.1400	1.4547	0.0000				
H	-0.1521	3.1758	0.0000				
H	-2.2670	1.8186	0.0000				
H	2.06243	2.0259	0.0000				
O	2.43060	-0.5575	0.0000				
O	0.16250	-2.0661	0.0000				
F	-2.3120	-0.8147	0.0000				

Table 6.25 (cont'd).

H	-0.7092	-2.4893	0.0000
H	2.3042	-1.5196	0.0000

Table 6.26 Geometry Optimized Coordinates of the library of quinones: 3,4,5-trihydroxybenzoic acid (23).

Q				$Q^{\cdot-}$			
Atom	X	Y	Z	Atom	X	Y	Z
C	-1.0323	-0.0672	0.0354	C	0.9924	-0.0760	0.0000
C	-0.2683	1.1773	0.0921	C	0.2775	1.1657	0.0000
C	1.0863	1.1962	0.0840	C	-1.0943	1.1754	0.0000
C	1.8429	-0.0766	-0.0091	C	-1.8827	-0.0525	0.0000
C	1.0081	-1.4016	-0.0766	C	-1.1198	-1.3460	0.0000
C	-0.4342	-1.2886	-0.0442	C	0.3125	-1.2832	0.0000
H	-0.8370	2.1006	0.1380	H	0.8303	2.0993	0.0000
H	-1.0220	-2.1992	-0.0752	H	0.8624	-2.2185	0.0000
O	3.0616	-0.1205	-0.0356	O	-3.1408	-0.0293	0.0000
O	1.6245	-2.4638	-0.1453	O	-1.7455	-2.4510	0.0000
O	1.8700	2.2992	0.1511	O	-1.8317	2.3335	0.0000
H	1.3246	3.0991	0.2057	H	-1.2360	3.0967	0.0000
C	-2.5608	0.0554	-0.0020	C	2.4674	-0.0977	0.0000
O	-2.9938	1.0741	-0.6097	O	3.0307	1.1394	0.0000
O	-3.2268	-0.8603	0.5461	H	3.9956	1.0198	0.0000
				O	3.1661	-1.1065	0.0000
Q^{2-}				QH^{-}			
C	-1.0633	-0.0187	0.0000	C	1.0887	-0.0368	0.0000
C	-0.3231	1.1750	0.0000	C	0.3961	1.1849	0.0000
C	1.0760	1.1331	0.0000	C	-1.0077	1.1962	0.0000
C	1.8457	-0.0639	0.0000	C	-1.7103	-0.0009	0.0000
C	1.0762	-1.3199	0.0000	C	-1.0444	-1.2682	0.0000
C	-0.3401	-1.2343	0.0000	C	0.3713	-1.2469	0.0000
H	-0.8424	2.1312	0.0000	H	0.9517	2.1175	0.0000
H	-0.8945	-2.1704	0.0000	H	0.9147	-2.1866	0.0000
O	3.1559	-0.0494	0.0000	O	-1.8091	-2.3332	0.0000
O	1.6984	-2.4800	0.0000	O	-1.7374	2.3779	0.0000
O	1.8008	2.3424	0.0000	H	-1.1214	3.1236	0.0000
H	1.1611	3.0669	0.0000	C	2.6162	-0.0391	0.0000
C	-2.5720	0.0106	0.0000	O	3.2062	1.0870	0.0000
O	-3.1563	1.1485	0.0000	O	3.2045	-1.1650	0.0000
O	-3.2014	-1.1014	0.0000	O	-3.0865	-0.0605	0.0000
				H	-3.2273	-1.0389	0.0000
QH_2							
C	1.1104	-0.0116	0.0000				
C	0.4152	1.2048	0.0000				
C	-0.9812	1.2304	0.0000				
C	-1.7050	0.0311	0.0000				
C	-1.0047	-1.1830	0.0000				

Table 6.26 (cont'd).

C	0.38777	-1.2129	0.0000
H	0.9773	2.1332	0.0000
H	0.92231	-2.1572	0.0000
O	-1.7111	2.39500	0.0000
H	-1.1084	3.1520	0.0000
C	2.6402	-0.0290	0.0000
O	3.2285	1.0927	0.0000
O	3.2018	-1.1645	0.0000
O	-3.0755	0.0633	0.0000
H	-3.3994	-0.8513	0.0000
O	-1.8061	-2.3048	0.0000
H	-1.2679	-3.1086	-0.0000

Table 6.27 Geometry Optimized Coordinates of the library of quinones: 3,4-dihydroxyphenylactic acid (24).

Q				$Q^{\cdot-}$			
Atom	X	Y	Z	Atom	X	Y	Z
C	0.4174	-0.2103	-0.5265	C	0.4128	0.0088	-0.5386
C	-0.4565	-1.2045	-0.2100	C	-0.4581	-1.0495	-0.3568
C	-1.8475	-0.9237	0.1047	C	-1.8491	-0.8846	-0.0238
C	-2.3138	0.5682	0.0534	C	-2.3626	0.5178	0.1124
C	-1.3094	1.5683	-0.3068	C	-1.4135	1.5821	-0.0940
C	-0.0373	1.1929	-0.5658	C	-0.0929	1.3420	-0.4047
H	-0.1444	-2.2447	-0.1818	H	-0.1012	-2.0733	-0.4608
H	-1.6258	2.6057	-0.3526	H	-1.7843	2.6009	-0.0002
H	0.7031	1.9411	-0.8290	H	0.5877	2.1779	-0.5539
O	-3.4815	0.8448	0.3070	O	-3.5834	0.7480	0.3927
O	-2.6671	-1.7922	0.3992	O	-2.6225	-1.8821	0.1448
C	1.8561	-0.4822	-0.8327	C	1.8649	-0.2080	-0.8784
C	2.8402	0.0349	0.2723	C	2.9000	-0.0632	0.2819
H	2.1424	0.0273	-1.7626	H	2.1784	0.4871	-1.6666
H	2.0293	-1.5505	-0.9834	H	2.0068	-1.2163	-1.2871
O	4.0183	-0.4012	0.1911	O	4.1122	-0.0280	-0.0868
O	2.3803	0.8436	1.1249	O	2.4817	-0.0190	1.4719
Q^{2-}				QH^{-}			
C	0.4279	0.3632	-0.5583	C	-0.4621	-0.0826	-0.5361
C	-0.2938	-0.8456	-0.3954	C	0.4208	1.0028	-0.4339
C	-1.6641	-0.9269	-0.0343	C	1.8050	0.8864	-0.0988
C	-2.3840	0.3497	0.1730	C	2.2522	-0.4643	0.1196
C	-1.6306	1.5365	0.0028	C	1.3901	-1.5499	0.0158
C	-0.2607	1.5585	-0.3544	C	0.0338	-1.3758	-0.3136
H	0.2244	-1.7930	-0.5568	H	0.0488	2.0118	-0.6119
H	-2.1571	2.4818	0.1511	H	1.7792	-2.5542	0.1868
H	0.2528	2.5134	-0.4693	H	-0.6188	-2.2419	-0.3941
O	-3.6612	0.3701	0.4878	O	2.6022	1.9081	-0.0033
O	-2.2768	-2.0807	0.1029	C	-1.9193	0.1262	-0.8918
C	1.9033	0.3438	-0.9310	C	-2.9538	0.1046	0.2722
C	2.8460	-0.0982	0.2183	H	-2.2426	-0.6231	-1.6227
H	2.2038	1.3533	-1.2379	H	-2.0421	1.1030	-1.3802
H	2.0719	-0.3288	-1.7815	O	-4.1245	-0.2738	-0.0412
O	3.0690	0.7399	1.1456	O	-2.5894	0.4967	1.4176
O	3.3366	-1.2684	0.1599	O	3.5994	-0.6315	0.4351
				H	3.7743	-1.5751	0.5543
QH_2							
C	-0.5059	-0.2512	-0.5385				
C	0.3030	0.8944	-0.4663				

Table 6.27 (cont'd).

C	1.6531	0.8016	-0.1373
C	2.2276	-0.4531	0.1212
C	1.4421	-1.6004	0.0464
C	0.0848	-1.4966	-0.2829
H	-0.1143	1.8782	-0.6642
H	1.8896	-2.5724	0.2387
H	-0.5151	-2.4007	-0.3415
C	-1.9706	-0.1379	-0.8820
C	-2.9646	0.1331	0.2906
H	-2.3123	-1.0550	-1.3753
H	-2.1264	0.6700	-1.6074
O	-4.1851	0.1629	-0.0496
O	-2.5103	0.3051	1.4552
O	3.5718	-0.4376	0.4304
H	3.8972	-1.3334	0.5957
O	2.4162	1.9419	-0.0749
H	3.3247	1.6947	0.1591

Table 6.28 Geometry Optimized Coordinates of the library of quinones: 3,4-dihydroxy-DL-phenylalamine (25).

Q				Q^{-}			
Atom	X	Y	Z	Atom	X	Y	Z
C	-0.4088	-0.1698	-0.5275	C	-0.3590	0.0092	-0.6059
C	-1.0178	0.9704	-0.1101	C	-1.1321	1.0709	-0.1710
C	-2.4448	1.0021	0.1968	C	-2.5277	0.9416	0.1581
C	-3.2517	-0.3255	0.0248	C	-3.1472	-0.4216	0.0173
C	-2.5094	-1.4996	-0.4409	C	-2.2931	-1.4845	-0.4463
C	-1.1852	-1.4114	-0.6929	C	-0.9622	-1.2810	-0.7457
H	-0.4756	1.9049	0.0046	H	-0.6955	2.0626	-0.0641
H	-3.0603	-2.4254	-0.5720	H	-2.7421	-2.4682	-0.5616
H	-0.6489	-2.2897	-1.0412	H	-0.3620	-2.1092	-1.1184
O	-3.0287	2.0122	0.5744	O	-3.2191	1.9303	0.5513
O	-4.4495	-0.3421	0.2766	O	-4.3712	-0.6132	0.2909
C	1.0713	-0.2011	-0.8577	C	1.1192	0.1806	-0.8928
C	2.0104	0.1056	0.3147	C	1.9988	0.2253	0.3750
C	3.5008	0.3454	-0.1236	C	3.5168	0.2743	0.0158
H	1.6825	1.0045	0.8417	H	1.7275	1.0838	0.9906
H	1.2895	0.5625	-1.6105	H	1.3066	1.1202	-1.4201
H	1.3412	-1.1644	-1.3028	H	1.4723	-0.6283	-1.5432
N	2.0622	-0.9978	1.3456	N	1.8039	-1.0210	1.2083
H	3.0903	-1.0354	1.5631	H	2.6593	-1.5830	1.0011
H	1.5099	-0.8137	2.1844	H	1.7923	-0.8202	2.2095
O	4.3576	-0.2551	0.5907	O	4.1558	-0.7979	0.2360
O	3.6783	1.1168	-1.0870	O	3.9330	1.3475	-0.4730
H	1.7857	-1.9088	0.9739	H	0.9457	-1.5322	0.9802
Q^{2-}				QH^{-}			
C	-0.3273	0.0195	-0.6741	C	-0.2950	-0.0625	-0.6362
C	-1.1565	1.0753	-0.2232	C	-1.1013	1.0244	-0.2162
C	-2.5223	0.9243	0.1311	C	-2.4346	0.82064	0.08533
C	-3.1010	-0.4420	0.0315	C	-3.0738	-0.4682	0.00119
C	-2.2378	-1.4697	-0.4206	C	-2.2475	-1.5341	-0.4215
C	-0.8803	-1.2624	-0.7631	C	-0.8898	-1.3279	-0.7295
H	-0.7355	2.0799	-0.1418	H	-0.6808	2.0251	-0.1344
H	-2.6621	-2.4709	-0.5089	H	-2.6812	-2.5276	-0.5130
H	-0.2851	-2.0942	-1.1418	H	-0.2951	-2.1731	-1.0738
O	-3.2508	1.9335	0.5259	O	-4.3402	-0.5284	0.3107
O	-4.3509	-0.6675	0.3409	C	1.1780	0.1348	-0.9188
C	1.1441	0.2475	-0.9385	C	2.0414	0.2715	0.3591
C	1.99365	0.27541	0.36218	C	3.56214	0.28970	0.02809
C	3.51729	0.23261	0.06779	H	1.75922	1.16727	0.91365
H	1.7397	1.1549	0.9551	H	1.3576	1.0423	-1.5040

Table 6.28 (cont'd).

H	1.3276	1.2013	-1.4438	H	1.5603	-0.7069	-1.5094
H	1.5379	-0.5437	-1.5895	N	1.8071	-0.9205	1.2540
N	1.6615	-0.9459	1.1803	H	2.6210	-1.5406	1.0664
H	2.4358	-1.6088	0.9868	H	1.8190	-0.6761	2.2451
H	1.6440	-0.7595	2.1834	O	4.1818	-0.7886	0.2721
O	4.0800	-0.8877	0.2580	O	4.0052	1.3482	-0.4733
O	4.0279	1.2946	-0.3613	H	0.9118	-1.3809	1.0470
H	0.7407	-1.3229	0.8918	O	-3.2640	1.8393	0.4864
				H	-4.1192	1.3607	0.6101

QH_2

C	-0.2706	-0.0979	-0.6158
C	-1.0406	1.0021	-0.1994
C	-2.3913	0.8522	0.0960
C	-3.0006	-0.4120	-0.0184
C	-2.2508	-1.5078	-0.4308
C	-0.8898	-1.3495	-0.7287
H	-0.5980	1.9901	-0.1075
H	-2.7231	-2.4818	-0.5248
H	-0.3217	-2.2102	-1.0708
C	1.2077	0.0666	-0.9043
C	2.0754	0.2292	0.3607
C	3.5934	0.3087	0.0031
H	1.7740	1.1158	0.9198
H	1.3889	0.9573	-1.5125
H	1.5720	-0.7927	-1.4791
N	1.9190	-0.9675	1.2697
H	2.7955	-1.5102	1.1018
H	1.8935	-0.7058	2.2565
O	4.2686	-0.7216	0.2994
O	3.9714	1.3605	-0.5569
H	1.0808	-1.5216	1.0712
O	-3.1214	1.9390	0.4933
H	-4.0388	1.6619	0.6470
O	-4.3373	-0.4460	0.2964
H	-4.7021	-1.3342	0.1776